Failure Analysis for Molten Salt Thermal Energy Storage Tanks for In-Service CSP Plants

Julian D. Osorio,[1] Mark Mehos,[1] Luca Imponenti,[2] Bruce Kelly,[2] Hank Price,[2] Jose Torres-Madronero,[3] Alejandro Rivera-Alvarez,[3] Cesar Nieto-Londono,[4] Chen Ni,[5] Zhenzhen Yu,[5] William Hamilton,[1] and Janna Martinek[1]

1 National Renewable Energy Laboratory
2 Solar Dynamics LLC
3 Ingeniería Térmica Ltda
4 Universidad Pontificia Bolivariana
5 Colorado School of Mines

NREL is a national laboratory of the U.S. Department of Energy
Office of Energy Efficiency & Renewable Energy
Operated by the Alliance for Sustainable Energy, LLC

This report is available at no cost from the National Renewable Energy Laboratory (NREL) at www.nrel.gov/publications.

Contract No. DE-AC36-08GO28308

Technical Report
NREL/TP-5700-89036
March 2024

Failure Analysis for Molten Salt Thermal Energy Storage Tanks for In-Service CSP Plants

Julian D. Osorio,[1] Mark Mehos,[1] Luca Imponenti,[2] Bruce Kelly,[2] Hank Price,[2] Jose Torres-Madronero,[3] Alejandro Rivera-Alvarez,[3] Cesar Nieto-Londono,[4] Chen Ni,[5] Zhenzhen Yu,[5] William Hamilton,[1] and Janna Martinek[1]

1 National Renewable Energy Laboratory
2 Solar Dynamics LLC
3 Ingeniería Térmica Ltda
4 Universidad Pontificia Bolivariana
5 Colorado School of Mines

Suggested Citation
J.D. Osorio, M. Mehos, L. Imponenti, B. Kelly, H. Price, J. Torres-Madronero, A. Rivera-Alvarez, C. Nieto-Londono, C. Ni, Z. Yu, W. Hamilton, and J. Martinek. 2024. *Failure Analysis for Molten Salt Thermal Energy Storage Tanks for In-Service CSP Plants.* Golden, CO: National Renewable Energy Laboratory. NREL/TP-5700-89036. www.nrel.gov/docs/fy24osti/89036.pdf.

NREL is a national laboratory of the U.S. Department of Energy
Office of Energy Efficiency & Renewable Energy
Operated by the Alliance for Sustainable Energy, LLC

This report is available at no cost from the National Renewable Energy Laboratory (NREL) at www.nrel.gov/publications.

Contract No. DE-AC36-08GO28308

Technical Report
NREL/TP-5700-89036
March 2024

National Renewable Energy Laboratory
15013 Denver West Parkway
Golden, CO 80401
303-275-3000 • www.nrel.gov

NOTICE

This work was authored in part by the National Renewable Energy Laboratory, operated by Alliance for Sustainable Energy, LLC, for the U.S. Department of Energy (DOE) under Contract No. DE-AC36-08GO28308. Funding provided by the U.S. Department of Energy, Office of Energy Efficiency and Renewable Energy, Solar Energy Technologies Office (Award number 38475). The views expressed herein do not necessarily represent the views of the DOE or the U.S. Government.

Cover Photo: SolarReserve's Crescent Dunes CSP Project, near Tonopah, Nevada. Photo from SolarReserve.

Final Technical Report

Project Title:	Failure Analysis for Molten Salt Thermal Energy Storage Tanks for In-Service CSP Plants
Project Period:	10/01/2021 – 01/31/2024
Recipient:	National Renewable Energy Laboratory (NREL)
Address:	15013 Denver West Parkway Golden, CO 80401-3305
Website	www.nrel.gov/csp
Award Number:	38475
Project Team:	Solar Dynamics, Colorado School of Mines, Ingeniería Térmica, Universidad Pontificia Bolivariana
Principal Investigator:	Julian D. Osorio, Ph.D. Phone: (303) 384-6996 Email: Julian.Osorio@nrel.gov
Business Contact:	Craig Turchi Phone: (303) 475-4668 Email: Craig.Turchi@nrel.gov
Technology Manager:	Shane Powers

List of Acronyms

API	American Petroleum Institute
ASME	American Society of Mechanical Engineers
BPVC	Boiler and pressure vessel code
CFD	Computational fluid dynamics
CPU	Central processing unit
CSP	Concentrating solar power
DNI	Direct normal irradiance
DOE	U.S. Department of Energy
FEA	Finite element analysis
FFS	Fitness-For-Service
FZ	Fusion zone
GMAW	Gas metal arc welding
GTAW	Gas tungsten arc welding
HAZ	Heat-affected zone
HTF	Heat transfer fluid
IEA	International Energy Agency
MSPT	Molten salt power tower
MW	Megawatt
MW_e	Megawatt electric
MW_t	Megawatt thermal
NOx	Nitrogen oxides
NDA	Non-disclosure agreement
NIMS	National Institute for Materials Science
NREL	National Renewable Energy Laboratory
PCM	Phase change material
PEEQ	Equivalent plastic strain
PWHT	Post-weld heat treatment
SAM	System Advisor Model
SR	Sparger ring
SRC	Stress relaxation cracking
SS	Stainless steel
TES	Thermal energy storage
YS	Yield strength

Subscripts

cm	Cumulative
avg	Average
Inv.	Inventory
In	Inlet
out	Outlet
max	Maximum
min	Minimum

Executive Summary

Thermal energy storage (TES) is a fundamental component in concentrating solar power (CSP) plants to increase the plant's dispatchability and capacity factor while reducing the levelized cost of electricity. In central receiver CSP plants, nitrate molten salts have been used for several years for operation temperatures of up to 565°C, which is currently considered the state-of-the-art. This report focuses on tank design and performance at the current state-of-the-art temperature of 565°C. Although molten salt tanks have been successfully deployed in commercial parabolic-trough CSP plants worldwide at temperatures from 290°C to 390°C, several failures have been reported in tanks at central receiver plants operating at 565°C after a few months or years of operation, causing significant economic loss and mistrust in the technology. Most of these failures are associated with the infancy of the central receiver CSP technology and multiple issues related to tank design, fabrication, commissioning, and aggressive operation. A technical standard dedicated to the design and fabrication of molten nitrate TES tanks does not exist today. Current in-service molten salt tanks have been generally designed based on the American Petroleum Institute's (API) 650 and ASME Section II standards. The API 650 code provides guidelines for dimensions and fabrication for flat bottom tanks, including oil storage tanks, up to 260°C. The ASME standard provides allowable stress values for various materials at a range of temperatures and conditions. Both standards seem to be limited for molten salt TES tanks where high temperatures, thermal cycling, and transient conditions are expected.

In 2020, NREL released the *Concentrating Solar Power Best Practices Study* (NREL/TP-5500-75763)[1] that summarized issues and lessons learned in CSP plants, along with recommendations to address those issues based on information collected from participants representing about 80% of operating CSP plants in the world. One of the recommendations from that study was the development of accurate and validated models to evaluate the plant's transient operation, capable of capturing the effect of short-term clouds and operator response, while being adaptable to various spatial and temporal resource data. This project, "Failure Analysis for Molten Salt Thermal Energy Storage Tanks for In-Service CSP Plants," was inspired by this recommendation and focused on (1) developing and validating a physics-based model for a representative, commercial-scale molten salt tank, (2) performing simulations to evaluate the behavior of the tank as a function of typical plant operating conditions, (3) understanding tank failures mechanisms, (4) determining the residual stresses and distortion in the tank floor after welding fabrication and evaluating their impact in the stresses developed in the tank during operation, (5) assessing the impact of key operating parameters on the temperature and stress distributions, (6) conducting a preliminary evaluation of design features to reduce stresses and improve the tank's reliability, and (7) estimating the tank's service life based on the stress developed under diverse operating scenarios.

From the analysis conducted in the project and presented in this report, it was found that maximum stresses surpassing the yield strength of the stainless steel (SS) 347H may be developed on the tank floor near the perimeter. These large stresses are strongly influenced by the initial residual stresses and distortion of the tank floor after welding fabrication. During operation, large stresses are developed in the tank floor at high operating temperatures with low salt inventory levels during transient operation. High stresses are also related to elevated temperature gradients in the tank floor that could be attributed to insufficient mixing between the salt inflow and the salt inventory. Based on the analysis, creep is the predominant failure mechanism. However, the large stress levels could favor plastic deformation

[1] Available at https://www.nrel.gov/docs/fy20osti/75763.pdf.

developing buckles in the floor, and crack formation due to stress relaxation cracking during cycle operation. A lifetime below 3 years was estimated for the tank for representative plant operating conditions and a specific initial residual stress and deformation distribution of the tank floor. The estimated life agrees with the service time to failure reported in several commercial molten salt tanks.

SS 347H has been considered the state-of-the-art for molten nitrate salt hot tanks for central receiver CSP plants. It is worth noting that this report does not intend to demonstrate whether SS 347H is still a feasible material for the next generation of commercial plants. Several challenges for SS 347H have been identified, including its susceptibility to stress relaxation cracking, in addition to the challenges associated with performing post-weld heat treatment on large tanks and performing repairs due to its high potential for hot reheat cracking. Even when research is recommended to evaluate design, fabrication, and implementation alternatives to reduce stresses and cracking susceptibility of this material, alternative stainless steel materials other than SS 347H also deserve further consideration to evaluate their potential to contribute to solving current tank failures.

Design and operation guidelines can be extracted from the analysis presented in this report to help tank manufacturers and CSP operators reduce residual and operational stresses to achieve a tank service life of at least 30 years. Based on the lessons learned in this study, further R&D is required to understand how various factors influence the tank failures, and the best long-term solution. Addressing failures in molten salt TES tanks is fundamental for the CSP industry's survivability, but it is also important for other industrial and power generation applications using this TES technology, including nuclear and concentrating solar thermal.

Table of Contents

List of Figures

List of Tables

1 Introduction

1.1 Background

The current generation of central receiver (solar tower) concentrating solar power (CSP) plants typically uses a two-tank molten salt thermal energy storage (TES) configuration integrated with a conventional steam-Rankine power generation cycle. Usually, hot tanks for central receiver CSP applications are composed of stainless steel (SS) 347H shell and floor; a tank foundation made of sand, firebrick, cellular glass, and concrete; a piping system that transports the molten salts (usually a sodium/potassium nitrate blend) in and out of the tank; internal piping and static mixers that distribute the salt inside the tank; and an exterior insulation (Figure 1). Several failures in molten salt hot TES tanks in commercial CSP plants have occurred around the world [1], including the Crescent Dunes Solar Energy Project in the United States, causing significant economic loss and mistrust in this CSP technology. The majority of these failures are associated with the design and fabrication procedures of the tank floor, leading to high residual stresses after welding fabrication, as well as the friction between the floor and the foundation and the temperature gradients in the tank floor that result in high stress (that routinely exceed the SS 347H yield strength) during operation, stress relaxation cracking (SRC), buckling, and creep [2,3]. Technical standards for design, fabrication, and implementation of molten salt tanks operating at temperatures up to 565°C do not exist today. While molten salt tanks operating at 290°C to 390°C have generally performed well, those designed for and run at higher temperatures have experienced costly failures. In general, in-service hot tanks in the CSP industry have been designed based on the American Petroleum Institute's (API) 650 and ASME Boiler and Pressure Vessel Code (BPVC) standards [4-7]. The API 650 code provides guidelines about dimensions and fabrication for flat bottom tanks, including oil storage tanks, for operating temperatures of up to 260°C. The ASME BPVC includes several guidelines for different components; however, none of these is directly applicable to the molten salt tank due to high operating temperatures (up to 565°C), thermal cycling, and transient conditions.

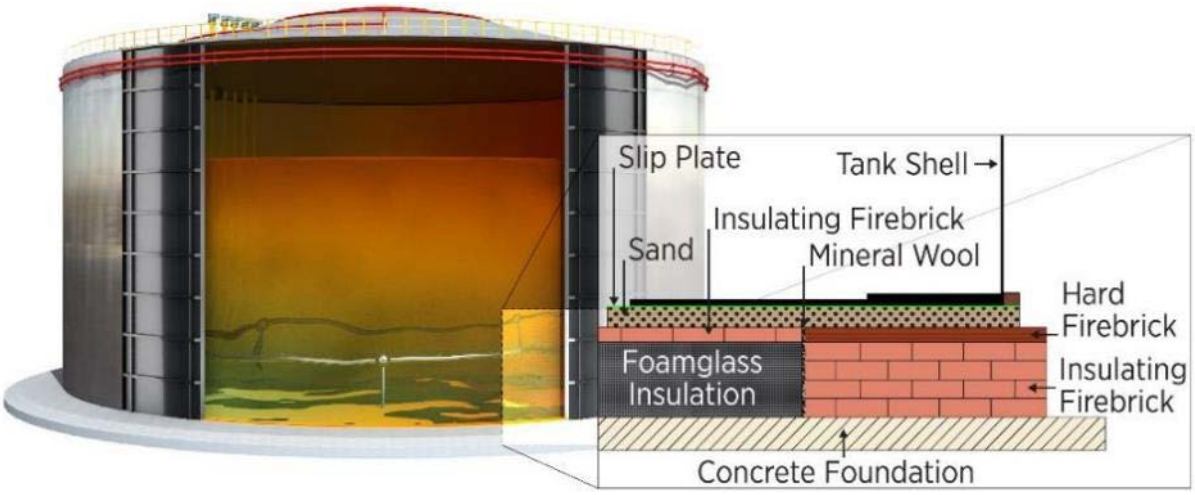

Figure 1. Schematic diagram of a molten salt thermal energy storage tank

The use of a TES system is essential for CSP economics as it can increase the plant's reliability, capacity factor, and dispatchability. The TES system is also integral to plant operation, and one of the most expensive subsystems in the plant, so its failure is highly undesirable [8]. A proper quantification

of the impact of transient and off-design operating conditions on TES systems' lifetime is challenging, but required to improve reliability of current and next generation CSP technologies.

Few studies related to 2-dimensional (2D) and 3-dimensional (3D) modeling and simulation of molten salt tanks are available in the literature. Most of these studies are focused on evaluating heat transfer and thermal losses [9-12], stresses on tanks for parabolic trough plants [13,14], performance evaluation of the hot tank for various operating conditions [9,11,15], small tanks (below 22.4 m in diameter) [13,14,16,17] and tanks fabricated with materials different from SS 347H such as SS 321H [14], carbon steel (SA-516 Gr-70) [18], or SS 304 [16]. However, none of these works analyze the effect of the resulting stress and/or the effect of receiver thermal transients on the tank's lifetime for in-service CSP plants. Beside some work related to buckling failure [20], to the best of our knowledge, studies on failure analysis on molten salt tanks, tank floor design and fabrication optimization, and evaluation of alternatives to address those failures are not available in the literature.

One of the most relevant publications in terms of operating conditions is a design basis document from Sandia National Laboratories [21]. The report, published in 2001, provides some initial design considerations for the major CSP components, including the TES system, based on experience from the Solar Two project. Published operational and heat loss data are available for the 10 MWe Solar Two project [22] and a pilot-scale system at the University of Lleida (Spain) [23] for operational temperatures up to 400°C [23]. The experimental and theoretical results from analysis conducted on small tanks provide important information on the heat transfer mechanisms but do not fully apply to commercial-scale tanks, where higher inertia and an increased thermal stratification impact temperature gradients and stress distribution.

This report presents the main outcomes of the project "Failure Analysis for Molten Salt Thermal Energy Storage Tanks for In-Service CSP Plants." This project was focused on conducting in-depth engineering analysis in commercial-scale molten salt TES tanks, evaluating temperature and stress distribution in the tank, and estimating lifetime under typical plant operating conditions. Based on the analysis, some design and operation alternatives are proposed and evaluated.

1.2 Failures in SS 347H Molten Salt Tanks

In 2020, NREL published the *Concentrating Solar Power Best Practices Study* [1] that evaluated causes of past issues and failures in parabolic trough and central receiver CSP plants. For central receiver plants, key issues have been identified that are related to the design of the steam generation system and the design of the hot tank and its foundation. Additional information on central receiver CSP issues sorted by severity and number of occurrences is presented in Figure 2. In central receiver hot tanks, failures have been reported after several months or years of operation and could be associated with corrosion (stress corrosion cracking and pitting corrosion), cracks across weldments, cracking related to a combination of creep, low-cycle fatigue, friction forces between the tank floor and the foundation, and high-stress generation in the tank floor and the foundation due to expansion/contraction during thermal cycling and other transient events. The project team has had access to detailed information on hot tank failures that have occurred in multiple plants around the world. Confidential information, provided by CSP plants under non-disclosure agreements, has been very useful during the execution of the project to understand failure mechanisms and their root causes, and to direct our simulations and analysis efforts to design, fabrication, operation, and implementation alternatives to advance toward a definitive solution to avoid these failures.

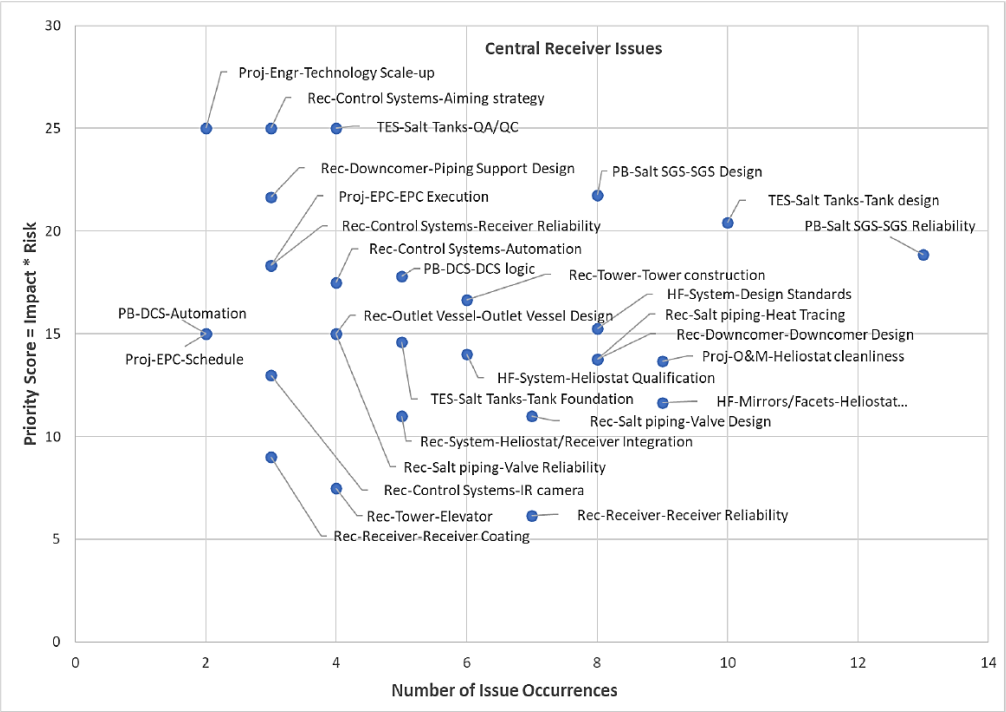

Figure 2. Central receiver CSP issues plotted by priority score and number of occurrences [1]

1.2.1 Factors Influencing Tank Failures

Based on the project team's experience with commercial CSP plants and research conducted on molten salt TES tanks during the last three years in this project[2] and previous projects,[3,4] **four main failure behaviors in SS 347H hot tanks have been identified: (1) low-cycle fatigue, (2) SRC, (3) creep, and (4) buckling**. These failure behaviors are strongly influenced by design, fabrication, and operation factors, including:

1. Floor fabrication using plates that plastically deform and buckle
2. Defects in weldments—lack of fusion and misalignment—within tank floor and walls
3. Use of the matching filler E347 for the SS 347H base material that is susceptible to SRC
4. Non-optimal designs of floor plates layout and welding procedure introducing distortion and large residual stress in the tank floor after welding fabrication (Figure 3a) that lead to high stresses during operation (Figure 3b)
5. Insufficient mixing between the incoming salt and the salt inventory that leads to large radial and circumferential temperature gradients in the tank floor

[2] 38475 – "Failure Analysis for Molten Salt Thermal Energy Storage Tanks for In-Service CSP Plants" – PI: J. Osorio, NREL.
[3] 37373 – "Mechanical Failure Risk Management for In-Service CSP Nitrate Hot Tanks." – PI: C. Agustine, NREL.
[4] 33458 – "Stress relaxation cracking (SRC) of alloys at temperatures higher than 540°C" – PI: J. Vidal, NREL.

6. Non-uniform friction coefficient between the floor and foundation, mainly attributed to the initial distortion of the floor and the presence of backing plates that lead to high localized friction forces and stresses and non-uniform thermal expansion of the floor during operation

7. Challenging transient operation conditions

8. Aggressive plant operation at low inventory levels, during cloudy sky conditions, and at startup.

A flow diagram of the failure behaviors and the key factors influencing SS 347H tank failures is summarized in Figure 4. In general, failures presented in current in-service SS 347H hot tanks can be explained as a combination of several of these behaviors and the influence of design, fabrication, implementation, and operation factors. Note that other failure mechanisms such as molten salt corrosion and stress corrosion cracking have not been seen in SS 347H tanks.

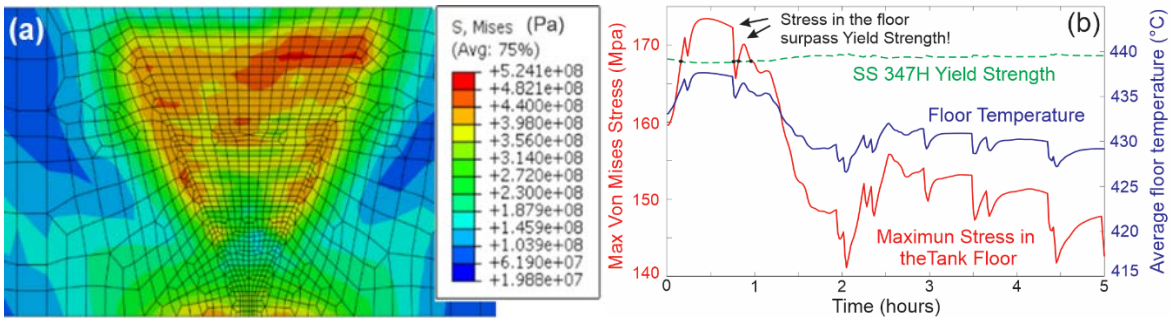

Figure 3. High stress values have a negative impact on the tank's lifetime. (a) Residual stresses in two-plate floor welds after fabrication [3][24]**; (b) Maximum stress in the floor during typical plant operating conditions. SS 347H yield strength is surpassed within the first hour of operation**

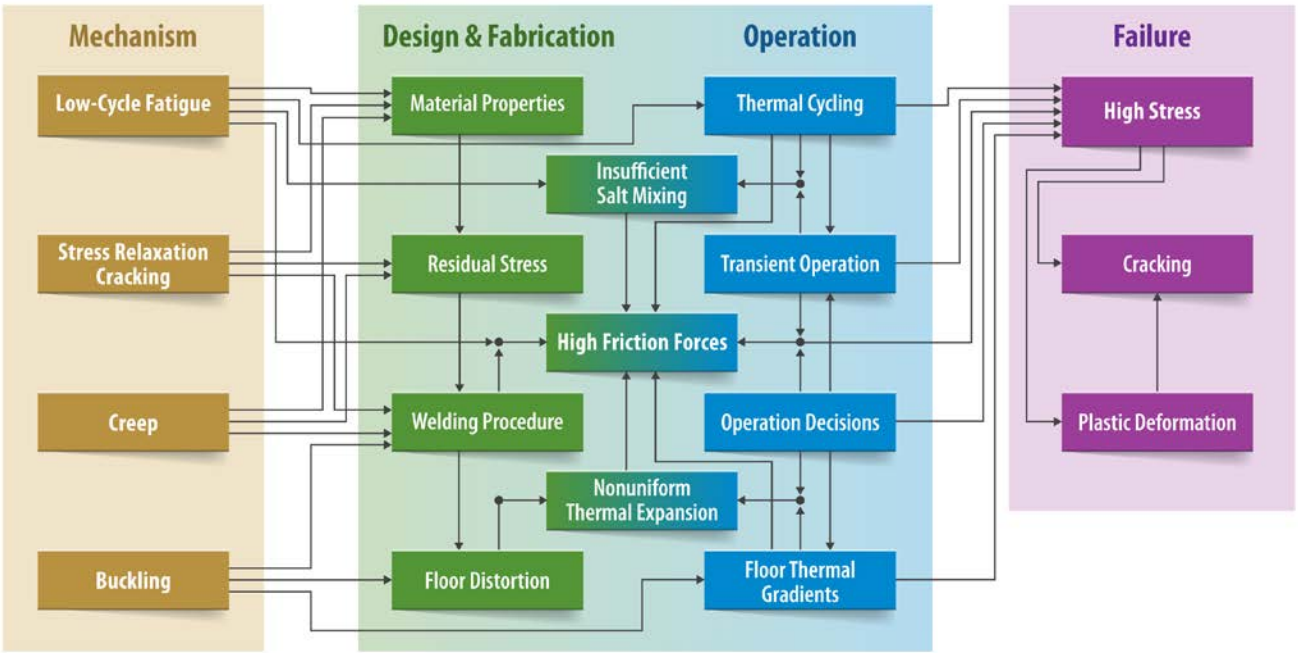

Figure 4. Failure behaviors in SS 347H molten salt hot tanks

1.2.2 Low-Cycle Fatigue

In addition to SRC, the major parameters that contribute to storage tank floor damage are friction forces and thermal gradients. In a typical commercial project, salt from the receiver is introduced into the hot salt tank through a distribution ring (or sparger ring). During plant operation, rapid transient conditions—mainly attributed to variable solar radiation due to the presence of clouds—lower the temperature of the salt entering the hot tank; such events can increase temperature gradients and thus thermal stresses in unforeseen ways. As the tank expands and contracts with each thermal cycle, friction forces are present throughout the tank floor. The combination of thermal stresses and friction forces during expansion/contraction can result in periodic high stresses that compromise the low-cycle fatigue life of the tank. In situations where the inlet salt flow is colder than the inventory and the flow rate is low, buoyancy forces cause the incoming fluid to sink and contact the tank floor. This flow pattern initially generates radial thermal gradients along the tank floor, and eventually causes vertical stratification when enough salt has entered the tank. Temperature gradients in either direction are potentially important stress generators.

1.2.3 Stress Relaxation Cracking

SRC is a failure mechanism associated with the relief of high residual stress during a high-temperature operation, leading to cracking. SS 347H has been widely adopted for molten salt hot tanks due to its corrosion resistance and higher yield and creep strength for temperatures up to 650°C when compared with other steels such as SS 304 and SS 316. It also exhibits good sensitization resistance due to the addition of Niobium (Nb) that favors the formation of carbonitride (C,N) precipitates [25,26]. However, several issues have been reported in SS 347H welds made with matching E347 filler including SRC in the fusion zone (FZ) or heat-affected zone (HAZ) during service or even during post-weld heat treatment (PWHT) [3,25,27-29]. Creep and SRC mechanisms are intrinsically related during floor welding fabrication. Stabilized niobium carbonitrides are dissolved in the FZ and HAZ. Then, during operation at high temperatures (up to 565°C) fine Nb (C,N) particles reprecipitate in the grain interiors on dislocation cores, while coarse precipitates form along the grain boundaries [25,26], leading to the formation of soft precipitate free zones (PFZs) adjacent to the grain boundaries. In the PFZs, the weld-induced residual strain preferentially relaxes, exhausting the local creep strain, leading to creep cavities and finally cracking in the HAZ or FZ [28,30-33].

1.2.4 Creep

Current tank design and operation conditions result in long-term exposure of high stresses that, even below the yield strength of the material, cause slow and continuous deformation. This behavior is exacerbated by the high operation temperatures of the hot tank. Based on analyses conducted within this project, creep is expected to be a more dominant failure mechanism than low-cycle fatigue for typical plant operations. However, the combination of creep and fatigue results in a synergetic behavior that is expected to accelerate failures in hot tanks. Currently, there is no evidence of failures in hot tanks that have been caused only by creep, but by a combination of multiple mechanisms including creep.

1.2.5 Buckling

The permanent deformation of the tank floor forming narrow ridges or buckles is associated with the development of high compression stress in the tank floor during operation. Key factors contributing to buckle formation include the high-temperature gradients in the tank floor (usually larger than 30°C; the temperature gradient is defined as the temperature difference between the outer annular ring and the

central part of the floor plate), the slope in the floor, non-uniform distribution of the friction coefficient between the floor and the foundation (mainly attributed to the effect of backing plates that remain between the floor and the foundation after welding fabrication) leading to localized high friction forces, thin floors, tank pre-heating, and the initial condition (stress and distortion) of the tank floor after welding fabrication. The direct effect of high radial temperature gradients in the tank and the friction coefficient (> 0.5) on the buckling sensitivity have been analyzed [20]. In particular, a finite element analysis (FEA) conducted in rectangular plate layout floors has shown permanently deformed ridges that can be initiated under very small temperature variations, see Figure 5.

The residual stresses and deformation (distortion) in the tank floor after welding fabrication [2] have been analyzed and quantified. This initial floor condition results in a pre-loaded, pre-deformed state that makes it easy for the floor to plastically deform into local buckles during pre-heating and operation. The backing plates and the non-flat initial characteristics of the floor—deformed floor with elevated regions near the center of each floor plate, and depressed regions near the weld seams—result in a non-uniform distribution of friction forces between the floor and the foundation. This condition implies higher localized stress at specific points in the floor and high strain in the top of the buckles, reducing the resistance to further buckling. The permanent and continual plastic deformation of the tank floor during cyclic plant operation will eventually result in cracking.

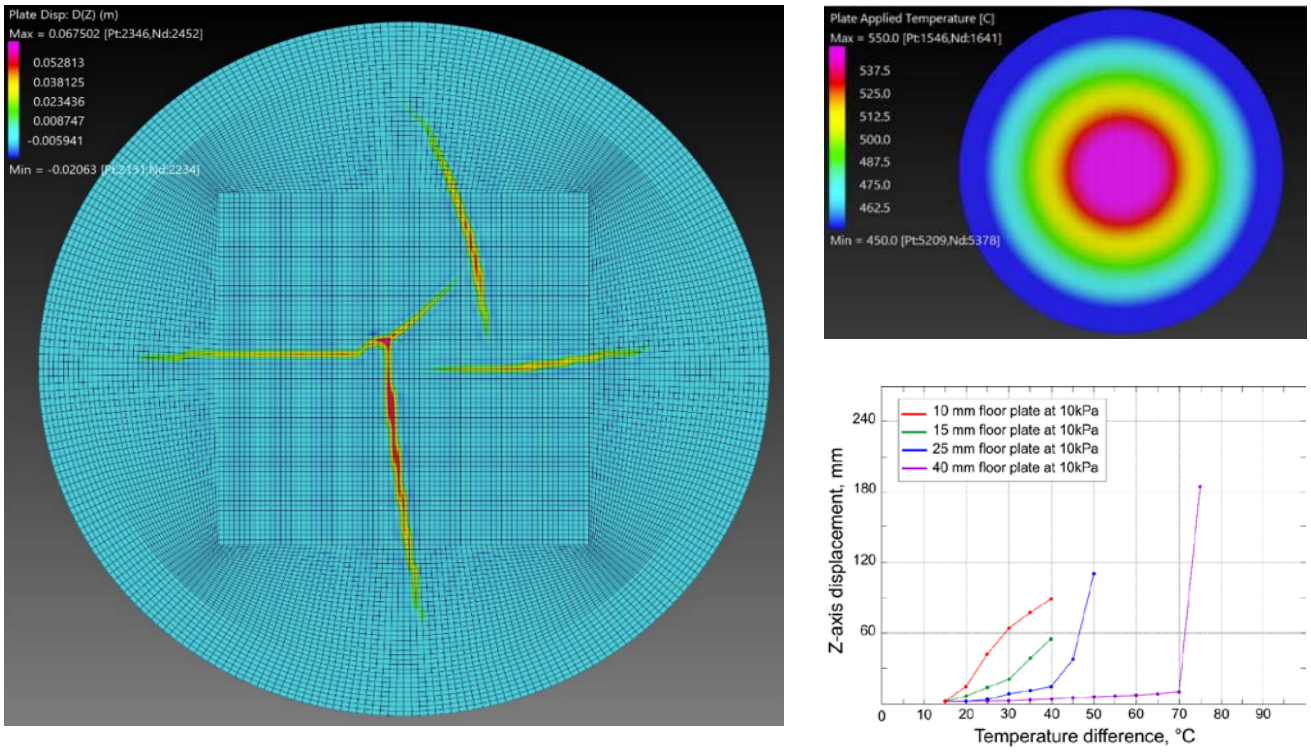

Figure 5. Buckling modeling on the tank floor [20]**. Left: FEA simulation results showing permanently deformed floor shape (buckles). Right top: radial floor temperature gradient distribution used in the FEA simulation. Right bottom: buckling initiation as a function of temperature difference (from the center to the half of floor radius) for several floor thicknesses. Note that z-axis is normal to the floor plane.**

1.3 Project Description and Approach

This project is intended to gain understanding of mechanical failure mechanisms in commercial-scale molten salt TES tanks and quantify the temperature distribution and the corresponding stresses as a function of typical plant operating conditions and their impact on tank life.

1.3.1 Project Objectives

The main goal of the project was to investigate failure mechanisms by evaluating temperature and stress distributions in commercial hot tanks for central receiver CSP plants operating at temperatures of up to 565°C and estimate the tank's lifetime as a function of stresses developed during operation. In-depth engineering analysis, multiphysics simulation tools, and high-performance computing capabilities at the National Renewable Energy Laboratory (NREL) have been used to establish the relationship between transient events, plant operation variables, and failures in the hot tanks. Specific project objectives are summarized as follows:

- Characterize in-service tank designs, plant operating conditions, and failures in commercial molten salt TES tanks for central receiver CSP plants.
- Formulate and implement a physical representation of a commercial molten salt hot tank in a Multiphysics (that combines multiple physical disciplines including heat transfer, thermodynamics, fluid mechanism, material science) simulation environment.
- Evaluate stresses developed in the tank and estimate the service life as a function of plant operating parameters and characteristic transient events.
- Investigate the correlation between fundamental operation parameters—inlet salt flow rate, inlet salt temperature, inventory level—and the temperature and stress distribution in the tank.
- Propose and preliminarily evaluate design and operation alternatives to reduce stresses and increase the tank's reliability.

1.3.2 Technical Approach

This project was divided into five tasks and six milestones. A detailed diagram with the tasks, activities, and milestones is presented in Figure 6.

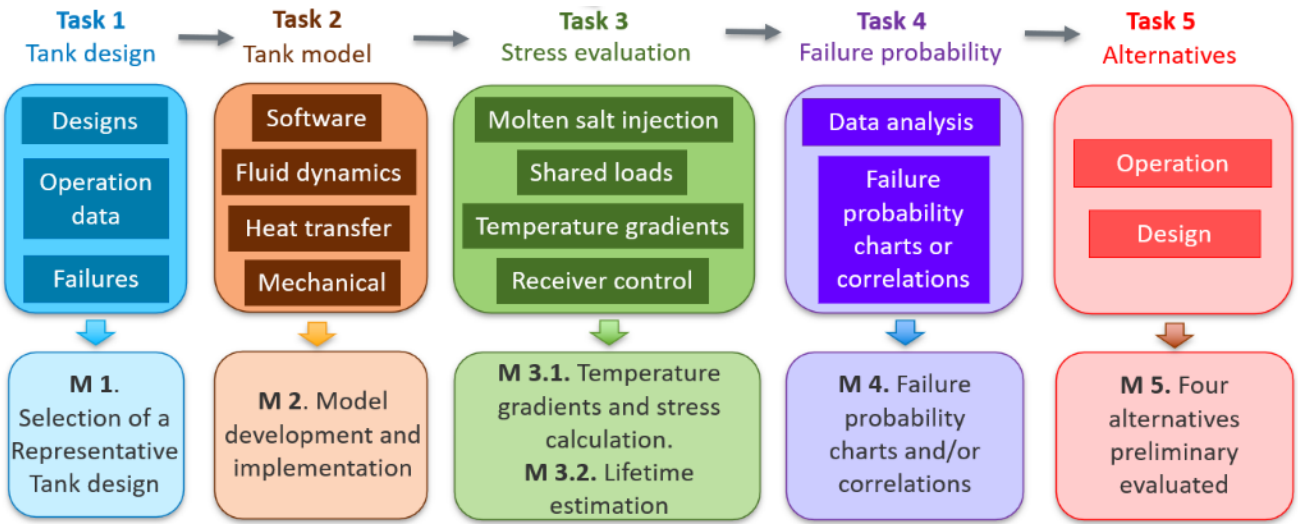

Figure 6. Diagram of the technical scope summary of the project

The first milestone of the project was the selection of a representative commercial hot tank design. To achieve this milestone, a survey and literature review were conducted about different hot tank designs, dimensions, and foundations; characteristic plant operating conditions; and tank failures reported for in-service CSP plants. Most of the operational central receiver CSP plants were contacted to request their participation in the project. Every plant contacted has a power output capacity ≥ 20 MWe and uses molten salt tanks. Table 1 lists the CSP plants approached.

Table 1. Contacted Central Receiver CSP Plants (Nominal Capacity ≥20 MW and Using Molten Salt TES)

Project	Capacity (MW)	Location (Country)	Started Operation (Year)	Storage Capacity (Hours)
SUPCON Delingha	50	China	2018	7
Shouhang Yumen	100	China	2021	10
Shouhang Dunhuang Phase II	100	China	2018	11
Power China Qinghai Gonghe	50	China	2019	6
NOOR III	150	Morocco	2018	7
Noor Energy 1 / DEWA IV	100	UAE	2021	15
LuNeng Haixi15	50	China	2019	12
Gemasolar Thermosolar Plant	20	Spain	2011	15
Crescent Dunes	110	USA	2015	10
CEEC Hami	50	China	2019	8
Atacama I / Cerro Dominador	110	Chile	2021	17.5

A questionnaire for an initial collection of design information was developed. The questionnaire was distributed to interested central receiver CSP plant participants to acquire general tank design information from plants including dimensions for the shell, floor, sparger ring, foundation type and materials, and general operating conditions (Table A1 in Appendix A). A multiple-choice format avoided asking for exact design details while still providing important information for comparison of in-service plants. More detailed information including tank drawings, welding procedure specifications, and historic operational data were requested of participating plants later in the project. The information received from the plants was used to develop a representative commercial tank design that was the subject of analysis for the project. The representative tank geometry was implemented in Solid Edge, and then exported to ANSYS. The model was refined, optimized, and then validated using historic plant operation data. All the simulations were conducted on NREL's supercomputer Eagle. The historic operational data were used to produce several representative plant operational cases for the model. These operational cases were created by extracting, scaling (multiplying), and reorganizing multiple transient events from multiple days for several plants. This procedure was necessary to develop a new dataset of typical and representative commercial plant operating conditions different from the received proprietary information. A similar approach was adopted to produce the representative tank design to protect the received proprietary information. The temperature and stress distributions were evaluated in all the tank's components as a function of typical operating conditions, and the regions in the tank experiencing the larger stresses, and thereby more susceptible to failures, were identified. Finally, some design and operating alternatives were proposed and evaluated in terms of reduction of stresses. This report provides information that might serve as guidance to mitigate failure of existing tanks and could be considered in the design of new tanks. The technical description and approach of the project are summarized in Figure 7.

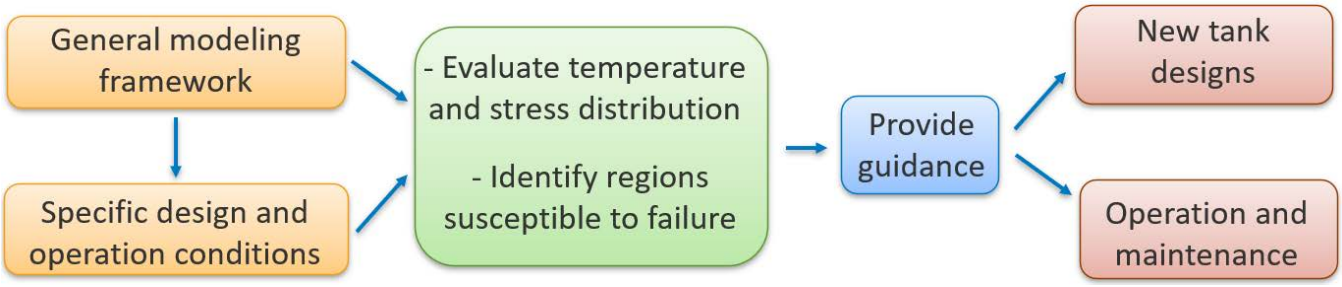

Figure 7. Summary of the project description and approach

2 Molten Salt Tank Model Development

2.1 Representative Tank Design

The tank design information received from the plants was the basis for the development of a general, representative hot tank design for analysis with computational fluid dynamics (CFD) and finite element (FE) models. The design information received corresponded to central receiver CSP plants with a nominal capacity between 50 and 150 MWe with a storage capacity ranging between 300 and 1200 MWh_e per tank (~1400 and ~2800 MWh_t), estimated based on tank volume assuming cycle temperatures of 290° and 560°C. This project was focused on hot tanks using molten salts for central receiver plants. To the best of our knowledge, commercial-scale, in-service parabolic trough plants around the world do not use molten salt in the solar field. Hot tanks in parabolic trough plants operate at lower temperatures (~390°C) and present significant differences in the solar field geometry and flow configurations compared to molten salt tower projects. A sketch of the representative tank design is presented in Figure 8. Additional design diagrams for the tank are presented in Figures B1 to B6 in Appendix B.

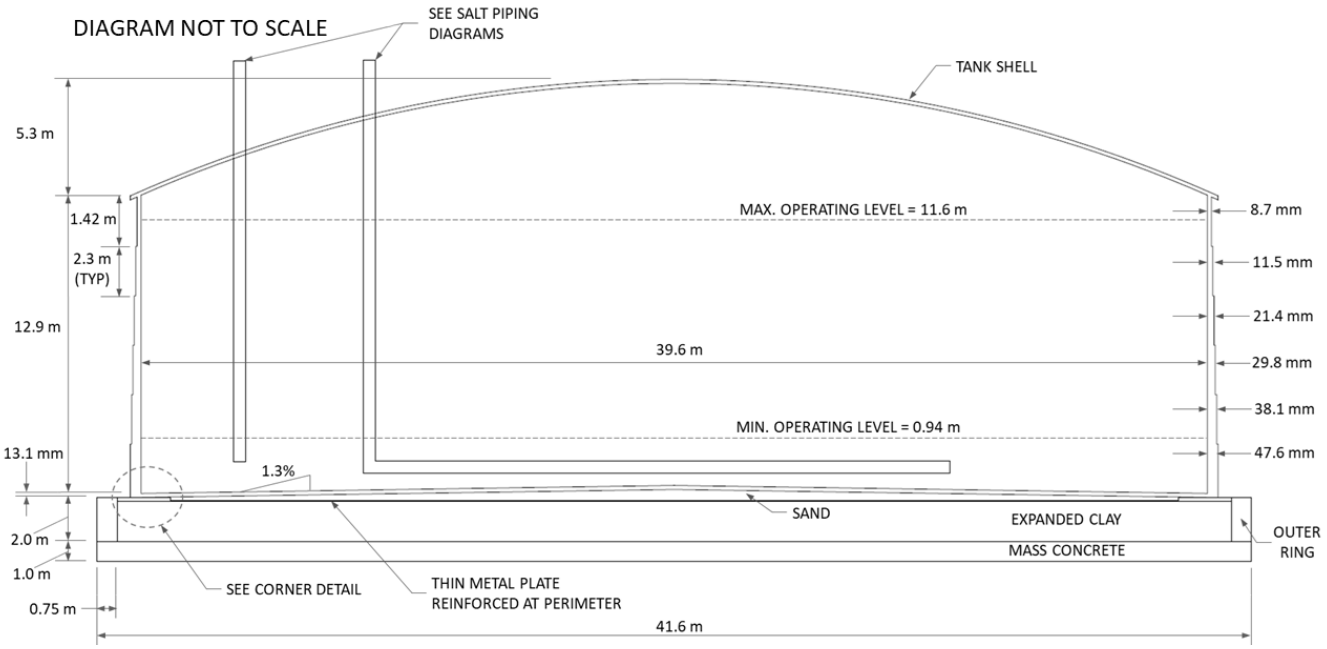

Figure 8. Representative hot tank design

The main dimensions of the tank were initially determined as the average value for each specific feature of actual tanks. However, due to the different sized tanks surveyed around the world, this calculation may result in tank dimensions that are not appropriate for a commercial design in the U.S. market. For the market of interest, techno-economic analysis looking at CSP projects often results in plants with gross capacity >100 MWe with at least 6 hours of storage [34]. Considering the project goal of representing a commercial storage tank, the weighted mean based on plant or tank capacity was considered. Weighting the mean based on plant capacity increases the tank diameter by 2 m and results in a slight decrease in the maximum operating inventory level; a similar increase in diameter is achieved when weighting based on tank capacity without decreasing the inventory level. Weighting based on tank capacity results in a 12.6% increase in the representative tank storage capacity compared to the arithmetic mean. Using this methodology, the estimated capacity of the representative tank design is 2.64 GWh_t, i.e., 111 MWe for 10 hours, assuming 42% gross power-cycle efficiency.

For the sparger ring and foundation, the most frequent design was selected. Additional details for the sparger ring are presented in Figure 9. The foundation is composed mainly of expanded clay with sand and a metal slip-plate. The tank will include 16” (40.6 cm) of mineral wool on both the wall and roof. Some design features (for example the presence of anchor bolts) were determined based on the API 650 standard due to the large variation in the information received from the plants. For the foundation, for instance, the most common material used was expanded clay and sand as solid lubricant. About half the plants indicated the use of metal slip-plates at the perimeter of the tank, while the other tanks do not use slip-plates and have a floor without any difference between the perimeter and the center. The foundation for the representative tank design is composed mainly of expanded clay with sand and a metal slip-plate in the perimeter and the floor has a slope of 1.3%, see Figure 8.

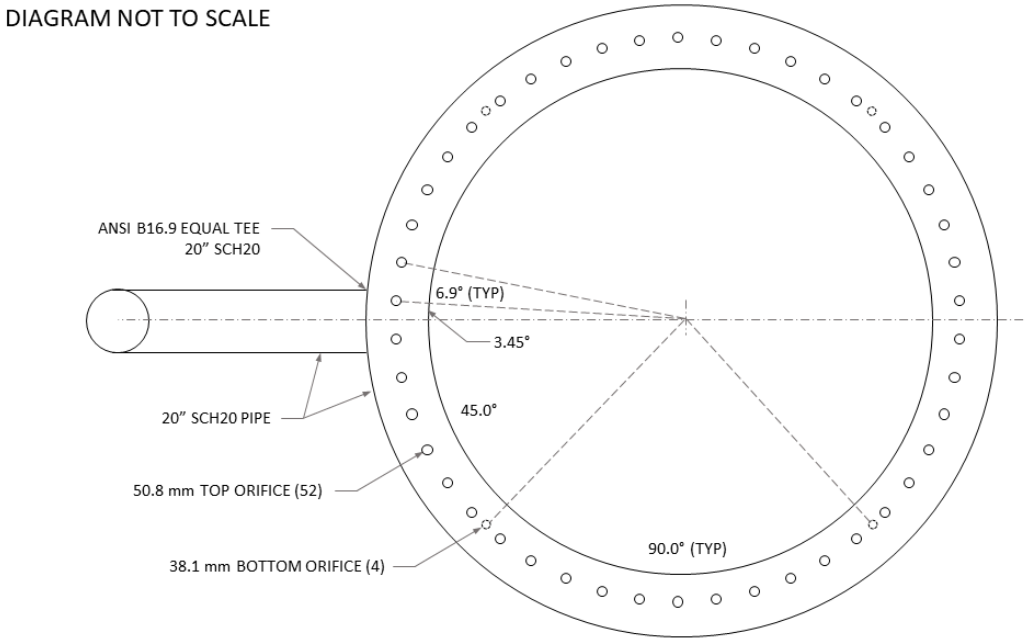

Figure 9. Salt distribution top view

From the design data received, some interesting trends were identified:

- The tank diameter increases with plant capacity while the wall height is relatively constant. The wall height is generally limited by the soil bearing capacity with the maximum inventory level.
- The minimum floor thickness is larger for smaller plants (8–11 mm), but lower for the higher capacity plants (6–8 mm). It seems that larger floor thicknesses have been adopted in new plants, having small tanks, to reduce failure susceptibility.
- In all cases, the tank wall and floor satisfy the minimum design criteria outlined in the API 650 standard [4]. Because this standard does not cover the operating temperatures of interest for the maximum allowable stress, ASME Section II is commonly used in tank design calculations [5].
- Similar values to the surveyed wall thicknesses could be calculated through the hoop stress equation with an added 0.7 mm corrosion allowance, considering the maximum inventory level.

Table 2. Similarities and Differences in Design Features Among Surveyed Molten Salt Hot Tanks

Similar Design Features	Distinct Design Features
• Constructed of stainless steel 347H • Sloped floor (1–1.5% slope) • Self-supported roof • Wall heights (12–15 m) • The inlet piping system consists of a distribution ring near the tank floor • External insulation around tank wall and roof • Concrete mat foundation with forced air cooling • At least one layer of foundation insulation in between the concrete foundation and tank shell • Reinforced concrete ring wall for supporting the foundation insulation • Sand as solid lubricant for the foundation if considered in the design	• Interior diameter (20–42 m) • Minimum floor thickness (6–11 mm) • Maximum wall thickness (30–50 mm) • Diameter of distribution ring, % of tank shell interior diameter (40–80%) • Angle of injection (0–30°). 0° vertical up • Number of orifices in the distribution ring • Not all tanks use eductors • Material composition at perimeter (metal slip-plate, expanded clay, refractory) • Material composition at center (for foundation)

Table 3. Deviation of Key Tank Design Features With Respect to the Representative Tank Design for Plants With Net Capacity Larger Than 100 MWe

Design Feature	Value	Deviation Respect to the Representative Tank (%)
General		
Storage capacity electric [MWh]	1063	3.5–9.4
Storage capacity (thermal) [MWh]	2620	2.8–11.0
Tank shell		
Interior diameter [m]	39.57	3.6–11.5
Minimum floor thickness [mm]	6.67	2.5–5.0
Maximum wall thickness [mm]	47.67	5.6–15.4
Wall height [m]	12.93	0.5–1.0
Floor slope [%]	1.30	7.7–23.1
Internal mixing ring header		
Diameter of distribution ring, % of tank shell interior diameter	55	0–21.1
Height from tank floor [m]	0.97	6.9–55.2

Regarding the salt distribution system, a larger variation in design parameters was observed. There were no clear trends with plant capacity, other than the use of static mixers in tanks with capacity above 2 GWh thermal. Eductors (also known as static mixers) can reduce stratification by entraining bulk inventory into the inlet flow. Based on the information, stratification and stagnation zones are a greater concern in larger tanks. In general, significant variation in the inlet piping arrangement between tanks was observed despite the relatively similar tank shell and foundation designs. Key similarities and

differences in design features among surveyed molten salt hot tanks are presented in Table 2. Table 3 presents the range of the percentage of deviation (% Dev) for the design features (DF) of surveyed tanks with plant capacities larger than 100 MW with respect to the representative tank design. The % deviation is calculated from Equation 1.

$$\% \, Dev. = \frac{\left| DF_{tank,i} - DF_{rep.,tank} \right|}{DF_{rep.,tank}} * 100 \quad (1)$$

2.2 Typical Plant Operating Conditions

Operational information from commercial-scale CSP plants is not publicly available and is considered proprietary information. Our initial approach was extracting typical receiver and tank operating conditions using the molten salt power tower (MSPT) module in NREL's System Advisor Model (SAM) [35]. These types of models capture the general range of conditions experienced by the hot tank, but they cannot capture the exact control strategies in place at operating plants, operator decisions, response time for molten salt valves, or real-world emergency conditions such as power, pump, or valve failures that can produce large and rapid temperature changes in the salt inflow to the hot tank.

Table 4 presents the typical operating conditions for a 115 MW_e central receiver plant (565 MW_t receiver), and 10-hour storage capacity, operating under clear sky day conditions at Tonopah, Nevada. The direct normal irradiance (DNI) and weather data were obtained for this location in 2018 for the National Solar Radiation Database (NSRDB) [36]. Table 4 provides minimum and maximum limits and percentiles of the annual distributions of receiver outlet temperatures, flow rates, hot tank salt-fill fraction, and tank average temperature. Plant control strategies govern the flow rate and temperature of the salt inflow into the tank, the timing of energy dispatch from the hot tank, and the tank levels and temperatures. The receiver is usually operated in a way that the DNI is sufficient to maintain mass flows above the receiver's minimum turndown ratio. Mass flow rates to the receiver are controlled based on the target outlet temperature (565°C) for an expected (forecasted) clear sky day DNI at each time. This control strategy is known to be employed at existing plants to protect the receiver from sudden and unpredictable changes in DNI during periods with the presence of clouds. However, this operation strategy produces a receiver outlet temperature that fluctuates with DNI and can deviate substantially from the design point temperature. The salt flow output from the receiver is typically sent to the hot tank but is diverted to the cold tank when the temperature drops below a certain predefined value (for example, 430°C in some plants). Salt stored in the hot tank is then dispatched to the cold tank, passing through the primary heat exchanger to operate the power cycle.

The information obtained from simulations using the SAM-MSPT Model was initially considered to set the boundary conditions of the hot tank model. Then, initial and simulation conditions were replaced with historic operational data received from participating plants through non-disclosure agreements (NDA). Similar to the development of the representative tank design, real plant operational data were utilized to develop a set of typical operating conditions used in the model. These operational cases were created by extracting, scaling (multiplying), and reorganizing multiple transient events from multiple days for several plants to produce typical plant operation data, different from the received proprietary information. Key operation variables for the representative tank design used in the model are presented

in Table 5. The deviation of these variables with respect to the surveyed plants with net capacity larger than 100 MW_e is also presented in this table.

Table 4. SAM-MSPT Model-Predicted Conditions Experienced by the Receiver and Hot Tank; Minimum and Maximum Limits and Percentiles Are Shown for the Annual Simulation

Operation Condition/Variable	Percentiles						
	Min	5th	25th	50th	75th	95th	Max
Receiver Operation							
Receiver outlet T (°C)	353	440	565	565	565	565	565
Receiver mass flow (kg/s)	311	695	1078	1270	1376	1468	1651
Receiver Operation and Salt Flow Sent to Hot Tank							
Receiver outlet T (°C)	427	478	565	565	565	565	565
Receiver mass flow (kg/s)	311	686	1068	1267	1374	1464	1651
Hot tank average T (°C)	441	516	558	564	564	565	565
Difference between receiver outlet and hot tank average (°C)	-132	-36	0.4	0.7	4	24	103
Hot tank fraction	0	0.01	0.10	0.29	0.54	0.82	1.0
Receiver Startup or Shutdown							
Hot tank fraction at receiver startup	0	0	0	0	0.01	0.47	0.95
Hot tank fraction at receiver shutdown	0	0	0.03	0.3	0.6	0.88	0.98

Table 5. Key Operation Variables Used in the Model and Deviation with Respect to the Surveyed Plants with Net Capacity Larger Than 100 MW_e

Operation Variable	Value	Deviation Respect to the Representative Tank (%)
Maximum salt inventory level (operation) (m)	11.57	4.9–12.4
Minimum salt inventory level (m)	0.93	3.6–7.1
Salt inventory temperature at beginning of startup (°C)	489.2	2.9–5.8
Incoming salt temperature when switching from cold to hot tank (°C)	509.2	1.8–3.6
Incoming salt temperature rate of change (°C/min)	5.7	55.9–111.8

The typical plant operating conditions used in the model are presented in Figure 10. This set of operation conditions consists of four days—or four cases used in the analysis—with different characteristics. The first day (case 1) corresponds to clear sky day conditions (Figure 10a) where a smooth variation in the salt inlet temperature and mass flow rate are appreciated. The highest salt inventory temperature was achieved during this day, and the lowest salt inventory level at the beginning. The second day (case 2) corresponds to a cloudy sky day condition, with the presence of multiple transient events (Figure 10b). The presence of clouds during the day could represent challenging operation conditions and multiple operator decisions. Operators seek to produce maximum power, while avoiding operations that could lead to large temperature variations that overly stress plant components. The lowest inlet temperatures

occur during case 2. The cases 3 and 4 (third and fourth days) correspond to partly cloudy sky day conditions with the presence of some transient events (Figure 10c and Figure 10d). Evaluating the behavior of the tank with operation under the presence of clouds is fundamental to capture the transient events and their potential effect on the system's lifetime. It is worth noting that partly cloudy sky days usually account for a large percentage of the days during the year.

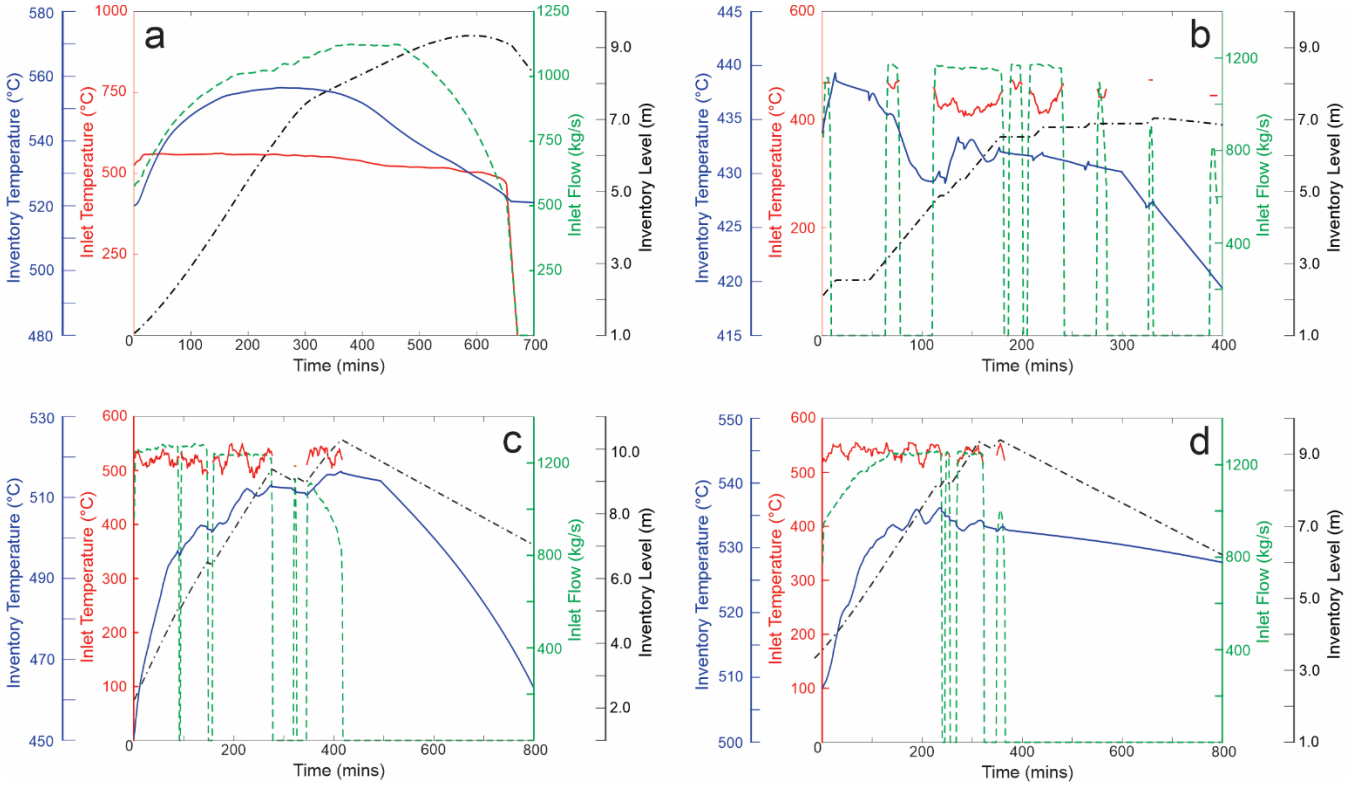

Figure 10. Typical plant operating conditions used in the model. (a) clear sky day, (b) cloudy sky day, (c) and (d) partly cloudy sky day conditions

2.3 Model Formulation and Implementation

The tank geometry was constructed using the computer-aided design program Solid Edge based on the representative tank design (see Figure 8). The 3D solid representation of the tank is presented in Figure 11. The external appearance is displayed in Figure 11 (left). The tank interior is presented in Figure 11 (right), where the sparger ring and outlet salt pipes can be appreciated. The 3D solid tank geometry was then implemented into ANSYS.

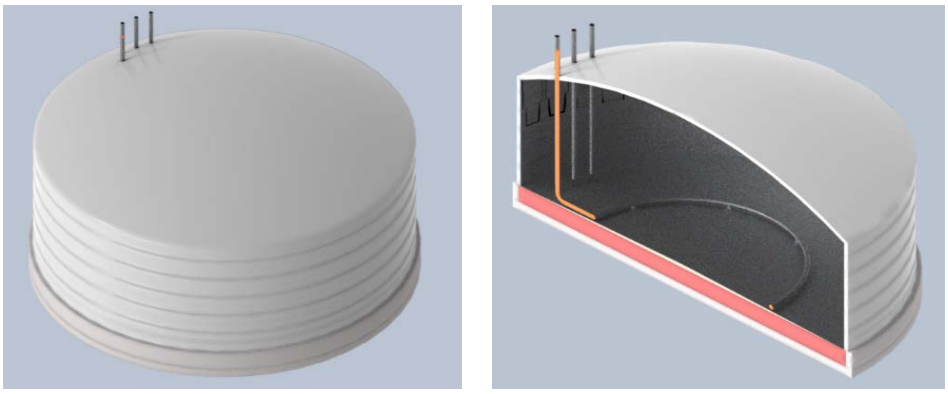

Figure 11. 3D solid representation of the representative tank. Left: exterior. Right: interior.

2.3.1 Initial 2D Model

Initially, a 2D simplified model of a tank was developed to tune the model and verify that all the components (tank shell, molten salt, foundation) were responding accordingly. This approach was also used with the intention of determining the mesh attributes and the calibration of the characteristic time step of the process. The following assumptions were considered for the 2D model:

- The tank roof was simplified as a flat plate.
- Tank walls have a constant thickness of 25 mm.
- No slope was considered for the tank floor.
- The tank has one inlet and one outlet (SCH 20 pipes).
- The soil under the tank has a depth of 20 m and a width of 60 m.

Diagrams of the 2D tank geometry implemented in ANSYS and the corresponding mesh are presented in Figure 12.

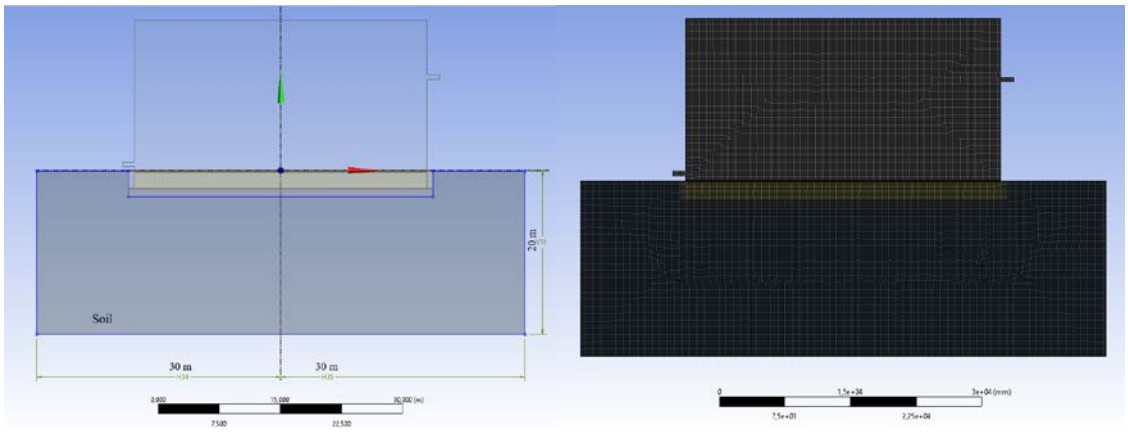

Figure 12. 2D tank model representation in ANSYS. Left: Dimensions. Right: Mesh generated.

The behavior of the molten salt is determined by solving the governing continuity and momentum conservation equations (Equations 2 and 3). For the viscous model, a standard $\kappa - \varepsilon$ approach was considered with enhanced wall treatment [37], which accounts for the heat transfer between the molten salt and the tank wall.

$$\frac{\partial \rho}{\partial t} + \nabla \cdot (\rho \vec{v}) = 0 \tag{2}$$

$$\rho \frac{D\vec{v}}{Dt} = \rho \left(\frac{\partial \vec{v}}{\partial t} + \vec{v} \cdot \nabla \vec{v} \right) = \mu \nabla^2 \vec{v} - \nabla P + \rho \vec{g} \tag{3}$$

where $\vec{v}$ is the average velocity vector, P is the pressure distribution, ρ is the fluid density, μ is the dynamic viscosity, and $\vec{g}$ is the acceleration of gravity. The operator D/Dt is given by Equation 4:

$$\frac{D}{Dt} = \frac{\partial}{\partial t} + \vec{v} \tag{4}$$

In addition, the turbulent kinetic energy and turbulence dissipation can be computed from Equations 5 and 6, respectively. This model is appropriate to accurately predict the flow away from the tank walls. It also offers a good quality prediction on the flow near the walls when the velocity oscillations near the wall are not critical [38,39]; these oscillations are relatively low for the larger diameter of the representative tank design [40].

$$\frac{\partial}{\partial t}(\rho \kappa) + \frac{\partial}{\partial x_i}(\rho \kappa u_i) = \frac{\partial}{\partial x_j}\left[\left(\mu + \frac{\mu_t}{\sigma_\kappa} \right) \frac{\partial \kappa}{\partial x_j} \right] + G_\kappa + G_b - \rho \varepsilon - Y_M + S_\kappa \tag{5}$$

$$\frac{\partial}{\partial t}(\rho \varepsilon) + \frac{\partial}{\partial x_i}(\rho \varepsilon u_i) = \frac{\partial}{\partial x_j}\left[\left(\mu + \frac{\mu_t}{\sigma_\varepsilon} \right) \frac{\partial \varepsilon}{\partial x_j} \right] + C_{1\varepsilon} \frac{\varepsilon}{k} (G_\kappa + C_{3\varepsilon} G_b) - C_{2\varepsilon} \rho \frac{\varepsilon^2}{\kappa} + S_\varepsilon \tag{6}$$

where u_i represents the velocity component in a specific i (x or y), G_κ is the generation of turbulence kinetic energy by mean velocity gradients, G_b is the generation of turbulence kinetic energy due to buoyancy, Y_M is the contribution of the fluctuating dilatation, S_κ and S_ε are user-defined source terms, σ_k and σ_ε are Prandtl numbers, and $C_{1\varepsilon}$, $C_{2\varepsilon}$ and $C_{3\varepsilon}$ are model constants. The energy equation solved in ANSYS fluent is given by Equations 7 and 8 for fluid and solid regions, respectively [41].

$$\frac{\partial}{\partial t}(\rho E) + \nabla \cdot \left(\vec{V}(\rho E + p) \right) = \nabla \cdot \left(k_{eff} \nabla T \right) \tag{7}$$

$$\frac{\partial}{\partial t}\left(\rho c_p T \right) = \nabla \cdot (k \nabla T) \tag{8}$$

where E is the sum of enthalpy and kinetic energy (total energy), k_{eff} is the effective thermal conductivity that accounts for the thermal conductivity of the molten salt and turbulence-induced conductivity [41], c_p is the solid specific heat, and k is the thermal conductivity of the tank shell.

For the initial approach, a SS 304 was considered for the tank shell and floor. For the 3D analysis, the material was replaced by SS 347H. The thermophysical properties for the tank shell and foundation are listed in Table 6.

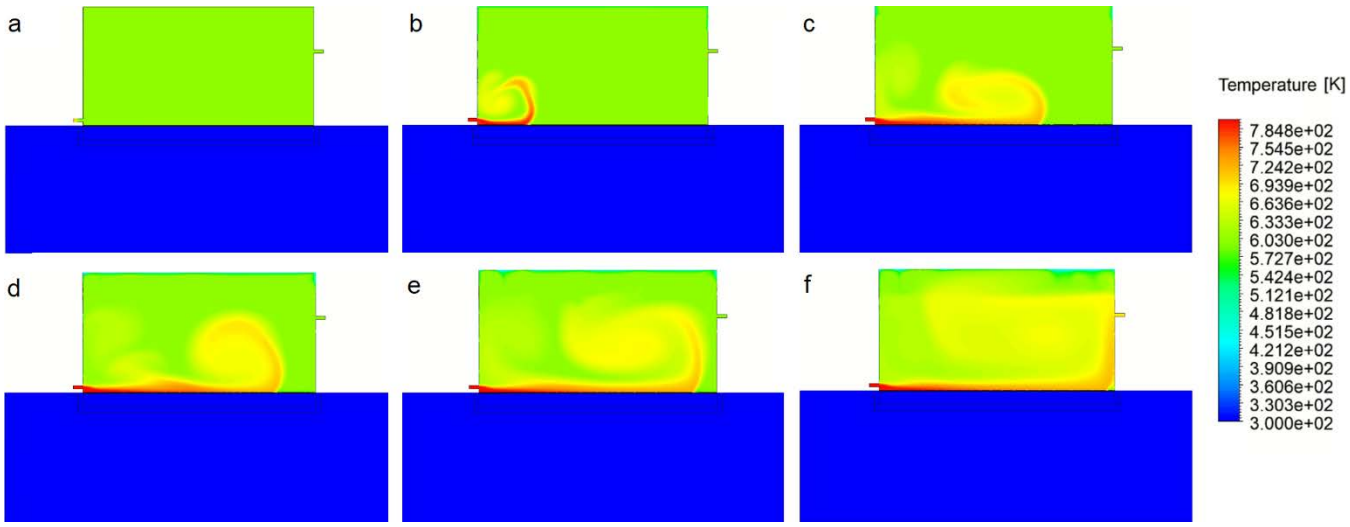

Figure 13. Temperature profile evolution of the molten salt inside the tank. (a) 0 seconds, (b) 10 seconds, (c) 30 seconds, (d) 40 seconds, (e) 50 seconds, (f) 70 seconds.

Table 6. Thermophysical Properties of Tank Components [16] Used in the 2D Model; Temperature in K

Material	ρ [kg/m^3]	k [W/m K]	c_p [J/kgK]
Tank Walls	7830	22.02	502.5
Sand	1600	0.25	840
Thin Plate (Steel)	7830	16.27	502.5
Clay	1702	0.6	878
Concrete	2400	2.25	880
Soil	1200	0.25	800

The exposed walls were set as convection walls with a heat transfer coefficient of 15 W/m^{2}K and a free stream temperature of 300 K. A temperature of 300 K was set for the bottom edge of the soil. For the simulation, molten salt enters the tank at 5 m/s and 800 K. All internal overlapping edges between materials were set as coupled wall interfaces. Also, the initial temperature (model initialization value) for the molten salt and air was 600 K. The model uses 0.05 second time steps and convergences after 75 seconds. The evolution of the temperature distribution inside the tank is displayed in Figure 13 and the corresponding velocity distribution contours are presented in Figure 14. Note that the results presented in Figure 13 and Figure 14 are used for model development and calibration. These results do not correspond to a real tank geometry.

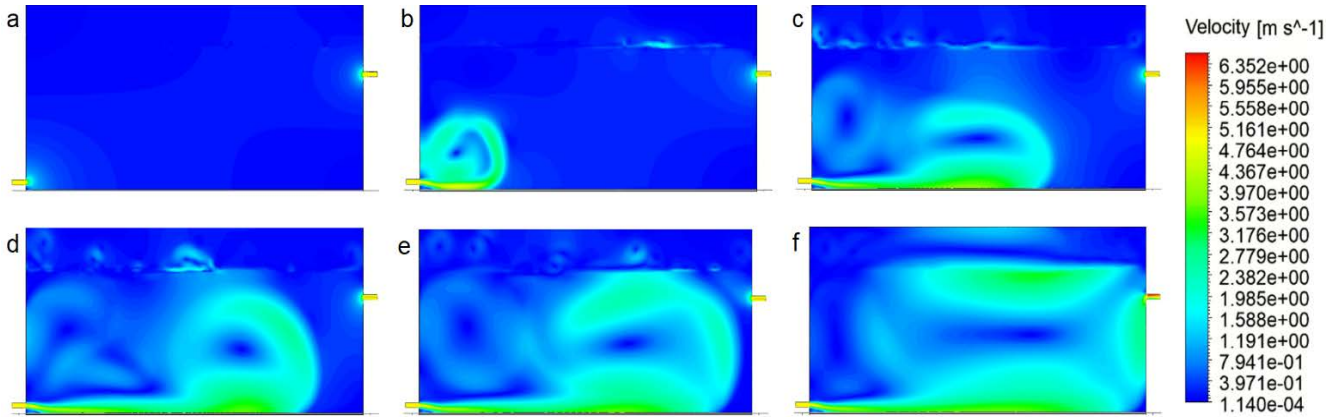

Figure 14. Velocity profile evolution of the molten salt inside the tank. (a) 0 seconds, (b) 10 seconds, (c) 30 seconds, (d) 40 seconds, (e) 50 seconds, (f) 70 seconds.

2.3.2 Sparger Ring CFD Model

The ANSYS CFD simulation was conducted using two models, one for the sparger ring and the other one for the salt inventory in the tank. Using a separate model for the sparger ring allowed a reduction in the parametrization complexity due to structured mesh and boundary conditions. The initial analysis included a theoretical validation of salt velocity and mass flow for the sparger ring. The sparger ring model was imported, meshed, parametrized, and simulated to get the outlet velocity components for every outlet (total of 52 orifices). The velocity profiles at each orifice corresponded to the inlet velocity profiles for the molten salt flow entering the tank.

The molten salt inlet conditions obtained from the sparger ring model are continuously streamed to the salt inventory CFD model. The sparger ring model does not consider structural effects such as stress and deformation because failures have not been consistently reported in this component similar to the floor. The geometry and dimensions for the sparger ring are presented in Figure 15 and the corresponding finite element mesh for its implementation in ANSYS is presented in Figure 16. The mesh for this component is composed of 3,185,646 elements and 634,534 nodes.

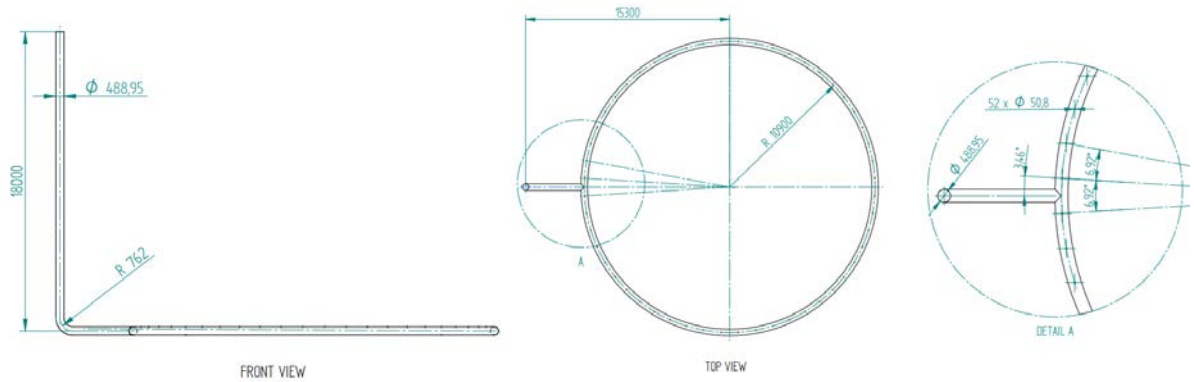

(a) (b)

Figure 15. Sparger ring dimensions. (a) Front view; (b) Top view.

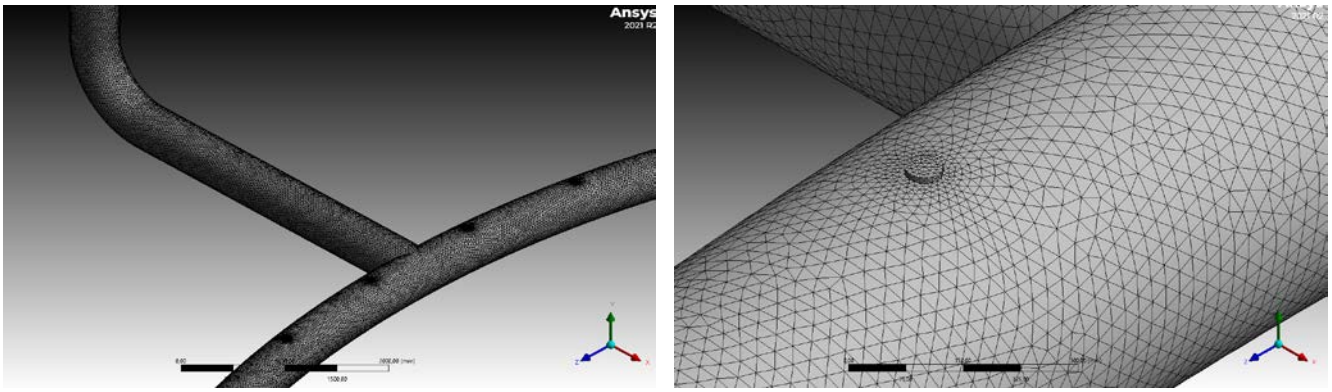

Figure 16. Mesh for ring molten salt. (a) General meshing; (b) Detail for outlet fluid meshing.

The molten salt inflow through the sparger ring was simulated using the transient continuity model and considering the viscous $\kappa - \varepsilon$ standard model. Properties for the molten salt as a function of temperature are listed in Table 7. All exposed walls were set as no-slip walls.

The pressure drop inside the sparger ring between two orifice positions is given by:

$$dP_o = \frac{f\,\rho\,{u_o}^2\,(a_o - a_i)}{2\,D} \tag{9}$$

where u_o is the salt velocity in the ring at the position a_o, a_i is the previous position, D is the inner ring diameter, and f is the friction factor for a fully developed turbulent flow [43]:

$$\frac{1}{\sqrt{f}} = 3.4735 - 1.5635\,ln\left[\left(\frac{\varepsilon}{D/2}\right)^{1.11} + \frac{63.6350}{Re}\right] \tag{10}$$

where Re is the Reynolds number ($Re = \rho\,u_o D/\mu$), and ε is the tube's roughness, assumed equal to 0.045 mm for commercial steel pipes.

The mass flow through each orifice, at the position a_o, was calculate from [44]:

$$q_o = C_d A_o\,\rho\sqrt{2\left(\frac{P_o - P_{bottom}}{\rho}\right)} \tag{11}$$

where A_o is the area of the orifice, C_d is the discharge coefficient (fixed at 0.7 [44]), P_{bottom} is the molten salt pressure head on the sparger ring (set at 193.58 kPa), and P_o is the pressure inside the ring at position a_o, which is given by:

$$P_o = P_{ref} - dP_o \tag{12}$$

where P_{ref} is the required pressure to move the fluid through the half of the sparger ring—set at 285.0 kPa. The velocity through each orifice can be determined from:

$$u_o = \frac{q_o}{A_o\,\rho} \tag{13}$$

The mass flow inside the ring q_r reduces when the molten salt flow passes through each orifice:

$$q_{r,next\ orifice} = q_r - q_o \tag{14}$$

The velocity of the salt for the next orifice yields:

$$u_{o,next\ orifice} = \frac{q_{o,next\ orifice}}{A\rho} \tag{15}$$

where A is the cross-section area of the ring. For every position p_o, the theoretical model can predict P_o, u_o, q_o and u_o.

A preliminary simulation was conducted using a molten salt flow velocity of 7m/s and a temperature of 800 K at each orifice. In this case, the initial salt inventory in the tank was set at a temperature of 600 K and a level of 11.9 m. A constant temperature of 300 K was set for the bottom layer of the foundation. The prediction of streamline profiles for each tank inlet at three different times is presented in Figure 17.

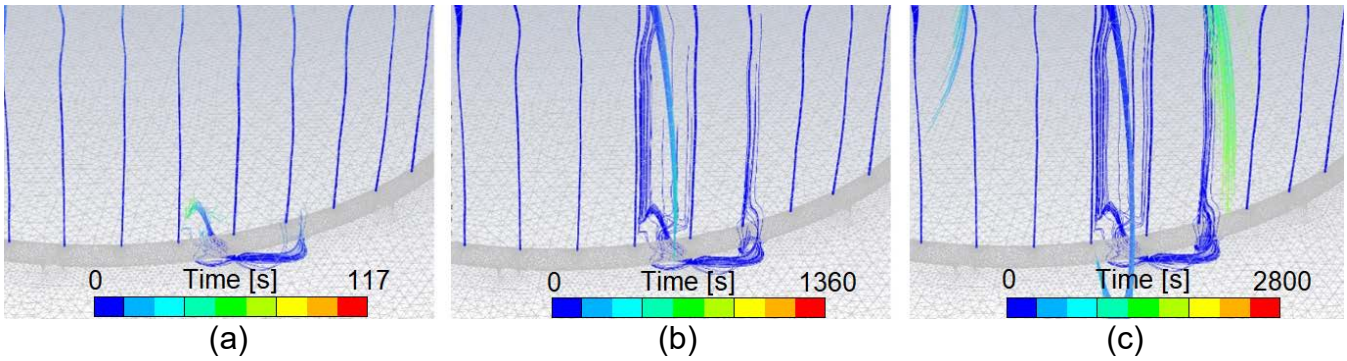

Figure 17. Prediction of time streamline profiles at the tank's inlets (sparger ring outlets) at (a) 117 seconds, (b) 1360 seconds, (c) 2800 seconds

2.3.3 Molten Salt Inventory Model

The interaction between the inflow and the salt inventory was simulated using a CFD approach by solving the governing continuity and momentum conservation equations (Equations 2 and 3) and the standard $\kappa - \varepsilon$ approach [37] for the viscous model. The molten salt inventory model also considers a multiphase treatment to solve the momentum interaction between the phases (molten salt and air). The fluent simulation was parametrized with the volume of fluid multiphase model, where each cell of the mesh is parametrized with only one fluid phase. The model parametrization allows obtaining the level of the tank from the creation of cell registers, one for the air at the top of the tank and the other for the molten salt phase at the bottom of the tank. It is important to note that gravitational acceleration was considered. The volume of fluid formulation is given by Equation 16.

$$\frac{1}{\rho_q}\left[\frac{\partial}{\partial t}\left(\alpha_q \rho_q\right) + \nabla \cdot \left(\alpha_q \rho_q \overrightarrow{v_q}\right) = \sum_{p=1}^{n}\left(\dot{m}_{pq} - \dot{m}_{qp}\right)\right] \quad (16)$$

where p and q are the phases of the fluid, $\dot{m}_{qp}$ is the mass transfer from q to p phase, $\dot{m}_{pq}$ is the transfer mass form p to q phase, and α_q is the volume fraction in the cell. If $\alpha_q = 0$, the cell is empty, and if $\alpha_q = 1$ the cell is full of q fluid.

The solid bodies (shell, floor, roof, foundation, internal piping) and the inventory fluids (molten salt and air) were implemented in ANSYS. For the inventory, the meshing depends on the geometry of the sparger ring and its supports, the salt outlet pipes, the floor geometry, and the roof joint. A structured mesh for fluid phases was created using automatic sizing control in critical zones, see Figure 18. The mesh was refined to have higher resolution in regions of interest. The quality of the mesh was monitored using orthogonal and skewness quality factors according to ANSYS best practices. Each body (floor, shell, and so on) was sectioned into sub-bodies to obtain face splits and edges to obtain the structured mesh. The model did not integrate the sparger ring supports to improve the mesh quality. In addition, all the simulations were conducted on one half of the tank—using a *symmetry* boundary condition—to take advantage of the tank geometry and reduce computational time by reducing the number of elements.

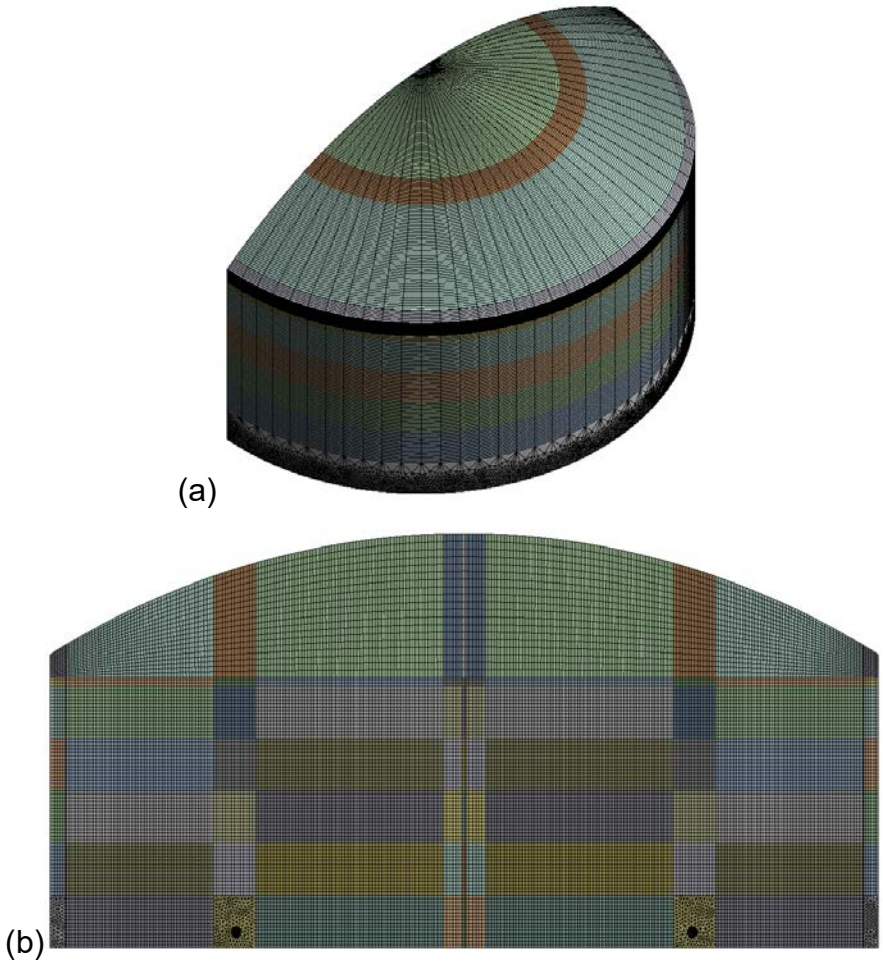

Figure 18. Mesh for tank inventory fluids (molten salt and air); (a) isometric and (b) cross-section view

The model included heat losses through the insulated walls and roof and through the tank floor toward the foundation. For the shell and roof, a convection heat transfer coefficient of 15 W/m^{2}K, an ambient temperature of 300 K, and an atmospheric pressure of 101 kPa were applied. In the floor, a heat loss boundary condition was implemented following the profile presented in Figure 19 and Equation 17, which corresponds to the heat exchange as a function of the tank's radius. A shell conduction model was activated for the foundation layers. It is worth noting that the heat loss profile as a function of the tank radius (Figure 19) was derived from a previous modeling effort by Solar Dynamics. The model was validated by comparing the soil temperature beneath the tank to the temperature predicted by the model. The output of the conduction model was incorporated into the hot tank model as a polynomial equation (Equation 17) using a user-defined function. Near the center of the tank, the heat transfer from the floor to the foundation is one dimensional (i.e., straight down), and the heat flux is moderate due to the large conduction heat transfer path from the center of the tank to the environment. In contrast, near the edge of the tank, the heat transfer through the floor is two-dimensional (i.e., down vertically, and across horizontally). Because the conduction heat transfer distance from the tank perimeter to the environment is short, the heat flux at the perimeter is almost double the heat flux near the center. This simplified heat loss model for the tank floor should only be used when salt is in the tank.

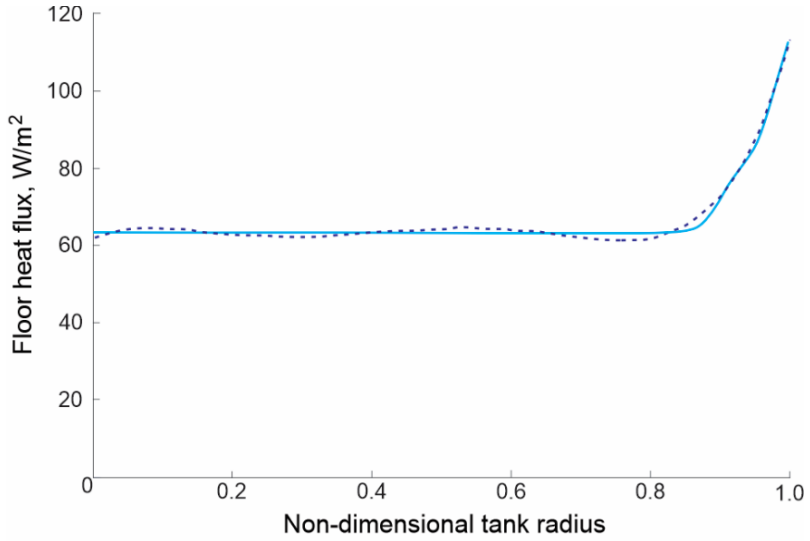

Figure 19. Floor heat loss in the tank floor

The floor heat flux (Q_f), in W/m^2, was estimated through the following polynomial interpolation:

$$Q_f = 0.0005302\hat{r}^5 - 0.02174\hat{r}^4 + 0.3114\hat{r}^3 - 1.8233\hat{r}^2 + 3.7728\hat{r} + 62.197 \qquad (17)$$

where $\hat{r}$ represents the non-dimensional radial distance from the center point of tank in meters.

Other important considerations for the model included:

- All the exposed walls were set as no-slip walls.
- The orifices through the sparger ring were set as pressure outlet conditions based on the tank's level and hydrostatic pressure formulation.
- The inlets were the face areas of the sparger ring orifices and were set considering the outlet mass flow results from the sparger ring simulation.

- The lateral face area corresponding to outlet flow was set as a mass flow outlet boundary condition.

The thermophysical properties for the nitrate molten salt (60% $NaNO_3$ – 40% KNO_3) and air are listed in Table 7 and Table 8, respectively.

Table 7. Nitrate Molten Salt Properties [42]**; Temperature in K**

Property	Polynomial Approximation
Density (kg/m^3)	$2263.72 - 0.64T$
Thermal Conductivity (W/m K)	$0.39 + 1.9x10^{-4}T$
Specific Heat (J/kg K)	$1443 + 0.172\,T$
Dynamic Viscosity (Pa. s)	$7.55x10^{-2} - 2.78x10^{-4}T + 3.49x10^{-7}T^2 - 1.47x10^{-10}T^3$

Table 8. Thermophysical Properties of Air [45]**; Temperature in K**

Property	Polynomial Approximation
Density (kg/m^3)	1.225
Thermal Conductivity (W/m K)	$2.03x10^{-2} + 4.8x10^{-5}T$
Specific Heat (J/kg K)	1006.43
Dynamic Viscosity (Pa. s)	1.7894e-05

2.3.4 Tank Structural Model

The finite element simulation of the tank shell takes the temperature and pressure at the wall boundary from the molten salt CFD simulation. The tank structural mesh is presented in Figure 20. The molten salt outlet was simplified as a single element located in the tank wall at the same height as the inlets of the three vertical pipes that extract the salt out of the tank. This simplification was adopted to improve the convergence of the salt inventory CFD model and to reduce the computational time. It has a minor impact on the temperature distribution in the tank shell and floor, which was evaluated by comparing the temperature results obtained when considering the salt outlet pipes.

Table 9. Thermophysical Properties of Tank Components; Temperature in K

Material	ρ (kg/m^3)	k (W/m K)	c_p (J/kg K)
Sand [41]	1400	0.66	879.09
Slip Plate (Steel)	8030	16.27	502.48
Clay [46]	1587	0.28	1170
Concrete [47]	2391.7	2.07	936.35
Thermal Insulation Wool (width = 18 in.)	128	$3x10^{-4}\,T - 0.1025$	956
Wall, Floor, Roof (ss347H) [48]	7650.8	$8.2x10^{-3}\,T - 18.50$	$0.16\,T - 559.44$

The tank shell was made of austenitic SS 347H. This material has a Poisson ratio of 0.31 and a thermal expansion coefficient of 1.89×10^{-5} K^{-1} [49]. The Young's modulus, yield strength (YS), and ultimate tensile strength for SS 347H as a function of temperature are presented in Figure 21. The thermophysical properties of tank components used in the structural model are listed in Table 9. For this model, the floor's symmetrical edge was restricted for displacement in the x-axis (i.e., displacement in x is 0 mm), and no restriction was imposed on the y-axis and z-axis. The central node in the bottom edge of the floor was set as a fixed support to avoid a displacement of the tank with respect to its initial position, whereas the floor was analyzed as an elastic support with a constant foundation stiffness of 0.015 N/mm^3 [50]. The friction coefficient between the floor and the first layer of the foundation (sand) was set to 0.5. The weight of the sparger ring (10,800 kg) was equally distributed over eight supports.

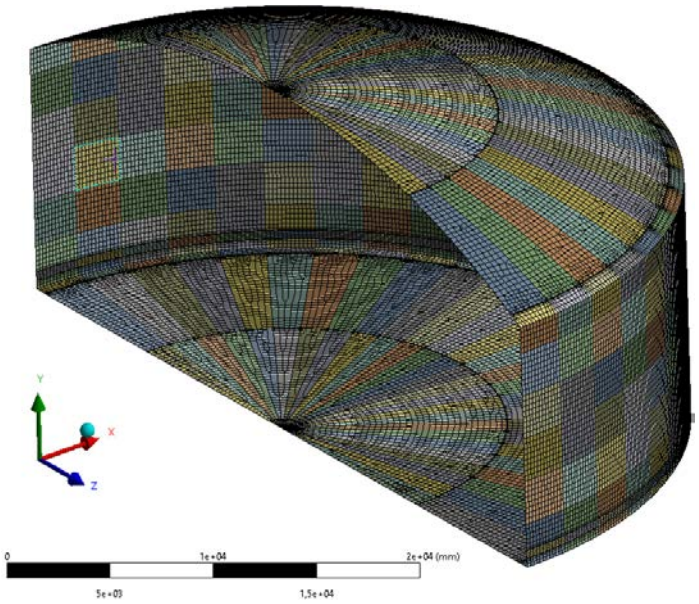

Figure 20. Tank structural mesh

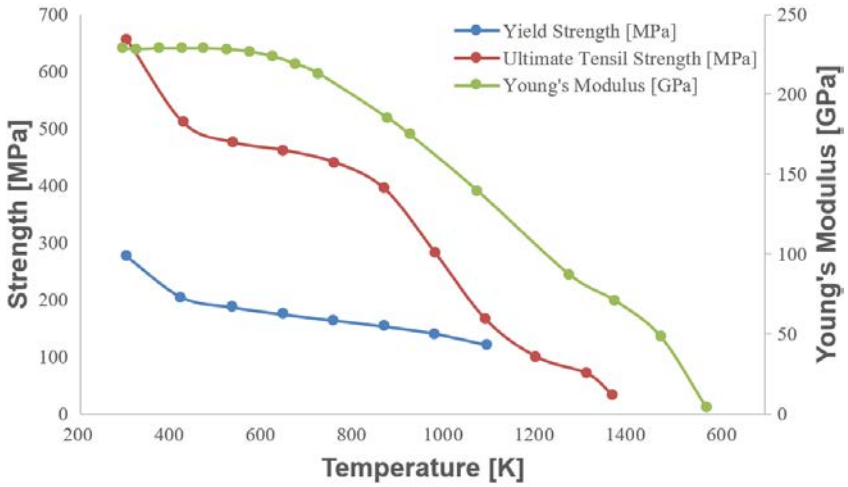

Figure 21. Mechanical properties of stainless steel 347H [48]

The Kirchhoff plate theory for thin plates was employed to conduct a structural assessment. It assumes that the line normal to the mid-surface remains straight and normal after applying the load, which means

that the deformations will only occur in the x- and z-axis in the tank floor. This condition is associated with the shell element model approach. The corresponding plate displacements in x- and z-axis (u and v, respectively) are presented in Equations 18 and 19 [51]:

$$u = -y\frac{\partial w(x,z)}{\partial x} \tag{18}$$

$$v = -y\frac{\partial w(x,z)}{\partial z} \tag{19}$$

where w is the main y-axis deflection as a function of the deflection in x and z coordinates. The strain component in y direction ε_y is equal to 0 for a thin plate (due to the shell element approach); additionally, due to the deflection is free in y-axis, the stress in this component is also zero. The corresponding mechanical strain ε_e and stress (σ_x, σ_z, τ_{xz}) are given by:

$$\varepsilon_e = \begin{Bmatrix} \varepsilon_x \\ \varepsilon_z \\ \gamma_{xz} \end{Bmatrix}_e = \begin{Bmatrix} -y\dfrac{\partial^2 w}{\partial x^2} \\ -y\dfrac{\partial^2 w}{\partial z^2} \\ -2y\dfrac{\partial^2 w}{\partial x \partial z} \end{Bmatrix}_e \tag{20}$$

$$\begin{Bmatrix} \sigma_x \\ \sigma_z \\ \tau_{xz} \end{Bmatrix} = \frac{E}{1-v^2}\begin{bmatrix} 1 & v & 0 \\ v & 1 & 0 \\ 0 & 0 & (1-v)/2 \end{bmatrix}\begin{Bmatrix} \varepsilon_x \\ \varepsilon_z \\ \gamma_{xz} \end{Bmatrix} \tag{21}$$

where E is Young's modulus and v is the Poisson's ratio. Note that γ_{xz} is the shear strain due to the shear stress τ_{xz}.

The force $q(x,y)$ is equal to the equilibrium equation of a shell in the z-axis, as follows [51]:

$$\frac{Eh^3}{12(1-v^2)}\left(\frac{\partial^4}{\partial x^4} + 2\frac{\partial^4}{\partial x^2 \partial z^2} + \frac{\partial^4}{\partial z^4}\right)w = q(x,z) \tag{22}$$

where h is thickness of the thin plate.

Because the model considers thermal loads, the strain due to temperature changes must be included. Equations 23 and 24 correspond to the plane stress and plane strain, respectively [49,51]:

$$\varepsilon_o = \begin{Bmatrix} \varepsilon_x \\ \varepsilon_z \\ \gamma_{xz} \end{Bmatrix}_o = \begin{Bmatrix} \alpha\Delta T \\ \alpha\Delta T \\ 0 \end{Bmatrix} \tag{23}$$

$$\varepsilon_o = \begin{Bmatrix} \varepsilon_x \\ \varepsilon_z \\ \gamma_{xz} \end{Bmatrix}_e = \begin{Bmatrix} (1+v)\alpha\Delta T \\ (1+v)\alpha\Delta T \\ 0 \end{Bmatrix} \quad (24)$$

Where α is the coefficient of thermal expansion and ΔT is the temporal (each timestep) temperature change at each shell element. The total strain is then defined as the sum of mechanical and thermal loads:

$$\varepsilon = \begin{Bmatrix} \varepsilon_x \\ \varepsilon_z \\ \gamma_{xz} \end{Bmatrix}_e + \begin{Bmatrix} \varepsilon_x \\ \varepsilon_z \\ \gamma_{xz} \end{Bmatrix}_o \quad (25)$$

Finally, the stress is determined from the expression [49]:

$$\sigma = E\ (\varepsilon - \ \varepsilon_o) \quad (26)$$

This structural model applies when the stresses of thin plate or shell are evaluated in a quasi-static state step by step. During the transient simulation, the time step was set as Auto Time Stepping between 0.0001 s and 1 s. It is worth noting that the study presented in this report is focused on fatigue and creep failure mechanisms. To capture the plastic deformation in the y-axis requires a different approach different to the shell element model, having a representation of the tank floor as multiple finite elements, which can be used to capture buckling formation. The shell element model was considered in this work to reduce computation time and considering that the focus of the project was creep and fatigue lifetime analysis.

Based on the shell element approach the following assumptions and implications of the tank structural model need to be considered:

- The stresses are calculated in the floor plane, but not in the vertical direction.
- The deformation in the vertical direction does not vary with time.
- The effect of having a deformation only in the floor plane (x- and z-axis) is assumed to have a minor impact on the total stress state.
- Initial residual stresses and distortion in the tank floor after welding fabrication are imported into the tank structural model as a boundary condition.

In addition to the mechanical model used to determine stress distribution and evolution in the tank shell and floor, a finite element model for the floor fabrication was conducted. The model was used to determine residual stresses and deformation in the tank floor after welding. This analysis is the subject of Section 3.

2.3.5 Model Integration

As discussed in the previous sections, the hot tank model is composed of four models: (1) a sparger ring CFD model, (2) a CFD molten salt inventory model, (3) a floor welding fabrication model, and (4) a tank mechanical (structural) model. The first model uses typical tank operating conditions (see Figure 10)—molten salt flow at a specific temperature that comes from the downcomer—as an input time series, simulates the flow through the sparger ring, and predicts the salt flow rates entering the tank through the sparger ring orifices. The outlet mass flows for the sparger ring orifices are then used as

inflow boundary conditions for the second model (tank CFD model). This model simulates the mixing between the incoming salt flow and the salt inventory and determines the velocity field, change in the inventory level, and the temperature and pressure distributions of the salt at every timestep for all nodes. The third model is used to evaluate residual stresses and distortion of the tank floor after fabrication through welding. The temperature distribution obtained from the second model and the residual stress distribution and deformation of the tank floor are then used by the fourth model to determine the associated stress induced in the tank shell, floor, and roof during operation. The model has the flexibility to integrate design features of interest to analyze. Initially, the model considered an ideal flat floor, which was replaced by a more realistic floor that considered distortion and residual stress after fabrication obtained from the third model. A diagram for the hot tank model, describing the integration of the sparger ring CFD model, the CFD molten salt inventory model, the floor fabrication model, and the tank structural model is presented in Figure 22.

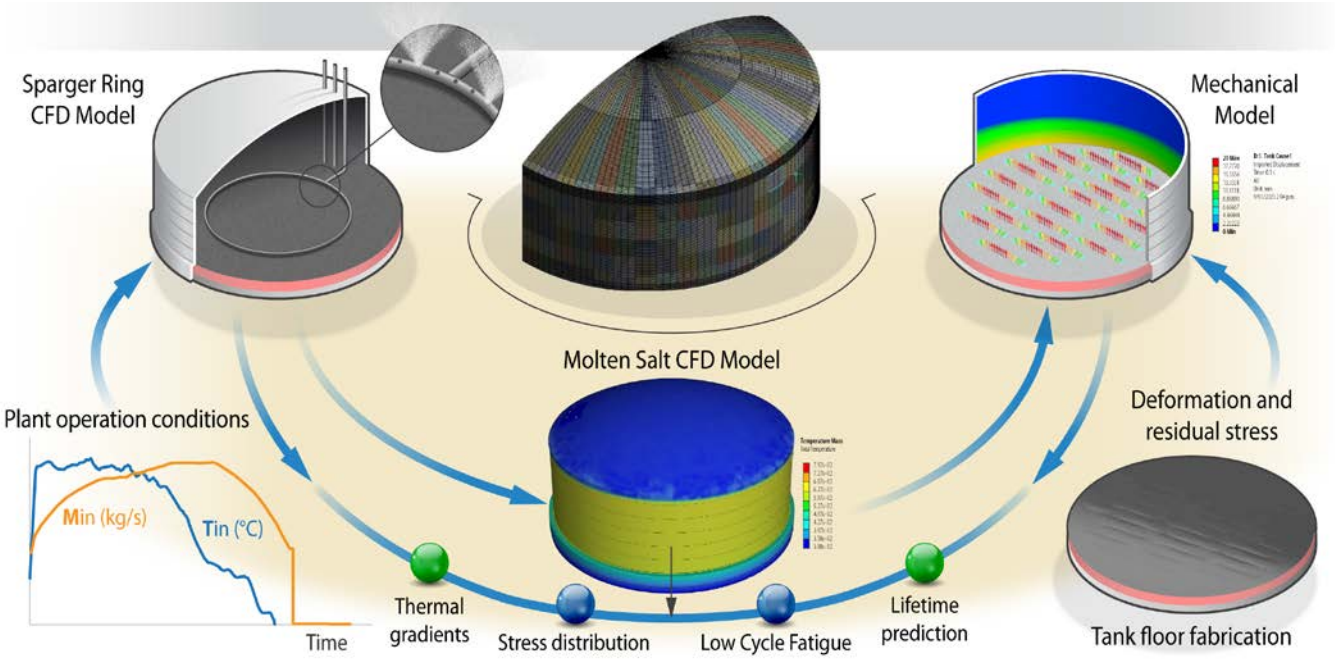

Figure 22. Schematic diagram of the hot tank model

A cross-section view of the representative tank, including all components, is presented in Figure 23.

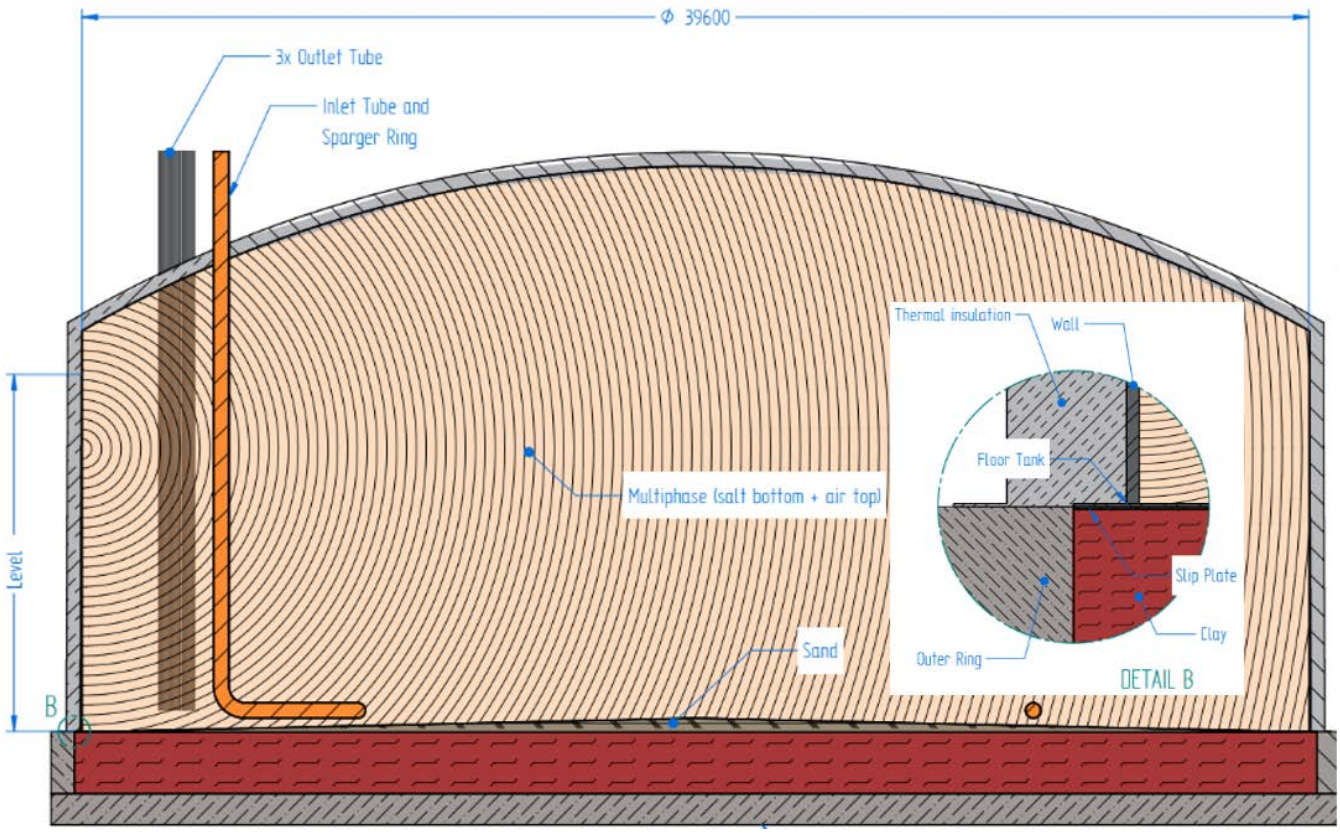

Figure 23. Cross-section view of the tank geometry

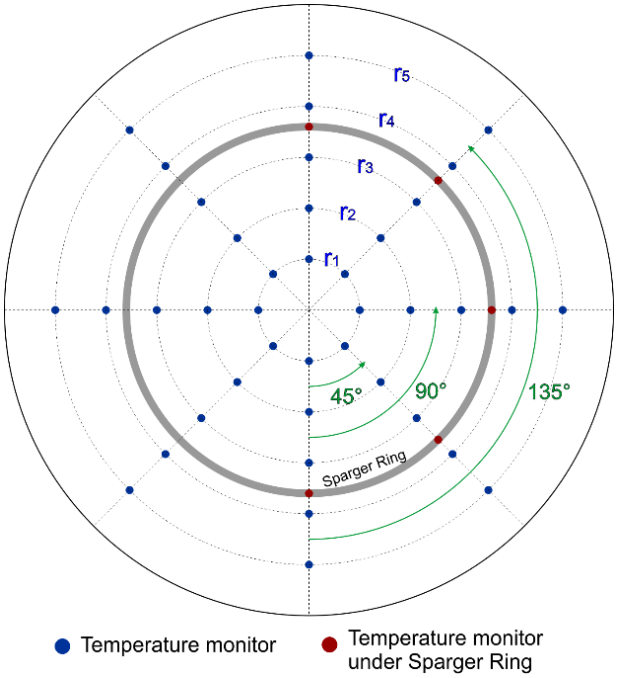

Figure 24. Top view of representative tank floor with monitors

Multiple monitors (points of fast collection of physical variables such as temperature, pressure, strain, and stress) were implemented in the model at different positions in the salt inventory, and the tank wall

and floor. Figure 24 presents the distribution of monitors in the tank floor; 36 monitors for half of the floor, 71 in total. Five of the monitors (for the half floor) were placed right under the sparger ring. Also, one monitor was positioned at the center of the tank floor.

2.4 Model Validation

A mesh independence analysis was conducted for all models to determine the number of volumes and nodes from which the results are not affected by the mesh. The L_2 norm difference [52] was the criterion used in this analysis. The final mesh resolution for each model was selected once the L_2 norm difference reaches a constant value. For instance, for the sparger ring, the selected mesh consisted of 1,156,823 elements and 236,210 nodes, corresponding to a finite element size of 50 mm, while for the molten salt inventory, the number of elements was 2,333,932 elements and 2,385,043 nodes, corresponding to a finite element size of 100 mm. After the mesh independence analysis, a convergence analysis of each of the models was performed to determine the maximum timestep. This time step was dynamically adjusted (reduced) in the model when significant changes in the salt inflow temperature happen, i.e., during transient operating conditions due to clouding. Timesteps in the model dynamically changed from 0.0001 to 10 seconds.

For the mesh independence and convergence analyses, the clear sky day operating condition was considered (see Figure 10a). The validation procedure followed a different approach for each model. For the sparger ring, the conservation of mass (in and out of this element) was verified. For the hot tank model (integrated sparger ring, CFD salt inventory, and structural models) a validation was conducted using real plant operation data that were scaled accordingly with the variation in the representative tank dimensions. This validation process considered multiple full day profiles—clear sky and partly cloudy sky day conditions. The maximum relative error ($\%\ error$) obtained during the validation was below 4% (about 18°C difference) and was observed a few times only during the larger sudden changes (transients) between the inflow and the inventory temperature, mainly at low inventory levels (<2 m). This temperature difference (between the model and the real data) was always registered on the monitors located in the floor right underneath the sparger ring, which are more susceptible to capturing variations in the temperature of the incoming molten salt flow. Apart from these few cases, the error was always less than 2% (temperature difference below 10°C). The $\%\ error$ is defined in Equation 27 and the temperature difference ($T_{diff,avg}$) is defined in Equation 28. The temperature is in °C in both equations.

$$\%\ error = \frac{|T_{real} - T_{model}|}{T_{real}} * 100 \tag{27}$$

$$T_{diff,avg} = |T_{real} - T_{model}| \tag{28}$$

The validation results using real data cannot be released in this report due to the proprietary nature of this information. However, we were able to conduct the validation procedure using a set of short operational cases extracted from real plant operational data (with minor modifications); see Figure 25a and 25d. The average temperatures registered by the monitors located in the floor and at the salt outlets located at the tank wall were compared with the corresponding average temperatures in the floor and the outlet salt flow deducted from the real plant operating conditions. Figure 25a presents the average tank floor temperature comparison for a transient event occurring over about 20 minutes, while Figure 25d shows the comparison for the average outlet flow temperature considering a smooth clear sky day profile. The corresponding error and average temperature difference curves are presented in Figure 25b,

25c, 25e, and 25f. In general, all predicted temperatures are relatively close to the real temperature measurements. The more pronounced changes in temperature are very well captured by the model.

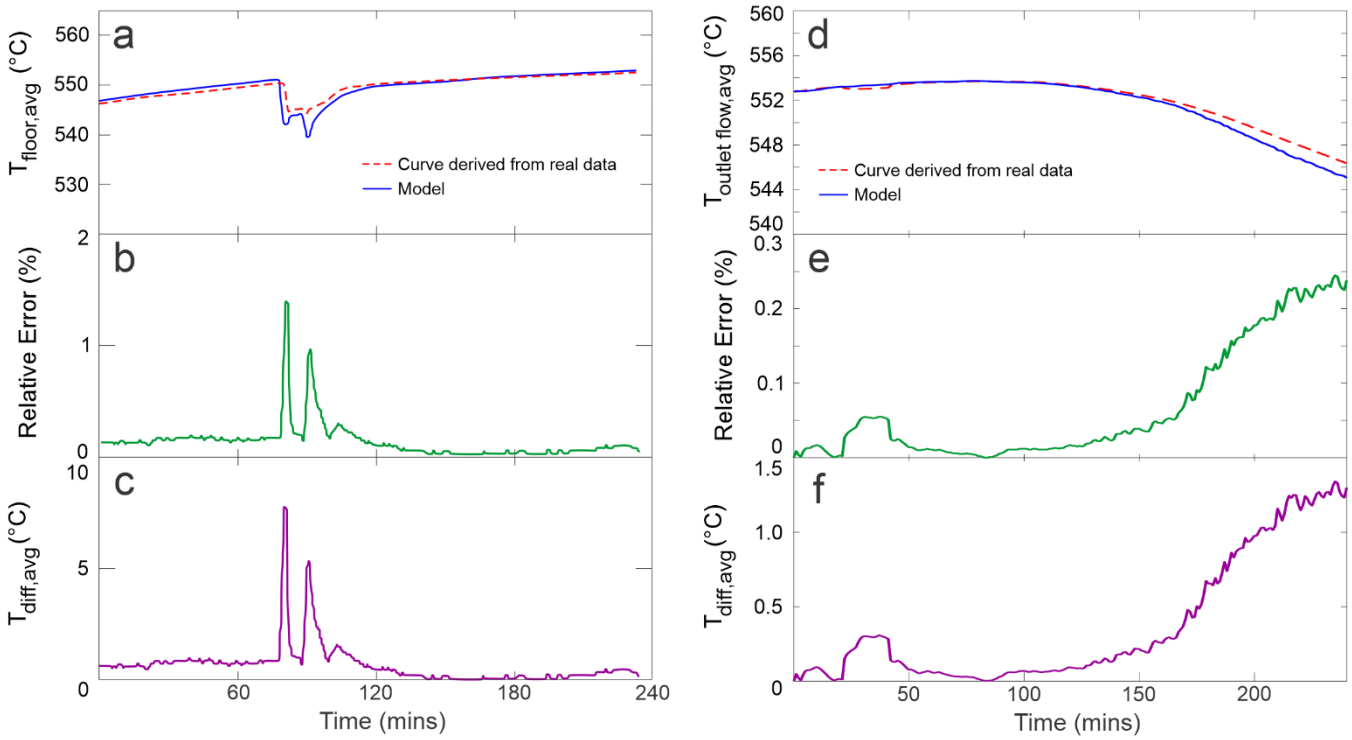

Figure 25. Hot tank model CFD validation: (a) Comparison between average floor temperatures. (b) Relative error for the average floor temperatures. (c) Average floor temperature difference. (d) Comparison between average outlet flow temperatures. (e) Relative error for the average outlet flow temperatures. (f) Average outlet flow temperature difference.

The mechanical model was verified by comparing the level of stress obtained from the hot tank model and the stress reported in the literature for different systems sharing some commonalities, see Table 10. It is important to highlight that stress measurements in commercial molten salt hot tanks are not available in the literature. Maximum stresses predicted for the hot tank model are about 80 MPa at ~510°C for an ideal flat floor and reach values close to 260 MPa at high temperatures (~560°C) and large inventory levels (> 8 m), when the initial distortion and residual stresses in the floor—after welding fabrication—are considered (see Section 3).

Table 10 summarizes structural tank analyses conducted for TES tanks that are used to compare and verify the mechanical portion of the hot tank model. It is important to note that none of these studies use real or typical plant operating conditions as input or boundary conditions. Some studies are focused on design, heat transfer fluid evaluation, techno-economic analysis, and stress analysis. These studies were selected because, despite the differences, the TES tank has some level of commonality with the current system, such as material, heat transfer fluid, dimensions, or maximum operating temperatures. It can be observed from Table 10 that the level of stress for the hot tank lies within the stress values (ranges) for the tank analyses reported in the literature for similar operating conditions. However, it is important to highlight that a direct comparison between studies is not adequate as the stress results depend on multiple fabrication, design, and operation parameters. As expected, the larger variation of the maximum stress between these studies (80 to 478 MPa) are associated with different conditions and parameters been considered.

Table 10. Related Structural Analyses of Storage Tanks for CSP Systems

Study	System	Tank Design	HTF	Max Temp (°C)	Max Stress (MPa)	Notes
This work	Solar tower	Shell: SS347H Insulation: Mineral wool Diameter: 39.6 m	Molten nitrate salt $NaNO_3$-KNO_3	565	**80** @ 510°C (ideal floor) **260** @ 560°C (deformed floor)	Transient ANSYS CFD/mechanical
Gabbrieli et al. 2009 [13]	Parabolic trough	Shell: Carbon steel (SA-516 Gr-70) Insulation: Ceramic fiber Diameter: 22.4 m	Molten nitrate salt $NaNO_3$-KNO_3	550	**130**	Transient model. No input transient data—24 hours. SAP2000 software
Gonzalez et al. 2015 [17]	Not reported	Shell: ASTM A533 Class 2 Grade A Insulation: Fiberglass Diameter: 18.2 m	Caloria HTF+ rock and sand	300	**120** for flexible filler, **300** for rigid filler	Transient. No input transient data
Wan et al. 2020 [19]	Solar tower	Shell: SS 304 Insulation: Mineral wool Diameter: 11.6 m	Molten salt $NaNO_3$-KNO_3	565	**100**	2D steady state—ANSYS. Tank design: Solar Two project
Gage et al. 2021 [18]	Solar tower	Shell: Carbon steel (SA-516 Gr-70) Diameter: 41.8 m	Molten chloride salt	720	**135–161**	Transient. ANSYS CFD/mechanical Gen3
Riahi et al. 2021 [49]	Not reported	Shell and tube TES Shell: SS347H	Sodium + PCM	750	**106–250**	ANSYS CFD/mechanical
Jiang et al. 2021 [53]	Not reported	Shell: Steel (no specification) Diameter: 5m	Nitrates, chlorides, lead-bismuth eutectic, liquid sodium	450	**96.6–168.8**	2D analysis ANSYS Fluent
Du et al. 2023 [14]	Solar tower/ parabolic trough	Shell: SS 321H Insulation: Aluminum silica fiber Diameter: 18.7 m	Molten chloride salt + PCM	563	**80** @ discharge, **478** @ charge	2D ANSYS Fluent

3 Tank Floor Fabrication Model

3.1 Floor Fabrication

The tank floor has been identified as a critical component of this analysis due to the combination of high friction loads and thermal transients. The tank floor is manufactured from several thin rectangular plates that are welded together; see Figure 26. The welding fabrication process can result in residual stresses and a non-flat floor, with elevated regions and depressed regions that contribute to the plastic deformation of the floor during operation and increase the susceptibility to develop local buckles. Further, the non-flat characteristics of the floor could result in an undesirable non-uniform distribution of friction forces between the floor and the foundation.

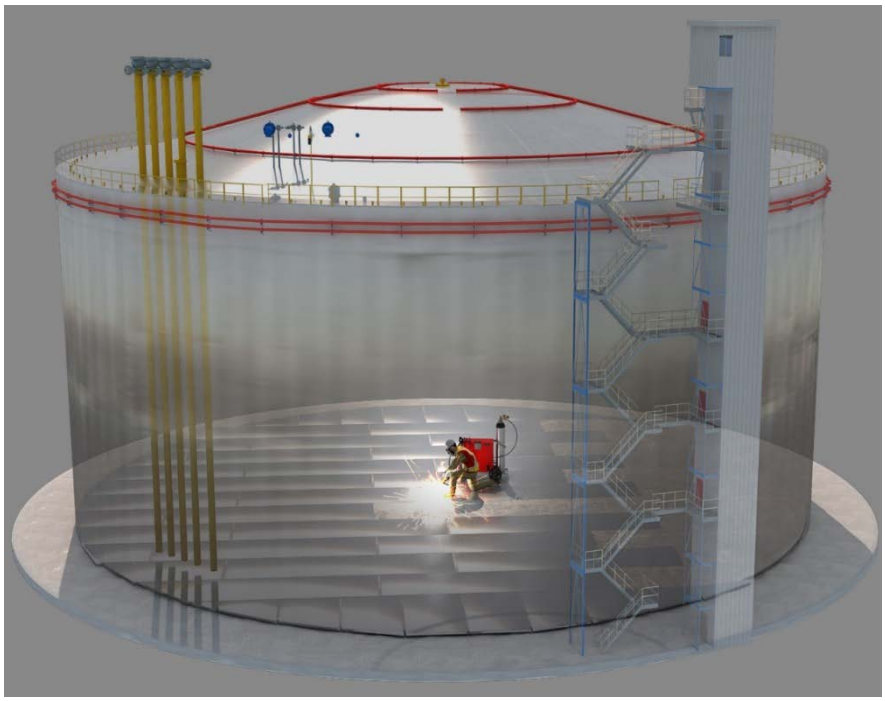

Figure 26. Schematic representation of the tank floor fabrication

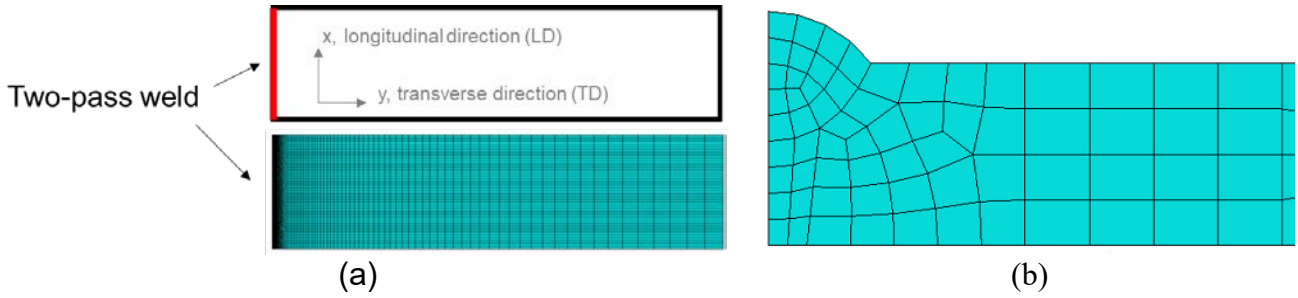

Figure 27. (a) Top view of a half symmetric model of two plates. X is the longitudinal direction, which is parallel to the welding direction; Y is the transverse direction. (b) Transverse cross-sectional enlarged view in the weld region of the mesh model; Z is the normal (thickness) direction.

An FEA model was developed in the Abaqus software to simulate the floor welding and to determine the residual stress magnitude and the deformation distribution of the floor after its fabrication. The model considered SS 347H plates—32 feet (9,754 mm) long, 8 feet (2,440 mm) wide, and 9/32 inches (7 mm) thick. The matching E347 welding filler was considered during the simulations. The model development started with the welding simulation of two plates, then three plates, and finally half of the tank floor. A half symmetric model was established for the welding procedure for plate welding and for the entire floor to reduce the calculation time. Figure 27 presents a half symmetric FEA model of two floor plates. The mesh of the weld bead area was refined to ensure calculation accuracy. Gradient mesh was used away from the weld to reduce the element number and thus further minimize the calculation time.

The welding parameters used for the floor fabrication modeling were determined from information received from welding procedure specification of CSP plants and the results of metallurgical characterization on field welds conducted by Colorado School of Mines. Gas tungsten arc welding (GTAW) was used for the root pass (pass 1), and gas metal arc welding (GMAW) was used for pass 2. The time between passes was 300 seconds, to allow for sufficient cooling of the plate after the root pass below 80°C. Note that a dwell time of 1–2 seconds was determined to be mandatory through modeling to ensure sufficient melting, i.e., avoid lack-of-fusion defect, at the start point of pass 2 welding. Table 11 summarizes the input welding parameters for the finite element modeling of the two passes, including the heat input—calculated as voltage (U), times current (I), times arc efficiency (η)—and travel speed.

In the two-pass welding model, only elements of pass 1 were activated during the welding of pass 1, whereas pass 2 elements remained deactivated. After pass 1 was completed, elements for pass 2 were activated. In this simulation, the material properties were assumed to be the same for both the weldment and the base metal. Table 12 tabulates the temperature-dependent material properties of SS 347H [48,54]. Figure 28 presents the temperature-dependent flow stress/strain data for SS 347H. These data were obtained (1) at room temperature (in black); (2) at 600°C–1,050°C (in red) from Colorado School of Mines thermo-mechanical testing, which used a Gleeble machine for the microstructure of the HAZ of SS 347H [3,55]; and (3) at 100°C–400°C (in gray), from the National Institute for Materials Science (NIMS) data sheets [56]. Note that the material database used for SS 347H and the finite element weld modeling method used in this work were validated through neutron diffraction measurement [3]. 3D finite element models using the sequentially coupled thermo-elastic-plastic method were established to systematically investigate the dependence of residual stress distribution in SS 347H on base plate thickness, joint geometry design, and pre-heating condition [3]. The elastic strain profiles calculated from the weld model agreed well with those measured from neutron diffraction mapping, which indicates that stress contours calculated from strain evolution from the weld model are reasonably accurate.

Table 11. Welding Parameters Used in the FEA Model Simulation

Parameter	Pass 1	Pass 2
Welding method	GTAW	GMAW
Heat input (ηUI), Watt	1920	2720
Arc efficiency, (η)	0.6	0.85
Welding speed (v), mm/s	5	5

Table 12. Temperature-Dependent Material Properties of SS 347H [48], [54]

Temp (°C)	Density (e-9 kg/mm^3)	c_p (e-8 mJ/kg-K)	k (mW/mm-K)	Young's Mod. (GPa)	Expansion Coeff. (e-6)/s	Poisson's Ratio
20	7.9	4.43	15	200	16.5	0.278
100					17.5	
200	7.8	5.15	17.5	185	18	0.288
400	7.7	5.63	20	170	18.5	0.298
538				156		0.298
600	7.6	5.81	22.5	153	19	0.313
800	7.5	6.09	25.5	135	20	0.327
900	7.4				20	
1000		6.31	28.3	96	20.5	0.342
1100	7.3			70	21	0.342
1200		6.54	31.1	50	21	0.350
1300				10	22	0.351
1340		6.69	33.1			
1400		6.75			22.5	
1500	7.2				22.5	

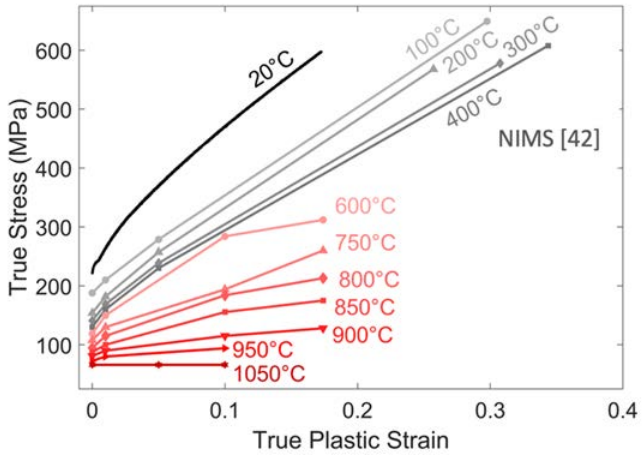

Figure 28. Temperature-dependent stress/strain curves used in this materials database for 347H stainless steel [55], [56]

3.2 Welding Heat Input Parameter Calibration

The welding heat source was simulated using Goldak's double ellipsoidal model, which is a type of body heat flux typically used in the modeling of arc welding processes. Figure 29 presents the schematic diagram of Goldak's double ellipsoidal heat source [57].

The heat source equations are presented in Equations 29, 30, and 31 [58]:

$$q_f(x,y,z) = \frac{6\sqrt{3}f_f Q}{a_f bc\pi\sqrt{\pi}} e^{-3\frac{(x+vt)^2}{a_f^2}} e^{-3\frac{y^2}{b^2}} e^{-3\frac{z^2}{c^2}} \tag{29}$$

$$q_r(x,y,z) = \frac{6\sqrt{3}f_r Q}{a_r bc\pi\sqrt{\pi}} e^{-3\frac{(x+vt)^2}{a_r^2}} e^{-3\frac{y^2}{b^2}} e^{-3\frac{z^2}{c^2}} \tag{30}$$

$$Q = \eta UI \tag{31}$$

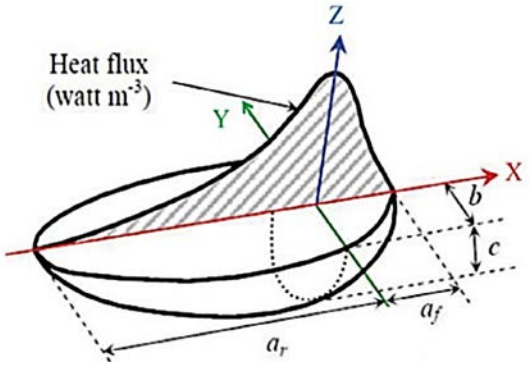

Figure 29. Schematic diagram of Goldak's double ellipsoidal heat source [57]

where q_f and q_r are the front and rear of the heat flux at a point (x, y, z) in the ellipsoid, respectively; $a, b,$ and c are the three semi-axes of ellipsoid; f_f and f_r are the heat distribution between the front and rear ellipsoid, respectively, the sum of which is equal to 2; Q is the total heat of welding; U is voltage; I is current; and η is arc efficiency.

In the heat resource model (Equations 29 and 30), a, b, and c determine the shape of the fusion zone and f_f and f_r affect the heat distribution of the front and rear half of the ellipsoid. The peak temperature of the fusion zone decreases with increasing $a, b,$ and c. The values of a, b, c, f_f, and f_r were calibrated for pass 1 and pass 2 to match the experimental fusion zone shapes. Table 13 and Table 14 present the trials performed for calibration purposes for pass 1 and pass 2, respectively. The trial results indicated that the influence of f_f and f_r on the temperature field is marginal.

Table 13. Trials of Shape Parameters for Pass 1

***f* value**	**Trial 1**	**Trial 2**	**Trial 3**
$f_f + f_r = 2$	$a_f = 3.5$	$a_f = 4$	$a_f = 4$
$f_f = 0.6$	$a_r = 11$	$a_r = 12$	$a_r = 12$
$f_r = 1.4$	b = 4	b = 4	b = 3
	c = 3.5	c = 4	c = 5

Figure 30 presents an example of trials resulting in insufficient heat input and lack of fusion in both pass 1 and pass 2. Figure 31 presents the thermal profiles calculated from the shape and heat distribution parameters of trial 3 for pass 1 in Table 13, and of trial 1 for pass 2 in Table 14, which matches the experimentally observed fusion zone boundaries of pass 1 and 2 reasonably well. It should be noted that the heat source parameters may experience further change with a change in dwell time at the start point

of weld pass 2. We determined that a dwell time of 2 seconds was required to avoid a lack of fusion defects at the beginning of weld pass 2, although a full penetration could be achieved in the middle and end of the weld length using the same welding parameter without the 2-second dwell time. The contours in Figure 30 and Figure 31 were generated using the mirroring function in the half symmetric model to illustrate the complete profile of the temperature distribution in the weldment.

Table 14. Trials of Shape Parameters for Pass 2

***f* value**	**Trial 1**	**Trial 2**	**Trial 3**
$f_f + f_r = 2$ $f_f = 0.6$ $f_r = 1.4$	$a_f = 5$ $a_r = 15$ $b = 6$ $c = 5$	$a_f = 4$ $a_r = 12$ $b = 4.5$ $c = 4.5$	$a_f = 4.5$ $a_r = 10$ $b = 5$ $c = 5$
	Trial 4	**Trial 5**	**Trial 6**
$f_f + f_r = 2$ $f_f = 0.8$ $f_r = 1.2$	$a_f = 4$ $a_r = 12$ $b = 4.5$ $c = 4.5$	$a_f = 4.5$ $a_r = 10$ $b = 4$ $c = 4$	$a_f = 4.5$ $a_r = 10$ $b = 5$ $c = 5$
	Trial 7	**Trial 8**	**Trial 9**
$f_f + f_r = 2$ $f_f = 1$ $f_r = 1$	$a_f = 4$ $a_r = 9$ $b = 6$ $c = 5$	$a_f = 3.5$ $a_r = 7$ $b = 6$ $c = 5$	$a_f = 3$ $a_r = 6$ $b = 6$ $c = 6$

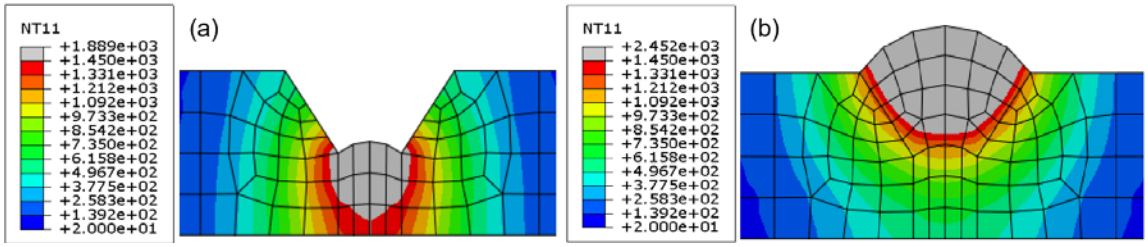

Figure 30. Fusion zone boundary of (a) pass 1 and (b) pass 2 without dwell time in a calibration process that showed a lack of fusion

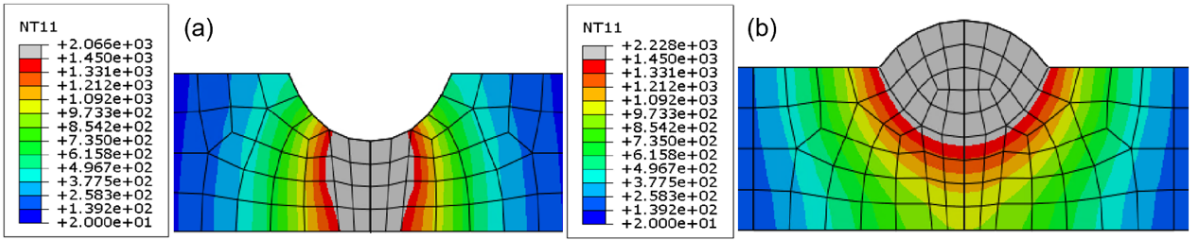

Figure 31. Fusion zone boundaries matching the experimental bead shapes of (a) pass 1 and (b) pass 2 with a dwell time of 2 seconds at pass 2 start

3.3 Convergence Analysis in Thermal and Mechanical Models

Sequential coupling simulation in the thermo-elastic-plastic analysis of tank floor welding was used. The first step was the transient heat transfer calculation under Goldak's heat source. The temperature field results were then imported into the second step as a temperature field load to conduct the elastic-plastic analysis for calculation of stress and deformation.

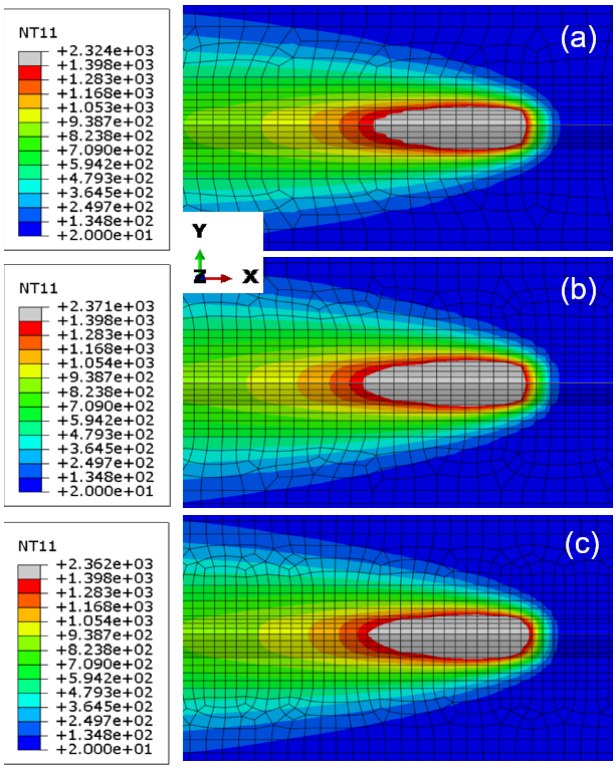

Figure 32. Temperature contours of pass 2 for (a) Model I, (b) Model II, and (c) Model III at half of the welding time

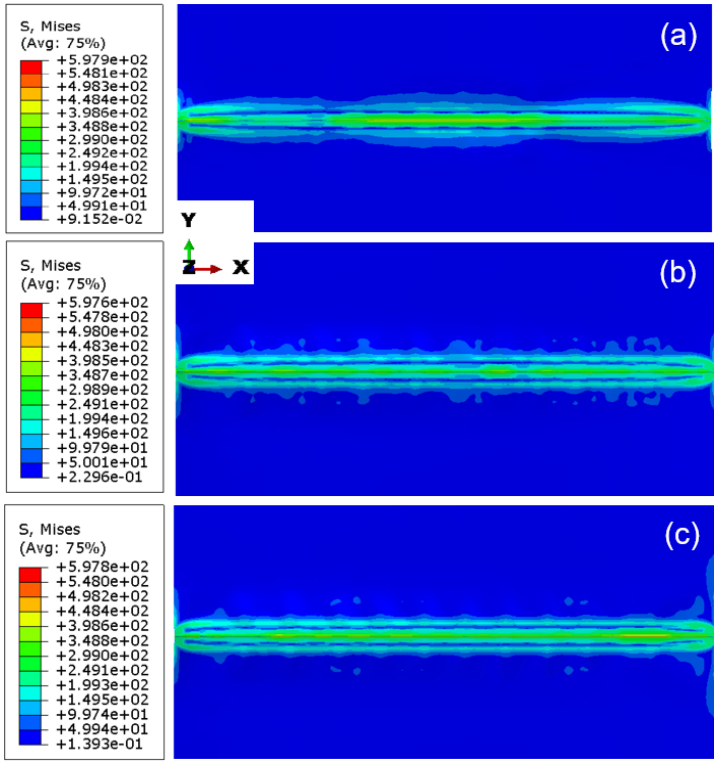

Figure 33. Von Mises stress contours around the entire weld length of (a) Model I, (b) Model II, and (c) Model III after welding completion

An eight-node linear hexahedral element type was used in the heat transfer calculation with DC3D8 (D: diffusive heat transfer or mass diffusion elements, C: solid element, 3D: three-dimensional element, 8: each element has 8 nodes) and the non-linear elastic-plastic calculation with C3D8R (R stands for reduce integration). Table 15 tabulates three trials of the model with different longitudinal mesh sizes in the weld bead to evaluate convergence. We analyzed the impact of mesh size on computation time, thermal results, and mechanical results to identify a meshing strategy with a reasonable number of elements that maintained the accuracy of the analysis.

From Table 15, by decreasing the mesh size, the calculation time of the thermal model increases. Figure 32 presents the temperature fields generated during pass 2 for the three mesh models at half the welding time. By comparing Figure 32a and 32b, it can be seen that the coarser mesh size in Model I leads to a less smooth fusion zone boundary, especially toward the tail of the gray colored region. For more refined meshes, Figure 32b and 32c, the peak temperature values are very close and their contour lines are less impacted by the mesh element geometry than those of Model I. Note that the mesh shapes of

weld passes were slightly different among the three models, leading to some variations among absolute values predicted from the three models.

Table 15. Three Trials of the Model with Different Longitudinal Mesh Sizes in the Weld Bead

	Model I	Model II	Model III
Longitudinal mesh size in weld bead (mm)	3	2.5	2
Number of elements	62533	80623	104296
Number of nodes	84227	109165	141630
Calculation time—CPU time—(seconds)	336776	551544	863528

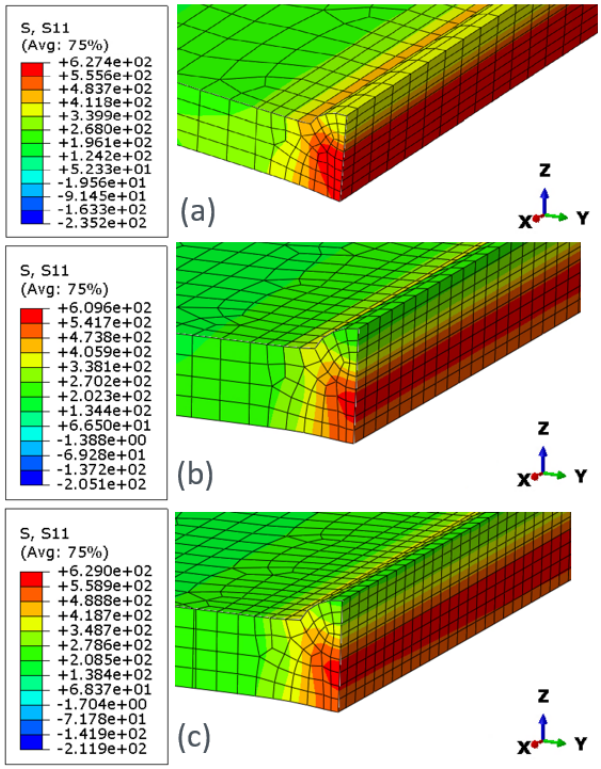

Figure 34. Cross-sectional view of the contours of longitudinal residual stress (S11) in the two-pass welding procedure for (a) Model I, (b) Model II, and (c) Model III, sectioned at the middle of the weld length and along the weld centerline

Figure 33 presents the contours of the Von Mises stress along the entire weld length of Models I, II, and III after welding completion. The stress distribution and peak stress value—critical factors that determine cracking susceptibility—were not impacted noticeably, as can be seen by comparing Figure 33a, 33b, and 33c. Figure 34 compares the cross-sectional views of longitudinal stress (S11) after welding completion for Models I, II and III, while Figure 35 and Figure 36 contrast transverse stress (S22) after welding completion for Models I and II, respectively. These cross-sectional views are taken from the middle of the plate along the welding direction. Figure 34a, 34b, and 34c indicate that the weldment experiences high longitudinal tensile stresses at the weld toe on the top surface, and underneath the top weld bead (pass 2) where reheating occurred. Similarly, the maximum transverse

tensile stress occurs underneath the top weld bead, see Figure 35 and Figure 36. Model I, with a coarser mesh, underpredicts the peak stress values and outputs slightly more homogeneously distributed stress fields than Model II, which has a finer mesh. However, as it was mentioned, this was partly influenced by the difference in heat input shape parameters.

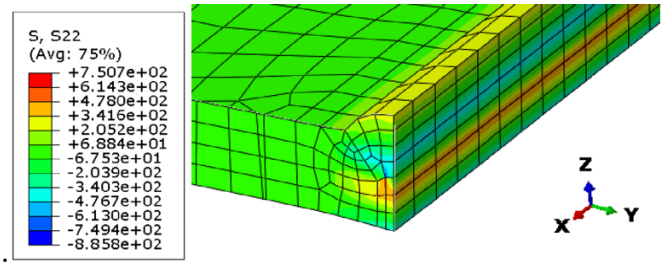

Figure 35. Cross-sectional view of the contours of transverse (S22) residual stress in the two-pass welding procedure for Model I, sectioned at the middle of the weld length and along the weld centerline

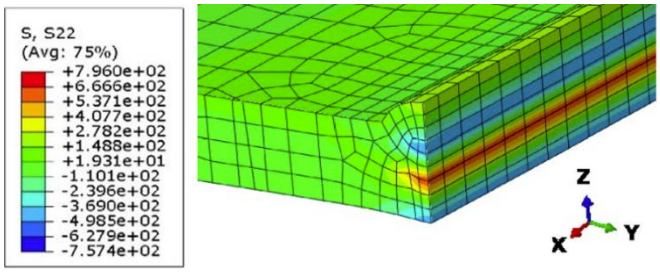

Figure 36. Cross-sectional view of the contours of transverse (S22) residual stress in the two-pass welding procedure for Model II, sectioned at the middle of the weld length and along the weld centerline

Figure 37 presents a comparison of longitudinal residual stresses in the peak region (red region in Figure 34a, 34b, and 34c) within pass 1 along the x-axis (welding direction) extracted from Model I, II, and III. The longitudinal stresses from Model II and Model III exhibit a better agreement than that of Model I. Figure 38 compares the transverse residual stress in the peak region (red region in Figure 35 and Figure 36) along the y-axis (transverse direction) extracted from Model I and Model II. Model I, which has a coarser mesh, underpredicted the peak transverse stress in the weld centerline.

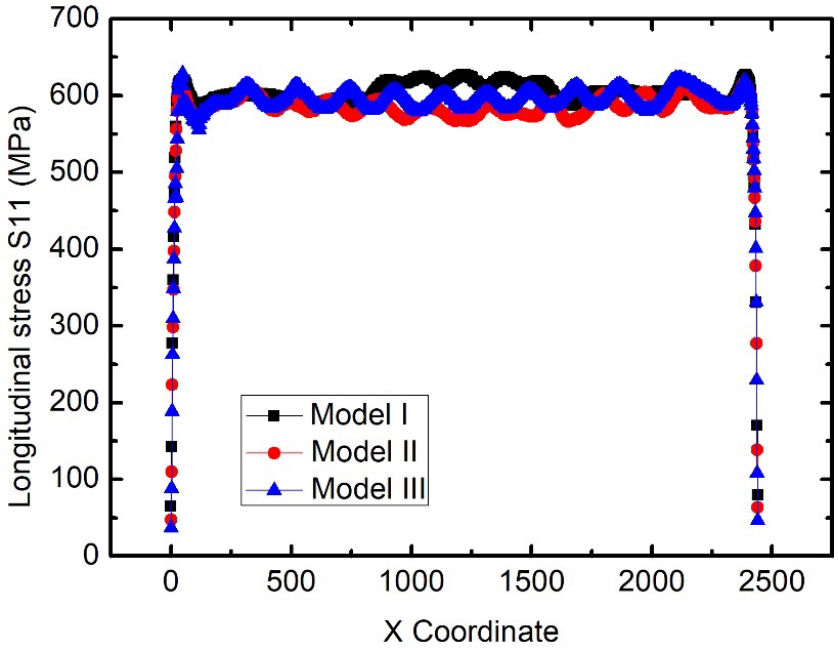

Figure 37. Longitudinal residual stress in the peak region (red region in the left figure) within pass 1 along the x-axis (welding direction) extracted from Model I (black), Model II (red), and Model III (blue)

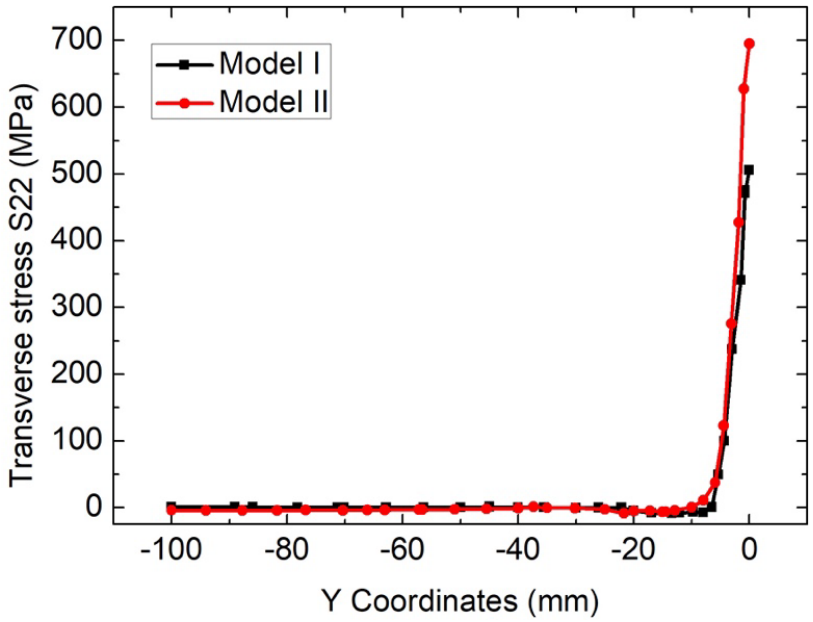

Figure 38. Transverse residual stress in the peak region (red region in Figure 35 and Figure 36) along the y-axis (transverse direction) extracted from Model I and Model II

In summary, with the refinement of element size, the Model II meshing strategy demonstrates adequate data accuracy, as it was evidenced by its outputs aligning closely with those generated from more refined mesh Model III. In comparison, the coarse Model I mesh strategy tends to underpredict the transverse peak residual stress and overpredict the HAZ longitudinal peak residual stress. Taking into account calculation time and accuracy, the mesh size of Model II is chosen for the two-tank floor plate weld model for the subsequent analysis.

3.4 Modeling Approach Analysis and Down Selection

There are multiple methods to create a weld model, including: implicit thermo-elastic-plastic FE solid model, implicit thermo-elastic-plastic FE shell model, explicit analysis approach, and inherent strain method. These methods are systematically compared here to assist in determination of the appropriate approach to generate reliable residual stress and distortion profiles in the entire tank floor with sufficient spatial resolution within a reasonable calculation time.

The thermo-elastic-plastic FE method with solid element and two-pass welding procedure provides the most detailed thermal profile during welding and accurate residual stress and distortion of plates after welding completion. However, this method is computationally intensive and encounters excessive weld-induced deflection due to the large floor dimensions, resulting in unresolved convergence issues when activating the elements of Pass 2 weld, especially for the long-edge welds. To address this convergence challenge—inherent in implicit thermo-elastic-plastic FE solid models when simulating extreme large-scale welds that induce significant plastic deformation—the two-pass weld model was firstly simplified into a one-pass weld model. To identify the proper heat input parameters for this simplification in a time-efficient manner, a small-plate two-pass weld model was first built in Section 3.4.1. The impacts of plate geometry on the stress and distortion profiles are evaluated by comparing the results from welding on two small and large plates, respectively. Additionally, in Section 3.4.2, a two-pass implicit solid model is established for three small plates welding, which is not achievable for large plates due to the convergence challenge. This modeling effort provides valuable inputs as a comparison or validation for

other weld modeling methods to be evaluated next. Section 3.4.3 describes details of heat input parameter adjustment for weld pass simplification using the small-plate model. In later sections of 3.4, a systematic investigation of weld modeling methods is performed using the simplified one-pass weld including (1) implicit thermo-elastic-plastic method with one weld pass, (2) explicit thermo-elastic-plastic model with one weld pass, (3) inherent strain model with two weld passes, and (4) shell element model with one weld pass. A thorough comparison is made between the outputs from these different tank floor welding models and the small-plate model to identify the most appropriate modeling method(s).

3.4.1 Implicit Thermo-Elastic-Plastic Finite Element Model of Small-Plates with Two-Pass Welds

The plate dimensions used in the model were 12” (304.8 mm) long, 6” (152.4 mm) wide, and 9/32” (7 mm) thick. Figure 39 presents the mesh model of the two small plates with a two-pass weld along the x-axis. The mesh of the weld bead area is refined to ensure calculation accuracy.

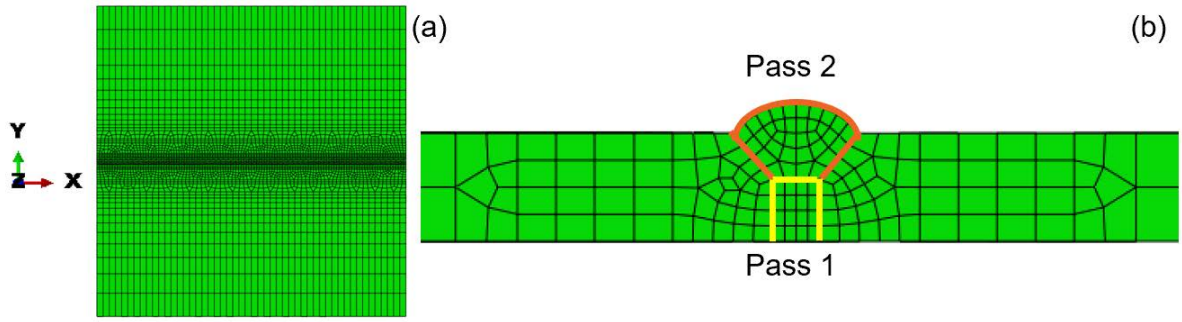

Figure 39. Mesh model of two small plates with a two-pass weld along the x-axis: (a) top view and (b) transverse cross-sectional view of the two-pass weld

All welding parameters were kept the same as those used in the tank floor plate simulation. Note that a dwell time of 1–2 seconds was added at the weld start point for the second pass to ensure sufficient melting, i.e., to avoid lack-of-fusion defects. Table 16 summarizes the input welding parameters for modeling of the two passes. The heat input is calculated by multiplying the voltage (U), current (I), and arc efficiency (η).

Table 16. Welding Parameters Used in the Model to Simulate the Two-Pass Welding of Two Small Plates

Parameter	Pass 1	Pass 2
Welding method	GTAW	GMAW
Heat input (ηUI), watt (J/s)	1920	2720
Welding speed (v), mm/s	5	5

Figure 40 presents the calculated contours of the Von Mises stress along the whole weld length of a small-plate model. As shown in Figure 40a and 40b, peak stress values are comparable between the two weld models. Figure 41a and 41b present Von Mises stress contours in the transverse cross-sectional view around the weld bead along the red lines in Figure 40 of small plates and tank floor plates, respectively. Figure 42 to Figure 44 present the longitudinal stress, transverse stress, and normal stress in the transverse cross-sectional view around the weld bead of small plates and tank floor plates,

respectively. The overall magnitudes of the stresses from different directions are comparable, although the stress near the top surface may differ between the small-plate and large-plate model. The difference in the transverse stress distribution between the small-plate and tank floor plate models may be related to the different length-to-width ratios.

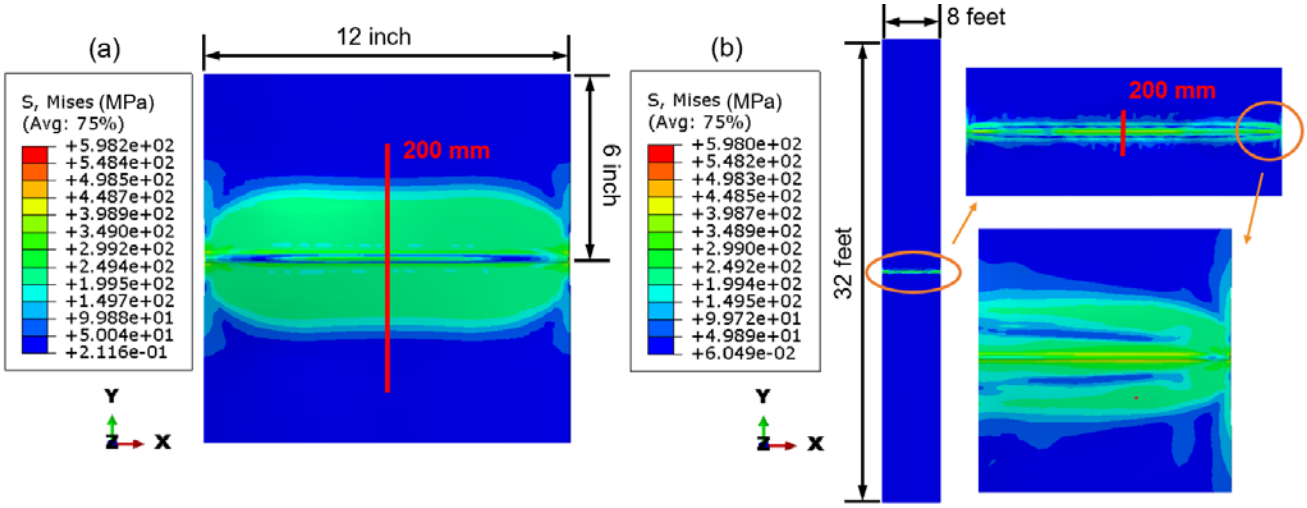

Figure 40. Top view of Von Mises stress contours calculated from (a) the small-plate model and (b) the tank floor plate model

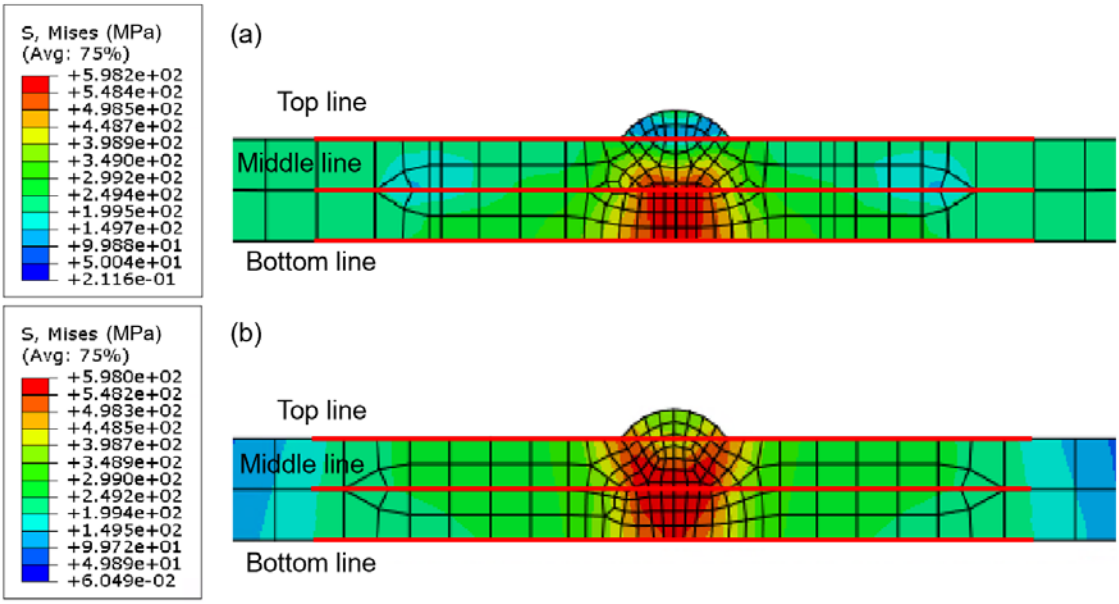

Figure 41. Transverse cross-sectional view of Von Mises stress contours along the red lines marked in Figure 40 from (a) the small-plate model and (b) the tank floor plate model

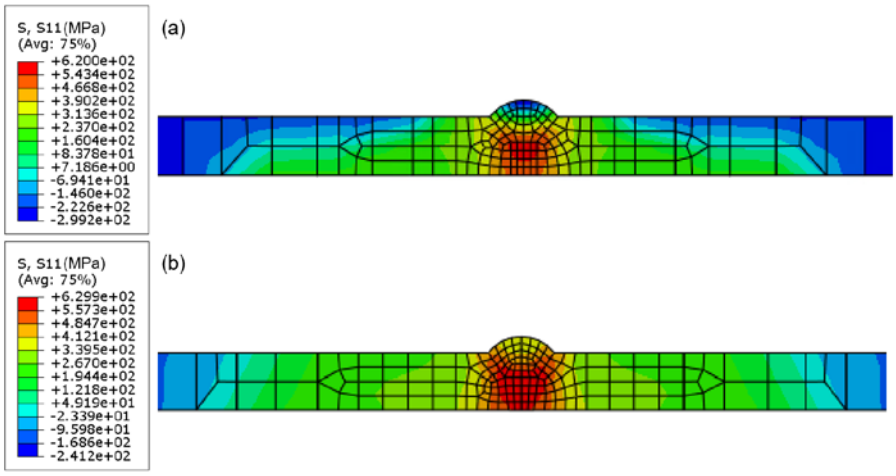

Figure 42. Transverse cross-sectional view of longitudinal stress contours along the red lines in Figure 40 from (a) the small-plate model and (b) the tank floor plate model

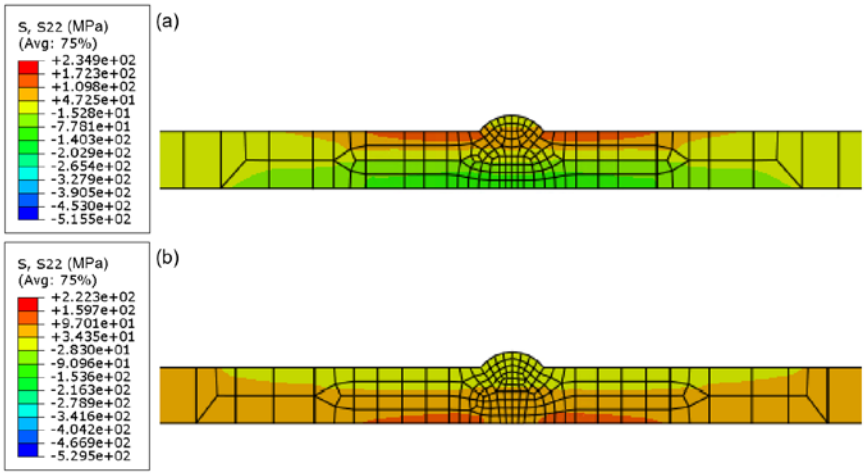

Figure 43. Transverse cross-sectional view of transverse stress contours along the red lines in Figure 40 from (a) the small-plate model and (b) the tank floor plate model

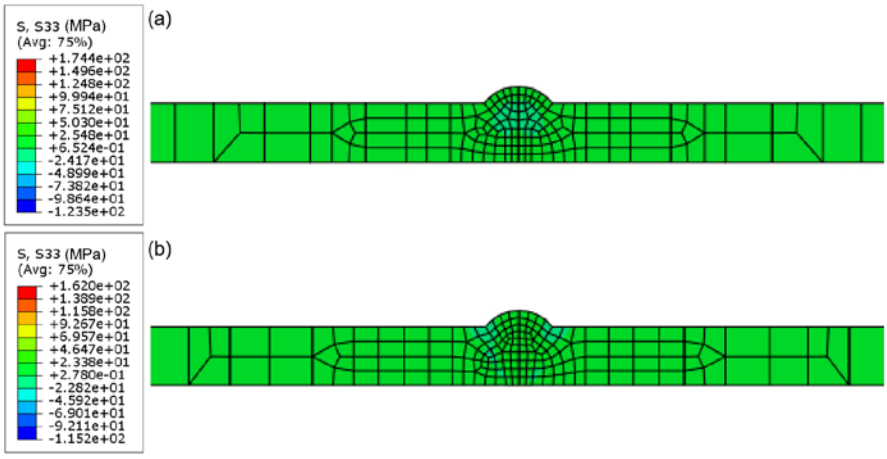

Figure 44. Transverse cross-sectional view of normal stress contours along the red lines in Figure 40 from (a) the small-plate model and (b) the tank floor plate model

Figure 45 compares the equivalent plastic strain (PEEQ) contours for the small-plate and tank floor plate models in the transverse cross-sectional view around the weld bead along the red lines in Figure 40. Comparable PEEQ distribution patterns and values are observed in both models. Figure 46 to Figure 48 present the plastic strain distributions along longitudinal, transverse, and normal directions on the same cross-section of the small-plate and tank floor plate models. Along all three directions, the distribution and magnitude of the plastic strains throughout the cross-section area near the welds are comparable. This justifies using strain fields calculated from the small model as inherent strain inputs for deflection calculation in the large tank floor.

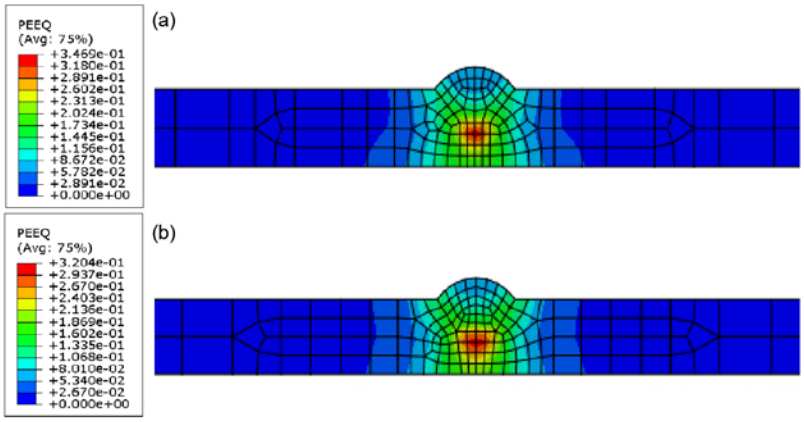

Figure 45. Transverse cross-sectional view of PEEQ contours along the red lines in Figure 40 from (a) the small-plate model and (b) the tank floor plate model

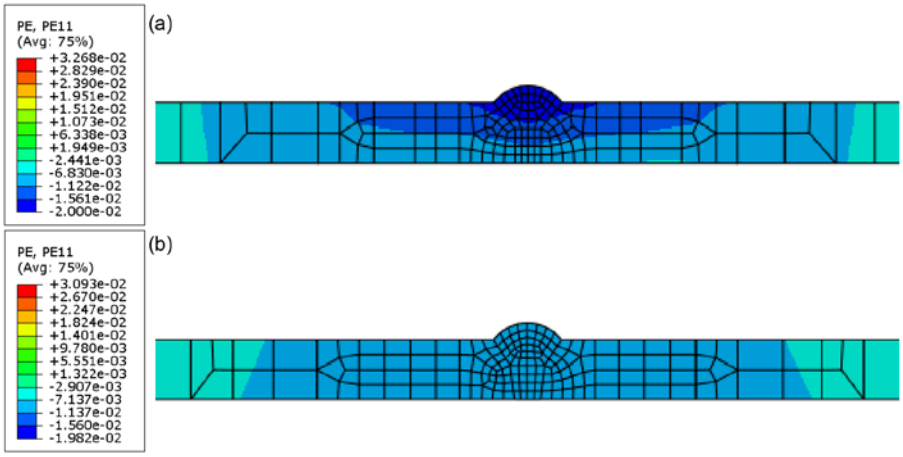

Figure 46. Transverse cross-sectional view of longitudinal plastic strain contours along the red lines in Figure 40 from (a) the small-plate model and (b) the tank floor plate model

Figure 49 presents the normal direction displacement patterns induced by welding of the small-plate and tank floor plate models from top and side views. With comparable plastic strain contours, the overall trend of distortion patterns is comparable between the small-plate and tank floor plate models, although the plate size difference leads to one-order of magnitude difference in absolute distortion. It was found that the small thermo-elastic-plastic FEA can provide valuable insights on the stress and strain profiles in large tank floor welding.

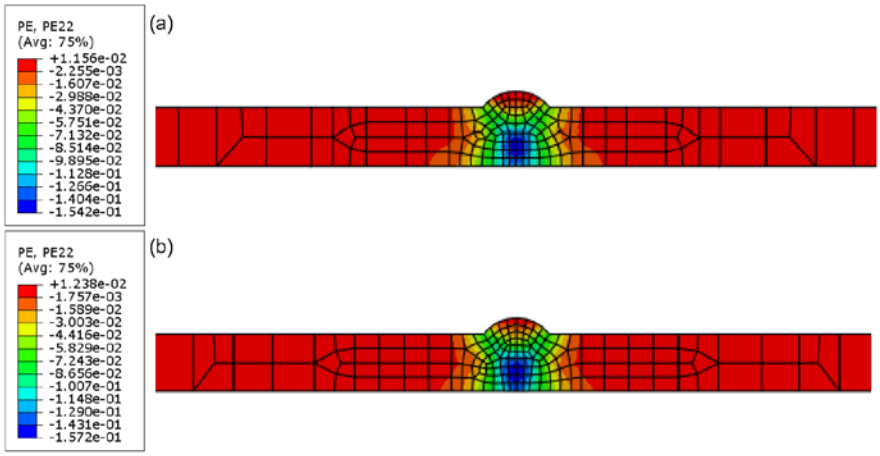

Figure 47. Transverse cross-sectional view of transverse plastic strain contours along the red lines in Figure 40 from (a) the small-plate model and (b) the tank floor plate model

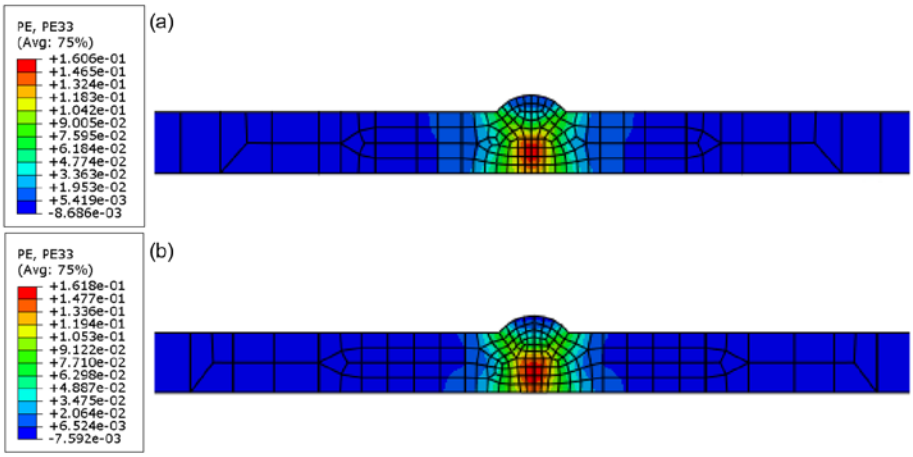

Figure 48. Transverse cross-sectional view of normal plastic strain contours along the red lines in Figure 40 from (a) the small-plate model and (b) the tank floor plate model

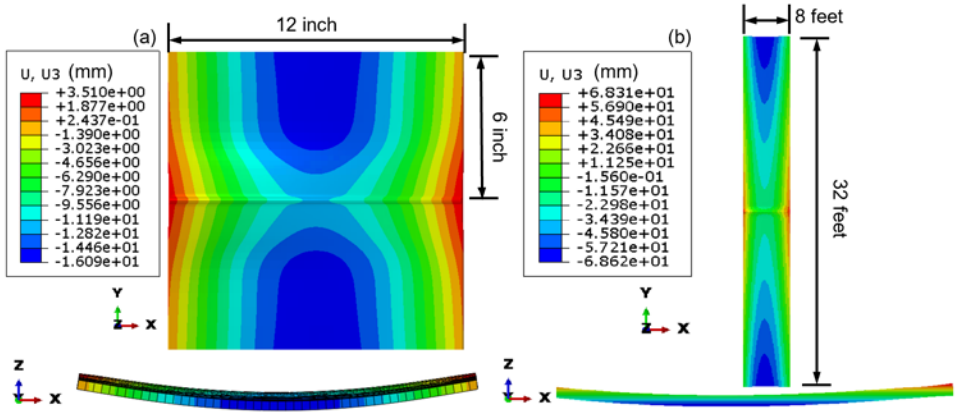

Figure 49. Top and side views of normal direction displacement contours of (a) the small-plate model and (b) the previous tank floor plate model

3.4.2 Modeling of the Three-Small-Plate Model with Two-Pass Welds

The dimensions of the plates in the small three-plate model are the same as those in the two-plate model: 12” (304.8 mm) long, 6” (152.4 mm) wide, and 9/32” (7 mm) thick for each plate. Figure 50 presents the mesh model of the three-small-plate model with two welds. The weld bead crown was removed and simplified with a flat top surface to create a mesh at the intersection of the weld beads. The mesh of the weld bead area was refined to ensure calculation accuracy. This model considered the welding heat input parameters listed in Table 16, which were calibrated to match experimental fusion zone geometry. In this model, the weld was first made along the short edge between plates 1 and 2, and then along the long edge to weld plate 3 onto plates 1 and 2. Table 17 tabulates the analysis steps of the three-small-plate model with two-pass welding. In Table 17, steps 1–5 are for the short-side weld, and steps 6–10 are for the long-side weld. Both welds introduced a dwell time of 2 s at the start point of the second weld pass to ensure sufficient melting, at the beginning of the transient stage.

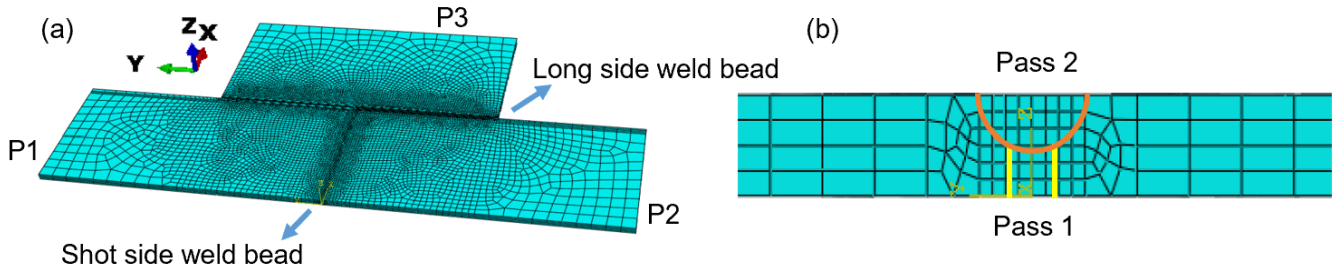

Figure 50. Mesh model of (a) three-small-plate model with two welds and (b) transverse cross-sectional view of the two-pass weld. P1–P3 represents plates 1–3.

Figure 51a and 51b present temperature contours during the pass 2 welding process at the short and long edges, respectively, from the three-small-plate model.

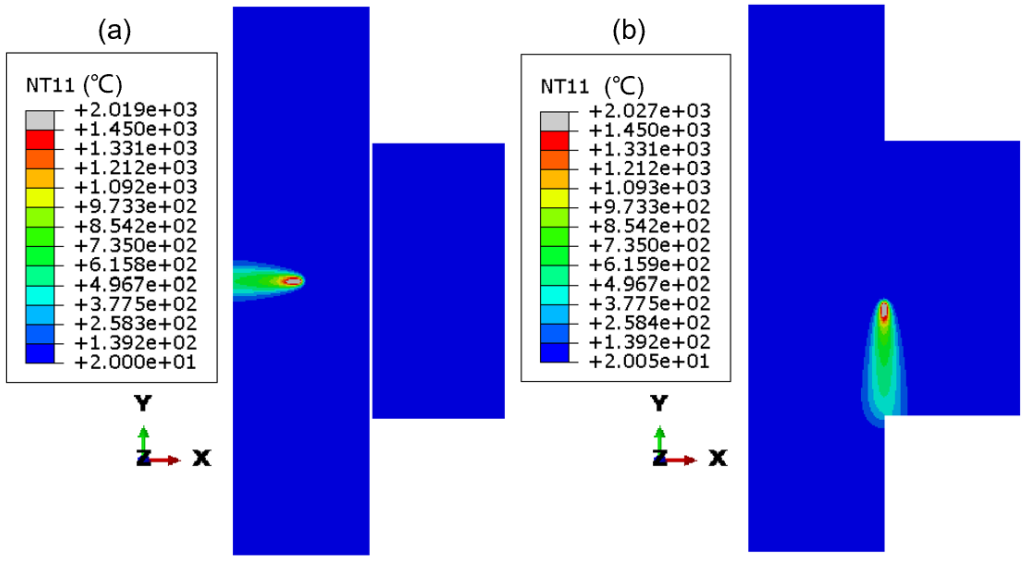

Figure 51. Example temperature contours during the pass 2 welding process at (a) the short edge and (b) the long edge from the three-small-plate model

Table 17. Analysis Steps of Three-Small-Plate Model with Two-Pass Welding

Step	Description	Step	Description
1	Pass 1 heating for short-edge weld	6	Activation of pass 1 elements and heating for long-edge weld
2	Pass 1 cooling for short-edge weld	7	Pass 1 cooling for long-edge weld
3	Activation of pass 2 elements and 2-s dwell time at the start of pass 2 for short-edge weld	8	Activation of pass 2 elements and 2-s dwell time at the start of pass 2 for long-edge weld
4	Pass 2 heating for short-edge weld	9	Pass 2 heating for long-edge weld
5	Pass 2 cooling for short-edge weld	10	Pass 2 cooling for long-edge weld

Figure 52 illustrates the boundary conditions set for stress and distortion analysis in the three-small-plate weld model. It should be noted that the boundary condition settings can also impact the displacement calculation. Currently, no information is available to confirm boundary conditions representing the actual field assembly process. A variety of boundary conditions that simulate potential field assembly practices can be evaluated to reveal the potential displacement variation range. Figure 53 shows the top view of the Von Mises stress and normal displacement calculated from the three-small-plate weld model under the assumed boundary conditions. These results demonstrate how the stress and displacement patterns on the top surface were impacted significantly by intersecting weld paths.

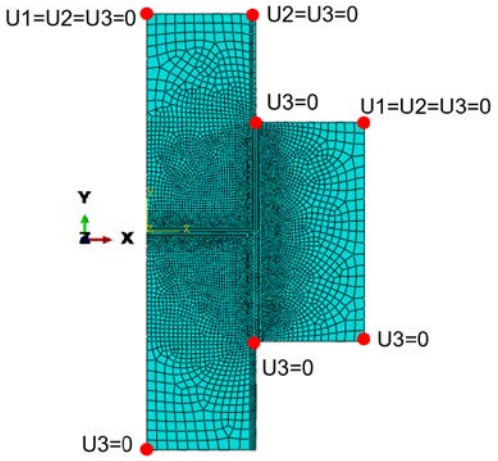

Figure 52. Boundary conditions set for the analysis in the three-small-plate weld model

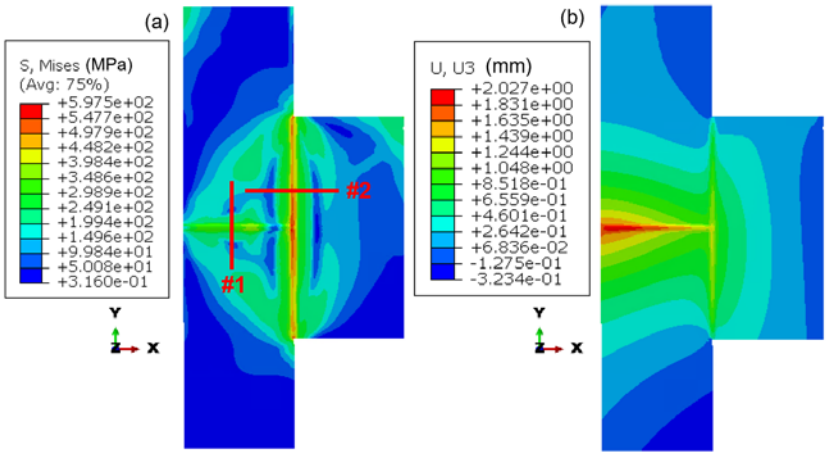

Figure 53. Top view of (a) Von Mises stress and (b) normal displacement contours calculated from the three-small-plate weld model

Figure 54 and Figure 55 show the transverse cross-sectional view of the Von Mises stress and PEEQ along lines 1 and 2, as marked by the red lines in Figure 53a, demonstrating the interaction of intersecting welds. Because the plate size is relatively small, the two long-edge welding passes reheated plates 1 and 2, which is expected to introduce significant changes in the stress and strain distributions of the previous short-edge weld as compared to the large tank floor welds.

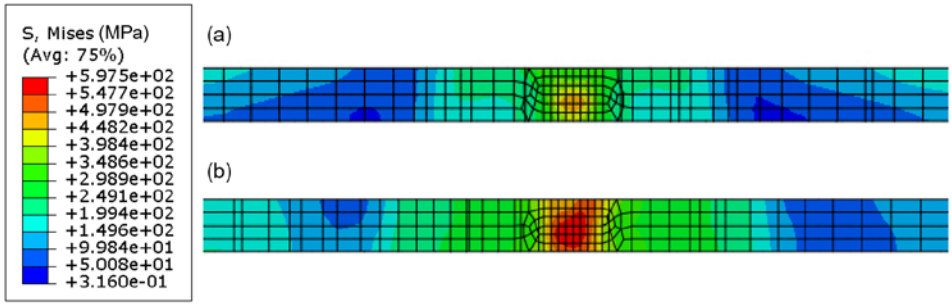

Figure 54. Transverse cross-sectional view of Von Mises stress contours along (a) line 1 and (b) line 2, as marked by the red lines in Figure 53a

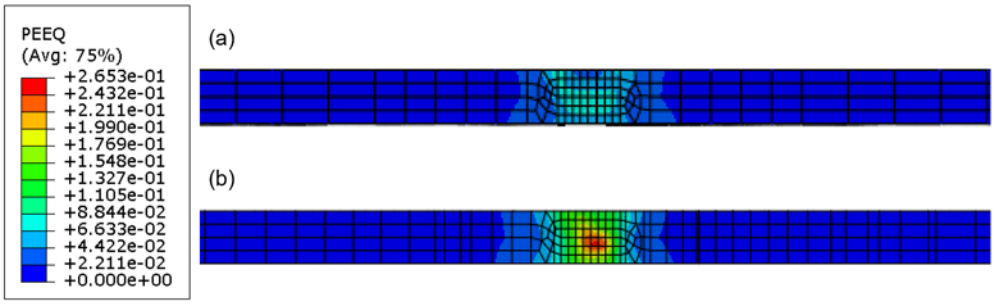

Figure 55. Transverse cross-sectional view of PEEQ contours along (a) line 1 and (b) line 2, as marked by the red lines in Figure 53a

3.4.3 Equivalent One-Pass Weld Model Calibration

This analysis considered an equivalent one-pass weld model as a base of the following explicit approach and shell element model. The welding parameters were calibrated to ensure that the calculated fusion zone boundary in the one-pass weld model matched the overall fusion zone shape of the previous two-pass weld. The two-small-plate (12” × 6”) model, discussed in Section 3.4.1, was used to calibrate welding parameters for the one-pass weld.

Goldak’s double ellipsoidal model [57] was used to the simulate the heat source in the one-pass weld model. The sequential coupled thermo-elastic-plastic FEA method was used. Note that a 2-s dwell time was added to ensure sufficient melting at the start point of welding. The analysis process included three steps: (1) dwell time of 2 s before the heat source starts moving, (2) heat source moving, and (3) cooling. Table 18 and Table 19 show the calibrated welding parameters and heat source shape parameters used in the one-pass weld model. Figure 56 presents the thermal profile calculated from the parameters in Table 18 and Table 19, which matches the experimentally observed fusion zone boundaries of total pass 1 and pass 2 reasonably well.

Table 18. Calibrated Welding Parameters Used in One-Pass Welding Simulation

Parameter	One-Pass Weld
Welding method	GMAW
Heat input (ηUI), watt (J/s)	4352
Welding speed (v), mm/s	5

Table 19. Calibrated Heat Source Shape Parameters Used in One-Pass Welding Simulation

Heat Distribution Parameters	Heat Source Shape Parameters
$f_f + f_r = 2$ $f_f = 0.6$ $f_r = 1.4$	$a_f = 5$ a_r15 b = 4 c = 12

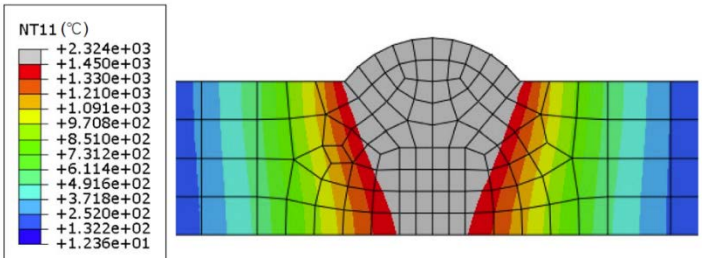

Figure 56. Fusion zone boundary generated from one-pass weld using calibrated heat input parameters

Figure 57 compares the top view of the Von Mises stress distributions around the whole weld length calculated from the one-pass and two-pass weld models with small plates. The overall distribution of Von Mises stress between the two cases is similar, although differences can be seen within the weld bead. The peak value of the Von Mises stress from the two-pass welding is larger than the one-pass welding, which is most likely caused by the reheating involved in two-pass welding. Figure 58 compares the normal displacement of the one-pass and two-pass weld models. The overall distortion patterns generated from the two models are very similar. The two-pass weld model had a peak deflection of 19.6 mm by adding the absolute values of maximum and minimum normal displacement in Figure 58b. In comparison, the one-pass weld model yielded slightly less distortion, with a peak deflection of 18.58 mm, 5.2% smaller than that of two-pass weld.

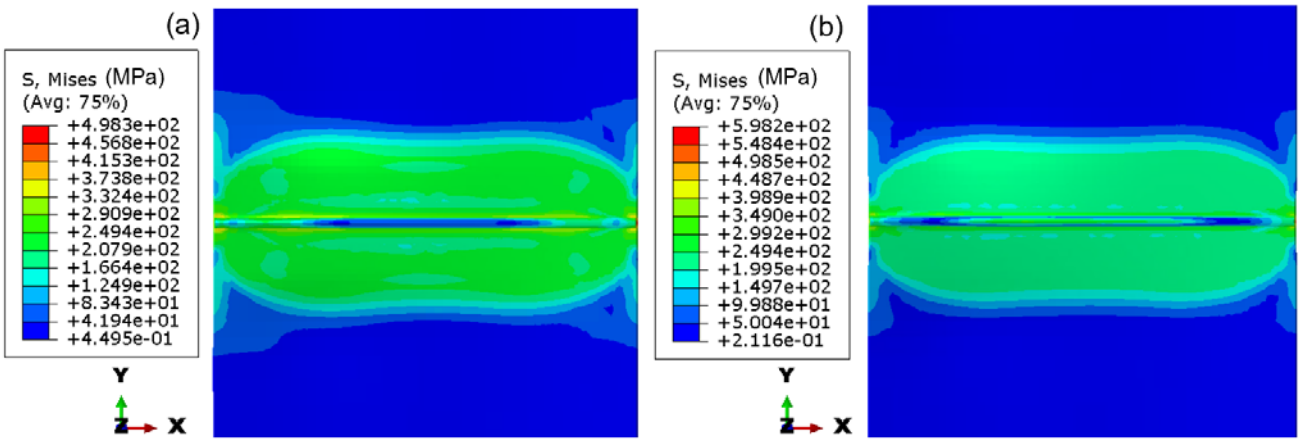

Figure 57. Top view of Von Mises stress contours around the whole weld length calculated from the (a) one-pass weld, explicit model and (b) two-pass weld implicit model with small plates

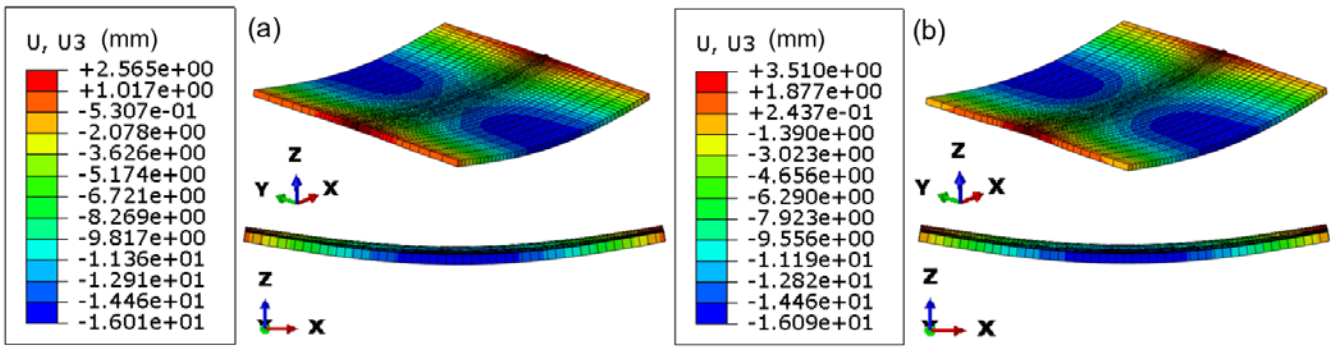

Figure 58. Normal displacement contours: (a) one-pass and (b) two-pass weld models with small plates

It can be concluded from this modeling effort that the simplified one-pass weld can reduce the simulation time by 30%–35% while predicting reasonably matching patterns of stress and deflection in the whole plate. One key takeaway from Sections 3.4.1–3.4.3 is that if area-of-interest is within the weld region itself, a two-pass small-plate model is preferred over the simplified one-pass large plate model, since the small plate model can provide a reliable analysis within the two-pass welds while the one-pass simplification leads to underprediction of peak stresses and strain (or deflection).

3.4.4 Explicit Model of Three-Tank Floor-Plate With One-Pass Weld

Abaqus software provides two different solvers: implicit and explicit, corresponding to two core analysis modules of ABAQUS/Standard and ABAQUS/Explicit, respectively. In general, implicit is the default analysis type in Abaqus. It is primarily used for static and quasi-static problems where the response of the structure is smooth and continuous throughout the loading process. In implicit analysis, the solution proceeds incrementally over time or load steps; this approach is well-suited for problems involving material nonlinearities, contact, and large deformations. Explicit analysis is often used for transient dynamic simulations and impact/crash analysis which is characterized by high-speed phenomena or where inertia effects dominate. In explicit analysis, the solution is computed explicitly at each time step without the need to iterate.

Typically, the welding procedure of sequentially coupled thermo-elastic-plastic analysis can be solved well by implicit method. But convergence issues caused by the extreme distortion due to the excessive dimensions of tank floor plates introduced inconsistent impacts on the analysis results. Compared to implicit analysis, explicit solution proceeds without iterating at each time step, which makes it well suited for solving cases with convergence concerns. However, the smaller time steps can make it computationally expensive for problems with long durations or slow processes. The explicit method does not allow for setup of element activation during the analysis steps. Therefore, the two-pass weld simulation was simplified into a one-pass weld case for the explicit model.

Figure 59 presents the mesh model for one-pass welding of three tank floor plates. The weld bead was simplified to be flat on the top surface to enable meshing at the intersection of two welds. The mesh of the weld bead area was refined to ensure calculation accuracy. The short edge between plates 1 (P1) and 2 (P2) was welded first in this model, followed by the long edge. Table 20 tabulates the analysis steps. Steps 1 to 3 are for the short-edge weld, and steps 4 to 6 are for the long-edge weld.

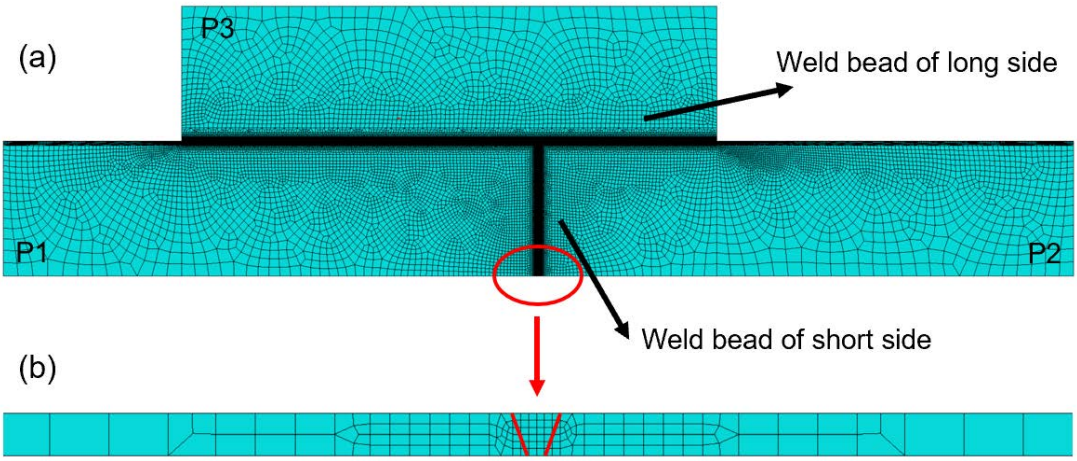

Figure 59. Mesh model of three tank floor plates with (a) top view and (b) transverse cross-sectional view of the short-edge weld bead of the one-pass weld

Figure 60a and 60b present example temperature contours during one-pass welding of the short edge and long edge, respectively, from the explicit three-tank floor-plate model.

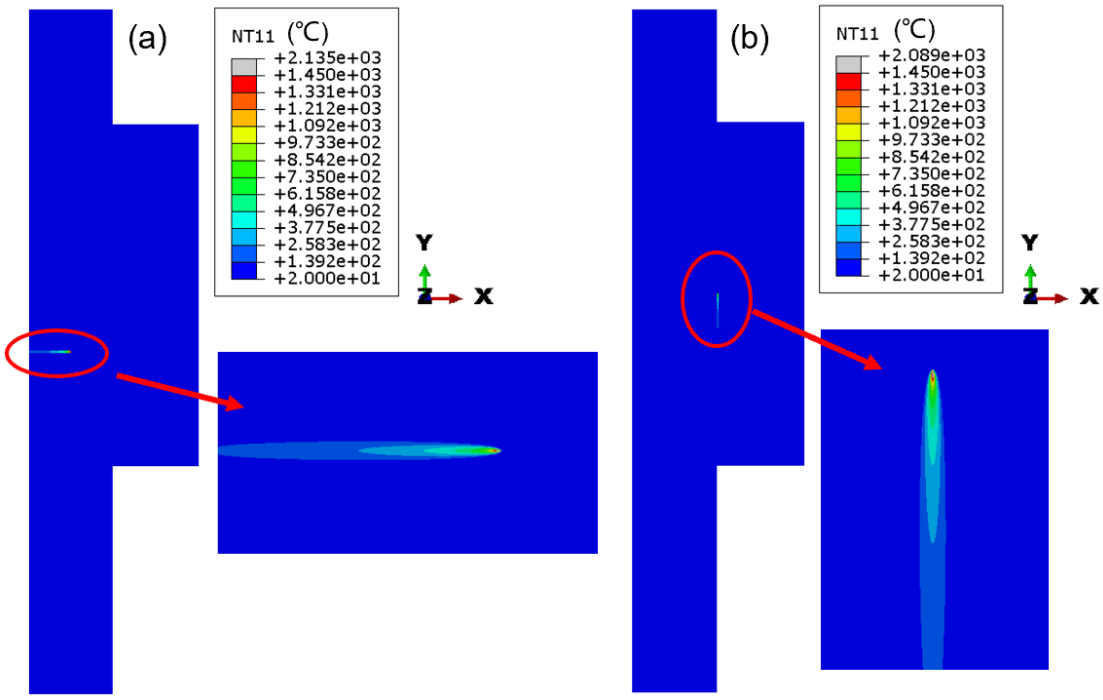

Figure 60. Example temperature contours during one-pass welding of (a) the short edge and (b) the long edge for the three-tank floor-plate model

Once the thermal analysis is completed, the explicit solving method to calculate the stress and distortion of three-plate tank floor welds was applied. Figure 61 illustrates the boundary conditions set for the explicit analysis of stress and distortion. The same boundary conditions as the small three-plate weld model were evaluated. Figure 62 shows the top view of the Von Mises stress calculated from the three-tank floor-plate weld model using the explicit solving method. As shown in Figure 62, due to the large

plate size, the intersecting impact is localized. The overall stress distribution pattern at the short edge and long edge remains unimpacted.

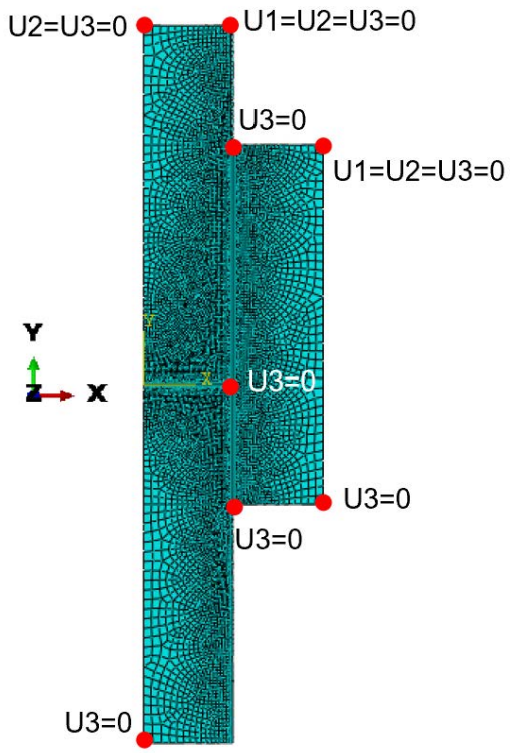

Figure 61. Boundary conditions set for the explicit analysis in the three-plate tank floor model

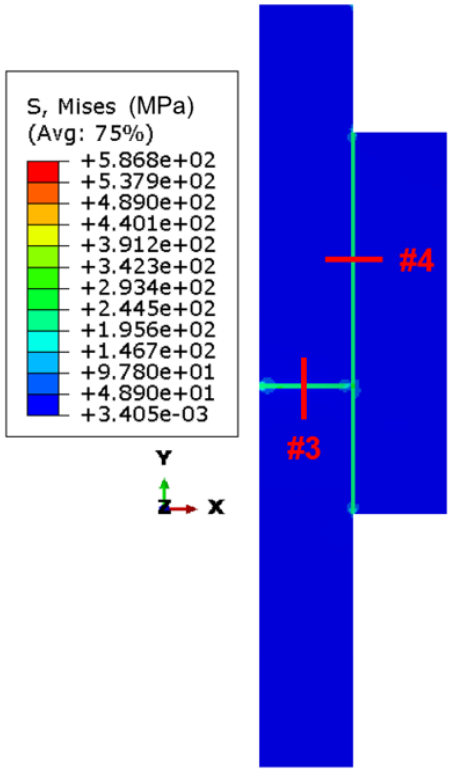

Figure 62. Top view of Von Mises stress contour calculated from three-tank floor-plate weld model using the explicit solving method

Table 20. Analysis Steps of Three Tank Floor Plate Model with One-Pass Welding

Step	Description	Time
1	Dwell time at start of short-edge weld	2 s
2	Heating for short-edge weld	487.6 s
3	Cooling for short-edge weld	1200 s
4	Dwell time at start of long-edge weld	2s
5	Heating for long-edge weld	1950.8 s
6	Cooling for long-edge weld	1200 s

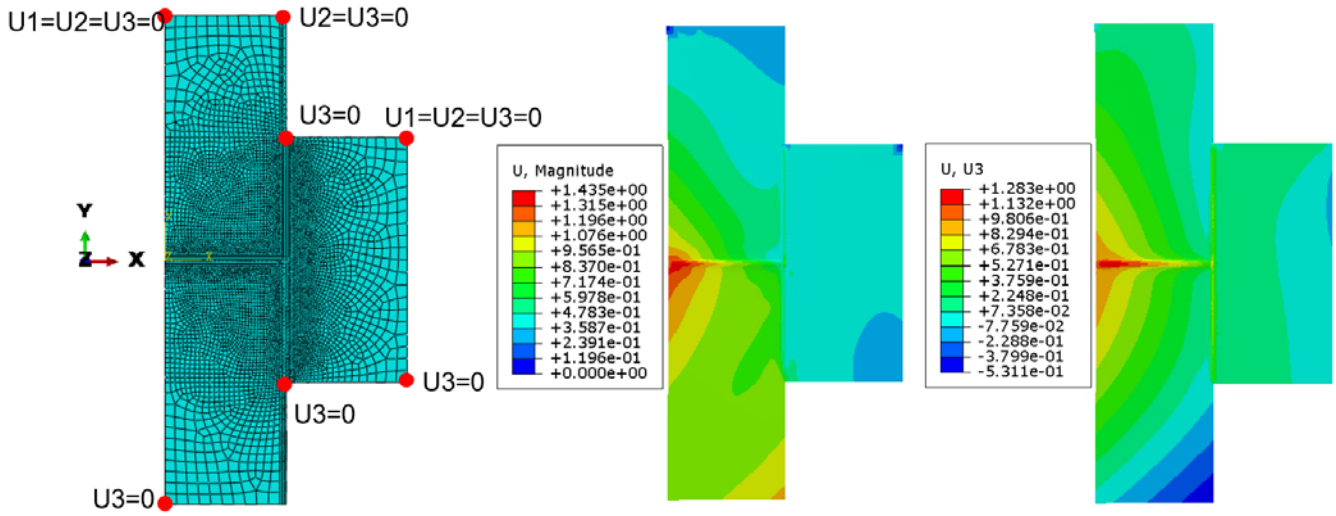

Figure 63. The pattern calculated from the three-small-plate weld model with (a) set of boundary conditions considered for the three-small-plate model under implicit solving, (b) deformation contour, and (c) normal displacement contour under explicit solving

The three-small-plate model was initially used to test the effect of different boundary conditions on the distortion of welded plates under explicit solving. Figure 63 and Figure 64 present the deformation and normal displacement patterns calculated from the three-small-plate weld models under implicit and explicit solving, respectively, with different boundary conditions, as can be seen in Figure 63a and Figure 64a. Comparing Figure 63 and Figure 64, it can be concluded that the constraint at the weld intersection restricted the deformation of the plates, leading to a very different distortion pattern in the three plates. Therefore, it is critical to obtain field assembly details to understand the boundary conditions that best represent real cases. It would also be beneficial to evaluate how to control distortion patterns by applying proper constraints during floor plate assembly.

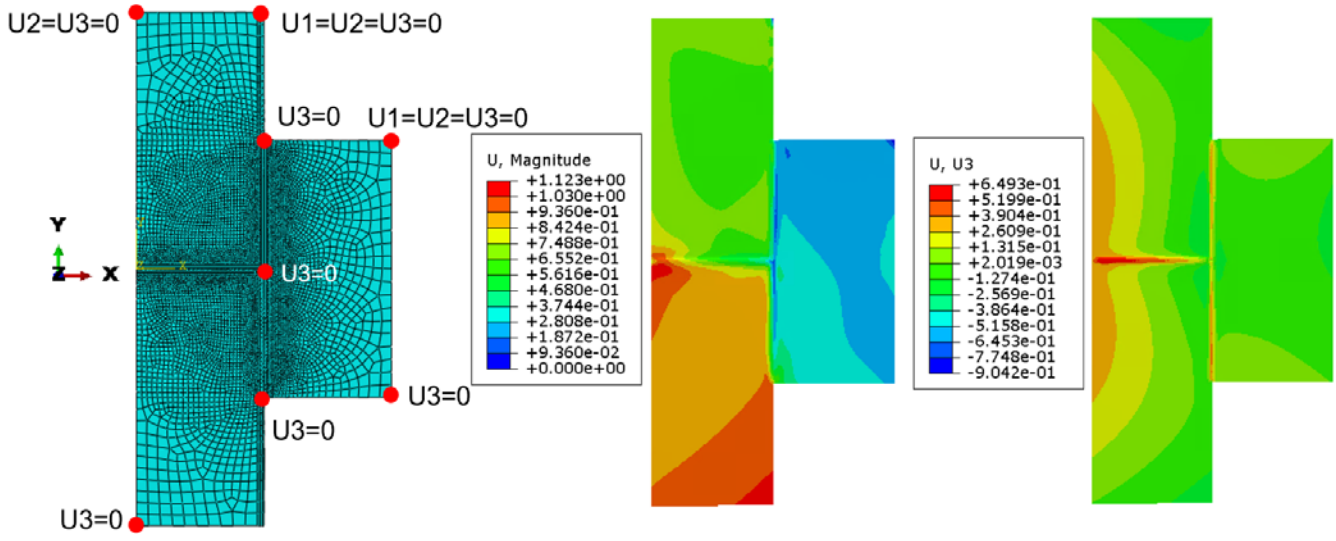

Figure 64. A three-small-plate weld model under explicit solving using (a) the same boundary conditions for the three-tank floor-plate model under implicit solving, (b) calculated deformation, and (c) normal displacement contours

Figure 65 and Figure 66 present the Von Mises stress and PEEQ in the transverse cross-sectional view along lines 3 and 4, as marked by the red lines in Figure 62. The distribution of Von Mises stress and PEEQ in the weld center (i.e., quasi-steady-state region) from the short- and long-edge welds are almost identical. This demonstrates that when the plate size is sufficiently large, the stress and strain distributions within the quasi-steady-state region are independent of weld length, except at the weld intersections.

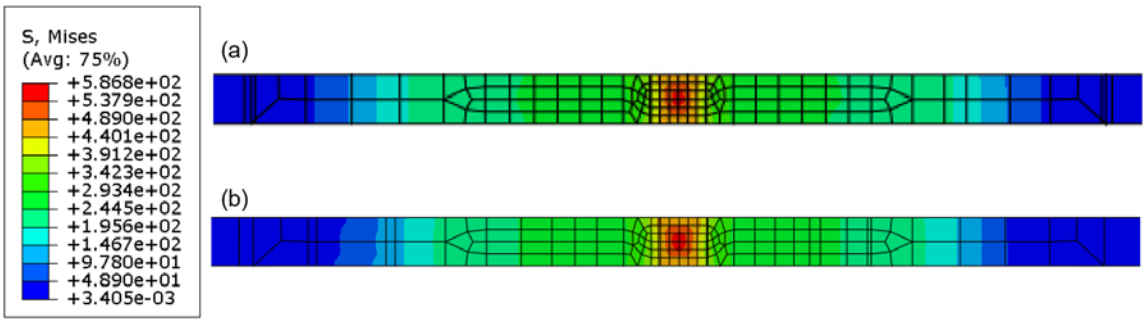

Figure 65. Von Mises stress contours in the transverse cross-sectional view along (a) line 3 and (b) line 4, as marked by the red lines in Figure 62

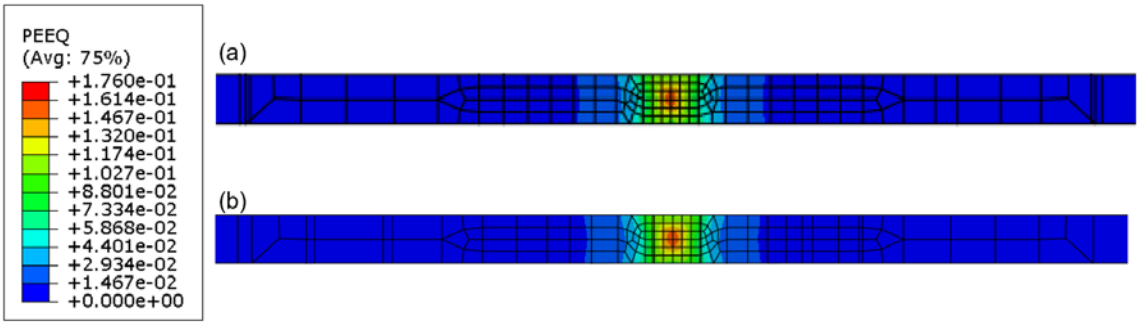

Figure 66. PEEQ contours in the transverse cross-sectional view along (a) line 3 and (b) line 4, as marked by the red lines in Figure 62

3.4.5 Inherent Strain Method for Deformation of Plates

The explicit thermo-elastic-plastic finite element method is an accurate alternative to determine residual stress in the hot tank after welding fabrication. However, the extensive calculation time limits the explicit simulation to a maximum of a quarter of the tank floor. In comparison, the inherent strain method can reduce the simulation time for a whole tank floor substantially. The inherent strain method has been demonstrated to be the most time efficient method for predicting welding distortion in large and complex welded structures. Table 21 compares detailed aspects of the inherent strain method and the thermo-elastic-plastic method.

The governing principle of the inherent strain method is to load the inherent strain obtained from analytic calculation or thermo-elastic-plastic FEA to the weldment as an initial strain, and then perform elastic FEA to calculate the corresponding stress and distortion of welded plates. To evaluate the feasibility of the inherent strain method, the first inherent model was established for the small model welding two 12” × 6” plates. The input inherent strain values as a function of location were extracted from the thermo-elastic-plastic implicit small-plate model.

Table 21. Comparison of the Thermo-Elastic-Plastic Method and Inherent Strain Method

Method	Thermo-Elastic-Plastic	Inherent Strain
Principle	Thermo-elastic-plastic theory	Inherent strain theory
Implementation	• Fine mesh is needed for convergence • A heat source model is applied • Thermal-mechanical coupling calculation	• Mesh requirement is not high • Inherent strain is applied • Only elastic calculation
Features	Includes the whole welding thermo-mechanical process	Focuses on the stress and distortion associated with localized weld-induced shrinkage during cooling
Costs	Large number of calculation steps and long calculation time	Fewer computation steps and short calculation time
Range of application	Small structure	Large, complex structure

According to the theory of thermo-mechanical-metallurgical FEA, the total strain can be expressed as:

$$\boldsymbol{\varepsilon^{Total} = \varepsilon^{e} + \varepsilon^{T} + \varepsilon^{p} + \varepsilon^{c} + \varepsilon^{Ph}} \quad (32)$$

where ε^{e} is elastic strain, ε^{T} is thermal strain, ε^{p} is plastic strain, ε^{c} is creep strain, and ε^{Ph} is phase-transformation-induced strain. Inherent strain, ε^{*}, is expressed as:

$$\boldsymbol{\varepsilon^{*} = \varepsilon^{T} + \varepsilon^{p} + \varepsilon^{c} + \varepsilon^{Ph}} \quad (33)$$

The creep strain during welding is typically small and is often ignored. Thermal strain will disappear after the plate temperature drops. Phase-transformation-induced strain becomes a part of plastic strain in the final structure. Therefore, the plastic strain is the main component of the inherent strain.

Figure 67 presents a schematic of the region where the inherent strain is obtained from the thermo-elastic-plastic model. The area of interest covers both the fusion zone and the heat-affected zone. The inherent strain can be assigned to the model as an average plastic strain. To improve the accuracy of the inherent strain method, the inherent strain model was divided into a few different regions with different average inherent strain values assigned to them. Figure 68 illustrates how different regions are set up to apply average inherent strains at all three directions in the inherent strain model. Along the longitudinal direction, i.e., the welding direction, the domain was divided into quasi-steady and transient regions. Along the transverse direction, the width of the region to be assigned for inherent strain is similar to the heat-affected zone width. Along the normal direction, the shrinkage of pass 1 and pass 2 beads are different, and two regions were defined accordingly for inherent strain application. In total, the model set up six regions for application of average inherent strains along the three coordinate directions. Abaqus software provides a function that uses the anisotropy coefficient of thermal expansion and temperature variation to simulate the generation of inherent strain.

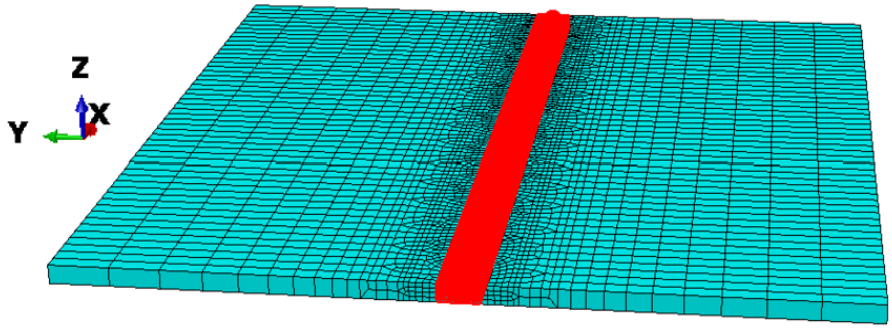

Figure 67. Schematic diagram of the region where the inherent strain is obtained from the thermo-elastic-plastic model

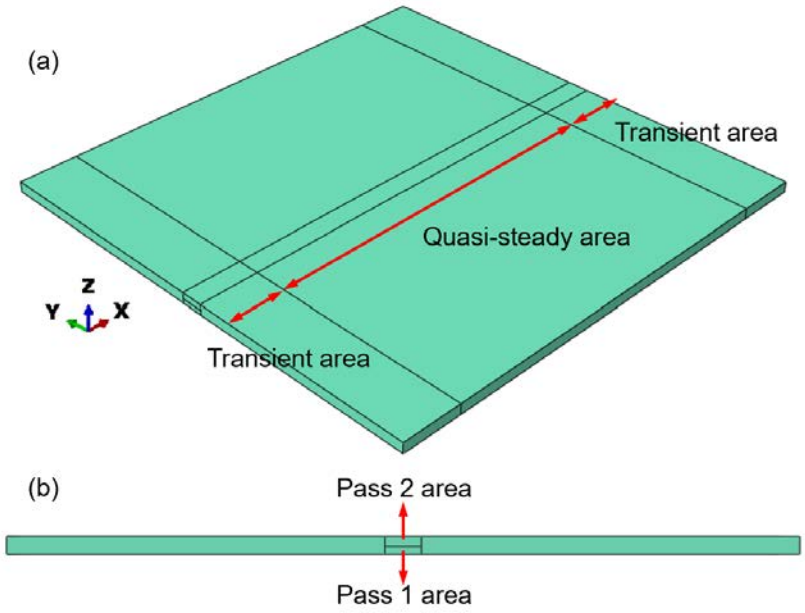

Figure 68. Schematic diagram illustrating the divided regions for applying the average plastic strain in (a) a 3D view and (b) a side view in the inherent strain model

Figure 69 summarizes and compares the distortion results calculated from the thermo-elastic-plastic model and the inherent strain model in the three coordinate directions. In this figure, U1, U2, and U3 represent the displacement along the x-axis (longitudinal direction), y-axis (transverse direction), and z-axis (normal direction), respectively. The overall distortion trends in all three directions from the two models are consistent. The observed discrepancy in the peak displacement value may be reduced by further calibrating the averaged inherent strain through adjustment of the averaging area selection and division.

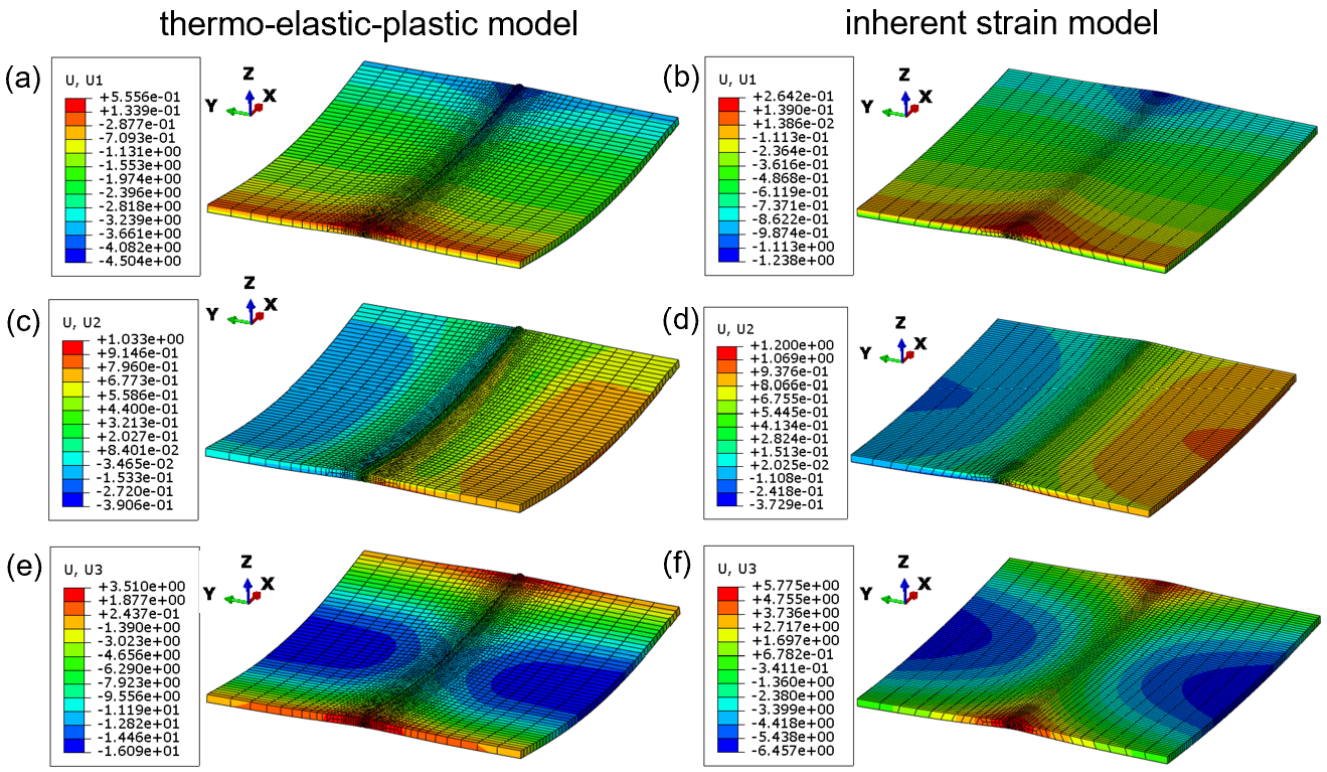

Figure 69. Comparison of distortion results calculated from the thermo-elastic-plastic and inherent strain models in the three coordinate directions: (a–b) longitudinal displacement of thermo-elastic-plastic and inherent strain, (c–d) transverse displacement of thermo-elastic-plastic with inherent strain model, (e–f) normal displacement of thermo-elastic-plastic with inherent strain model

3.4.6 Shell Element Model: Model Comparison and Selection

As discussed in the previous sections, the explicit thermo-elastic-plastic finite element method requires extensive calculation time, while the inherent strain method has limitations in prediction accuracy. In this section, another alternative method, implicit thermo-elastic-plastic FEM method with shell element and simplified one-pass weld, is evaluated. The shell model doesn't have geometric thickness due to the nature of shell elements, which is factored into the model through use of the section integration points. This approach can significantly reduce the calculation time. However, the impact of shell element on predication accuracy needs to be evaluated through a comparison to the implicit thermo-elastic-plastic solid model with two-pass welds.

The plates size, material properties, analysis steps, and boundary conditions of shell model are the same as that of solid model. Figure 70 presents the comparison of temperature contours after welding along short edge of two floor pates using (a) the solid element model and (b) shell element model, respectively. It can be seen that the overall temperature field and fusion zone shape from the top view are very similar between the solid and shell models, although the shell model with simplified one-pass weld overpredicted the peak temperature. This discrepancy is mainly attributed to a higher heat input used in one-pass weld model for the purpose of matching experimentally the observed fusion zone geometry (Figure 56), which is described in Section 3.4.3. Figure 71 presents the comparison of Von Mises stress contours after welding along short edge of two floor pates using (a) the solid element model and (b) shell element model. To better understand the stress distribution difference between the solid and

shell models, stress distributions along the two red lines, and also as a function of thickness depth, in Figure 72 are further investigated.

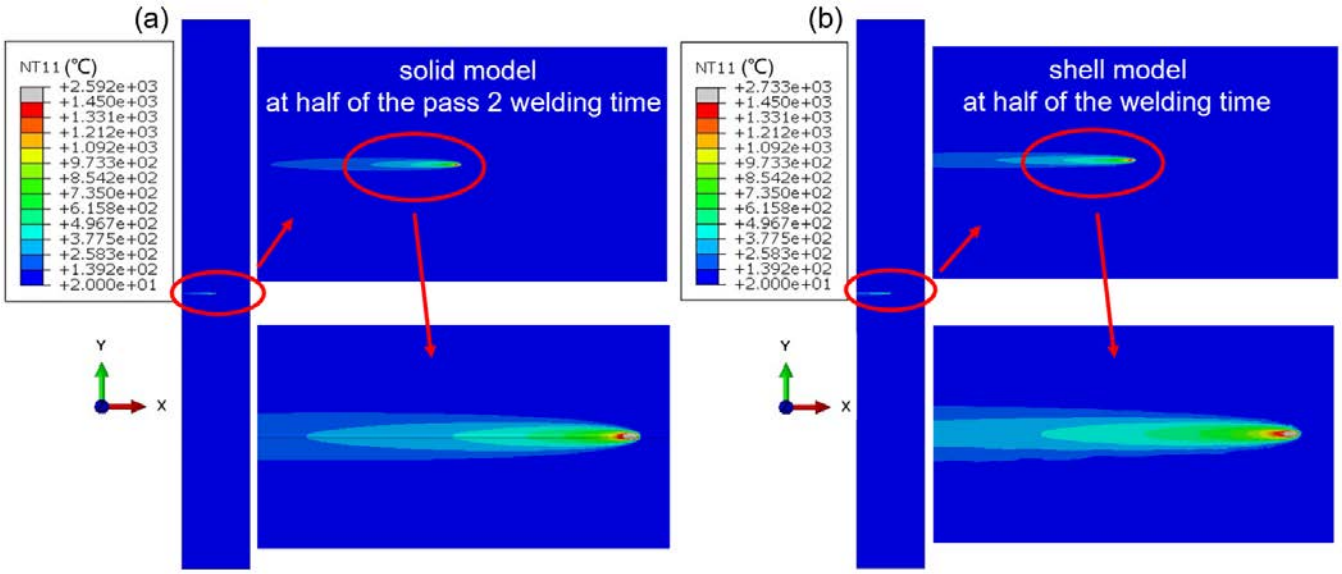

Figure 70. Temperature contours of two plates after welding with (a) solid element model and (b) shell element model, respectively

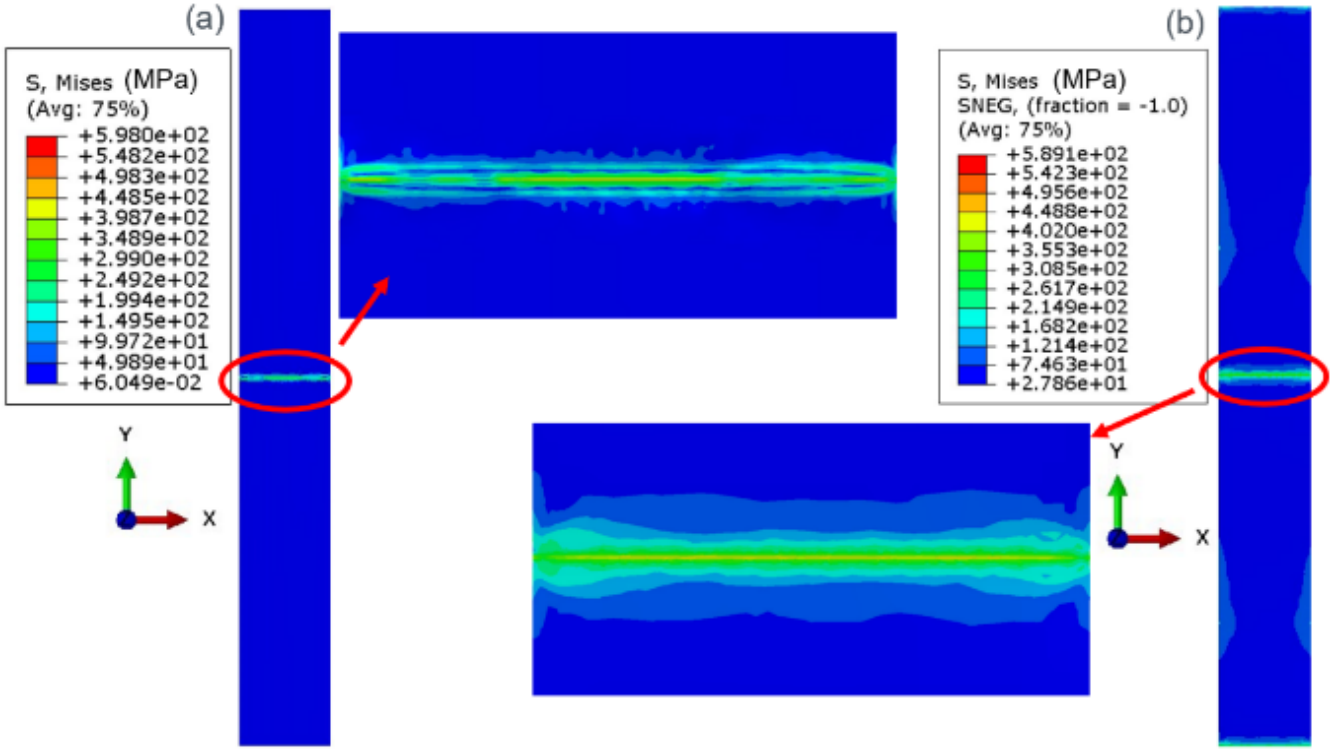

Figure 71. Von Mises stress contours of two plates after welding with (a) solid element model and (b) shell element model

As illustrated in Figure 72a, three stress profiles are extracted along three different thickness levels. The shell model doesn't have thickness direction information due to the nature of shell model. Therefore,

Figure 72b compares one line of stress distribution from shell model to three lines at different thickness of solid model. The shell model mostly averages the Von Mises stress results of the three different thickness levels from the solid model. It can be concluded that the shell model does not yield the most detailed stress distribution profile within a weld region, similar to what was observed in the explicit model, which is a combined impact of one-pass simplification and shell element. However, it does provide reasonable prediction of overall stress distribution in welded large plates for further investigation of service condition on stress and strain evolution.

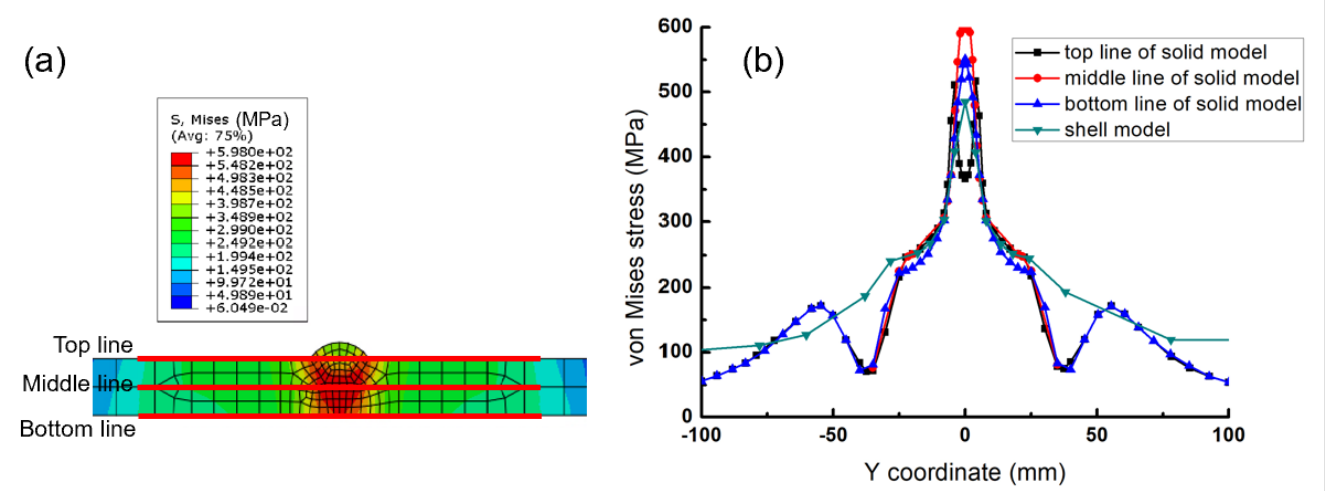

Figure 72. Comparison of residual stresses calculated from solid model and shell model: (a) contours of Von Mises stress in the cross-sectional view normal to the longitudinal direction, (b) Von Mises stress of three thickness levels (along the red lines in Figure 72a), in solid model and Von Mises stress in shell element in shell model

Table 22 compares the three methods based on weld plate size, simulation principle, mesh size, and time needed for stress and strain calculations. As seen in Table 22, for welding of two floor plates, the number of elements for the solid model is approximately 21 times larger than the elements for the shell model. In addition, the calculation time (CPU time) for the thermal analysis for the solid model is about 150 times greater when compared with the shell model. The calculation time in the shell model can be reduced significantly for the stress and distortion analysis, because it does not calculate the stress/strain along thickness direction and due to the simplification from a two-weld pass to a single-weld pass. The inherent strain model in turn takes only tens of seconds to calculate the stress and strain profiles corresponding to an applied averaged inherent strain from the weld zone for two small plates. However, implementing the thermo-elastic-plastic FEA method with solid element, which is the most accurate and common method, for the entire tank floor is unrealistic due to the extensive computation power requirement. In contrast, the thermo-elastic-plastic FE method with shell elements and simplified one-weld pass can provide sufficiently insightful results on thermal, stress, and strain profiles in a whole welded plate, which could be comparable to the solid element model, except for its limitation in providing results along the thickness direction due to the nature of shell element, especially within the weld region. The inherent strain method considers a simplified shrinkage force and a lump-pass modeling approach that allows a fast distortion calculation in the whole tank floor and can be useful for welding design optimization. To maintain the accuracy, efficiency, and reliability of the model, the thermo-elastic-plastic FE shell element model with a simplified one-weld pass is adopted for the analysis of residual stress and distortion for the tank floor fabrication model.

Table 22. Comparison of Three Types of Models for Tank Floor Analysis

Variable/Model	Solid	Shell	Inherent Strain
Element evaluated	Two tank-floor plates (32’ x 8’ x 9/32’’)	Two tank-floor plates (32’ x 8’ x 9/32’’)	Two small plates (12’’ x 6’’ x 9/32’’)
Simulation method	Thermo-elastic-plastic FEA method with two-pass weld	Thermo-elastic-plastic FEA method with one-pass weld	Inherent strain method
Longitudinal mesh in weld bead	2.5 mm	4.9 mm	2.5 mm
Number of elements	170638	8168	18792
Number of nodes	217137	24541	23550
Calculation time (CPU time) of thermal analysis	1540130 s	10279 s	/
Calculation time (CPU time) of stress and distortion analysis	411376 s	20573 s	/
Calculation time (CPU time) of applying inherent strain	/	/	28 s

3.5 Tank Floor Weld Model Setup and Calibration

The shell element model was built and implemented in Abaqus software, taking advantage of the symmetry of the tank by considering only half of the tank floor, as can be seen in Figure 73.

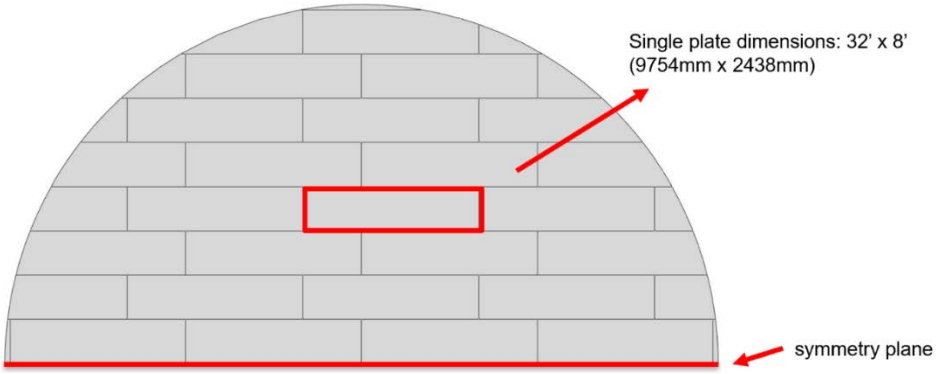

Figure 73. Layout of the hot tank floor used in the tank floor fabrication model

3.5.1 Model Parameters and Mesh Size

Two different mesh sizes were evaluated to identify a meshing strategy with a reasonable number of elements while maintaining the accuracy of the analysis. Figure 74 presents the half-tank floor mesh with two different sizes. The finer mesh has 1,048,103 elements and 1,036,337 nodes. The coarser mesh has 126,423 elements and 123,398 nodes. A mixture of four-node linear quadrilateral and three-node linear triangular element types was used in the heat transfer (defined as DS4/DS3) and non-linear elastic-plastic calculations (S4R/S3R).

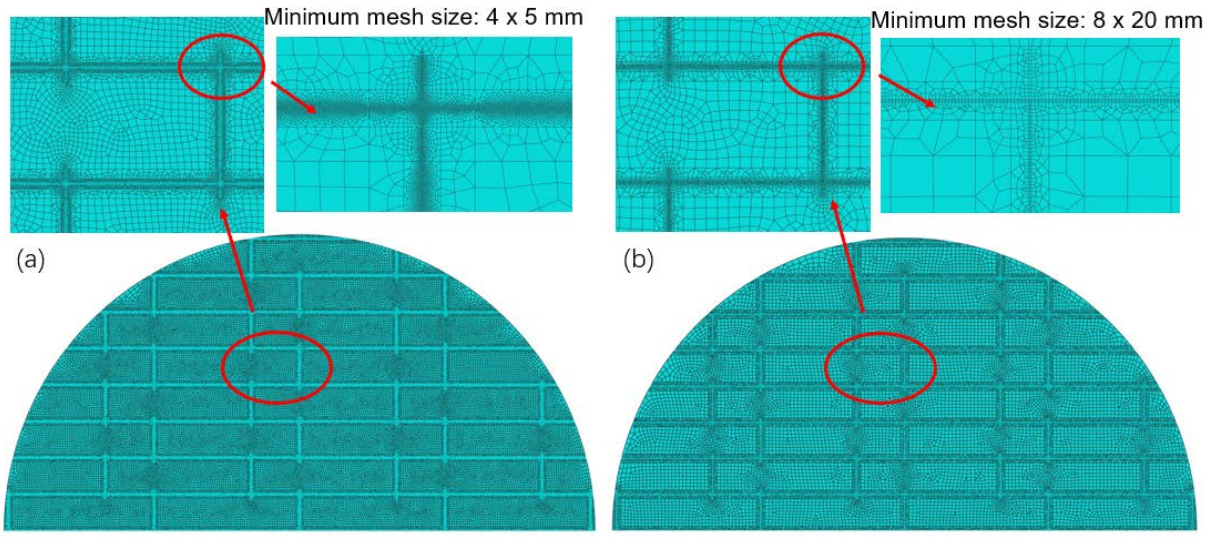

Figure 74. Mesh models of tank floor with (a) fine mesh and (b) coarse mesh

In the shell element model, the floor doesn't have geometric thickness, but this is factored into the model through use of the section integration points. In this case a shell thickness value of 7 mm was considered, with 5 thickness integration points and using Simpson thickness integration rule. Similar to the solid model, for the shell element model, the heat source used in one-pass welding was evaluated using the Goldak double ellipsoidal model [57].

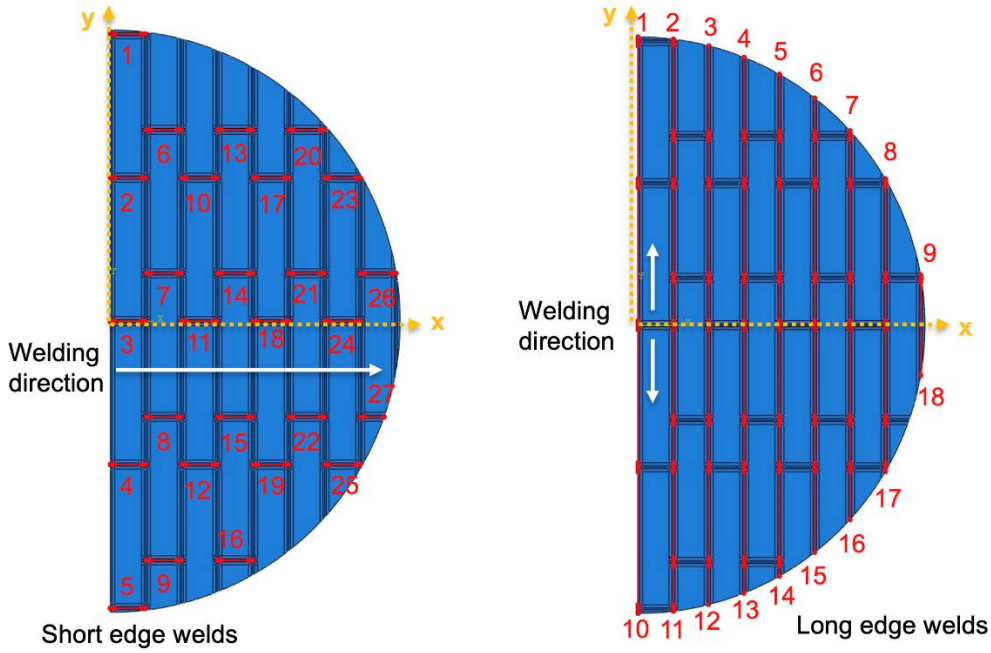

Figure 75. Welding simulation scheme along (a) short edges and (b) long edges

The sequentially coupled thermo-elastic-plastic FEA method was still used, and the welding simulation of tank floor fabrication was performed along short and long edges of each floor plate. All the short edges were welded at the same time, then all the long edges were also welded simultaneously in order to minimize the simulation time; see Figure 75. The 27 short-edge welding paths are marked with red lines

in Figure 75a, in which the welding direction is parallel to the positive direction of the x-axis. Similarly, the 18 long-edge welding paths are marked with red lines in Figure 75b and the long-edge welds start at the center of the plate (y=0), with welds 1 to 9 moving along the positive direction of the y-axis and welds 10 to 18 moving along the negative direction of the y-axis, respectively. In summary, the simulation started with the welding and cooling of the short edges, followed by the long edge welding and cooling. Note that a dwell time of 1 second was also added to ensure sufficient melting at the start point of welding. The welding simulation steps are tabulated in Table 23.

Table 23. Welding Simulation Steps in Shell Model of Tank Floor

Step	Description
1	Dwell before short edges welding
2	All short edges welding
3	All short edges cooling
4	Dwell before long edges welding
5	All long edges welding
6	All long edges cooling

The thermal analysis was performed using fine- and coarse-mesh models. Figure 76 and Figure 77 present the temperature contours of short-edge welds at a welding time of 224 s for fine- and coarse-mesh models, respectively. The computational time to complete the short-edge welds was 38.8 hours using the fine mesh, but it was only 2.75 hours using the coarse mesh. The peak temperature value and overall temperature field predicted by the two models match reasonably well, as can be seen in Figure 76 and Figure 77.

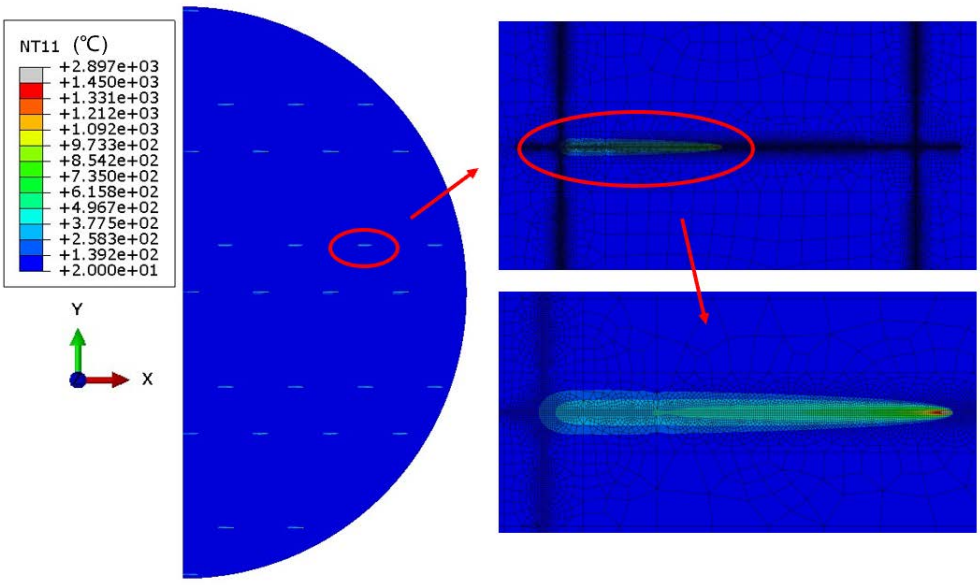

Figure 76. Temperature contours at the short edges of the tank floor for a fine mesh at 224 s welding time

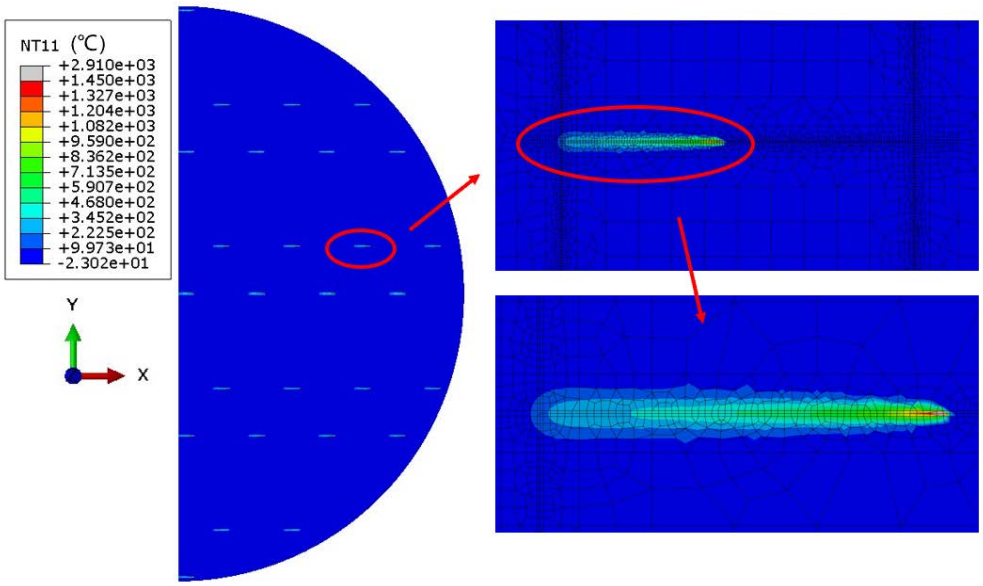

Figure 77. Temperature contours at the short edges of the floor for a coarse mesh at 224 s welding time

3.5.2 Impact of Long-Edge Weld Element Deactivation

For the tank floor welding simulation, there are two alternatives for setting up the welding bead elements. The first one is to deactivate long-edge weld elements when short edges are being welded, and then reactivate long-edge elements when they are going to be welded. In this setup, every vertical strip with short edges welded is an independent part of the model and the vertical strips do not exert an impact on the others during the heat transfer process. In the second alternative, the elements within welds on the long edges are activated while the short edges are being welded. It simulates the case when the stiffness is introduced by numerous spot welds to avoid misalignment between neighboring plates. Heat transfer exists between the neighboring vertical strips, but the offset of short-edge weld paths avoids the interplay between thermal profiles of short-edge weld passes.

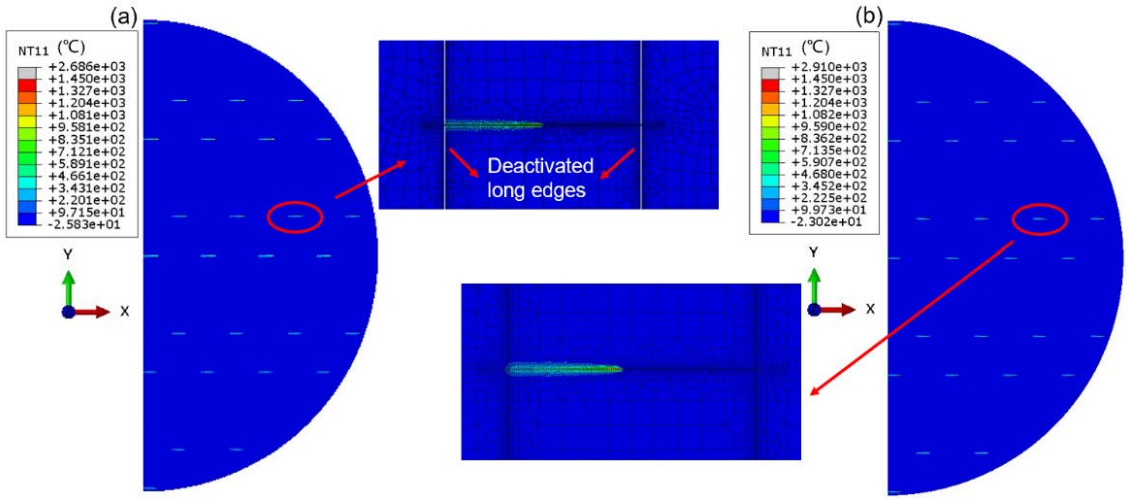

Figure 78. Temperature contours of the tank floor (a) with deactivated long-edge weld elements and (b) without deactivation at half of short-edge welding time

Figure 78 presents temperature contours obtained from welding modeling with and without deactivated long-edge weld elements. By comparing Figure 78a and 78b, it can be appreciated that the thermal profile contours from both models are similar, except that the model with deactivated elements exhibited a small extended temperature field into the left-side neighboring plate, as shown by the enlarged view of Figure 78b. The slight difference in peak temperature is attributed to the temperature fluctuation of each simulation increment.

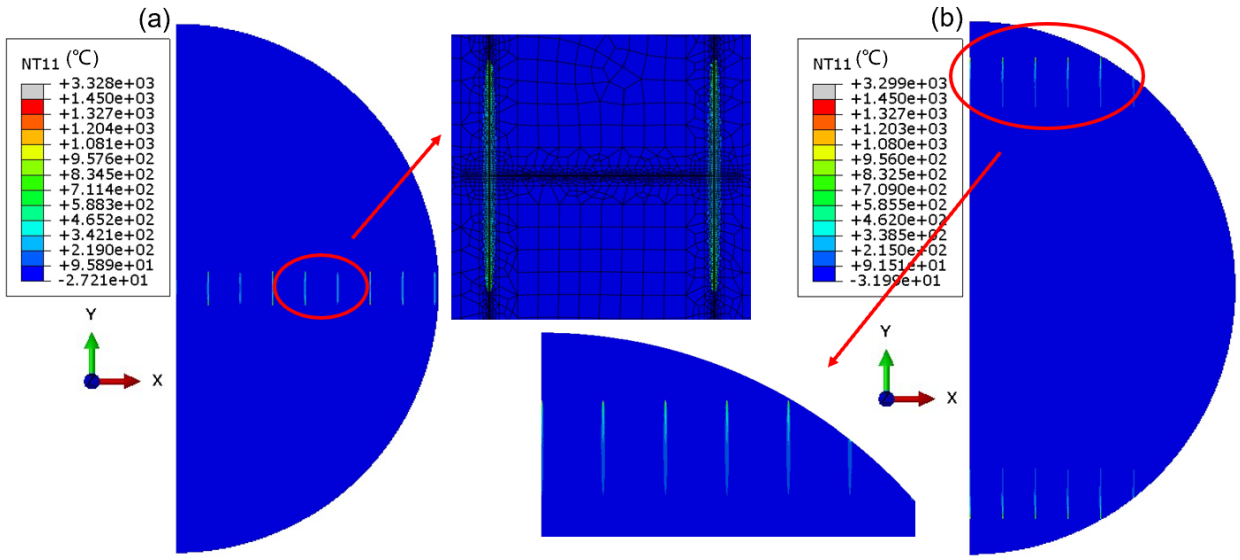

Figure 79. Temperature contours of the tank floor with deactivated long-edge weld elements at (a) early stage and (b) late stage of long edges' welding time

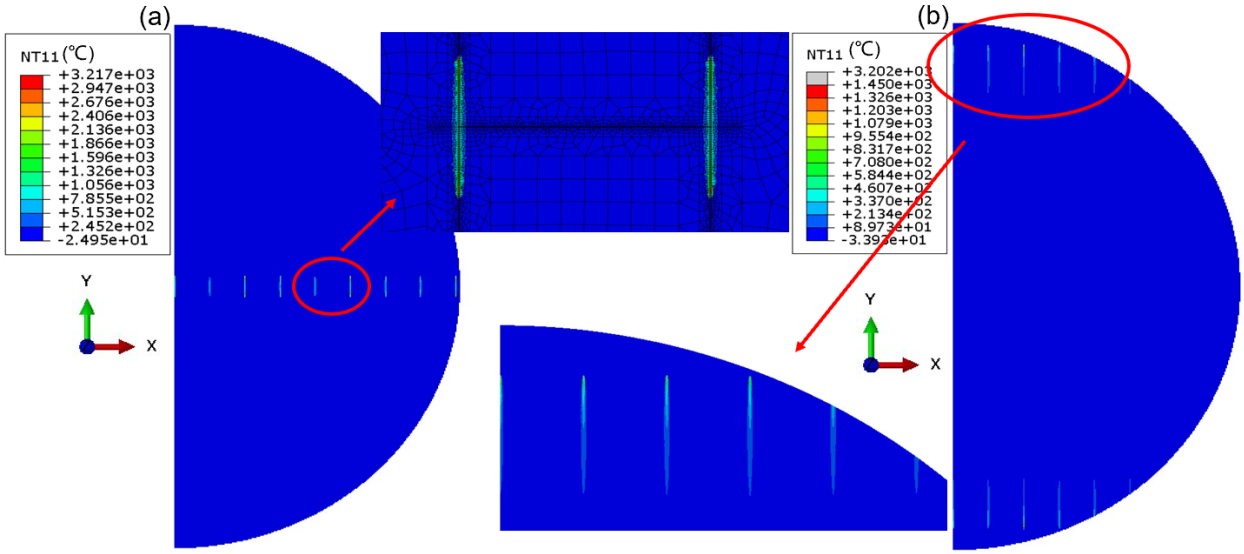

Figure 80. Temperature contours of the tank floor without deactivating long-edge welding elements at (a) early stage and (b) late stage of long-edge welding

Figure 79 and Figure 80 present temperature contours for the welding simulation with and without deactivated long-edge weld elements, respectively, during the long-edge welding. The difference between the thermal profile distribution and peak temperatures is very low. By comparing thermal profiles from welding simulations with and without deactivating the long edges, it can be stated that

both models are suitable to simulate the thermal profile of the tank floor during welding. The temperature field results were then imported into the model to conduct the elastic-plastic analysis.

3.5.3 Residual Stress and Distortion Analysis

Figure 81 and Figure 82 respectively present the constraints in models with and without deactivated long-edge weld elements for stress analysis. Three different symbols represent different constraint types used in the model. The bottom line is the plane of symmetry perpendicular to the x-axis. As shown in Figure 81, the model with deactivated long edges applies nine fixed constraints (Ui = 0, URi = 0, i = 1,2,3) on one corner of each long strip that is connected by the short edges (represented by the star symbol). In addition, to prevent rotation of strips around the z-axis (out-of-plane direction in Figure 81), nine open dots are applied at the left corners of the strips that restrict that specific rotation degree of freedom. The purpose of these constraints is to mitigate convergency issues in stress calculation. In turn, the model without deactivated long edges only applied one fixed constraint (star symbol) at the origin point (x = 0, y = 0) in Figure 82. In addition, solid dots with limited constraint (U3 = 0, UR1 = UR2 = 0) are applied to all the other corners of the plates.

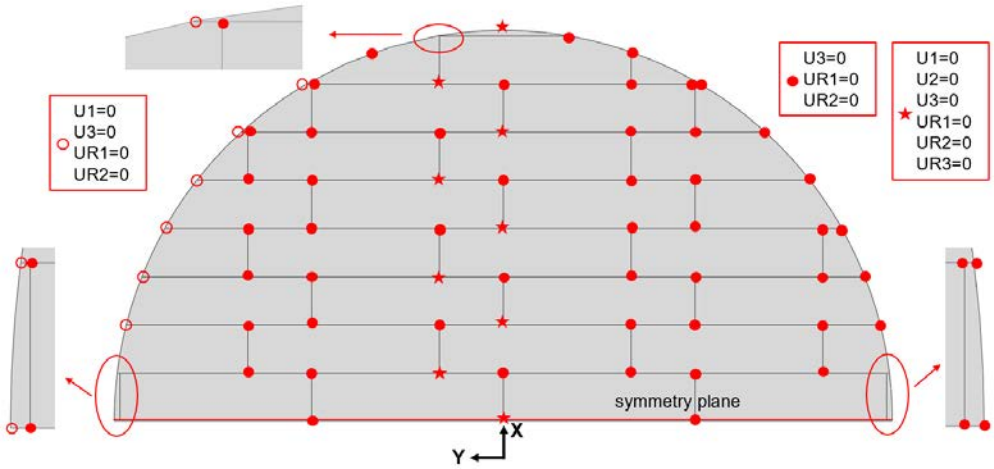

Figure 81. Constraints in the tank floor with deactivated long edges for residual stress and distortion analysis

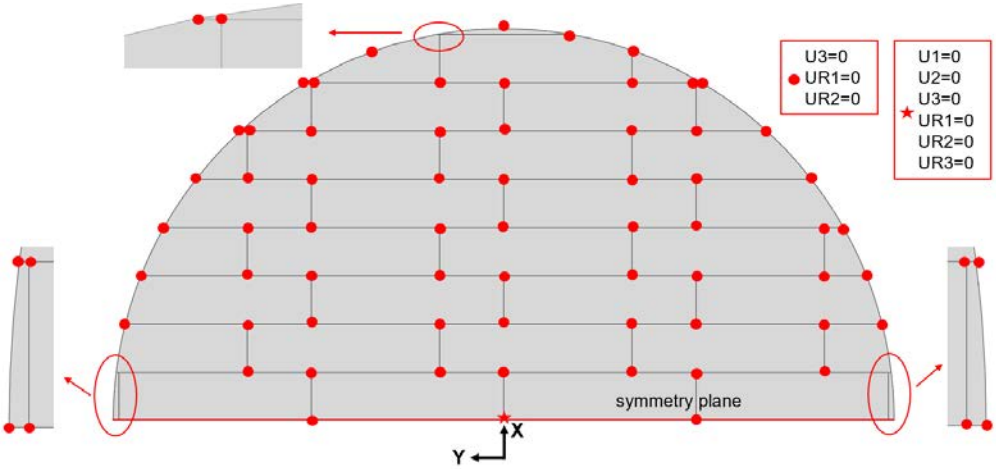

Figure 82. Constraints in the tank floor without deactivating long edges for residual stress and distortion analysis

Figure 83 and Figure 84, respectively, present the Von Mises, longitudinal, and transverse stress contours in the tank floor with deactivated long edges after completion of short-edge welding. The contours around two ends of the short edges are discontinuous because of the deactivation of long edges. The contours for the neighboring plates of the two ends of short edge are influenced by the constraints on them. Note that in Figure 84, for short-edge welds, S11 is the longitudinal stress and S22 is the transverse stress.

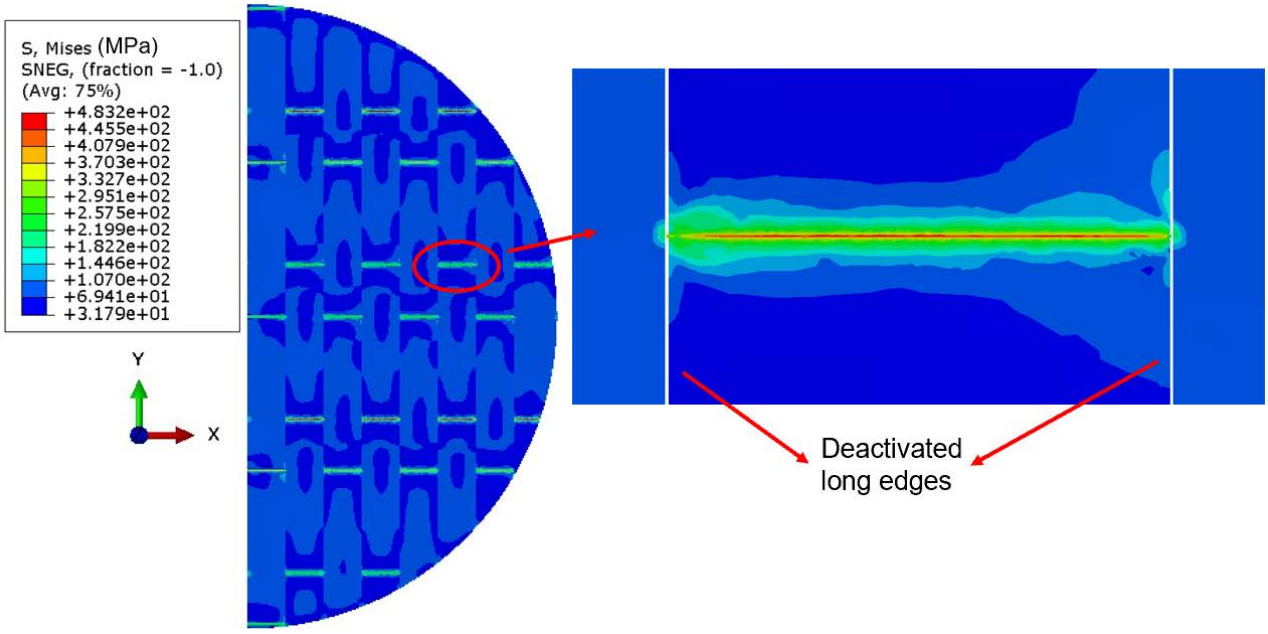

Figure 83. Von Mises stress contour of the tank floor with deactivated long edges after completion of short-edge welding

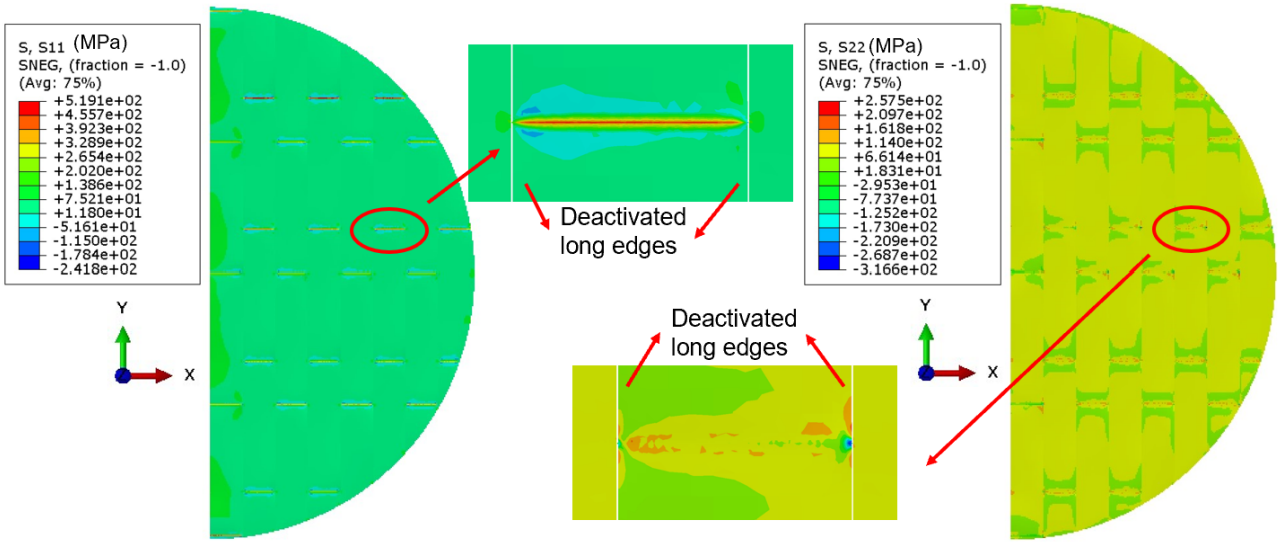

Figure 84. Longitudinal and transverse stress contours of the tank floor with deactivated long edges after the completion of short-edge welding

Figure 85 and Figure 86, respectively, present the Von Mises, longitudinal, and transverse stress contours in the tank floor without deactivating long edges after completion of short-edge welding. The contours around two ends of short edges are continuous. In Figure 86, S11 is the longitudinal stress and S22 is the transverse stress.

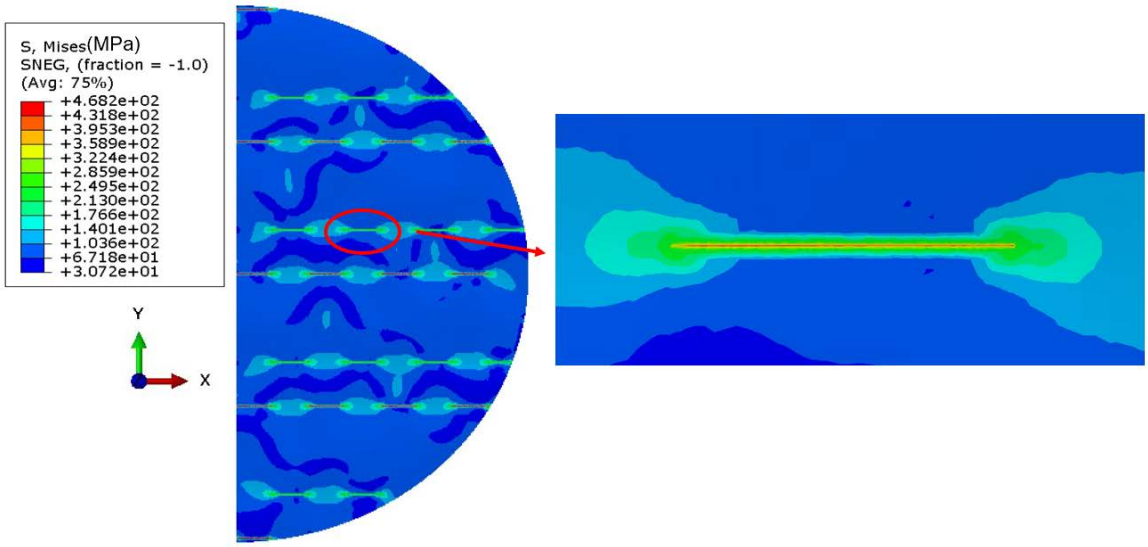

Figure 85. Von Mises stress contour of the tank floor without deactivating long edges after completion of short-edge welding

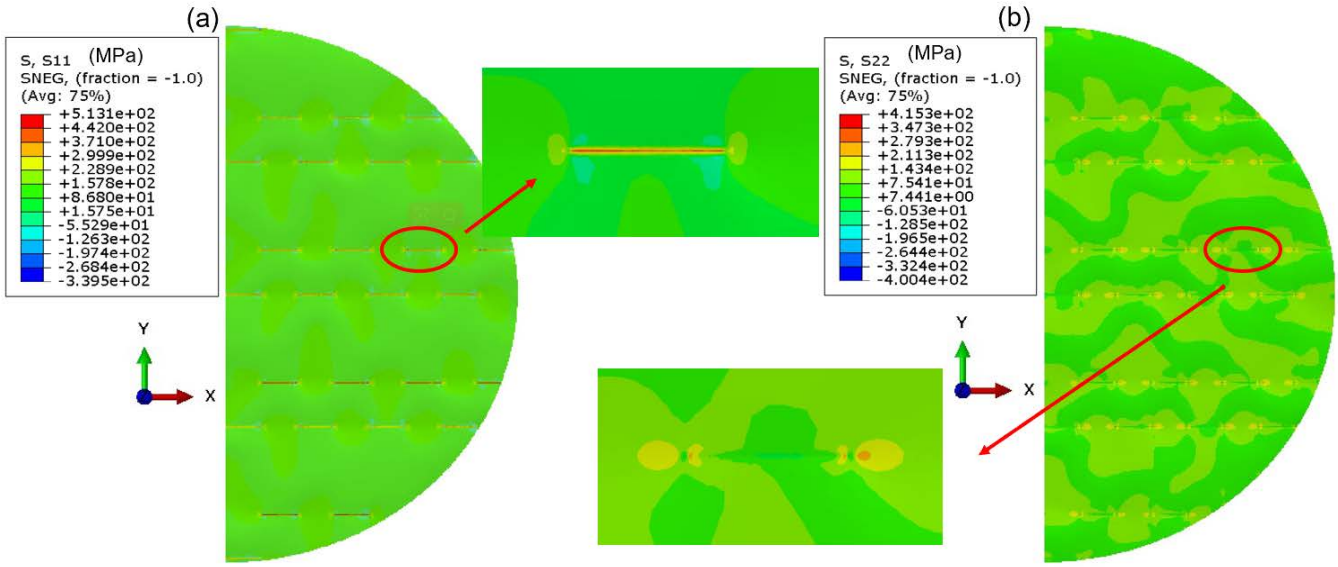

Figure 86. Longitudinal and transverse stress contours of the tank floor without deactivating long edges after completion of short-edge welding

Comparing Figure 83 to Figure 85, and Figure 84 to Figure 86, the stress distributions and peak stress values of Von Mises and S11 obtained from both models are similar. The differences in the distribution and peak stress value of S22 are attributed to the differences in the boundary conditions in the two models.

Figure 87 and Figure 88 present the normal displacement contours and deformation of the tank floor, with and without deactivating long edges after welding of the short edges, respectively. The peak normal displacement value of the model without deactivating long edges is higher than that of the model with deactivated ones, because the constraints applied on the model with deactivated long edges are stricter, allowing a lower level of deformation.

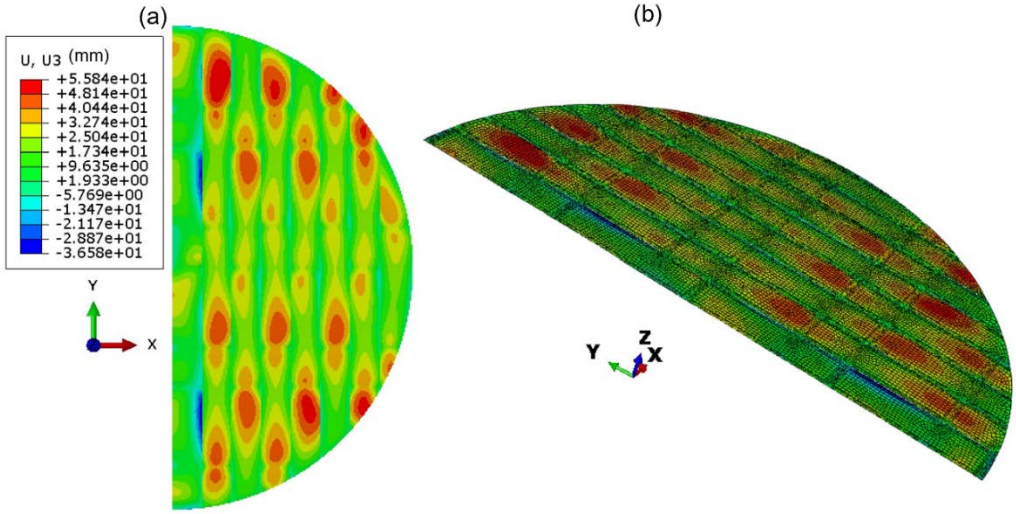

Figure 87. (a) Normal displacement contour and (b) deformed shape (deformation scale factor is 1) of model with deactivated long edges after completion of short-edge welding

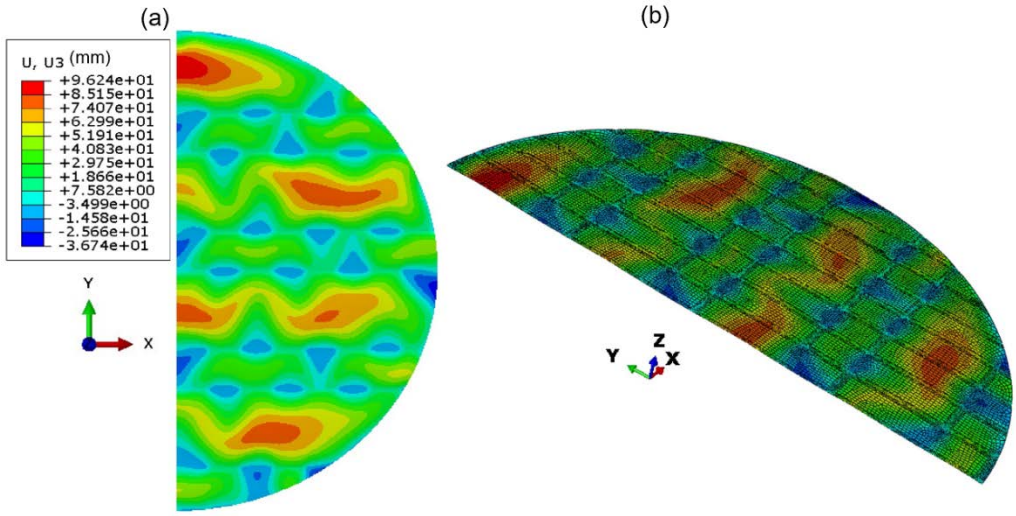

Figure 88. (a) Normal displacement contour and (b) deformed shape (deformation scale factor is 1) of model without deactivating long edges after completion of short-edge welding

Figure 89 presents the deformed tank floor after reactivating the long-edge elements as long-edge welding started. It is worth noting that the deformation scale factor in this figure was set to 10 for visualization purposes. The long edge elements have significant, visible distortions. The warping of each strip after completion of short-edge welds caused model convergency issues. Thereafter, the model without deactivating long edges is used to complete the analysis of the residual stress and distortion of tank floor induced by long-edge welds.

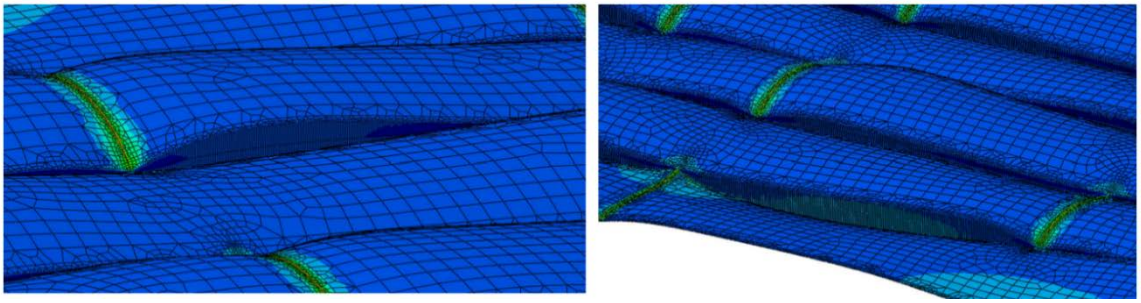

Figure 89. Deformed tank floor after reactivating the long-edge weld elements at start of long-edge welding. Deformation scale factor is exaggerated for visualization.

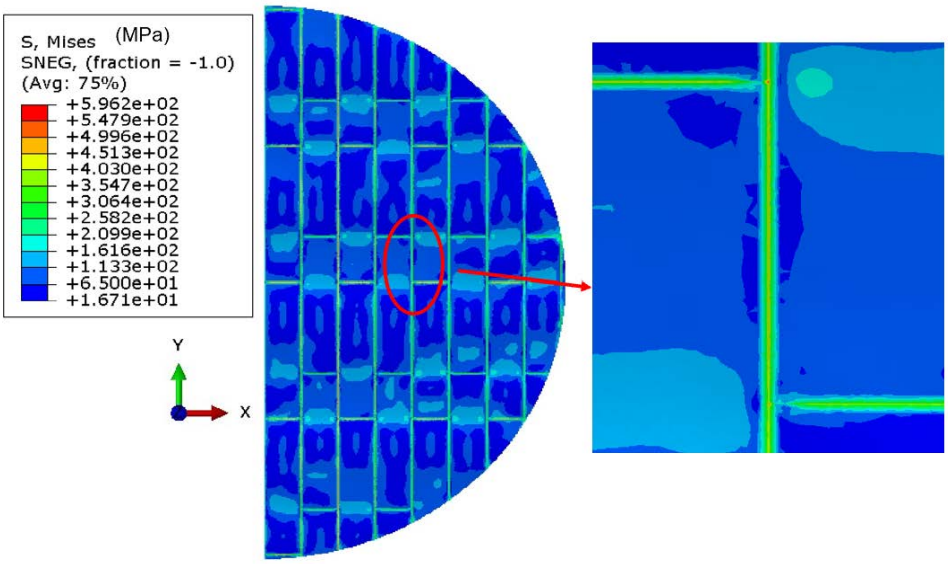

Figure 90. Von Mises stress contours of the tank floor obtained from the model without deactivating the long edges after completion of all the welds

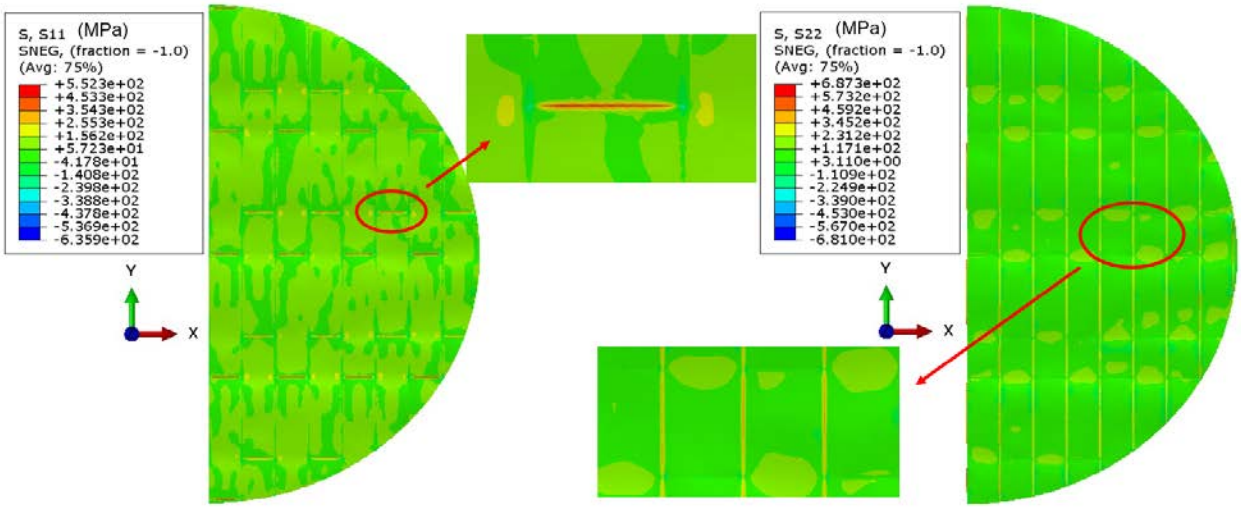

Figure 91. Longitudinal and transverse stress contours of the hot tank calculated without deactivating long edges after the completion of all the welds

Figure 90 and Figure 91 present the Von Mises, longitudinal, and transverse stress contours of the tank floor obtained from the model without deactivating long edges after completion of all the welds. Note that in Figure 91, for short-edge welds, S11 is the longitudinal stress and S22 is the transverse stress; for long-edge welds, S11 is the transverse stress and S22 is the longitudinal stress.

Figure 92 presents the normal displacement contours (parallel to *z* axis) and deformed tank floor determined from the model without deactivating long edges after completion of all the welds. By comparing Figure 88 to Figure 92, the long-edge welding procedure further increased the normal displacement along the z-axis. The alignment between short edges and the consistent space left between these short edges lead to formation of long extended distortion patterns parallel to the x-axis. The residual stress and the deformation distributions (Figure 90 and Figure 92, respectively) are integrated into the hot tank model to perform the temperature and stress behavior of the tank as a function of typical operating conditions. Since the weld-induced residual stress and distortion have an adverse impact on the performance of the tank floor during operation, the temperature and stress analysis results of tank floor with and without considering weld-induced residual stress and distortion should be compared, which assists to reveal how the weld-induced residual stress and distortion affect the tank floor performance during operation.

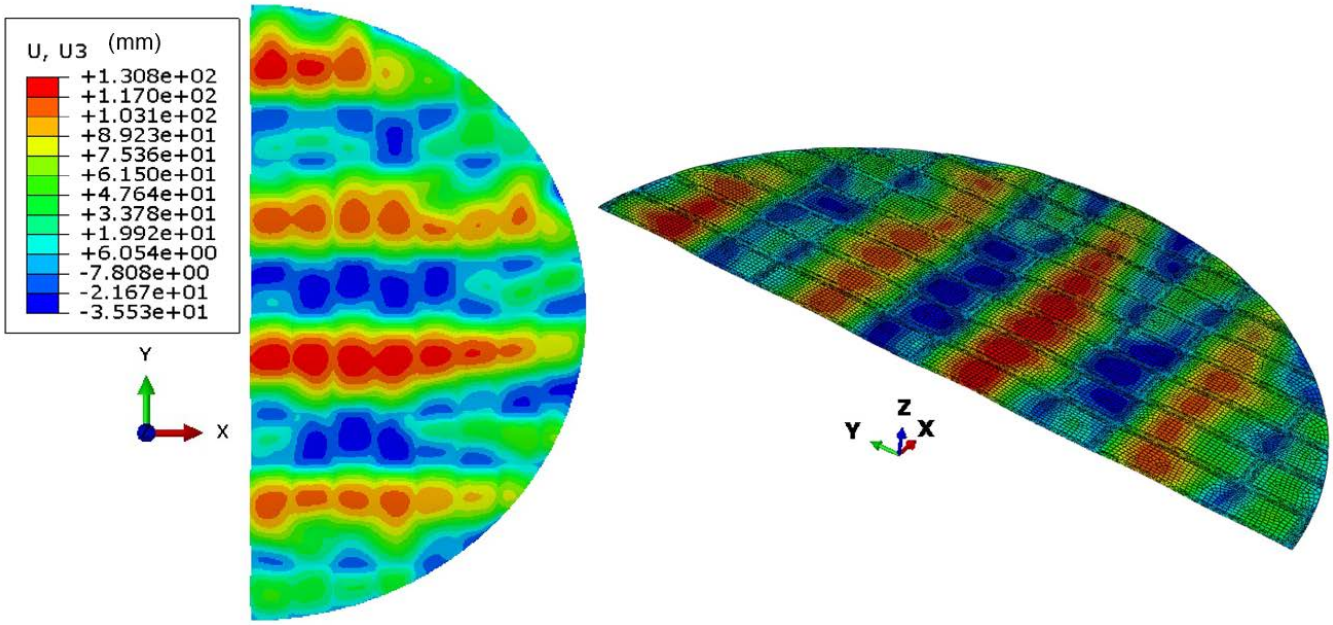

Figure 92. (a) Normal displacement contour and (b) deformed shape (deformation scale factor is 1) of model without deactivating long edges after completion of all the welds

4 Results and Analysis

4.1 Parametric Analysis

The effect of main operation variables, including the initial inventory level, initial inventory temperature ($T_{inv.}$), inlet mass flow rate ($\dot{m}_{in}$), inlet mass flow temperature (T_{in}), and outlet mass flow rate ($\dot{m}_{out}$) on the temperature distribution in the tank was analyzed. The values of the operation variables considered in this analysis are listed in Table 24. For each variable, a minimum and maximum value were selected and, except for the inventory temperature, an intermediate value. The ranges and values for each variable were determined based on an occurrence analysis over several months of historic plant operation data. Two main sets of parametric cases were analyzed: (1) low inventory level cases (1 and 2.33 m) with no molten salt being pumped out of the tank, (2) inventory levels ranging from 1 to 3.66 m with equal inlet and outlet mass flow rates. The first set characterizes a tank charging operation, while the second one represents an operating condition where the tank is being charged and discharged simultaneously.

Table 24. Tank Operation Variables Used in the Parametric Analysis

Parameter	Values		
Initial salt inventory level (m)	1	2.33	3.66
Initial Inventory temperature, $T_{inv.}$ (°C)	400	-	530
Inlet mass flow rate, $\dot{m}_{in}$ (kg/s)	800	1000	1200
Inlet flow temperature, T_{in} (°C)	500	536	560
Outlet mass flow rate, $\dot{m}_{out}$ (kg/s)	800	1000	1200

The parametric conditions for all the cases are listed in Tables C1 and C2 in Appendix C. For each case, the operation variables are maintained constant during the simulation; however, the inventory level and the inventory temperature change during the simulation. The parametric analysis was focused on the evolution of the temperature in the tank floor, considering that large spatial temperature differences (temperature gradients) in the floor are associated with large operation stress (exacerbated by high friction coefficients) and eventually buckle formation.

Figure 93 presents the effect of the inlet mass flow rate on the maximum temperature difference ($T_{max} - T_{min}$) in the tank floor for 1 and 2.33 m initial inventory levels; constant inlet flow temperatures of 500°C (Figure 93a, 93d, and 93g), 536°C (Figure 93b, 93e, and 93h), and 560°C (Figure 93c, 93f, and 93i); and initial inventory temperatures of 400°C and 530°C. For these cases, $\dot{m}_{out}$ = 0. In general, higher temperature differences between two points in the tank floor are observed at higher mass flow rates, and they usually occur between 10 and 40 minutes of operation. Maximum temperature differences of about 50°C are predicted at low inventory levels (1 m) for large discrepancies between the inventory and the flow inlet temperatures, i.e., for $T_{inv.}$ = 400°C and T_{in} = 560°C, see Figure 93f. As expected, the lower difference in temperature is obtained when $T_{inv.}$ and T_{in} are very close—for example $T_{inv.}$ = 536°C and T_{in} = 530°C (Figure 93b)—or when the inventory level is higher (2.33 m) due to the larger inertia, as can be seen in Figure 93g, 93h, and 93i. Figure 93a represents a common operation case where inflow having a lower temperature than the inventory is pumped into the hot tank. The inflow salt should be diverted to the cold tank until its temperature surpasses the hot tank inventory temperature.

Figure 94 presents the cumulative average of maximum temperature difference, $(T_{max} - T_{min})_{cm,avg}$, in the tank floor during 60 minutes of operation for the corresponding cases presented in Figure 93. $(T_{max} - T_{min})_{cm,avg}$, is defined as follows:

$$(T_{max} - T_{min})_{cm,avg} = \frac{\sum_1^i (T_{max} - T_{min})_i}{i}, \qquad i = 1,2,3 \ldots, n \tag{34}$$

where i is the difference counter, which denotes the number of differences calculated from the initial time (t_0) to a specific time. Equation 34 represents the evolution of the average maximum temperature in the tank floor with time and is useful to observe a more general behavior of the floor temperature without considering the short-term fluctuations. Note that Figure 94 is obtained from Figure 93 by applying Equation 34.

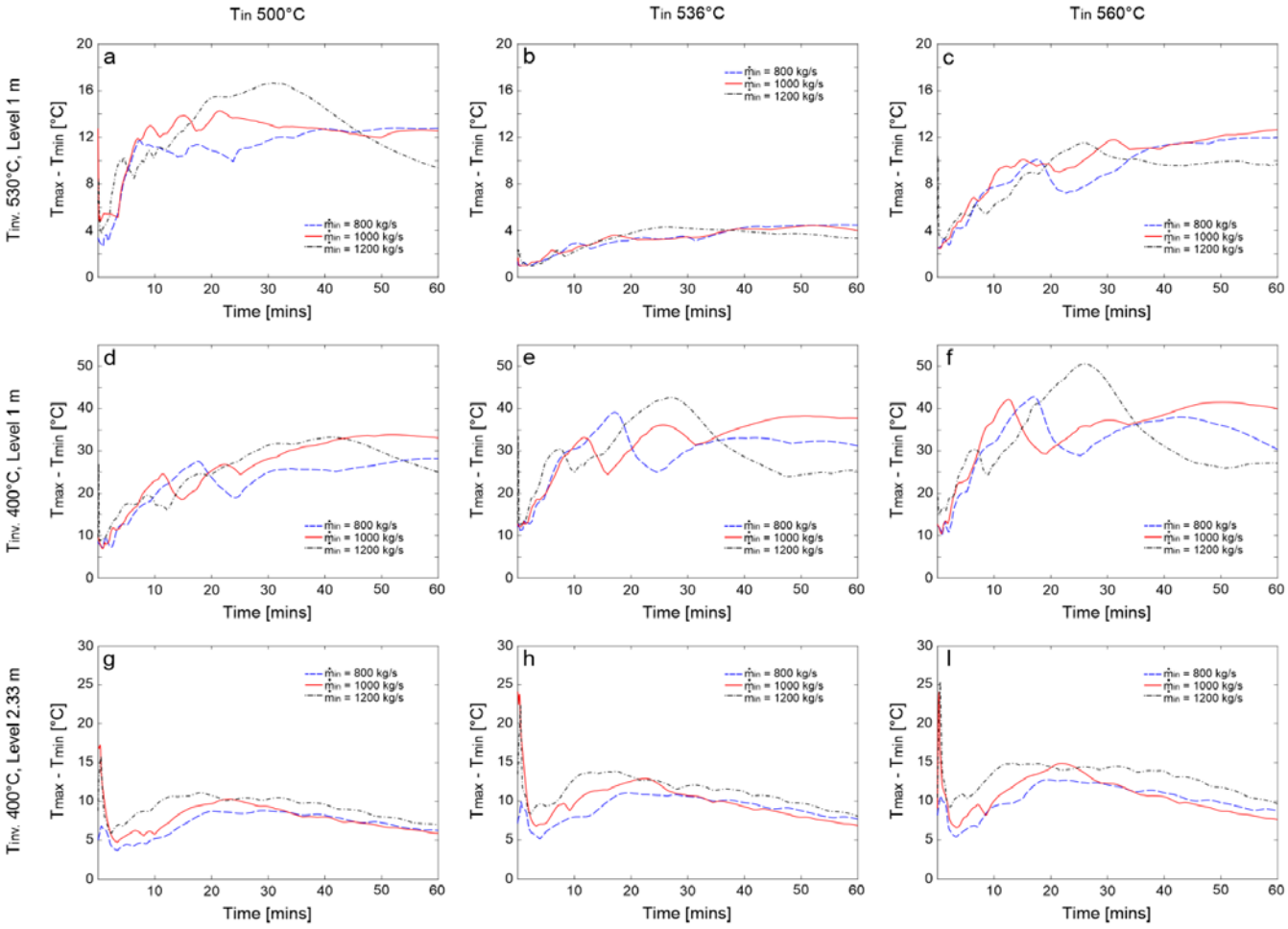

Figure 93. Maximum temperature difference in the tank floor for 60 minutes of charging operation for varying inventory temperature at time zero ($T_{inv.}$), salt level, and incoming salt temperature (T_{in})

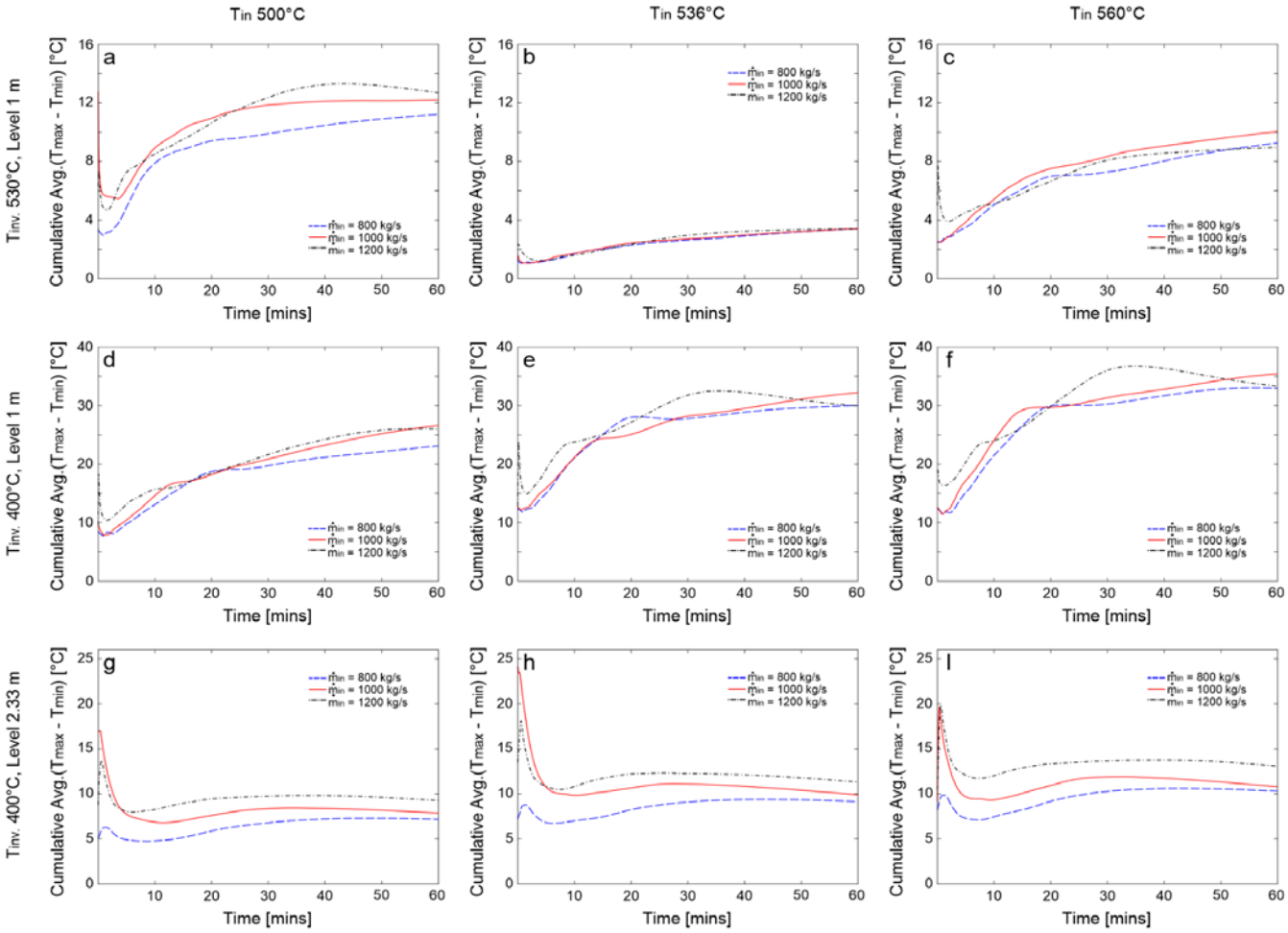

Figure 94. Cumulative average of maximum temperature difference in the tank floor during 60 minutes of charging operation for varying inventory temperature at time zero ($T_{inv.}$), salt level, and incoming salt temperature (T_{in})

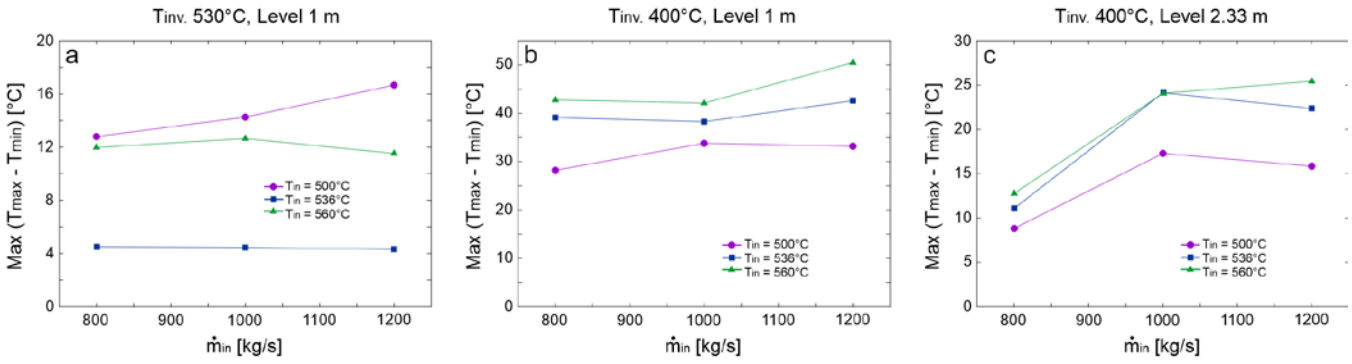

Figure 95. Maximum temperature difference in the tank floor during 60 minutes of operation as a function of the inlet mass flow rate and temperature

In general, the highest average for the maximum temperature difference in the floor of about 38°C is observed at the highest inlet mass flow rates for $T_{inv.}$ = 400°C and T_{in} = 560°C. Significant reduction in $(T_{max} - T_{min})_{cm,avg}$ and faster stabilization is predicted for larger salt inventory levels; see Figure 94g, 94h, and 94i. In general, for $\dot{m}_{in}$ = 800 kg/s, the $(T_{max} - T_{min})_{cm,avg}$ has lower values for the 60-

minute operational range, while higher values are obtained at different time intervals for $\dot{m}_{in}$ = 1000 kg/s and $\dot{m}_{in}$ = 1200 kg/s at inventory levels of 1m, see for example Figure 94a, 94c, 94d, and 94f. For a larger inventory level of 2.33 m, the largest $(T_{max} - T_{min})_{cm,avg}$ occurs most of the times for $\dot{m}_{in}$ = 1200 kg/s (see Figure 94g, 94h, and 94i,); however, the maximum value in these cases (below 15°C) is lower when compared with those obtained for an inventory level of 1 m and similar inventory and inlet flow temperatures, i.e., Figure 94d, 94e, and 94f.

The effect of the mass flow rate on the maximum $T_{max} - T_{min}$ (or $(T_{max} - T_{min})_{max}$) for the tank floor during 60 minutes of operation is presented in Figure 95 for $T_{inv.}$ = 530°C and inventory Level = 1 m (Figure 95a), $T_{inv.}$ = 400°C and inventory Level = 1m (Figure 95b), and $T_{inv.}$ = 400°C and inventory Level = 2.33 m (Figure 95c). In general, the influence of $\dot{m}_{in}$ on $(T_{max} - T_{min})_{max}$ is relatively small for low inventory levels, with $(T_{max} - T_{min})_{max}$ increase of about 7°C when $\dot{m}_{in}$ rises from 800 kg/s to 1200 kg/s for $T_{inv.}$ = 400°C, inventory Level = 1m, and T_{in} = 560°C, see Figure 95b. For an inventory level of 2.33 m, there is a strong influence of the $\dot{m}_{in}$ on $(T_{max} - T_{min})_{max}$ when $\dot{m}_{in}$ augments from 800 kg/s to 1000 kg/s, see Figure 95c; a trend is not seen when $\dot{m}_{in}$ increases from 1000 kg/s to 1200 kg/s.

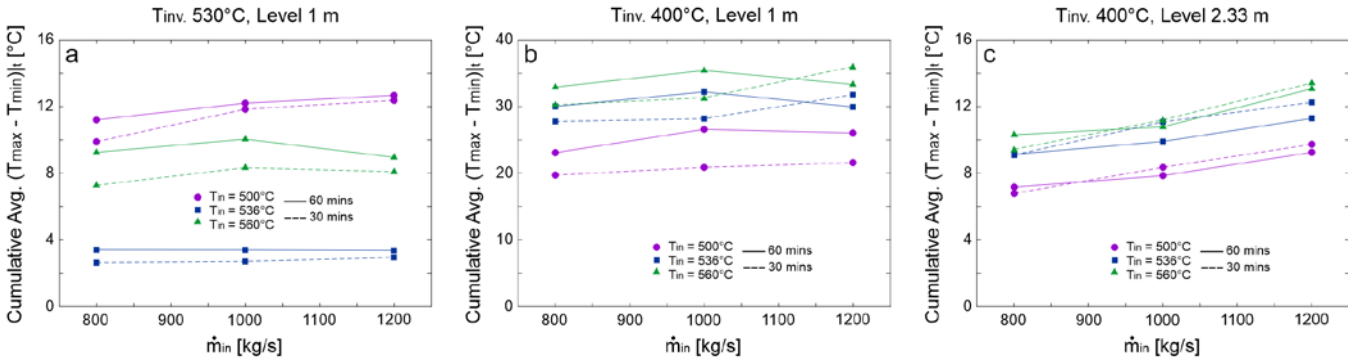

Figure 96. Cumulative average maximum temperature difference in the tank floor at 30 and 60 minutes of operation as a function of the inlet mass flow rate

The corresponding cumulative average maximum temperature difference in the tank floor as a function of $\dot{m}_{in}$ is presented in Figure 96. In this figure, this cumulative average is displayed to 30 and 60 minutes of operation. At inventory levels of 1 m and $\dot{m}_{in}$ of 800 and 1000 kg/s (Figure 96a and Figure 96b), $(T_{max} - T_{min})_{cm.,avg}$ is always higher at 60 minutes, which means that the temperature takes more time to stabilize. For the cases with an inventory level of 2.33 m (Figure 96c), a close to linear behavior is observed for $(T_{max} - T_{min})_{cm.,avg}$ with $\dot{m}_{in}$.

A similar parametric analysis was conducted but considering an outlet mass flow rate equal to the inflow, i.e., $\dot{m}_{in} = \dot{m}_{out} = \dot{m}$. Figure 97 and Figure 98, respectively, present $T_{max} - T_{min}$ and $(T_{max} - T_{min})_{cm.,avg}$ for different $\dot{m}$, $T_{inv.}$, T_{in}, and inventory levels of 1 m, 2.33 m, and 3.66 m. For these cases, the inventory level remains constant. From Figure 97, the $T_{max} - T_{min}$ strongly depends on the difference between $T_{inv.}$ and T_{in}. With low inventory levels, this behavior is exacerbated due to lower inertia. For instance, for the cases presented in Figure 97d, 97e, and 97f (having the maximum difference between $T_{inv.}$ and T_{in} among the analyzed cases and the low inventory level of 1m), $T_{max} - T_{min}$ values larger than 40°C are observed, reaching a maximum of more than 70°C for $\dot{m}$ = 1200 kg/s (Figure 97f). This large temperature difference between two points in the tank is not desirable because it could lead to large stress, and eventually, buckling. It is worth noting that, in general, the curve

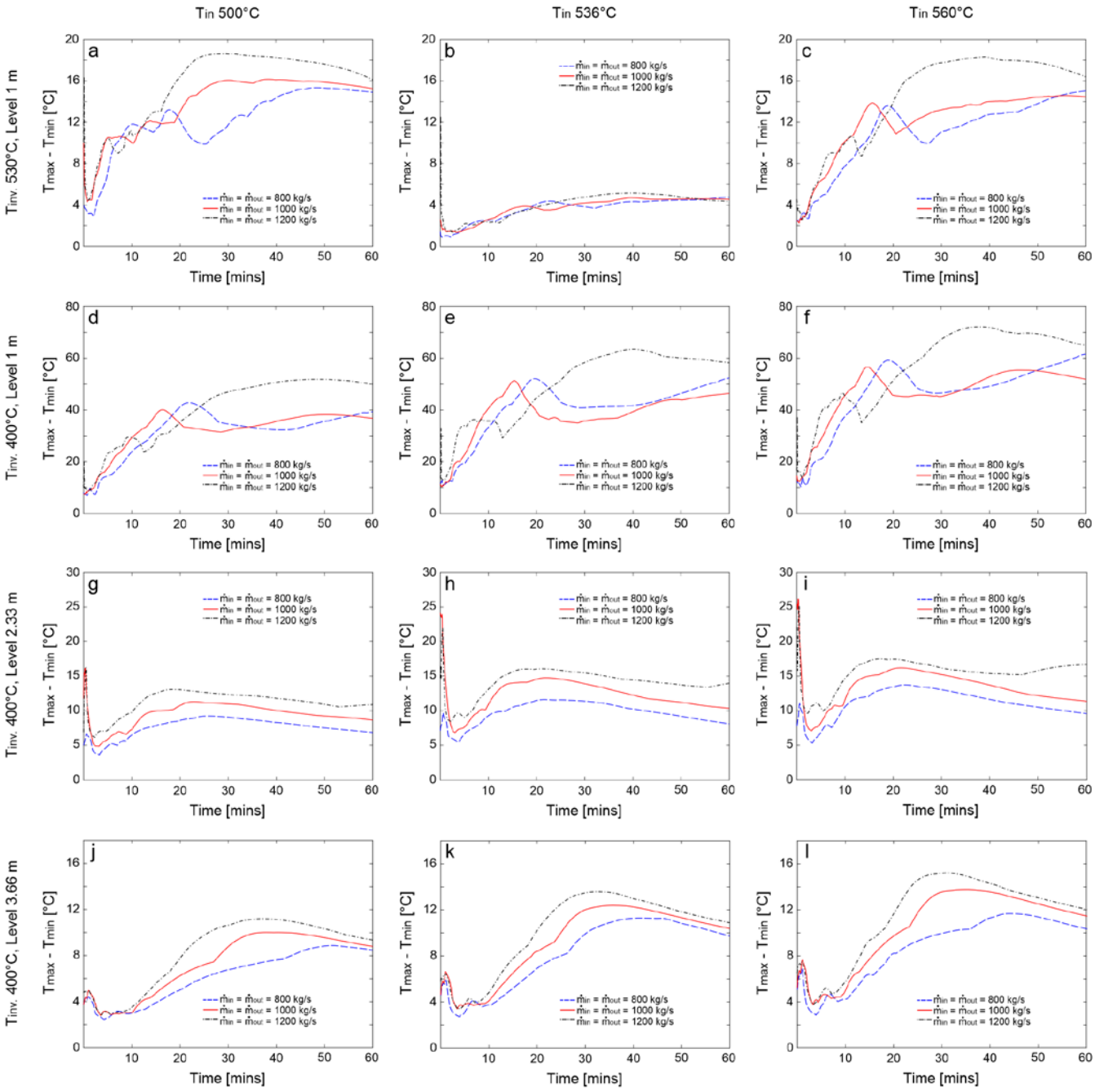

Figure 97. Maximum temperature difference in the tank floor for 60 minutes charging/discharging of operation for varying inventory temperature at time zero ($T_{inv.}$), salt level, and incoming salt temperature (T_{in})

$T_{max} - T_{min}$ has a local maximum at the beginning of the operation (startup) and a global maximum after 30 minutes. By the 60-minute of operation, this temperature difference seems to be more stable. Similarly to the case when $\dot{m}_{out} = 0$, the minimum $T_{max} - T_{min}$ values are obtained for T_{in} = 536°C and $T_{inv.}$= 530°C, which are practically independent on the mass flow rate (see Figure 97b). This could represent a proper operation alternative when large amount of salt needs to be pumped into the tank, without causing a large $T_{max} - T_{min}$ in the floor. Figure 97j, 97k, and 97l presents the results for an inventory level of 3.66 m. Besides the cases presented in Figure 97b (having close values of $T_{inv.}$ and

T_{in}), lower $T_{max} - T_{min}$ values are maintained at larger inventory levels. For inventory levels of 2.33 m and 3.66 m, a direct dependency is observed between $T_{max} - T_{min}$ and $\dot{m}$.

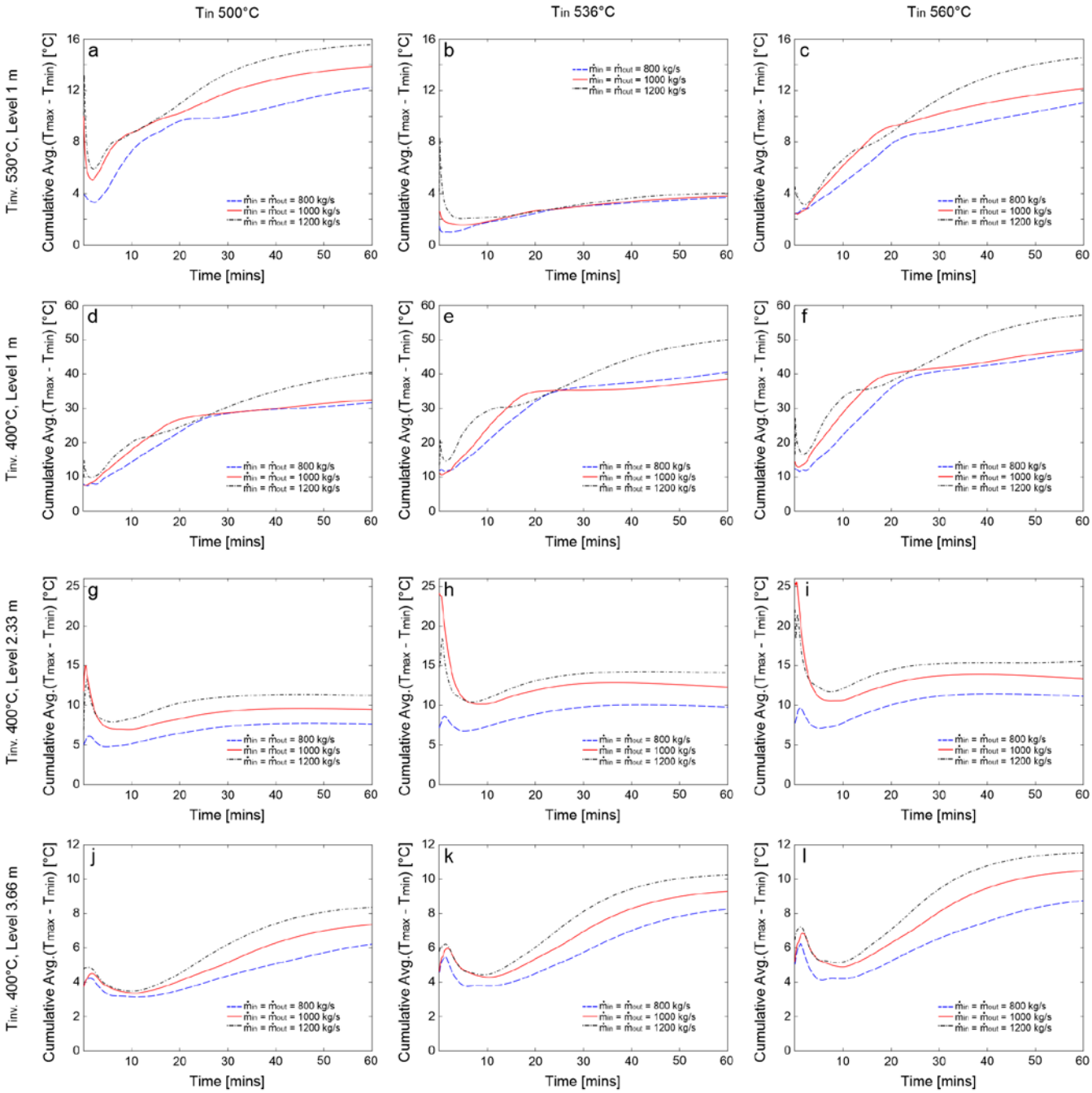

Figure 98. Cumulative average of maximum temperature difference in the tank floor during 60 minutes of charging/discharging operation for varying inventory temperature at time zero ($T_{inv.}$), salt level, and incoming salt temperature (T_{in})

The corresponding $(T_{max} - T_{min})_{cm.,avg}$ curves, for the cases shown in Figure 97, are presented in Figure 98. It can be appreciated after 30 minutes of operation that the larger $(T_{max} - T_{min})_{cm.,avg}$ is associated with the higher $\dot{m}_{in}$, i.e., 1200 kg/s. Also, the $(T_{max} - T_{min})_{cm.,avg}$ curves present lower

values and variation for inventory levels of 2.33 m and 3.66 m, almost independent on the difference between $T_{inv.}$ and T_{in}, as can be seen in Figure 98g to 98l. This implies that the tank operation is safer at higher inventory levels because transient events—leading to large differences between the inventory temperature and the temperature of the incoming flow—will produce a small $T_{max} - T_{min}$ in the floor.

Comparing similar parametric cases having $T_{inv.}$ = 400°C and an initial inventory level of 1 m for a tank charging scenario, i.e., $\dot{m}_{out} = 0$ (Figure 93d to 93f) and for a charging/discharging scenario, i.e., $\dot{m}_{in} = \dot{m}_{out} = \dot{m}$ (Figure 97d to 97f), it can be seen a similar behavior of $T_{max} - T_{min}$ during the first 10 minutes of operation. For the charging scenarios, the inertia augments with time, which leads to a maximum $T_{max} - T_{min}$ that reduces and/or stabilizes after 60 minutes; the maximum $T_{max} - T_{min}$ for these set of cases ranges between ~35° and ~50°C. In contrast, the salt inventory level remains constant for the charging/discharging cases, which leads to maximum $T_{max} - T_{min}$ values that range between ~50°C and ~72°C and take more time to stabilize.

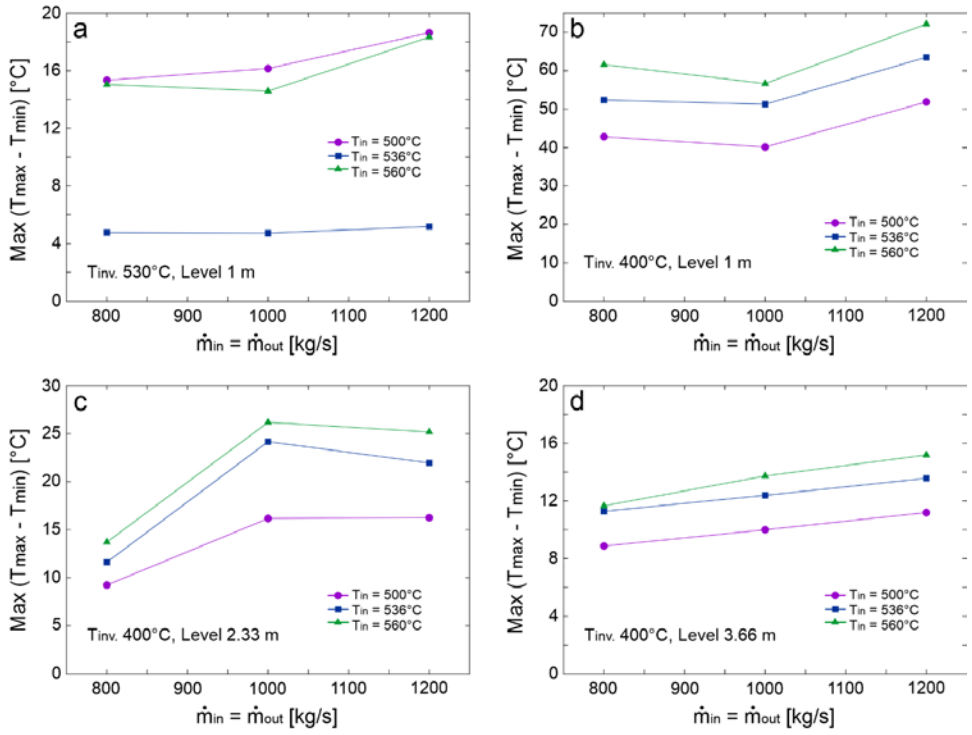

Figure 99. Maximum temperature difference in the tank floor during 60 minutes of charging/discharging operation as a function of the mass flow rate for varying inventory temperature at time zero ($T_{inv.}$), salt level, and incoming salt temperature (T_{in})

The behavior of $(T_{max} - T_{min})_{max}$ as a function of $\dot{m}$ is presented in Figure 99. In general, an increase of the $(T_{max} - T_{min})_{max}$ is observed with $\dot{m}$, except for the cases presented in Figure 99b that present the largest $(T_{max} - T_{min})_{max}$ values. It can be observed in Figure 95b and Figure 99b that the cause for the maximum temperature difference in the tank floor is mainly associated with the large temperature difference between the salt inflow and the inventory when the tank has a low inventory level. For these specific cases (presented in Figure 95b and Figure 99b), the effect of the inlet mass flow seems to be secondary. The corresponding $(T_{max} - T_{min})_{cm.,avg}$ for the cases presented in Figure 97 and Figure 98—calculated after 30 and 60 minutes of operation— are displayed in Figure 100. In this figure, it can

be appreciated that at high tank inventory levels, $(T_{max} - T_{min})_{cm.,avg}$ not only present relatively low values, but it behaves practically linear with the inlet mass flow, which makes it more predictable.

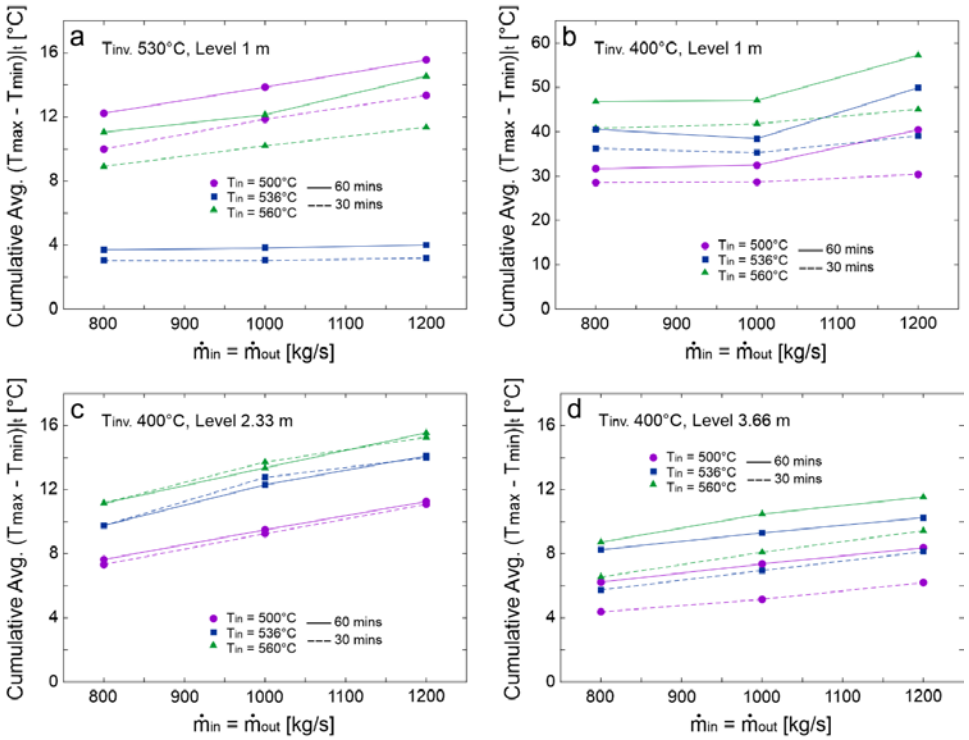

Figure 100. Cumulative average maximum temperature difference in the tank floor at 30 and 60 minutes of charging/discharging operation as a function of the mass flow rate for varying inventory temperature at time zero ($T_{inv.}$), salt level, and incoming salt temperature (T_{in})

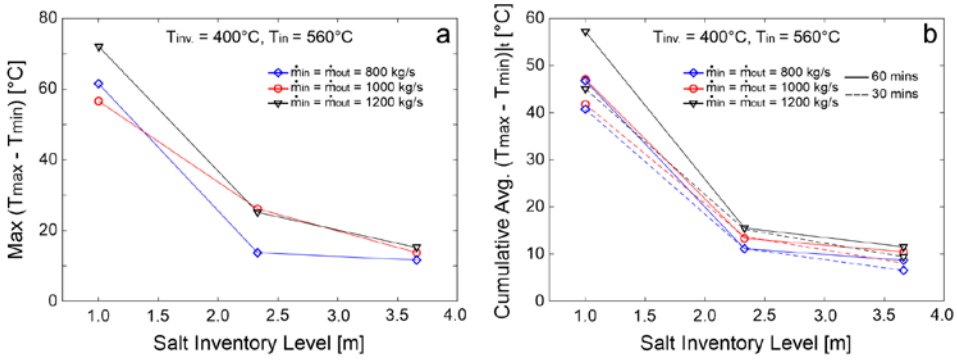

Figure 101. (a) Maximum temperature difference in the tank floor during 60 minutes of charging/discharging operation as a function of the inventory level. (b) Cumulative average maximum temperature difference in the tank floor at 30 and 60 minutes of charging/discharging operation as a function of the inventory level

Some results presented in Figure 99 and Figure 100 were reorganized and displayed in Figure 101 to better appreciate the effect of the inventory level. A significant reduction in $(T_{max} - T_{min})_{max}$ and $(T_{max} - T_{min})_{cm.,avg}$ with an inventory level of 2.33 m and 3.66 m is observed. These results suggest that the hot tank operation protocol should specify a minimum inventory level, which is a function of T_{in}, to avoid excessive temperature difference in the floor.

To better illustrate the impact of the temperature difference (or temperature gradients) on the stresses developed in the tank floor, Figure 102 presents the maximum Von Mises stress for three sets of cases: (1) cases with low difference between T_{in} and $T_{inv.}$ for an inventory level of 1 m, which presented the minimum $T_{max} - T_{min}$ and $(T_{max} - T_{min})_{cm.,avg}$ (see Figure 93b), (2) cases with a larger difference between T_{in} and $T_{inv.}$ also for an inventory level of 1m (see Figure 93e) that presented temperature differences in two location in the tank floor of more than 40°C, and (3) cases with a larger difference between T_{in} and $T_{inv.}$ but with an inventory level of 2.33 m (see Figure 93h). Figure 102 also shows the yield strength (YS) limit of SS 347H at the average tank floor temperature, which is presented for all the analyzed cases in Figure 103. It can be seen in Figure 102a that the lower $T_{max} - T_{min}$ below 5°C (see Figure 93b) leads to a low maximum stresses in the tank floor, far from the SS 347H YS limit. In contrast, the large $T_{max} - T_{min}$—obtained when T_{in} = 536°C and $T_{inv.}$= 400°C for a 1 m inventory level (see Figure 93e)—results in high maximum stresses that grow very fast and surpass the SS 347H YS point just after 15 minutes of operation, as can be seen in Figure 102b. It can be seen in Figure 103b that the average tank floor temperature is even lower for these last cases (with higher stresses), when compared with the cases presented in Figure 103a, which demonstrate the strong impact of the temperature spatial variations ($T_{max} - T_{min}$) in the floor on the resulting operation stresses. Figure 102c shows the stress reduction in the tank floor when the inventory level increases from 1 to 2.33 m for similar T_{in} = 536°C and $T_{inv.}$= 400°C.

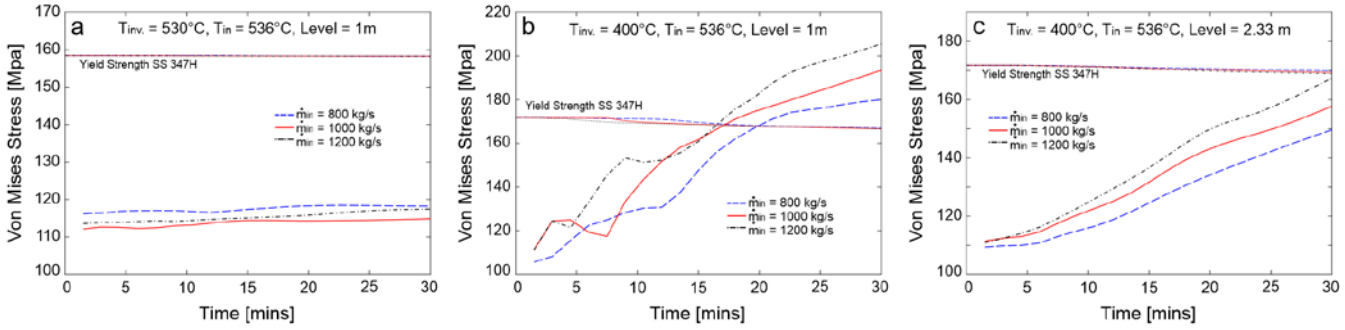

Figure 102. Maximum Von Mises stress in the tank floor during 30 minutes of charging operation for varying inventory temperature at time zero ($T_{inv.}$) and salt level

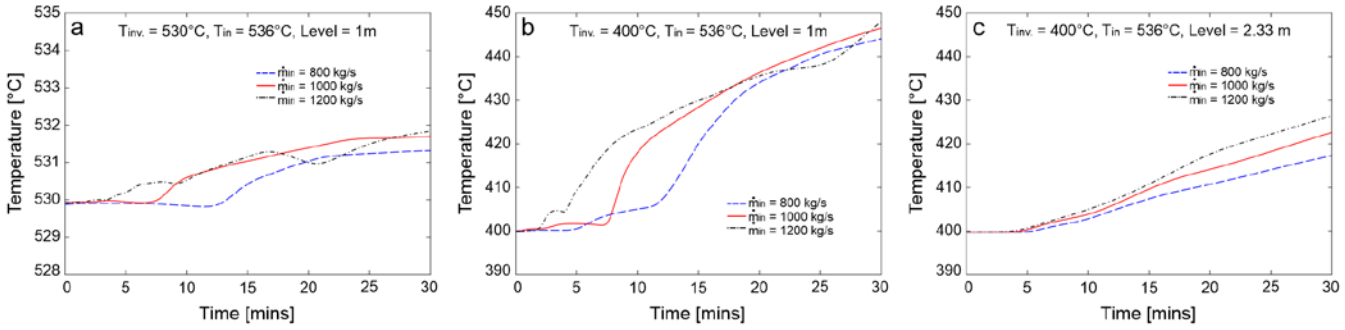

Figure 103. Average tank floor temperature during 30 minutes of charging operation for varying inventory temperature at time zero ($T_{inv.}$) and salt level

In summary, this parametric analysis demonstrates the impact of the key tank operating variables in the spatial temperature difference in the tank floor. These high-temperature differences are undesirable as they could favor the formation of buckles due to the larger mismatch in expansion and stresses between floor and foundation. In addition to some safe plant operating protocols, a better design of the sparger

ring should improve the mixing between the incoming salt and the inventory, reducing thermal gradients and stresses on the tank floor.

4.2 Temperature and Stress Distributions

In addition to the parametric analysis in the previous section, this section presents the temperature and stress distribution in the tank obtained for typical plant operating conditions (see Section 2.2). Figure 104 shows the variation of the average floor temperatures and the corresponding stresses during transient operating conditions. The average floor temperature exerts a direct impact on the stress; small fluctuations in the floor temperature could lead to large changes in stresses. It can be appreciated in this figure that under some specific operating conditions, the stress curve surpasses the SS 347H YS limit.

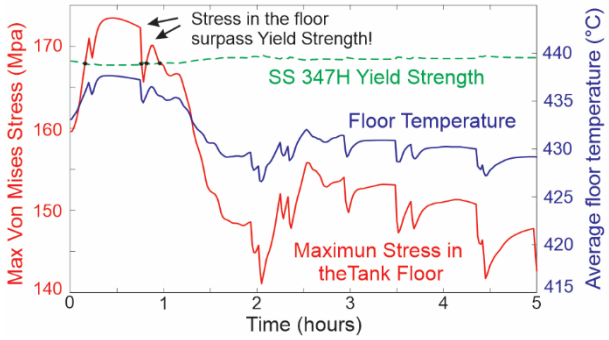

Figure 104. Typical maximum Von Mises stress evolution and average temperature in the tank floor during transient operating conditions. SS 347H yield strength is surpassed within the first hour of operation.

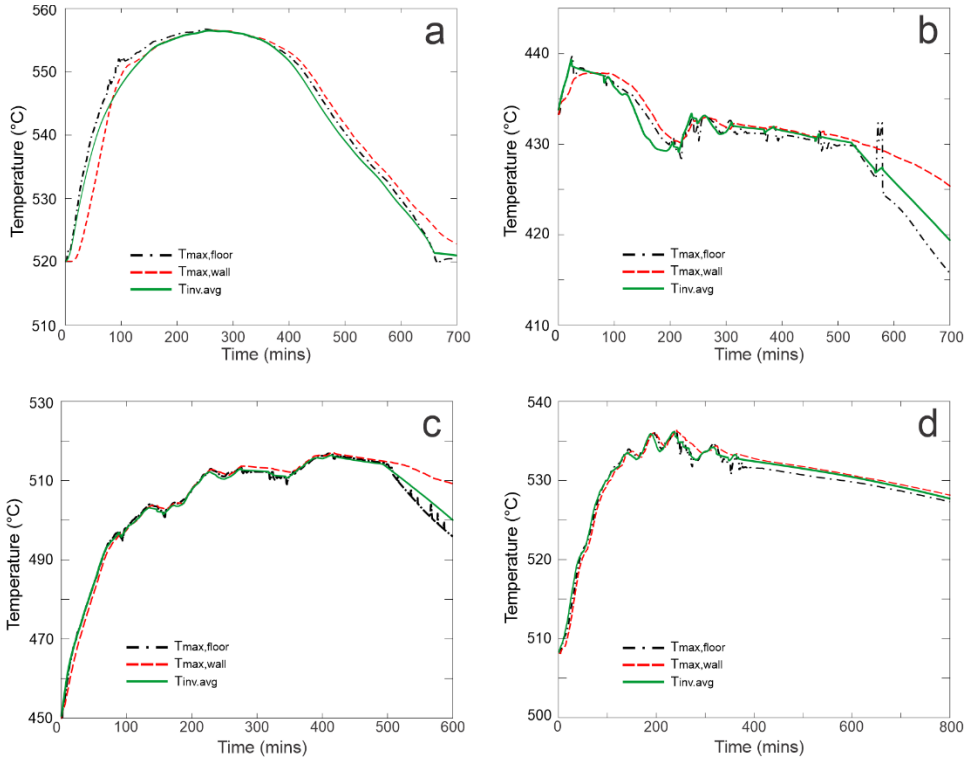

Figure 105. Tank temperature profiles: (a) case 1, (b) case 2, (c) case 3, and (d) case 4

The temperature and stress analyses considered four cases representing typical tank operating conditions, which are presented in Figure 10 and Section 2.2 Typical Plant Operating Conditions. Temperature profiles for the four cases are presented in Figure 105. These profiles correspond to the maximum temperature in the floor, the maximum temperature in the tank shell, and the average inventory temperature. Case 1 corresponds to a clear sky day operating condition where the temperature in the tank reaches values beyond 550°C; see Figure 105a. Cases 2 to 4 correspond to a partly cloudy sky day, with multiple transient events due to the presence of clouds. In particular, case 2 presents the large number of transient events among the analyzed cases, which lead to a relative low operating temperature; see Figure 105b.

As mentioned, multiple monitor nodes were set in the simulation for a fast evaluation of temperature and stress. Figure 106 presents the distribution of the monitors in the tank floor and the corresponding radial coordinate from the center. The stress and temperature evolution for nodes 1 to 6 for the 4 typical operational cases are presented in Figure 107. Stress levels of more than 250 MPa have been found for cases 1, 3, and 4 for node 6, which is closer to the tank perimeter. These high values could be influenced by the effect of the tank wall at the perimeter that becomes an addition barrier for the floor radial displacement. The stress in nodes 1, 2, 3, and 5 are relatively similar in each case. Node 4 is on the floor right under the sparger ring; stresses in this node present a different behavior, mainly influenced by the salt inflow. The high stresses obtained in the tank floor in cases 1, 3, and 4 surpass the YS point of SS 347H, which will lead to a plastic deformation. From Figure 107, a direct influence of the temperature on the Von Mises stress can be observed.

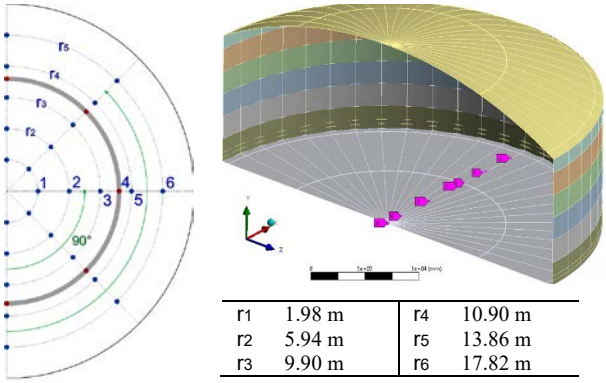

r1	1.98 m	r4	10.90 m
r2	5.94 m	r5	13.86 m
r3	9.90 m	r6	17.82 m

Figure 106. Distribution of tank floor monitors

Von Mises stress contours for the tank floor at different operating times for clear sky and partly cloudy sky operating conditions are presented in Figure 108. The clear sky and partly cloudy sky day operating conditions correspond to case 1 (Figure 10a) and case 2 (Figure 10b), respectively. Despite the transient events after 15 and 49 mins of operation during the partly cloudy sky, the contours stresses for this condition (Figure 108d to 108f) present lower values when compared with the stresses produced during the clear sky day (Figure 108a to 108c) driven by a higher operating temperature. Stresses of up to 260 MPa are developed in the tank floor during a clear sky day after 300 mins, when the temperature in the tank is about 554°C (see Figure 105a and Figure 107b). Note that the temperature for the partly cloudy sky day is below 500°C (see Figure 105b and Figure 107d) and the corresponding maximum Von Mises stresses are below 180 MPa.

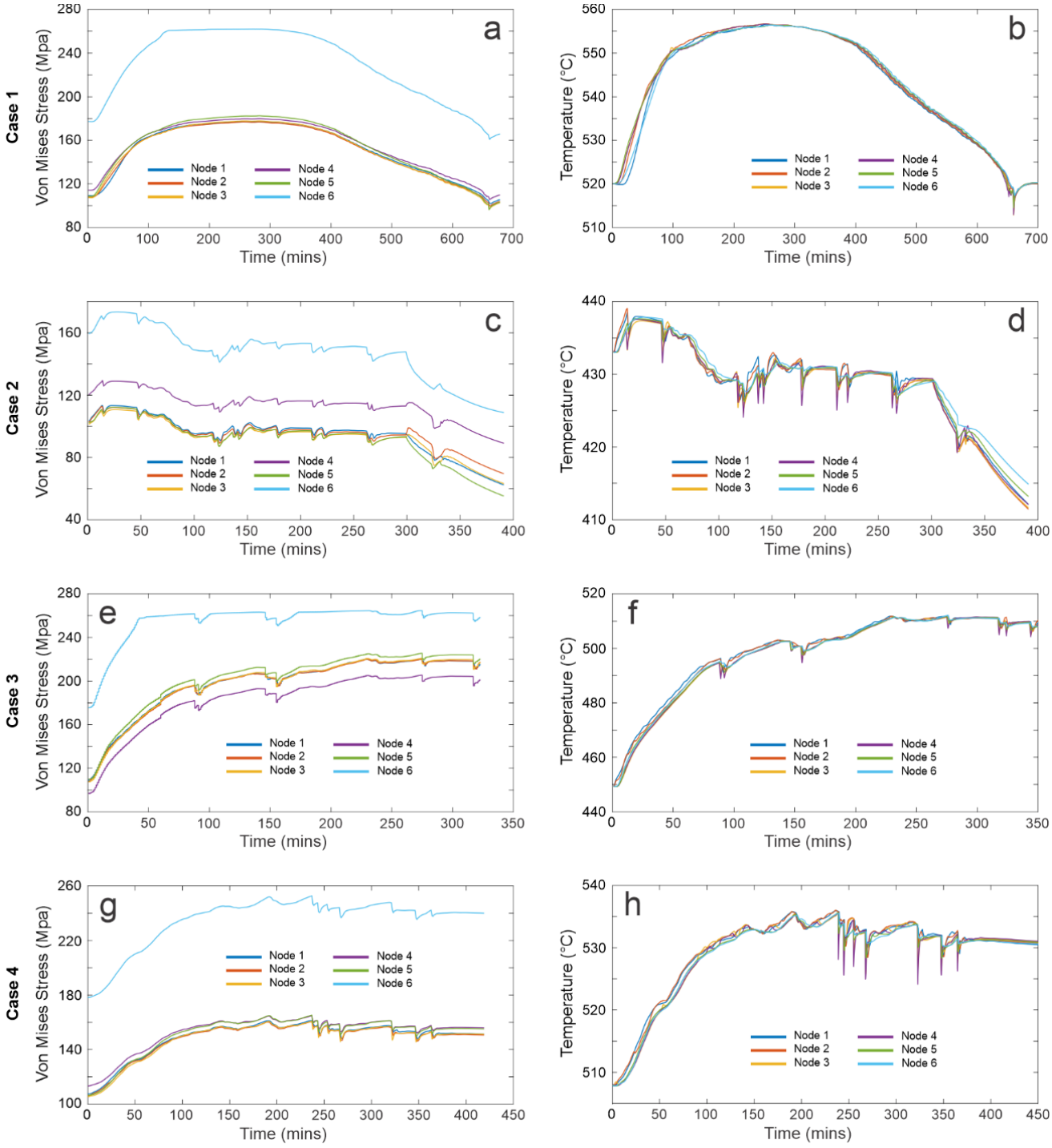

Figure 107. Von Mises stress (left column) and temperature (right column) evolution at the six radial monitor nodes located on the tank floor; friction coefficient = 0.5, floor thickness = 6.7 mm

Similar to the tank floor, Von Mises stress contours for the tank shell are presented in Figure 109. As seen in this figure, stresses in the tank shell are larger in the bottom, but they are lower than the maximum stresses in the floor. For the clear sky day operating conditions (Figure 109a to 109c), maximum stresses are around 180 MPa, while for the partly cloudy sky day (Figure 109d to 109f), these stresses are below 140 MPa. Based on the analysis of stresses developed in the tank floor and shell, there

are some regions in the tank floor near the perimeter and the bottom of the tank shell, whose values exceed the yield strength of the SS 347H. This situation implies that the tank floor will deform plastically with every cycle and eventually could lead to cracking.

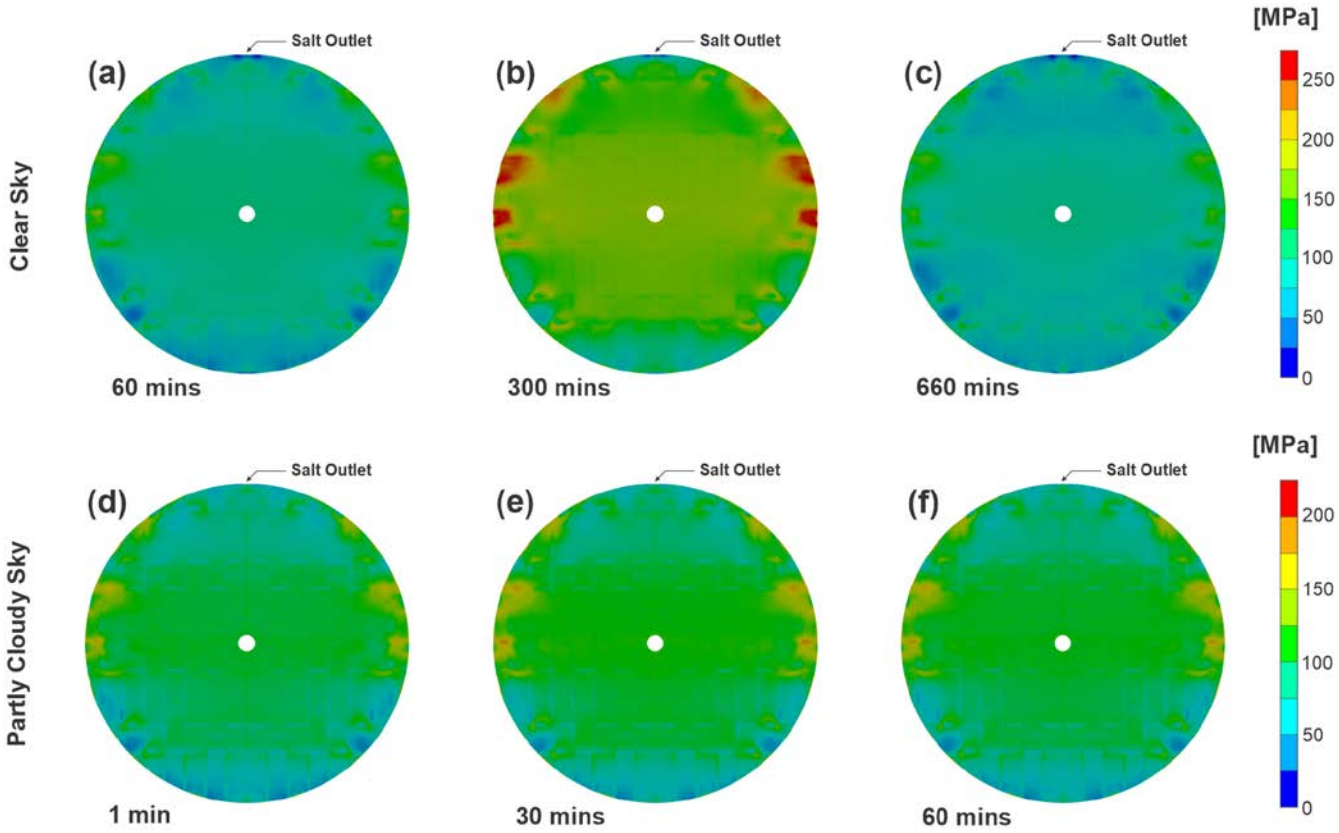

Figure 108. Von Mises stress contours in the tank floor at different operating times: (a)–(c) are clear sky day conditions; (d)–(f) are partly cloudy sky day conditions

A comparison of the stress distribution in the tank floor when residual stress and deformation are and are not considered is presented in Figure 110 for a clear sky day operation. Figure 110a to 110c correspond to the stress contours during operation when initial residual stresses and the distortion in the tank floor (after its fabrication) are included. The stress distribution in the floor changes considerably during operation. Stresses close to 260 MPa are observed after 300 mins of operation near the perimeter of the tank, which could be detrimental for the tank's lifetime. If the residual stress and the distortion are not considered, see Figure 110d to 110f, the stresses during operation in the tank floor are below 80 MPa, which are far below the SS 347H YS limit. It is clear from this analysis that the initial state of the floor after welding fabrication has a strong impact on the operating stresses. Ignoring this condition will lead to operating stresses that do not represent the real stress values experienced by in-service hot tanks and could lead to inaccurate conclusions on the failures that have occurred. It is worth noting that the stresses can be substantially reduced with a better tank design, fabrication procedures, implementation, and safer operation practices.

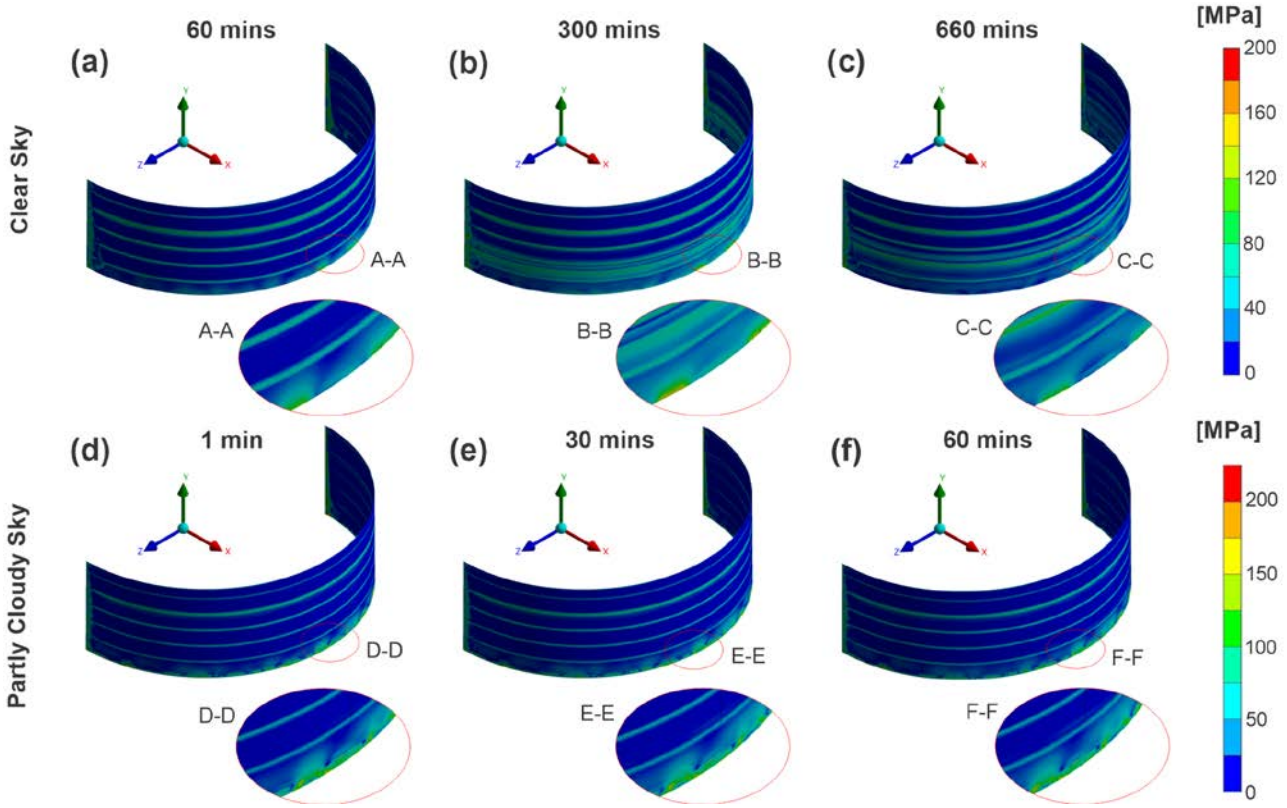

Figure 109. Von Mises stress contours in the tank shell at different operating times: (a)–(c) are clear sky day conditions; (d)–(f) are partly cloudy sky day conditions

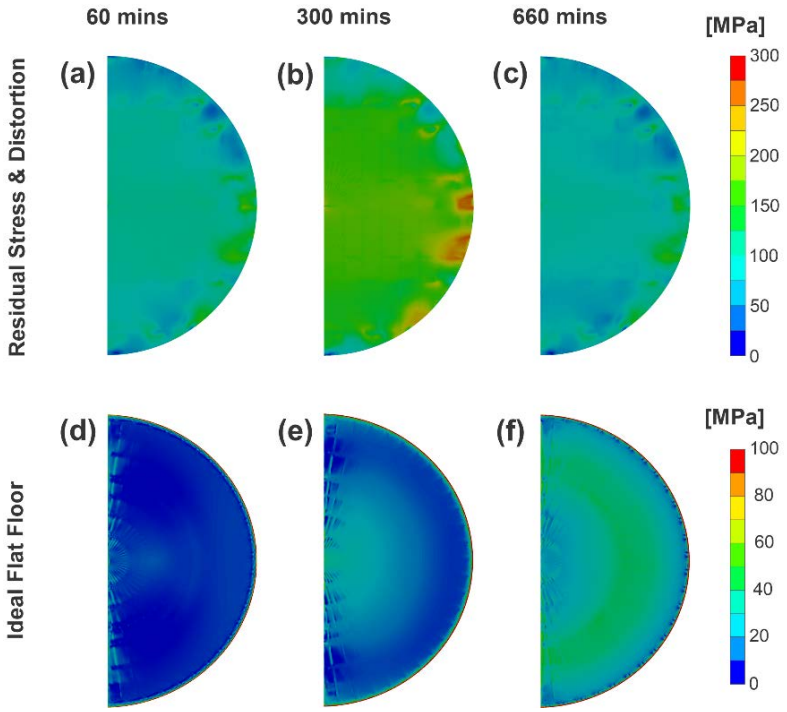

Figure 110. Von Mises stress distribution in the tank floor for clear sky operating conditions and at different times: (a) to (c) show residual stress and distortion after welding fabrication, (d) to (f) show flat floor (no stress and no deformation)

4.3 Design Alternatives

In this section, the effect of some design parameters on the temperature and stress distribution in the tank floor are evaluated, including the floor thickness, the friction coefficient between the floor and the foundation, the location of salt outlets, and the height of the sparge ring above the tank floor. Note that this analysis is focused on the floor because this component is critical due to the large loads and friction forces with the foundation during cycle operation. Stress levels in the shell are also significantly lower when compared with the levels in the floor. In addition, several tank failures of commercial molten salt hot tanks have occurred on the tank floor.

4.3.1 Floor Thickness

Several floors in commercial hot tanks have been fabricated with thin SS 347H plates. The logic of this design was the implementation of a thin layer to separate the molten salt from the foundation, which has been operating fine in tanks for the oil and gas industry. The use of this thin layer seems to be motivated by a lower cost and easier fabrication and implementation, considering that the tank support and mechanical loads during operation are the primary function of the foundation. The analysis presented in this section demonstrates that a proper design of the tank floor is required to withstand large mechanical and thermal loads for the high temperatures (up to 565°C) and cycling operating conditions presented in central receiver CSP plants. This analysis considered five different floor thicknesses—6.7 mm, 12 mm, 20 mm, 30 mm, and 40 mm—for 60 minutes of operation under the conditions corresponding to case 2.

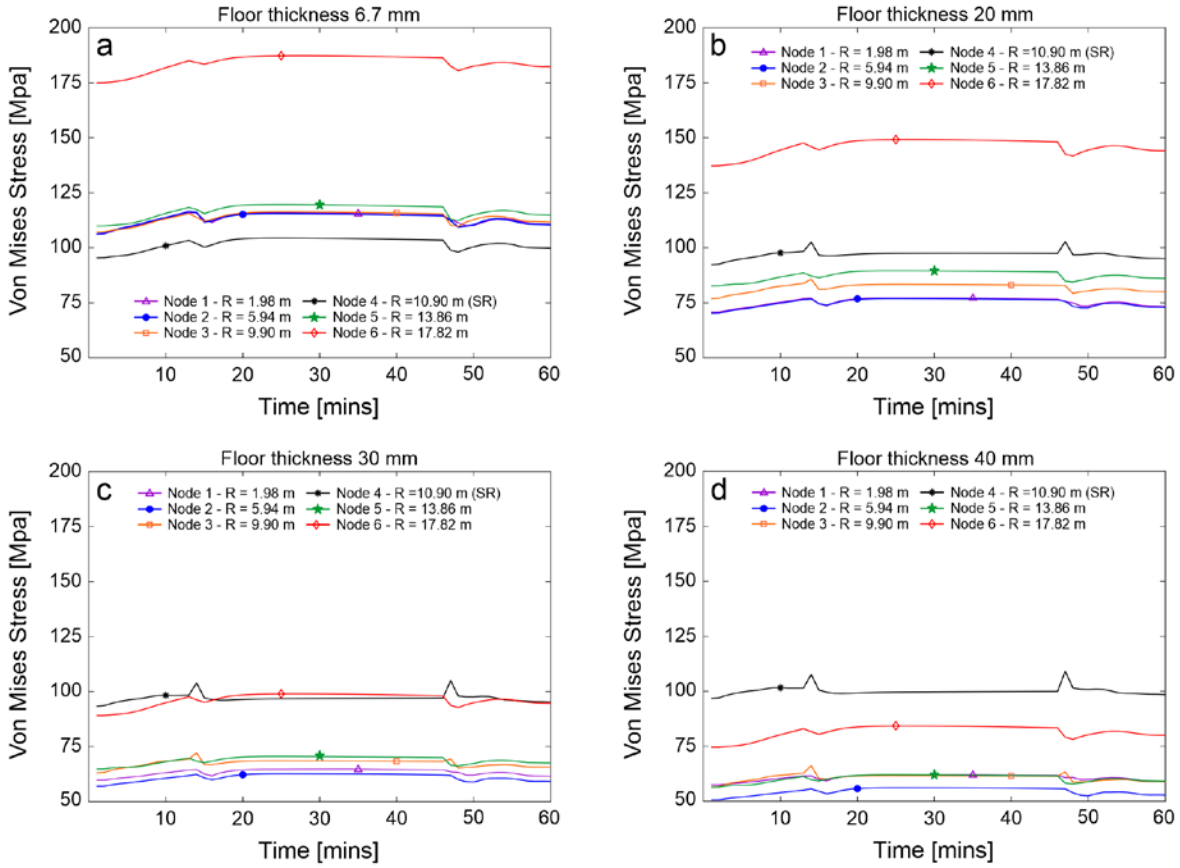

Figure 111. Von Mises stress evolution in the six nodes of the tank floor as a function of the floor thickness for a partly cloudy sky day condition; friction factor = 0.5; case 2

The Von Mises stress evolution in the six nodes in the tank floor during 60 mins of operation under a partly cloudy sky day conditions is presented in Figure 111 for different floor thicknesses. The Von Mises stresses in node 6 are higher for floors with thicknesses of 6.7 mm and 20 mm (see Figure 111a and 111b). In general, increasing the floor thickness substantially reduces the stress due to a better redistribution of the stress in the floor plate volume. In node 4, however, the effect of the floor thickness on the stress is very low, and the stress values are mainly determined by the temperature of the molten salt under the sparger ring. For a floor with a thickness of 6.7 mm, the Von Mises stress in node 6 surpasses the material yield strength, which is detrimental for the tank's lifetime. Increasing the tank floor to 20 mm will reduce the stresses in this node under the yield strength of the SS 347H. For a floor with a thickness of 30 mm, the stress in nodes 4 and 6 are very similar. Note that an additional increment in the floor thickness may not be effective as the stress in node 4 remains close to 100 MPa due to the larger temperature changes in the region in the floor under the sparger ring where node 4 is located.

4.3.2 Friction Coefficient

The temperature and hydrostatic pressure profiles from the CFD simulation were imported into the structural analysis for typical plant operation under a partly cloudy sky day condition (case 2). The contact between the floor and the sand (solid lubricant) was set as frictional contact with a constant friction coefficient. However, the effect of different magnitude constant friction coefficients on the stress evolution in the tank floor was analyzed.

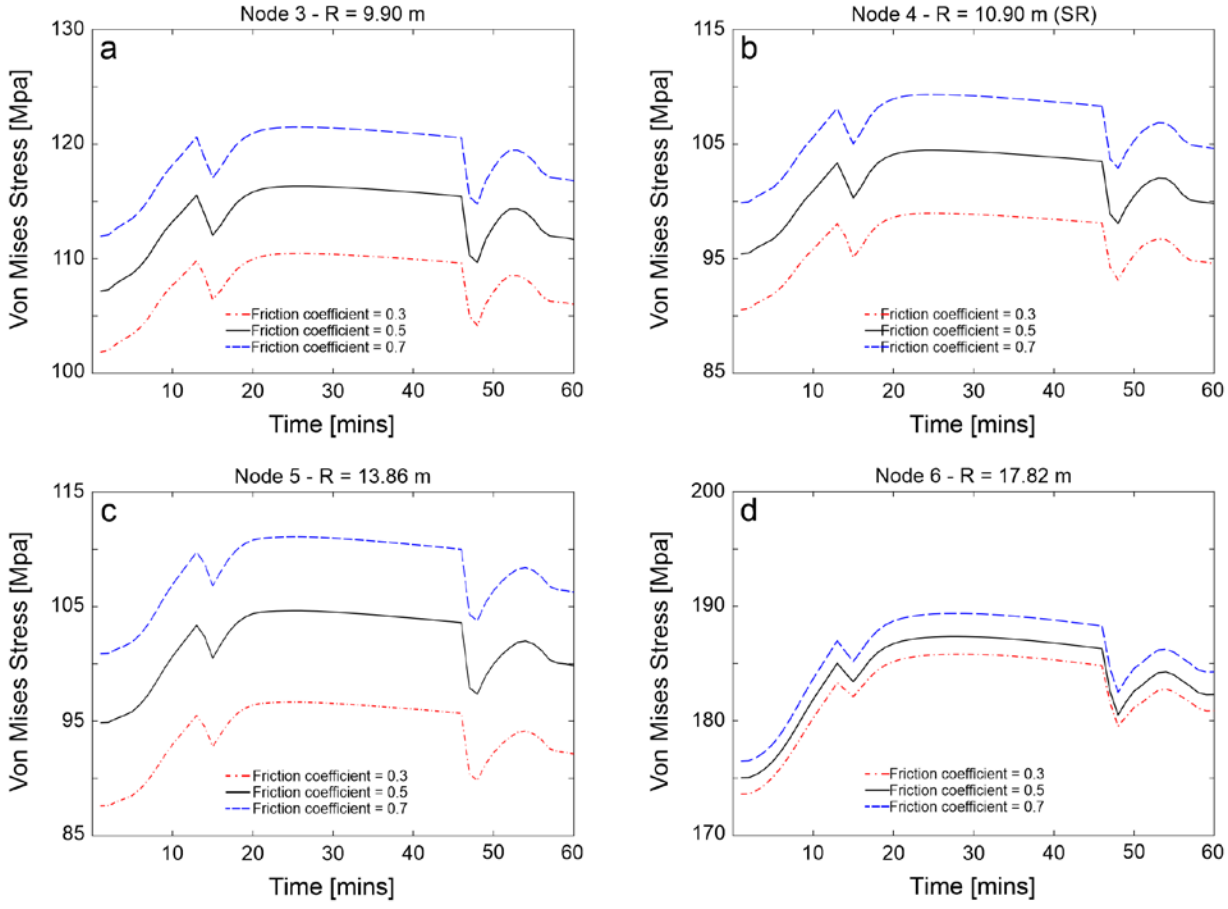

Figure 112. Von Mises stress evolution in six nodes of the tank floor as a function of the friction coefficient for a partly cloudy sky day condition; floor thickness 6.7 mm; case 2

The effect of the friction coefficient between the tank floor and the foundation is presented in Figure 112 for four different nodes. As expected, larger friction coefficients lead to higher stress. For nodes 3 to 5, the Von Mises stress increases between 4 and 7 MPa when the friction coefficient increases from 0.5 to 0.7. A reduction in the Von Mises stress is observed when the friction coefficient reduces from 0.5 to 0.3. For node 6, the effect of the friction coefficient on the Von Mises stress is proportionally smaller, i.e., about 2 to 3 MPa when the friction coefficient increases to 0.7 or decreases to 0.3, with respect to the case with a friction coefficient of 0.5. The large stresses in node 6 are highly influenced by the weight of the shell and the floor-shell joint. Changing the friction coefficient in the system might require the use of different materials between the floor and the foundation. The expected effect of reducing the friction coefficient seems to be lower when compared to the effect of implementing a floor with a larger thickness.

4.3.3 Tank Salt Outlets

The impact of the number of tank outlets on the temperature and stress distribution in the tank shell and floor was also analyzed. Commercial tanks usually consider several salt outlet points that are implemented in the tank using vertical pipes that hold the pumps and go through the roof (see Figure 11). The outlet pipes are connected to the molten salt pumps that are usually supported by a metallic frame located above a portion of the tank roof. This design implies that all the outlet pipes extract the salt in points at the tank volume that are relatively close to each other, which could be seen as a single extraction point. The effect of having extraction points distributed at different locations in the tank volume was analyzed in terms of the influence on the temperature of the tank floor. The initial hypothesis was that having a better distribution of salt outlets could lead to better mixing and, eventually, some reduction in the temperature gradients in the tank floor.

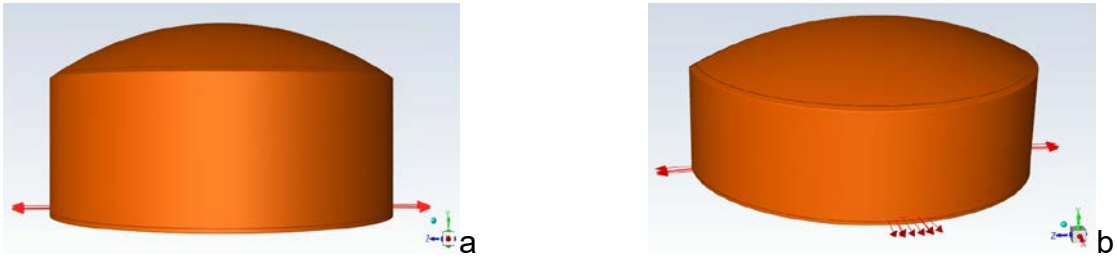

Figure 113. Molten salt tank design with (a) two outlets, and (b) four outlets

In addition to an outlet located at a single point extraction (representative tank design), two more cases were analyzed: (1) an additional outlet at the opposite radial location, see Figure 113a, and (2) four outlets, all of them at 90° from each other, see Figure 113b. The operational conditions corresponding to cases 2 and 4 (Figure 10b and Figure 10d) were simulated for two and four tank outlets and were compared with the representative tank design that features a single outlet. The total mass flow rate going out the tank remained constant for all cases, which means that 100%, 50%, and 25% of the molten salt mass exits the tank for the single-outlet, two-outlet, and four-outlet tanks, respectively.

Table 25 presents the maximum, minimum, and average temperature in the tank floor and shell for tanks with 1, 2, and 4 salt extraction points for cases 2 and 4, respectively. The results are presented for 1, 2, and 3 hours of operation. From Table 25, it can be appreciated that all temperatures practically remain unaffected across tank designs with different numbers of outlets, which demonstrates that the current

design having a single extraction point is satisfactory and, practically, does not exert any impact on the floor temperature distribution.

Table 25. Temperatures in the Tank Floor and Shell for Case 2 and 4 Conditions

			Case 2			Case 4		
# Outlets		Time (hr)	T_{min} (°C)	T_{avg} (°C)	T_{max} (°C)	T_{min} (°C)	T_{avg} (°C)	T_{max} (°C)
1	Floor	1	435.05	435.7	436.39	518.75	521.33	523.03
		2	424.58	427.84	429.43	528.99	531.16	532.12
		3	426.14	429.56	431.34	532.52	533.75	534.88
	Wall	1	379.17	401.98	437.38	446.48	476.28	522.02
		2	378.74	400.64	430.35	446.07	481.86	531.57
		3	378.07	402.85	432.26	446.09	485.99	534.84
2	Floor	1	435.00	435.67	436.37	518.73	521.35	522.92
		2	424.08	427.8	429.49	529.35	531.23	532.11
		3	426.34	429.56	431.30	532.57	533.81	535.03
	Wall	1	378.79	401.98	437.35	446.29	476.36	521.81
		2	378.46	400.6	430.36	445.95	481.92	531.45
		3	377.99	402.85	432.32	445.83	486.01	534.74
3	Floor	1	435.00	435.68	436.39	519.04	521.38	522.89
		2	424.07	427.81	429.46	529.30	531.23	532.12
		3	426.4	429.56	431.25	532.53	533.8	535.01
	Wall	1	378.79	402.01	437.37	446.29	476.32	521.61
		2	378.46	400.66	430.33	445.96	481.92	531.34
		3	377.98	402.96	432.26	445.94	486.09	534.68

4.3.4 Sparger Ring Position

The parametric analysis and the evaluation of temperature distribution in the tank for the four typical operating cases have shown that the inflow conditions exert an impact on the temperature and the corresponding stress distributions. Usually, commercial hot tanks have sparger rings located relatively close to the tank floor (between 0.5 and 1.5 m). In this section, the effect of the location of the inlet salt jets is analyzed through the position of the sparger ring with respect to the floor.

Figure 114 displays temperature contours for the tank floor for different sparger ring heights at 5, 15, and 30 minutes of operation, considering a 2 m salt inventory level, $T_{inv.}$= 400°C, T_{in}= 560°C, $\dot{m}_{in}$ = 1200 kg/s, and $\dot{m}_{out}$ = 0. Since the tank is charging, an increment in the temperature is observed in all cases with time. The contours capture the variation in the tank floor temperature of up to 20°C at a specific operating time. This temperature difference ($T_{max} - T_{min}$) is clearly lower when the sparger ring is located at 1.90 m from the floor after 5 and 30 minutes of operation.

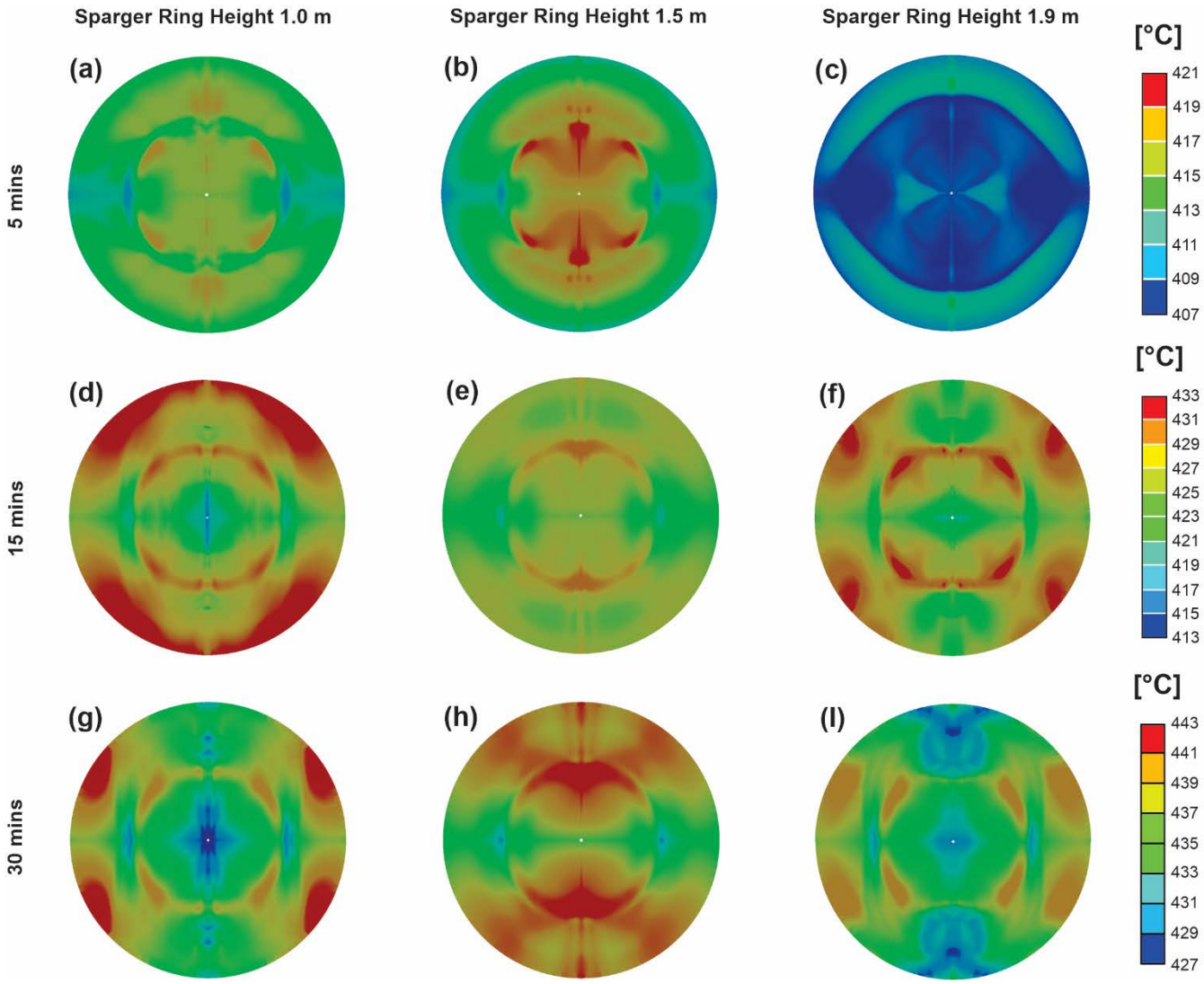

Figure 114. Temperature contours for the tank floor for different sparger ring heights at 5, 15, and 30 minutes of operation

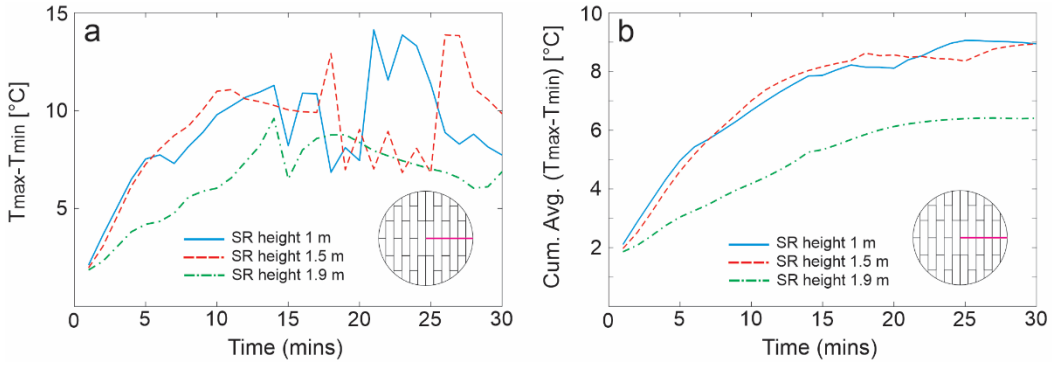

Figure 115. (a) Maximum temperature difference and (b) cumulative average of maximum temperature difference calculated on a radial line in the tank floor

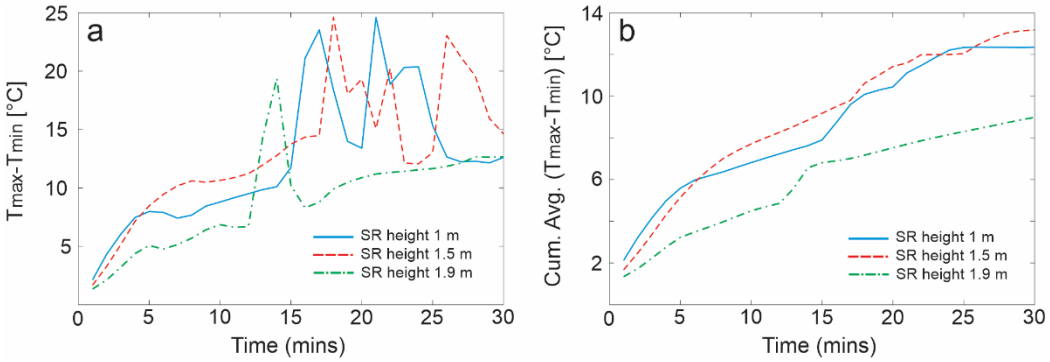

Figure 116. (a) Maximum temperature difference and (b) cumulative average of maximum temperature difference on the tank floor

The maximum temperature difference and the corresponding cumulative average for a radial line in the tank floor are presented in Figure 115a and Figure 115b, respectively. The line analyzed corresponded to a horizontal radius at 90° passing through nodes 1 through 6 in Figure 106. For the 30 minutes of operation, $T_{max} - T_{min}$ is lower during most of the time with a height of the sparger ring of 1.9 m; see Figure 115a. As can be observed in Figure 115b, $(T_{max} - T_{min})_{cm.,avg}$ is always lower for a sparger ring height of 1.9 m. Figure 116 presents the results of a similar analysis but considering the entire floor. Again, $T_{max} - T_{min}$ presents lower values for most of the operating range, having a peak value of about 19°C; see Figure 116a. From Figure 116b, $(T_{max} - T_{min})_{cm.,avg}$ is always lower for the sparger ring height of 1.9 m with values below 10°C for the 30 minutes of operation. The results obtained from this analysis suggest that the design of the sparger ring could be substantially improved to reduce temperature gradients, and consequently, stresses to enhance the tank reliability.

4.4 Lifetime Prediction

The lifetime prediction analysis for the tank is focused on low-cycle fatigue and creep failure mechanisms. The stress results obtained from the hot tank model for the four typical operating conditions (Figure 10) are used to estimate the tank's service life.

4.4.1 ASME Review Code

The lifetime calculations were based on the procedures outlined in the ASME BPVC: Section VIII, Division 2 and Section III, Division 5 and the API 579-1/ASME FFS (Fitness-For-Service [FFS])-1: Part 10 and Part 14 standards. None of the published ASME or API standards can be directly applied to the salt tank design due to the combination of high temperatures and cyclic operating conditions. There are design-by-analysis procedures in both the BPVC and FFS documentation that can be followed, but these procedures rely on an accurate estimation of stresses that the component will experience. BPVC Section VIII describes the procedure for estimating fatigue damage, while Section III discusses creep damage and combined creep-fatigue; both procedures are also described in detail in the FFS code, with additional details on estimating the lifetime of in-service components. In the salt tank, both failure mechanisms can be important due to the high temperature—for 347H creep is considered to occur for T > 485°C—and daily cyclic operation (charging and discharging).

Using the selected operational cycles, fatigue damage is calculated based on ASME BPVC Section VIII, Division 2, Part 5.5.5, Protection Against Failure from Cyclic Loading.[5] The main equations to evaluate the alternating stress to be considered are listed below:

$$\Delta S_{p,k} = \frac{1}{\sqrt{2}}\Big[\left(\Delta\sigma_{11,k} - \Delta\sigma_{22,k}\right)^2 + \left(\Delta\sigma_{11,k} - \Delta\sigma_{33,k}\right)^2 + \left(\Delta\sigma_{22,k} - \Delta\sigma_{33,k}\right)^2 + 6\left(\Delta{\sigma_{12,k}}^2 + \Delta{\sigma_{13,k}}^2 + \Delta{\sigma_{23,k}}^2\right)\Big]^{0.5} \quad (35)$$

$$S_{alt,k} = \frac{K_f K_{e,k} \Delta S_{p,k}}{2} \quad (36)$$

For each cyclical loading condition, k, the principal stresses are evaluated at the beginning and end of each cycle to calculate in Equation 35. The stress amplitude, $S_{alt,k}$, is then calculated using Equation 36, where K_f and $K_{e,k}$ are the fatigue strength reduction factor and the fatigue penalty factor, respectively. Once $S_{alt,k}$ for each load is known the number of cycles to failure, N_k, is calculated based on a correlation provided in the code, $N_k = f(S_{alt,k}, T_k)$, where T_k is the average temperature of each cycle. Then the total fatigue damage, D_f, can be calculated based on the estimated number of cycles for each loading condition, n_k, as follows:

$$D_f = \sum_k \frac{n_k}{N_k} \quad (37)$$

In the simplest case, failure is expected to occur when $D_f \geq 1$, although several different criteria exist. It is important to understand the impact of K_f and $K_{e,k}$. These factors account for imperfections due to manufacturing and the impact of welds on the lifetime; for instance, quality of welds. K_f is selected based on the level of examination done of the welds. A value for K_f of 1.2 represents a weld that can be observed (confirmed to not be misaligned) and subject to a volumetric non-destructive examination, such as X-ray analysis. For the tank floor, the root pass on the floor welds cannot be observed and it cannot be X-rayed. Because K_f and $K_{e,k}$ factors are direct multipliers on the value for $S_{alt,k}$, they have a large impact on the result. For instance, increasing K_f from 1.2 to 2.5 could increase the fatigue damage by an order of magnitude. The K_f value can vary from 1.2 to 4, while $K_{e,k}$ is calculated based on geometrical imperfections from manufacturing. $K_f \geq 2.5$ and $K_{e,k} = 1.35$ are likely reasonable values that were considered in the fatigue analysis of the tank floor. Considering the previously discussed challenges with the tank floor welds, the maximum value of $K_f = 4$ could be justified. If the modeling analysis captures the imperfections during welding fabrication, then the factors can generally be reduced to values of 1.0. Because the hot tank model incorporates residual stress and deformation of the floor after welding fabrication, it captures most of the nonideal conditions, then the factors will be set to a low value to account for other factors, such as plate misalignments.

In addition to fatigue, the hot tank operates at temperature ranges where creep is a consideration; however, creep is not explicitly considered in the ASME BPVC.VIII.2 code. To evaluate creep, the methodology published under the Welding Research Council Bulletin 541 was used. The methods

[5] "Design by Analysis Requirements," in BPVC.VIII.2 - Rules for Construction of Pressure Vessels, Alternative Rules. ASME, 2015.

described in Bulletin 541 optimize the Larson-Miller Parameter stress-rupture coefficients for use in the API 579-1/ASME FFS-1 standard.[6] The time to rupture, L [hours], is estimated as follows:

$$log_{10}[L] = \frac{LMP(\sigma)}{T} - C_{LMP} \tag{38}$$

Where LMP is the Larson-Miller Parameter corresponding to the applied stress, σ is the applied stress in MPa, T is the absolute temperature in K, and C_{LMP} is a constant for the material. The creep damage, D_c, is then calculated as the ratio of time spent at the applied stress and the time to rupture, which is calculated using Equation 38. Based on the simulation results, the welding procedure of the tank floor results in very high residual stresses which are only partially relaxed as the tank is filled with salt and conditioned to operating temperature. The initial state of the floor after welding fabrication significantly increases the mean stress during operation to levels where creep damage is significant.

To account for both creep and fatigue failure mechanisms, the damage attributed to each mechanism is calculated using the same methodologies previously described, and the total damage can be calculated as the sum of creep and fatigue components:

$$D_{tot} = D_c + D_f \tag{39}$$

The accumulation of fatigue damage reduces the ability of the material to withstand creep damage; then, the total damage that the material can tolerate before failure, D_{tot}, can be significantly less than 1, when both creep and fatigue are considered. Figure 117 presents the characteristic failure criteria line for 347H as a function of D_c and D_f. At the inflection point, failure is expected at approximately D_{tot} = 0.6.

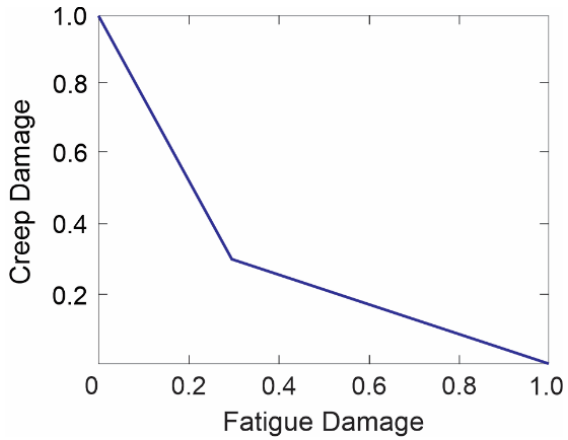

Figure 117. Failure criteria for combined creep-fatigue failures in 304 and 316 stainless steels[7]

4.4.2 Lifetime Calculations

The lifetime of the tank is estimated based on the modeling results for the four representative operating cases (see Figure 10) and the creep-fatigue analysis. Although each case is meant to represent a day of operation, the full 24-hour period is not modeled due to computational resources; therefore, for the

[6] API 579-1/ASME FFS-1 Fitness-For-Service. API Publishing Services, 2016.
[7] BPVC.III.1.NH - Rules for Construction of Nuclear Facility Components, Class 1 Components in Elevated Temperature Service. ASME, 2015.

purposes of this analysis, each stress profile is linearly interpolated to its starting point to complete the daily operating cycle. The four different cases represent different weather and operating conditions and are described in Table 26. The maximum compressive ΔT is comparable to the values measured for commercial projects.

Table 26. Description and Comparison of Typical Operating Cases

Case	Description	Min. T (°C)	Max. T (°C)	Max. Compressive ΔT (°C)
1	Clear sky day with ideal weather conditions, continuous steam generation	512.8	556.7	8.0
2	Fully cloudy day, minimal tank heating and steam generation in the afternoon	411.4	439.1	6.4
3	Intermittent cloudy day 1, tank is heated with cloud transients, steam generation in the afternoon	449.3	515.9	7.4
4	Intermittent cloudy day 2, tank is heated with cloud transients, continuous steam generation	507.8	536.4	12.5

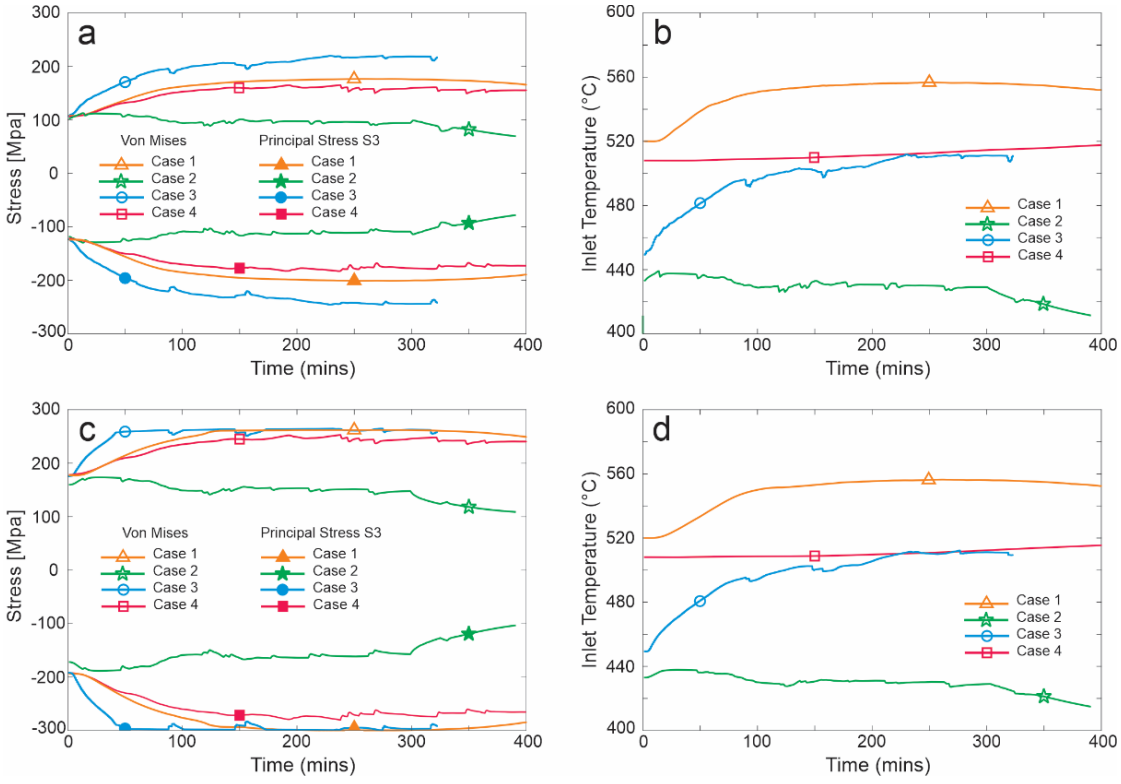

Figure 118. Von Mises stress and 3rd principal stress (S3), and temperature evolution of the tank floor; (a) and (b) r = 2.0 m, near the center; (c) and (d) r = 17.8 m, near the perimeter

The Von Mises stress and the 3rd principal stress (S3), as well as the temperature evolution of the tank floor temperature calculated for each case is presented in Figure 118. Two points are considered in this analysis: (1) a point located on the floor near the center (Figure 118a and 118b) and (2) a point near the tank perimeter (Figure 118c and 118d). Consistently higher stresses are predicted at the perimeter,

compared to the center, in all cases. As expected, for all cases, the 3rd principal stress (most negative value of the principal stresses) dominates the Von Mises stress value, indicating that compressive forces are dominant. The stress results are beyond the SS 347H YS limit for cases 1, 3, and 4. As a reference, the YS limit of SS 347H at 560°C is ~150 MPa. From Table 26, it is not surprising that case 2 has lower stresses, because this case has a lower average temperature, undergoes the smallest rise in temperature throughout the day, and is not subjected to a large ΔT. Case 4 undergoes a similar small temperature rise (< 30°C temperature increase), but more significant thermal gradients are present. Cases 1, 3, and 4 are subject to a combination of friction and thermal stresses due to the increase in average tank temperature and non-uniform temperature profiles; however, the conditions and results show enough variability that it is difficult to attribute the stresses to a specific mechanism.

Table 27. Fatigue Damage Calculated With K_f = 2 for Each Simulation Case at Several Different Radial Positions, From Point 1 Near the Floor Center to Point 8 Near the Floor Perimeter

Point	1	2	3	4	5	6	7	8
r (m)	**0.1**	**1.98**	**5.94**	**9.9**	**13.86**	**17.82**	**18.7**	**18.86**
Case 1	0.00%	0.00%	0.00%	0.00%	0.00%	0.52%	3.04%	1.91%
Case 2	0.00%	0.00%	0.00%	0.00%	0.00%	0.00%	0.01%	0.00%
Case 3	0.18%	0.17%	0.18%	0.14%	0.19%	0.00%	0.47%	0.75%
Case 4	0.00%	0.00%	0.00%	0.00%	0.00%	0.00%	0.84%	0.50%
Total D_f	0.18%	0.17%	0.18%	0.14%	0.19%	0.52%	4.36%	3.16%

Table 28. Time-to-Rupture in Years Calculated Using the Von Mises Stress Profiles for Each Simulation Case and Larson-Miller Parameters From the FFS-1 Standard

Point	1	2	3	4	5	6	7	8
r (m)	**0.1**	**1.98**	**5.94**	**9.9**	**13.86**	**17.82**	**18.7**	**18.86**
Case 1	13.08	13.29	12.91	11.69	11.31	0.67	0.86	0.89
Case 2	> 100	> 100	> 100	> 100	> 100	> 100	> 100	> 100
Case 3	56.53	57.25	56.67	101.14	47.99	9.90	9.93	9.93
Case 4	58.67	60.79	60.47	48.94	46.53	1.82	3.24	3.64
Combined	**28.83**	**29.38**	**28.76**	**27.46**	**24.42**	**1.45**	**2.01**	**2.12**

Fatigue damage is calculated using Equations 35 to 37 and assuming that each day of operation represents one fatigue cycle. The relative frequency (occurrence) of each case considered in the lifetime calculation was 29.7% for case 1, 0.8% for case 2, 29.7% for case 3, and 39.8% for case 4 based on analysis of solar irradiance data for one year near Las Vegas, NV [59,60]. It is assumed no damage accumulates during maintenance or commissioning procedures. The total fatigue damage and relative contribution from each case is tabulated in Table 27. For this analysis, a combined factor $K_f K_{e,k} = 2$ is selected to account for deviations in welding and geometrical imperfections in the floor such as plate misalignments. While much higher values of K_f may be appropriated, a relatively low value is selected for this analysis since the initial floor condition accounts for the residual stresses and deformations during welding. The calculation is performed for different locations—along a radial line at an angle of 90°, see Figure 106—starting near the center of the floor and moving out towards the perimeter of the

tank. It is worth noting that all the sampled points are located on thin floor plates, not in the outer perimeter ring. The fatigue damage is negligible for all points near the center and increases near the perimeter, reaching a maximum at r = 18.7 m (taper to annular plates begins at r = 18.8 m); in the annular floor plates, the fatigue damage drops compared to the outer perimeter of the thin rectangular floor plates (see points 7 and 8).

Creep damage was calculated on a minute-by-minute basis using the Von Mises stress as input to Equation 38, and temperature data from the simulations. Like fatigue, the creep damage is calculated at several different radial locations. The expected time (in years) to rupture for each location is listed in Table 28. While creep is an important consideration in cases 1, 3, and 4, it is negligible in case 2 due to the lower tank temperature throughout the day. Considering the combined case load percentages, failure is predicted within 3 years near the perimeter of the tank.

5 Final Remarks

5.1 Conclusions and Lessons Learned

The behavior of commercial-scale molten salt TES tanks for central receiver CSP plants was modeled and analyzed. A physics-based model was formulated and implemented in a multiphysics simulation environment considering a representative design of commercial hot molten salt TES tanks. The model considered a shell element approach where the stress and strain in the floor are calculated in the floor plane, but not in the vertical direction. This condition implied that the deformation of the floor does not vary in the vertical direction with time, which limits the current model to predict other failure mechanisms such as buckling. The model was validated using historic operational data of CSP plants and was utilized to evaluate temperature and stress distributions as a function of typical operating conditions, analyze the impact of key operating parameters, estimate lifetime, and conduct a preliminary assessment on potential design alternatives to reduce temperature gradients and stresses to increase the tank's reliability. The main conclusions and lessons learned from this work are summarized as follows:

- Based on the tank design information received from multiple CSP plants, it was clearly appreciated that despite some common features—mainly attributed to the guidelines followed from API 650 and ASME BPVC Section II—important design differences, mainly in the sparger ring and internal piping system and the foundation, exist among tanks, which demonstrates the need for a technical standard dedicated to molten salt TES tanks for high temperature and cycling operation.

- Failures in hot tanks can be attributed to multiple mechanisms, including low-cycle fatigue, stress relaxation cracking, excessive deformation (buckling), and creep. Multiple factors related to the design of the tank and its foundation, material characteristics, fabrication, commissioning, and challenging operating conditions play an important role in how these mechanisms evolve. This report was focused on estimating life expectancy through fatigue and creep mechanism. Based on the analysis, creep is expected to be a more dominant failure mechanism than low-cycle fatigue for typical plant operating conditions; the analysis on the combined effect of creep and fatigue predicts tank floor failure in less than 3 years of operation. This lifetime prediction agrees with the time of failures presented in several commercial tanks. Based on the high stress levels close to 260 MPa, a failure is expected in the thin section of the floor near the perimeter. Regions of maximum stress in the floor vary during operation and as a function of the initial residual stress and deformation, which implies that failures could potentially occur in other locations.

- The residual stresses and distortion of the tank floor after welding fabrication exert a strong impact on the stress levels developed during operation. Peak residual stresses of up to 596 MPa and deformation of about 130 mm were induced by welding during fabrication. The modeling results showed good agreement with strain measurements obtained from neutron diffraction for SS 347H weldments and distortions observed in the floor of commercial tanks, which provides validation for the models. The challenges with welding SS 347H in the field call into question the material selection for the tanks, suggesting that further R&D is required to identify the best option. It is worth noting that operational stress levels are much lower than residual stresses. The partial relaxation of residual stresses during operation (values under 260 MPa) could be related

to the mechanical pressure exerted on the floor by the salt during tank filling, but further investigation is required to confirm the mechanism behind the stress relaxation.

- Sand is commonly used as a solid lubricant between the floor and foundation to maintain friction coefficients between 0.4 and 0.6.; however, higher or lower friction coefficients are possible at different locations due to the use of backing plates and the initial floor deformation after welding fabrication. Non-uniform friction coefficient will lead to non-uniform friction forces that could have a negative impact on the floor integrity. The effect of backing plates on the friction coefficient and the stress distribution in the floor requires further investigation. The simulations considered a relatively low friction coefficient of 0.5 (other studies have considered friction coefficients of up to 0.8 [20]), which seems to be representative for commercial tanks. However, uncertainty about the friction coefficient exists and a methodology to reliably reduce the friction coefficient from the value considered in the model is not clear. Thus, reducing the friction coefficient is not considered a viable option without a significant R&D effort.

- Regarding operation, the maximum temperature difference of around 70°C was observed in the tank floor for inventory levels of 1 m, $T_{inv.}$= 400°C, T_{in}= 560°C, $\dot{m}_{in} = 1200$ kg/s, and $\dot{m}_{out} = 0$. Large temperature differences lead to high stresses in the tank floor that easily surpass the YS limit of SS 347H. A low temperature difference was observed for inventory levels of 2.33 m and 3.66 m, which implies that the tank operation could be safer at higher inventory levels. The most challenging operating conditions are related to low inventory levels—for example, during startup—and transient events implying large differences between the inventory and inflow temperatures. There is a relatively low temperature difference in the tank floor, considering the four typical operating cases ($\Delta T < 15$°C, Table 26); however a further reduction in thermal gradients could have some impact on the stresses in the floor. Comparing cases 2 and 4, the tank undergoes a similar increase in temperature but the stresses in case 4 are much higher. Case 4 is at a higher absolute temperature and has a larger ΔT compared to case 2, suggesting that relatively small changes in ΔT could have an impact.

- The effect of the floor thickness and the sparger ring height on the stresses and temperature distribution in the tank were analyzed. Large, localized stresses in the tank can be substantially reduced by increasing the floor thickness. For case 2, maximum stresses are reduced from ~180 MPa to ~150 MPa by increasing the floor thickness from 6.7 mm to 20 mm. However, further analysis must be done on thicker floors as other technical challenges might arise. For instance, thicker floors could develop higher residual stresses during fabrication. In turn, having a sparger ring located at 1.9 m above the floor will help to reduce the maximum temperature differences in the tank floor by several degrees Celsius. The proper location of the sparger ring could be even higher to reduce temperature differences in the tank floor, depending on the inlet mass flow rate and the inflow temperature.

- Regarding the buckling phenomena observed in several commercial tanks, it is believed that specific damaging events such as excessive thermal gradients are required to initiate the buckling phenomena; once initiated, the buckles get progressively worse during normal operating conditions. Furthermore, it is possible that buckle formation occurs during commissioning, when the thermal gradients can be high and the hydrostatic pressure of the salt weight (pushing the floor to the foundation) is absent. The typical operational data used to set the four analyzed cases

were selected by considering the most commonly occurring cases during multiple months of operation, but the tank commissioning was not simulated. While the selected cases are the best representation of the daily conditions experienced by the tank, they do not necessarily capture the worst-case conditions and may not be sufficient to cause buckling.

- Commissioning includes pre-heating of the tank followed by the initial filling with salt. Pre-heating is generally accomplished using a propane fired air heater and a specialized nozzle installed on the roof at a single location with another single port on the roof for the gases to leave. Pre-heating was not considered in this study; however, after reviewing data from commercial projects, the pre-heating was identified as a potentially damaging process. The tank is usually empty during the pre-heating process, which means that there are no hydrostatic forces pressing the floor into the foundation to stabilize the floor against compressive stresses and potential plastic deformations (i.e., buckling).

5.2 Design and Operation Recommendations

Solving failures in molten salt TES tanks is a priority for the future of the CSP technology. Current failures in molten nitrate hot tanks can be explained as a combination of multiple mechanisms and factors from the design conception through the execution and operation. A schematic diagram establishing the relationship between failure behaviors and the influencing factors related to the tank design, fabrication, commissioning, and operation is presented in Figure 4. A definitive solution to tank failures must consider addressing all these factors. Based on a better understanding of the root cause of tank failures and the findings presented in this report and in other related projects, the authors propose the following recommendations that will pave the path to advance towards a definitive solution:

- *Safe operation protocols:* Tank operation should not only be driven by power generation maximization, but by the conditions that allow a safe operation under low stresses to avoid the detriment of the tank's integrity. A minimum inventory level should be established to guarantee low temperature gradients. This minimum inventory level should be defined for each tank based on design characteristics and expected transient events (due to the presence of clouds) at each location. Minimum tank levels, as a function of inlet flow temperature, could assure that the floor will not experience temperature gradients larger than a pre-determined and safe designed value. For the representative tank design analyzed, "safe" temperature differences in the tank floor are obtained for a minimum inventory level of about 2 m. Another alternative to temperature gradients is through better control of the incoming salt temperatures. Since ΔT is a fundamental feature in a commercial tank, the distributed control system could be programmed and implemented in current operating projects to control incoming salt temperatures and flow rates based on the inventory level to mitigate large temperature gradients in the floor.

- *Sparger ring design enhancement:* Large radial and circumferential temperature gradients in the tank floor have been estimated, which demonstrate the lack of mixing between the salt inventory and salt inflow. Large floor temperature gradients have been determined as one of the main factors contributing to floor buckling. Sparger rings are usually located relatively close to the tank floor, usually around 1 m above. Based on the analysis presented in this report, increasing the height of this component will lead to a reduction in the maximum temperature differences in the floor (see Section 4.3.4 Sparger Ring Position). However, besides the higher location for the sparger ring, other design characteristics should be improved to create better mixing.

- *Improving welding procedures:* It was demonstrated that the tank floor welding fabrication results in high residual stresses and deformations. This initial condition of the floor has a strong influence on the stresses developed in the tank during operation. Higher residual stresses favor stress relaxation cracking in SS 347H weldments during cycling operation. The selection of welding parameters (heat input, welding speed, number of passes, welding path, and so on) should be focused on producing a floor with low residual stresses and distortions. Most welds during the tank fabrication are made using the SS 347H matching filler E347. An interesting alternative that has been preliminarily evaluated by the team is the use of new welding filler materials like E16.8.1, which could lead to a significant reduction in residual stress in the tank floor and shell after welding fabrication.

- *Post-weld heat treatment:* Preliminary analyses and simulations conducted by our team have shown that the high residual stresses and distortion could be substantially reduced through proper welding fabrication procedures and conducting well-designed PWHT. It is worth noting that PWHT to reduce residual stresses is not mandatory under API 650 or ASME BPVC. Several challenges remain for an effective PWHT implementation in the field, especially for large hot tanks (diameter >30 m). One alternative that could be further evaluated in this case is lifted floor fabrication, which should have some interesting advantages including enabling the implementation of PWHT, allows welding from both sides of the plates without using backing plates (or simplifies backing plate removal), and facilitates weld quality inspection. Further investigation is required to advance the development of a standardized PWHT procedure.

- *Floor design improvements:* New design and fabrication alternatives for the tank floor deserve special consideration and efforts to reduce its susceptibility to failure. Increasing the thickness is one of the recommended design changes that will reduce stress during operation. Based on the results, a thickness between 20 mm and 30 mm seems to be appropriate for the representative tank design under the analyzed typical operating conditions. It is important to highlight that a further analysis should be conducted to determine the proper thickness. Floor plates with high thickness not only imply higher materials and fabrication costs, but also, might introduce higher residual stresses from welding and crack directly prior to plastic deformation. Rather than increasing the whole floor thickness, another alternative will be reinforcing the locations where higher stresses are developed. For the analyzed cases, the recommendation is reinforcing the perimeter ring by increasing the radial spread of the perimeter ring or adding annular plate sections. In current tank designs, the perimeter ring generally sits under the tank wall and extends <1 m into the wetted tank volume. Extending the perimeter ring closer to the tank center and/or increasing the thickness could reinforce the areas of the tank subjected to creep failure. The use of additional annular plate sections could allow a smoother transition between the reinforced perimeter and thin floor plates.

Most of the recommendations presented in this report point toward reducing thermal stresses during operation. A definitive solution to tank failures must consider adopting new floor and sparger ring designs, and addressing multiple issues during tank fabrication, implementation, and operation. A summary of the potential alternatives to solve the tank reliability issues is schematically presented in Figure 119.

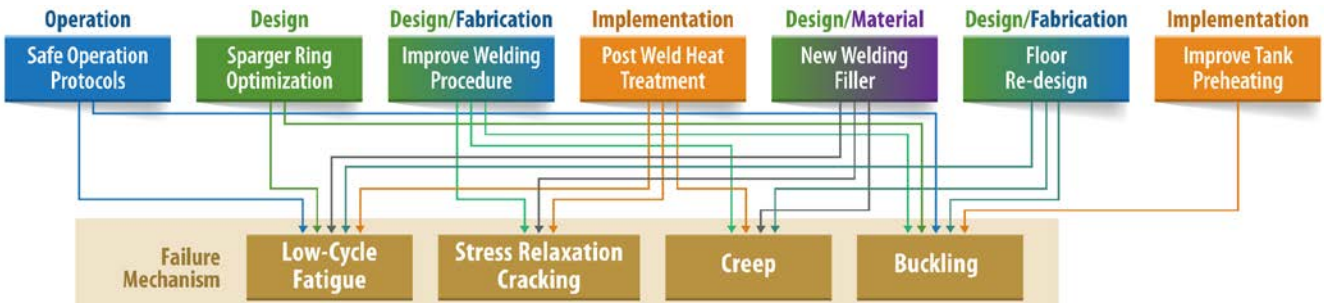

Figure 119. Potential alternatives to address molten salt TES tank failures

5.3 Recommendations for Future Work

From the work conducted under this and other related projects, the following research areas has been identified as critical to advance toward a more reliable molten salt TES technology:

- *Failure mechanisms analysis*: This project was mainly focused on creep and fatigue. Future studies should conduct research aimed at addressing buckling and SRC. In particular, the effect of the friction coefficient, temperature gradients, and floor slope on the buckling formation should be further investigated. Similarly, welding groove geometries and new welding fillers should be analyzed to reduce SRC susceptibility.

- *New floor design and fabrication*: New floor designs, including non-flat floors, floors using different plate layout geometries, and different welding fabrication procedures are fundamental to reduce residual stress and distortion in the tank floor.

- *New materials*: SS 347H has been considered the state-of-the art for molten nitrate salt hot tanks for central receiver CSP plants. However, several limitations, including its susceptibility to SRC and potential for hot reheat cracking during repairs, need to be reduced or suppressed. Other alternative alloys and welding fillers should be also explored to determine if they can perform better than SS 347H while still being cost-effective. To the author's knowledge, developers of new CSP projects are considering alternative materials for the new molten salt hot tanks.

- *Post-weld heat treatment*: Reducing residual stresses after fabrication is fundamental to improve tank's lifetime. Additional research should be done to advance the development of a standardized PWHT procedure that effectively reduces stresses, while avoiding excessive deformation, cracking, or affecting the tank's foundation.

- *Tank pre-heating*: Thermal gradients during pre-heating are likely to vary significantly for each tank with different procedures and tank sizes. Additional research should be conducted on tank pre-heating to understand the initial condition of the tank after construction and commissioning and to evaluate different pre-heating strategies to reduce the damage potential This is a critical step to improve the accuracy in the tank lifetime estimation.

- *Critical tank design and operation parameters:* Future research should be focused on establishing optimum design features and operation conditions that improve the tank's reliability (by reducing stress during operation) while being suitable for implementation and cost-effective.

Design features include floor thickness and diameter (tank size). Operation conditions include minimum inventory levels as a function of inflow temperatures.

- *Sparger ring optimization*: New studies on the design optimization of this component or using multiple sparger rings are fundamental to achieve a better mixing between the salt inflow and the inventory that avoids damaging temperature gradients in the tank floor.

- *Evaluation facilities*: Efforts to develop and deploy laboratory-scale facilities, capable of replicating typical tank operation conditions, are fundamental to experimentally demonstrate the value and feasibility of new materials, floor and sparger ring designs, operation strategies, fabrication, and commission procedures to enhance the tank's reliability.

- *Technical standard development:* A close collaboration between research institutions, industry, and universities is fundamental to share and gather information and conduct additional research focused on the development of a technical standard for the design and fabrication of molten salt TES tanks for high temperature (up to 565°C) and thermal cycling operation.

References

[1] M. Mehos *et al.*, "Concentrating Solar Power Best Practices Study," Golden, CO (United States), Jun. 2020. doi: 10.2172/1665767.

[2] J. D. Osorio, "Modeling of Stress Distribution in Molten Salt Thermal Energy Storage Tanks for In-Service Central Receiver Power Plants," in *5th Thermal-Mechanical-Chemical Energy Storage Workshop*, San Antonio, TX: NREL/PR-5700-87158, Aug. 2023.

[3] Y. HONG, T. PICKLE, Z. YU, J. VIDAL, and C. AUGUSTINE, "Impact of Plate Thickness and Joint Geometry on Residual Stresses in 347H Stainless Steel Welds," *Weld J*, vol. 102, no. 11, pp. 279–292, Nov. 2023, doi: 10.29391/2023.102.021.

[4] "Welded Tanks for Oil Storage - API Standard 650," Washington, DC 20005, Mar. 2013.

[5] "2019 Boiler and Pressure Vessel Code," in *Section II: Materials*, New York, NY 10016: American Society of Mechanical Engineers (ASME), 2019.

[6] "2019 Boiler and Pressure Vessel Code," in *Section VIII: Rules for Construction of Pressure Vessels*, New York, NY 10016: American Society of Mechanical Engineers (ASME), 2019.

[7] M. Stewart, *Surface Production Operations: Volume 5: Pressure Vessels, Heat Exchangers, and Aboveground Storage Tanks: Design, Construction, Inspection, and Testing*, 1st ed. Cambridge, MA, 02139: Gulf Professional Publishing, 2021.

[8] B. Kelly and D. Kearney, "Thermal Storage Commercial Plant Design Study for a 2-Tank Indirect Molten Salt System: Final Report, 13 May 2002 - 31 December 2004," Golden, CO, Jul. 2006. doi: 10.2172/887348.

[9] S. Torras, C. D. Pérez-Segarra, I. Rodríguez, J. Rigola, and A. Oliva, "Parametric Study of Two-tank TES Systems for CSP Plants," *Energy Procedia*, vol. 69, pp. 1049–1058, May 2015, doi: 10.1016/J.EGYPRO.2015.03.206.

[10] E. Rivas, E. Rojas, R. Bayón, W. Gaggioli, L. Rinaldi, and F. Fabrizi, "CFD Model of a Molten Salt Tank with Integrated Steam Generator," *Energy Procedia*, vol. 49, pp. 956–964, Jan. 2014, doi: 10.1016/J.EGYPRO.2014.03.103.

[11] I. Rodríguez, C. D. Pérez-Segarra, O. Lehmkuhl, and A. Oliva, "Modular object-oriented methodology for the resolution of molten salt storage tanks for CSP plants," *Appl Energy*, vol. 109, 2013, doi: 10.1016/j.apenergy.2012.11.008.

[12] C. Suárez, A. Iranzo, F. J. Pino, and J. Guerra, "Transient analysis of the cooling process of molten salt thermal storage tanks due to standby heat loss," *Appl Energy*, vol. 142, pp. 56–65, Mar. 2015, doi: 10.1016/J.APENERGY.2014.12.082.

[13] R. Gabbrielli and C. Zamparelli, "Optimal Design of a Molten Salt Thermal Storage Tank for Parabolic Trough Solar Power Plants," *J Sol Energy Eng*, vol. 131, no. 4, Sep. 2009, doi: 10.1115/1.3197585.

[14] B.-C. Du, Y.-F. Guo, C. Xu, L.-J. Huang, X.-F. Li, and Y.-G. Lei, "Dynamic creep and stress performances of the packed-bed thermal energy storage tank with molten salt EPCM particles," *Appl Therm Eng*, vol. 225, p. 120247, May 2023, doi: 10.1016/j.applthermaleng.2023.120247.

[15] F. Zaversky, J. García-Barberena, M. Sánchez, and D. Astrain, "Transient molten salt two-tank thermal storage modeling for CSP performance simulations," *Solar Energy*, vol. 93, pp. 294–311, Jul. 2013, doi: 10.1016/j.solener.2013.02.034.

[16] Z. Wan, J. Wei, M. A. Qaisrani, J. Fang, and N. Tu, "Evaluation on thermal and mechanical performance of the hot tank in the two-tank molten salt heat storage system," *Appl Therm Eng*, vol. 167, p. 114775, Feb. 2020, doi: 10.1016/j.applthermaleng.2019.114775.
[17] I. González, O. Lehmkuhl, C. D. Pérez-Segarra, and A. Oliva, "Dynamic Thermoelastic Analysis of Thermocline-like Storage Tanks," *Energy Procedia*, vol. 69, pp. 850–859, May 2015, doi: 10.1016/J.EGYPRO.2015.03.106.
[18] S. H. Gage *et al.*, "Technical and economic feasibility of molten chloride salt thermal energy storage systems," *Solar Energy Materials and Solar Cells*, vol. 226, p. 111099, Jul. 2021, doi: 10.1016/J.SOLMAT.2021.111099.
[19] Z. Wan, J. Wei, M. A. Qaisrani, J. Fang, and N. Tu, "Evaluation on thermal and mechanical performance of the hot tank in the two-tank molten salt heat storage system," *Appl Therm Eng*, vol. 167, p. 114775, Feb. 2020, doi: 10.1016/j.applthermaleng.2019.114775.
[20] K. Drewes *et al.*, "High Temperature Salt Tank Buckling Failure," in *SolarPACES*, Albuquerque, NM, Sep. 2022.
[21] A. B. ZAVOICO, "Solar Power Tower Design Basis Document, Revision 0," Albuquerque, NM, and Livermore, CA, Jul. 2001. doi: 10.2172/786629.
[22] R. BRADSHAW *et al.*, "Final Test and Evaluation Results from the Solar Two Project," Albuquerque, NM, and Livermore, CA (United States), Jan. 2002. doi: 10.2172/793226.
[23] G. Peiró, C. Prieto, J. Gasia, A. Jové, L. Miró, and L. F. Cabeza, "Two-tank molten salts thermal energy storage system for solar power plants at pilot plant scale: Lessons learnt and recommendations for its design, start-up and operation," *Renew Energy*, vol. 121, pp. 236–248, Jun. 2018, doi: 10.1016/J.RENENE.2018.01.026.
[24] T. Pickle, Y. Hong, J. Vidal, C. Augustine, and Z. Yu, "Stress relaxation cracking susceptibility evaluation in 347H stainless steel welds," *Welding in the World*, Jan. 2024, doi: 10.1007/s40194-024-01678-9.
[25] J. C. Lippold and D. J. Kotecki, *Welding Metallurgy and Weldability of Stainless Steels*. Hoboken, NJ: Wiley & Sons, 2005.
[26] T. M. Cullen and J. W. Freeman, "Metallurgical Factors Influencing Hot Ductility of Austenitic Steel Piping at Weld Heat-Affected Zone Temperatures," *Journal of Engineering for Power*, vol. 85, no. 2, pp. 151–164, Apr. 1963, doi: 10.1115/1.3675237.
[27] R. Kant and J. DuPont, "Stress Relief Cracking Susceptibility in High-Temperature Alloys," *Weld J*, vol. 98, no. 2, pp. 29–49, Feb. 2019, doi: 10.29391/2019.98.003.
[28] A. Dhooge, "Survey on reheat cracking in austenitic stainless steels and Ni base alloys," *Welding in the World*, vol. 41, pp. 206–219, 1988.
[29] A. Dhooge and A. Vinckier, "Reheat cracking—A review of recent studies," *International Journal of Pressure Vessels and Piping*, vol. 27, no. 4, pp. 239–269, Jan. 1987, doi: 10.1016/0308-0161(87)90012-3.
[30] C. Lundin, W. Delong, and D. Spond, "Ferrite-fissuring relationship in austenitic stainless steel weld metals," *Weld J*, pp. 241–246, 1975.
[31] J. Irvine, D. Murray, and F. Pickering, "The Effect of Heat Treatment and Microstructure on the High-Temperature Ductility of 18%Cr-12%Ni-1%Nb Steels," *Journal of Iron and Steel Institute*, pp. 166–179, 1960.
[32] R. Thomas, "HAZ Cracking in Thick Section of Austenitic Stainless Steels-Part 2," *Weld J*, pp. 355–368, 1984.

[33] R. Thomas and R. Messler, “Welding type 347 stainless steel -- An interpretive report,” *Bulletin - Welding Research Council*, no. 421, 1997.
[34] H. Price, “Dispatchable Solar Power Plant Project,” Golden, CO (United States), Jan. 2018. doi: 10.2172/1418902.
[35] National Renewable Energy Laboratory (NREL), “System Advisor Model (SAM).” https://sam.nrel.gov/.
[36] National Renewable Energy Laboratory (NREL), “National Solar Radiation Database (NSRDB),” https://nsrdb.nrel.gov/.
[37] J. R. Fanchi, “Reservoir Simulation,” in *Integrated Reservoir Asset Management*, Elsevier, 2010, pp. 223–241. doi: 10.1016/B978-0-12-382088-4.00013-X.
[38] S. Flueckiger, Z. Yang, and S. V. Garimella, “An integrated thermal and mechanical investigation of molten-salt thermocline energy storage,” *Appl Energy*, vol. 88, no. 6, pp. 2098–2105, Jun. 2011, doi: 10.1016/j.apenergy.2010.12.031.
[39] C. Zhang, Y. Lu, S. Shi, and Y. Wu, “Comparative research of heat discharging characteristic of single tank molten salt thermal energy storage system,” *International Journal of Thermal Sciences*, vol. 161, p. 106704, Mar. 2021, doi: 10.1016/j.ijthermalsci.2020.106704.
[40] F. Opoku, M. N. Uddin, and M. Atkinson, “A review of computational methods for studying oscillating water columns – the Navier-Stokes based equation approach,” *Renewable and Sustainable Energy Reviews*, vol. 174, p. 113124, Mar. 2023, doi: 10.1016/j.rser.2022.113124.
[41] S. M. Hosseinnia, H. Akbari, and M. Sorin, “Numerical analysis of thermocline evolution during charging phase in a stratified thermal energy storage tank,” *J Energy Storage*, vol. 40, p. 102682, Aug. 2021, doi: 10.1016/j.est.2021.102682.
[42] R. Ferri, A. Cammi, and D. Mazzei, “Molten salt mixture properties in RELAP5 code for thermodynamic solar applications,” *International Journal of Thermal Sciences*, vol. 47, no. 12, pp. 1676–1687, Dec. 2008, doi: 10.1016/j.ijthermalsci.2008.01.007.
[43] W. M. Rohsenow, J. P. Hartnett, and Y. I. Cho, *Handbook of Heat Transfer*, Third Edition. Ney York, NY 10011: McGraw-Hill, 1998.
[44] British Gas, “Flow of Fluids,” in *Combustion Engineering and Gas Utilisation*, Routledge, 2014, pp. 127–166. doi: 10.4324/9781315024714-11.
[45] S. M. Yang and W. Q. Tao, *Heat Transfer*, 4th Edition. Beijing: Higher Education Press, 1991.
[46] M. Arsenovic, Z. Lalic, and Z. Radojevic, “Clay brick walls thermal properties,” *International Journal of Modern Manufacturing Technologies*, vol. 2, no. 1, pp. 15–18, 2010.
[47] T. Nikiforova, M. Savytskyi, K. Limam, W. Bosschaerts, and R. Belarbi, “Methods and Results of Experimental Researches of Thermal Conductivity of Soils,” *Energy Procedia*, vol. 42, pp. 775–783, 2013, doi: 10.1016/j.egypro.2013.12.034.
[48] W. Kim, K. S. Kim, H. Lee, and K. Yoo, “Welding residual stress analysis of 347H austenitic stainless steel boiler tubes using experimental and numerical approaches,” *Journal of Mechanical Science and Technology*, vol. 30, no. 4, pp. 1773–1779, Apr. 2016, doi: 10.1007/s12206-016-0333-0.
[49] S. Riahi, M. Evans, M. Belusko, R. Flewell-Smith, R. Jacob, and F. Bruno, “Transient Thermo-mechanical analysis of a shell and tube latent heat thermal energy storage for

CSP plants," *Appl Therm Eng*, vol. 196, p. 117327, Sep. 2021, doi: 10.1016/j.applthermaleng.2021.117327.
[50] Z. K. Jahanger, S. J. Antony, and A. Hirani, "Foundation relative stiffness effects in sand under static loading," 2020, p. 020002. doi: 10.1063/5.0000110.
[51] X. Chen and Y. Liu, *Finite Element Modeling and Simulation with ANSYS Workbench*. CRC Press, 2014. doi: 10.1201/b17284.
[52] S. Bektas and Y. Sisman, "The comparison of L1 and L2-norm minimization methods," *International Journal of the Physical Sciences*, vol. 5, no. 11, pp. 1721–1727, 2010.
[53] T. Jiang, Z. Liu, G. Wang, and Z. Chen, "Comparative study of thermally stratified tank using different heat transfer materials for concentrated solar power plant," *Energy Reports*, vol. 7, pp. 3678–3687, Nov. 2021, doi: 10.1016/J.EGYR.2021.06.021.
[54] B. Brickstad and B. L. Josefson, "A parametric study of residual stresses in multi-pass butt-welded stainless steel pipes," *International Journal of Pressure Vessels and Piping*, vol. 75, no. 1, pp. 11–25, Jan. 1998, doi: 10.1016/S0308-0161(97)00117-8.
[55] T. J. Pickle, "Effect of PWHT and Filler Metal on Stress Relaxation Cracking Susceptibility in 347H Stainless Steel Welds for Elevated Temperature Service," Colorado School of Mines, Golden, CO, 2021.
[56] K. Sawada *et al.*, "Catalog of NIMS creep data sheets," *Sci Technol Adv Mater*, vol. 20, no. 1, pp. 1131–1149, Dec. 2019, doi: 10.1080/14686996.2019.1697616.
[57] J. Goldak, A. Chakravarti, and M. Bibby, "A new finite element model for welding heat sources," *Metallurgical Transactions B*, vol. 15, no. 2, pp. 299–305, 1984.
[58] M. Bjelic, B. Radicevic, K. Kovanda, L. Kolařík, and A. Petrovic, "Multi-objective calibration of the double-ellipsoid heat source model for GMAW process simulation," *Thermal Science*, vol. 26, no. 3 Part A, pp. 2081–2092, 2022, doi: 10.2298/TSCI210131181B.
[59] J. D. Osorio, R. Hovsapian, and J. C. Ordonez, "Dynamic analysis of concentrated solar supercritical CO2-based power generation closed-loop cycle," *Appl Therm Eng*, vol. 93, pp. 920–934, Jan. 2016, doi: 10.1016/j.applthermaleng.2015.10.039.
[60] J. D. Osorio, R. Hovsapian, and J. C. Ordonez, "Effect of multi-tank thermal energy storage, recuperator effectiveness, and solar receiver conductance on the performance of a concentrated solar supercritical CO2-based power plant operating under different seasonal conditions," *Energy*, vol. 115, pp. 353–368, Nov. 2016, doi: 10.1016/j.energy.2016.08.074.

Appendix A. Questionnaire

Table A-1. Questionnaire for Hot Molten Salt Storage Tank Design

	RANGE OF VALUES					NOTES
Tank Shell						
Interior Diameter	< 32 m ☐	32 - 38 m ☐	38.1 - 44 m ☐	44.1 - 50 m ☐	> 50 m ☐	
Minimum floor thickness	< 5 mm ☐	5 - 8 mm ☐	8.1 - 11 mm ☐	11.1 - 14 mm ☐	> 14 mm ☐	
Maximum wall thickness	< 30 mm ☐	30 - 40 mm ☐	40.1 - 50 mm ☐	50.1 - 60 mm ☐	> 60 mm ☐	
Wall height	< 8 mm ☐	8 - 10 m ☐	10.1 - 12 m ☐	12.1 - 14 m ☐	> 14 m ☐	
Floor slope	< 0.8% ☐	0.8 - 1.2% ☐	1.21 - 1.6% ☐	1.61 - 2% ☐	> 2% ☐	
Shell material	SS 347H ☐	SS 316H ☐	SS 304H ☐	Other ☐		
Roof type	Column-supported ☐	Self-supported ☐	Floating ☐	Other ☐		
Anchor bolt spacing	0.1 - 1.0 m ☐	1.01 - 2.0 m ☐	2.01 - 3.0 m ☐	No anchor bolts ☐		
Inlet Distribution Piping						
Diameter of distribution ring, % of Tank Shell - Interior Diameter	< 40 % ☐	40 - 50% ☐	50.1 - 60% ☐	60.1 - 70% ☐	> 70% ☐	
Height from tank floor	< 0.2 m ☐	0.2 - 0.7 m ☐	0.7 - 1.2 m ☐	1.2 - 1.7 m ☐	> 1.7 m ☐	
Number of inlet jets	< 4 ☐	4 - 20. ☐	21 - 40 ☐	41 - 70 ☐	> 70 ☐	
Angle of injection (0° vertical up, 90° horizontal towards shell)	270.1° - 359.9° ☐	0° - 60° ☐	60.1° - 120° ☐	120.1° - 180° ☐	180.1° - 270° ☐	
Use of eductors / static mixers?	Yes ☐	No ☐				
Tank Foundation						
Material composition at perimeter	Refractory ☐	Expanded Clay ☐	Metal slip-plates ☐	Other ☐		
Material composition at center	FoamGlas ☐	Expanded Clay ☐	Other ☐			
Solid lubricant under tank	No lubricant ☐	Sand ☐	Other ☐			
Operating Conditions						
Maximum salt inventory level (Operation)	< 8 m ☐	8 - 10 m ☐	10.1 - 12 m ☐	12.1 - 14 m ☐	> 14 m ☐	
Minimum salt inventory level	< 0.5 m ☐	0.5 - 0.8 m ☐	0.81 - 1.2 m ☐	1.21 - 1.5 m ☐	> 1.5 m ☐	
Salt inventory temperature at beginning of start-up	< 500°C ☐	500 - 525°C ☐	525.1 - 545°C ☐	545.1 - 565°C ☐	> 565°C ☐	
Incoming salt temperature when switching from cold to hot tank	< 520°C ☐	520 - 535°C ☐	535.1 - 550°C ☐	550.1 - 565°C ☐	> 565°C ☐	
Incoming salt temperature rate of change	< 1°C/min ☐	1 - 4°C/min ☐	4.1 - 7°C/min ☐	7.1 - 10°C/min ☐	> 10°C/min ☐	
Receiver flow turn-down ratio	< 3:1 ☐	3:1 - 4:1 ☐	4:1 - 6:1 ☐	6:1 - 8:1 ☐	> 8:1 ☐	
Switching valve type	Butterfly, pneumatic ☐	Butterfly, electric ☐	Globe, pneumatic ☐	Globe, electric ☐	Other ☐	

Appendix B. Design Drawings

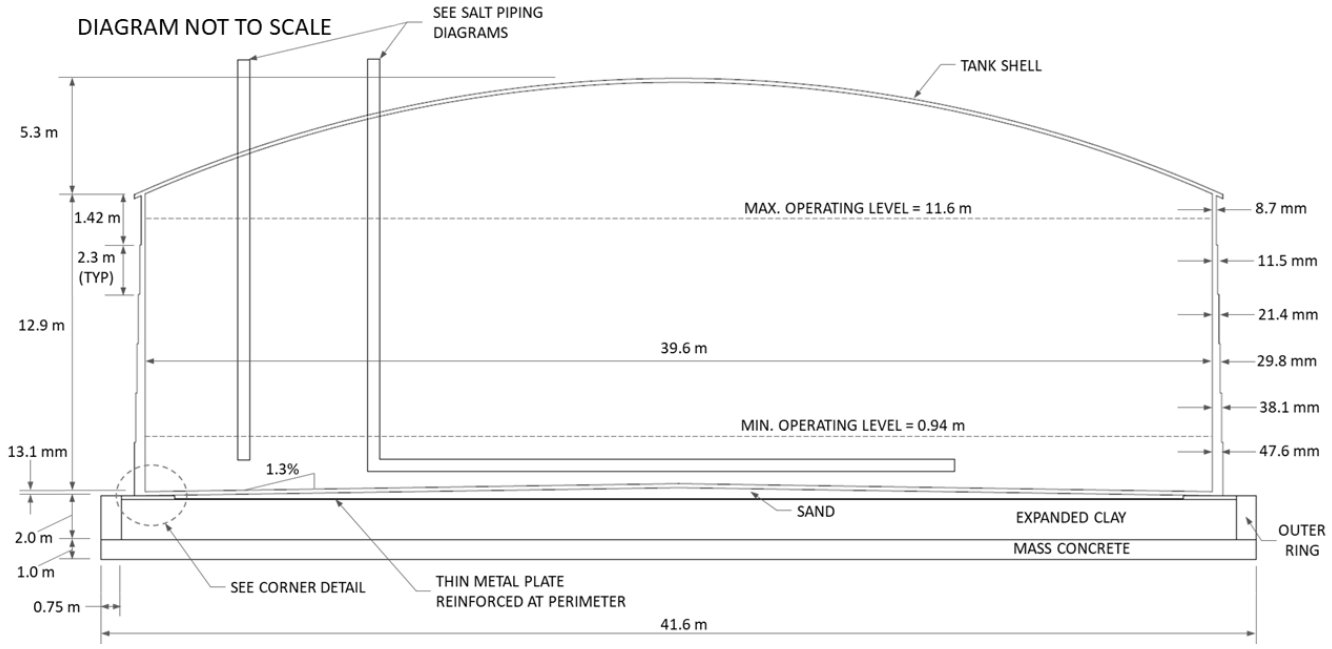

Figure B-1. General assembly

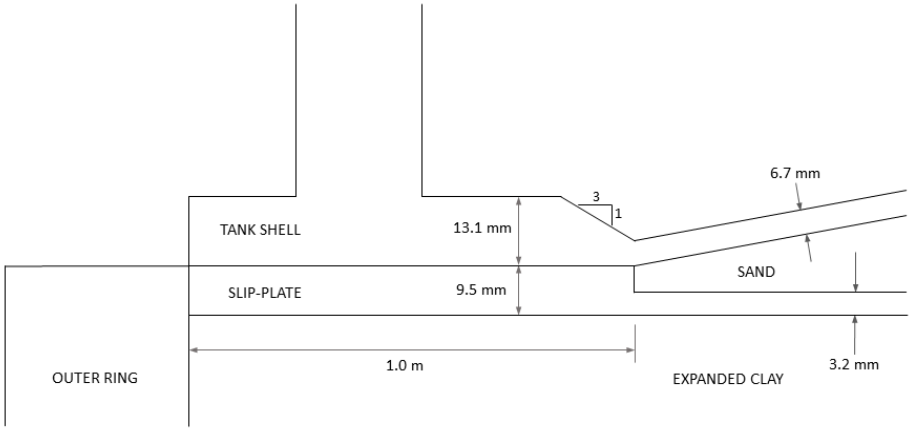

Figure B-2. Corner detail

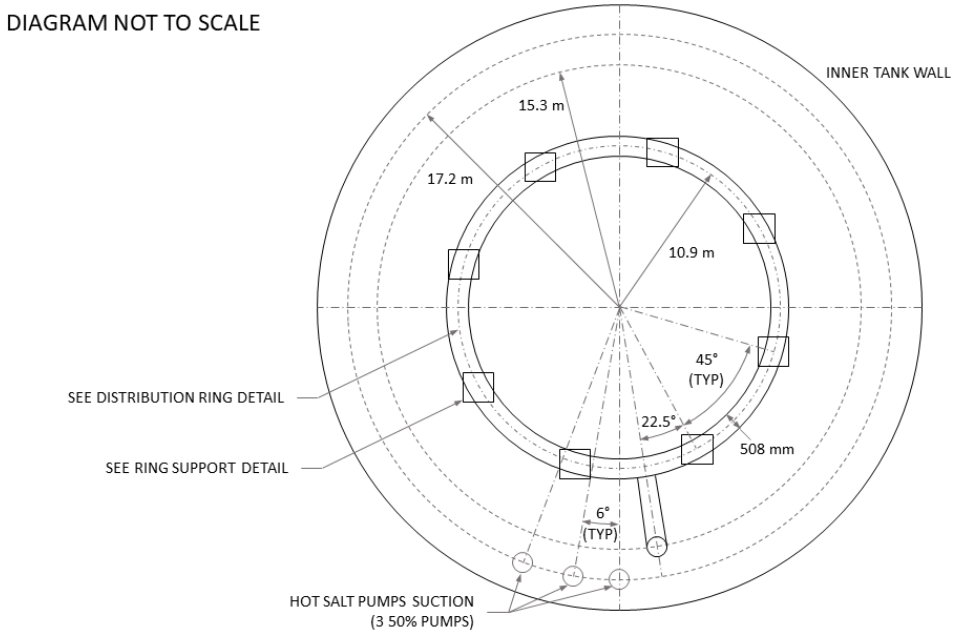

Figure B-3. Salt piping diagram – top view

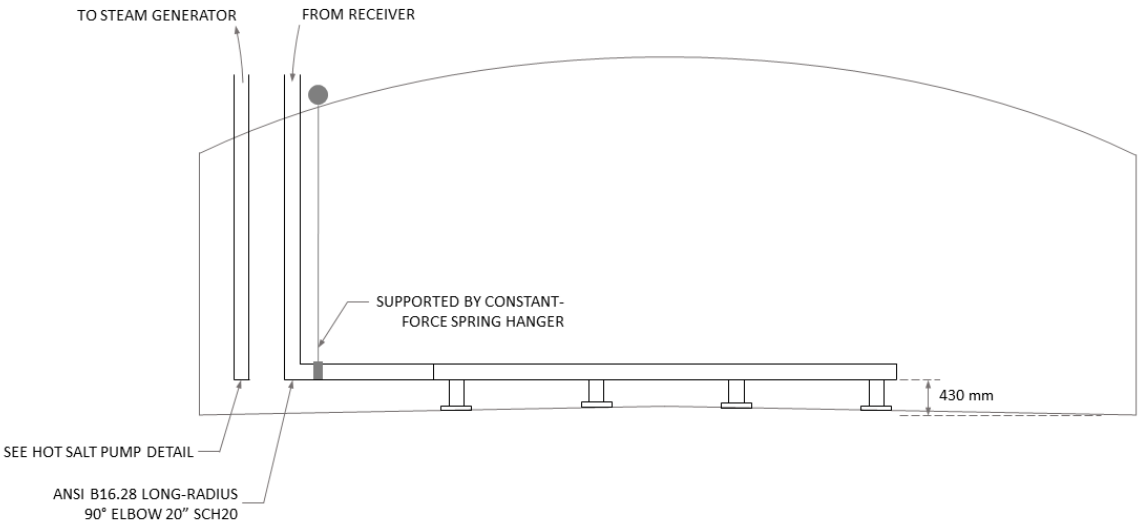

Figure B-4. Salt piping diagram – front view

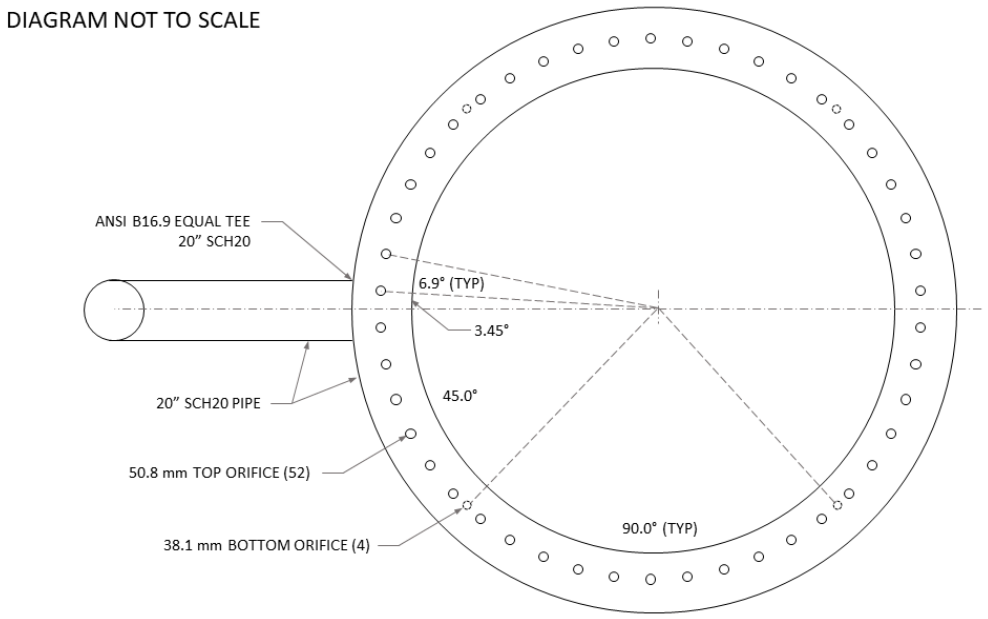

Figure B-5. Distribution ring detail

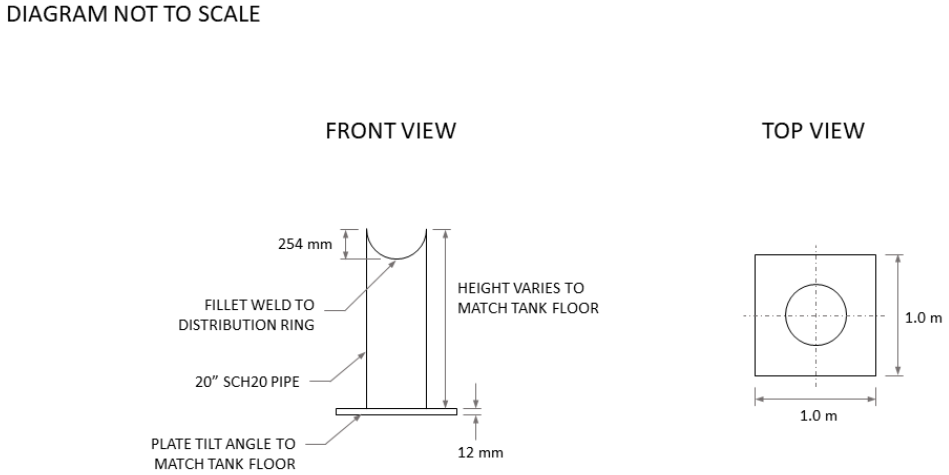

Figure B-6. Ring support detail

Appendix C. Cases Considered in the Parametric Analysis

Table C-1. Operating Conditions for All Cases in the Parametric Analysis; Tank Charging Process

Index Case	Level Salt (L) [m]	Inventory Temperature (T_{inv}) [K]	Inlet Mass Flow (m_{in})[kg/s]	Inlet Mass Flow Temperature (T_{in}) [K]	Outlet Mass Flow (m_{out}) [kg/s]
5	1	673.15	800	773.15	0
6	1	673.15	800	833.15	0
7	1	673.15	1200	773.15	0
8	1	673.15	1200	833.15	0
9	1	803.15	800	773.15	0
10	1	803.15	800	833.15	0
11	1	803.15	1200	773.15	0
12	1	803.15	1200	833.15	0
13	2.33	673.15	800	773.15	0
14	2.33	673.15	800	833.15	0
15	2.33	673.15	1200	773.15	0
16	2.33	673.15	1200	833.15	0
17	2.33	803.15	800	773.15	0
18	2.33	803.15	800	833.15	0
19	2.33	803.15	1200	773.15	0
20	2.33	803.15	1200	833.15	0
21	1	673.15	1000	773.15	0
22	1	673.15	1000	833.15	0
23	1	803.15	1000	773.15	0
24	1	803.15	1000	833.15	0
25	2.33	673.15	1000	773.15	0
26	2.33	673.15	1000	833.15	0
27	2.33	803.15	1000	773.15	0
28	2.33	803.15	1000	833.15	0
29	1	673.15	800	809.15	0
30	1	673.15	1000	809.15	0
31	1	673.15	1200	809.15	0
32	1	803.15	800	809.15	0
33	1	803.15	1000	809.15	0
34	1	803.15	1200	809.15	0
35	2.33	673.15	800	809.15	0
36	2.33	673.15	1000	809.15	0
37	2.33	673.15	1200	809.15	0
38	2.33	803.15	800	809.15	0
39	2.33	803.15	1000	809.15	0
40	2.33	803.15	1200	809.15	0

Table C-2. Operating Conditions for All Cases in the Parametric Analysis; Charging/Discharging Process

Index Case	Level Salt (L) [m]	Inventory Temperature (T_{inv}) [K]	Inlet Mass Flow (m_{in})[kg/s]	Inlet Mass Flow Temperature (T_{in}) [K]	Outlet Mass Flow (m_{out}) [kg/s]
5.1	1	673.15	800	773.15	800
6.1	1	673.15	800	833.15	800
7.1	1	673.15	1200	773.15	1200
8.1	1	673.15	1200	833.15	1200
9.1	1	803.15	800	773.15	800
10.1	1	803.15	800	833.15	800
11.1	1	803.15	1200	773.15	1200
12.1	1	803.15	1200	833.15	1200
13.1	2.33	673.15	800	773.15	800
14.1	2.33	673.15	800	833.15	800
15.1	2.33	673.15	1200	773.15	1200
16.1	2.33	673.15	1200	833.15	1200
17.1	2.33	803.15	800	773.15	800
18.1	2.33	803.15	800	833.15	800
19.1	2.33	803.15	1200	773.15	1200
20.1	2.33	803.15	1200	833.15	1200
21.1	1	673.15	1000	773.15	1000
22.1	1	673.15	1000	833.15	1000
23.1	1	803.15	1000	773.15	1000
24.1	1	803.15	1000	833.15	1000
25.1	2.33	673.15	1000	773.15	1000
26.1	2.33	673.15	1000	833.15	1000
27.1	2.33	803.15	1000	773.15	1000
28.1	2.33	803.15	1000	833.15	1000
29.1	1	673.15	800	809.15	800
30.1	1	673.15	1000	809.15	1000
31.1	1	673.15	1200	809.15	1200
32.1	1	803.15	800	809.15	800
33.1	1	803.15	1000	809.15	1000
34.1	1	803.15	1200	809.15	1200
35.1	2.33	673.15	800	809.15	800
36.1	2.33	673.15	1000	809.15	1000
37.1	2.33	673.15	1200	809.15	1200
38.1	2.33	803.15	800	809.15	800
39.1	2.33	803.15	1000	809.15	1000
40.1	2.33	803.15	1200	809.15	1200
41.1	3.66	673.15	800	773.15	800
42.1	3.66	673.15	800	833.15	800
43.1	3.66	673.15	1000	773.15	1000

Index Case	Level Salt (L) [m]	Inventory Temperature (T_{inv}) [K]	Inlet Mass Flow (m_{in})[kg/s]	Inlet Mass Flow Temperature (T_{in}) [K]	Outlet Mass Flow (m_{out}) [kg/s]
44.1	3.66	673.15	1000	833.15	1000
45.1	3.66	673.15	1200	773.15	1200
46.1	3.66	673.15	1200	833.15	1200
47.1	3.66	803.15	800	773.15	800
48.1	3.66	803.15	800	833.15	800
49.1	3.66	803.15	1000	773.15	1000
50.1	3.66	803.15	1000	833.15	1000
51.1	3.66	803.15	1200	773.15	1200
52.1	3.66	803.15	1200	833.15	1200
53.1	3.66	673.15	800	809.15	800
54.1	3.66	673.15	1000	809.15	1000
55.1	3.66	673.15	1200	809.15	1200
56.1	3.66	803.15	800	809.15	800
57.1	3.66	803.15	1000	809.15	1000
58.1	3.66	803.15	1200	809.15	1200